Universidad de Alcalá

PhD. Programme in Space Research and Astrobiology

Suprathermal and Energetic Electrons as Probes of Interplanetary Magnetic Field Topology

PhD. Thesis Presented by

Fernando Carcaboso Morales

2021

PhD. Programme in Space Research and Astrobiology

Suprathermal and Energetic Electrons as Probes of Interplanetary Magnetic Field Topology

PhD. Thesis Presented by

Fernando Carcaboso Morales

Advisors

Raúl Gómez Herrero and Javier Rodríguez-Pacheco Martín

Alcalá de Henares, July 16st, 2021

Acknowledgements

Siento la tesis como un final, pero no sé muy bien de qué. ¿De una etapa? Puede ser. Está claro que no es el final de mi formación, y está aún más claro que mi tesis no empezó hace cuatro años. Durante el desarrollo he utilizado cosas que he ido adquiriendo a lo largo de muchos tiempo y creo que no tendré más momentos en los que agradecer públicamente a todas las personas que dejaron un poso en mí, que me apoyaron y que hicieron que finalmente me encuentre donde estoy. Por eso, va una larga lista, tanto de académica y profesional como personal, de todos aquellos a los que les debo esto.

Los más directos son, valga la rendundancia, mis directores Raúl y Javier, guías en el desarrollo de mi investigación y apoyo moral. Creo que a la vista está su gran labor (yo no soy tan bueno). Especialmente, no hay palabras que puedan describir mi enorme gratitud hacia Raúl, que no sólo es de las más personas más profesionales e inteligentes que conozco, sino que encima es buena persona. Mañanas, tardes, madrugadas, paseando, por teléfono, por chat, en la montaña, en el mar o incluso en los aires... desde el primer día de mi carrera investigadora ha estado ahí, enseñándome y aguantando mis desvaríos.

También quiero dar las gracias a Miguel Ángel, sin el que gran parte de este trabajo no se hubiera realizado y quien me ha hecho crecer como persona y científico a base de inmensas nubes de trabajo sostenidas en el tiempo. Gracias también a Paco que, aunque no sea consciente, me ha ido radiando parte de su conocimiento durante todos estos años, y a Ignacio, quien sin duda ha estado ahí para todo lo que he necesitado. En general, agradezco a todo el equipo de EPD y las reuniones semanales, y a Teresa por ayudarme con la dichosa burrocracia. Por descontado queda mi agradecimiento al conjunto de integrantes del SRG, quienes han hecho posible que personas como yo podamos saber un poquitín más del espacio, entre los que cabe destacar a Chan, quien depositó su confianza en mí desde el máster y a Juanjo, que me ha hecho mejorar a base de mis errores.

Al resto de compañeros de Ciencias: Ángel y Paco, si todo el mundo fuera como vosotros, no habría guerras en el mundo; a mis compis de despacho Gonzalo y Alejandro; y a los de los buenos ratos y sobremesas, como Carlos, Judith, Germán, Uge, Lupe, Antonio... y sobre todo a Yolanda, con quien siempre he tenido un vínculo especial, y a quien le deseo que se recupere pronto, así como apoyo a la gente de su grupo, sobre todo a Consuelo y Elena.

I also want to thank the different scientists that helped me out abroad in different

centres. To Andrew, Yannis, Pedro, Dave, Alex and all the people in ESAC, it was my pleasure. Zu Nina, Bernd, und Andreas, herzlichen Dank für alles. Y claro está a las comidas, futbolines y tardes con César, Ali y Quinn, y el resto de gente de Kiel. Qué no decir de Teresa Nieves quien me acogió desde un primer momento sin más miramientos. Obrigado, Luiz, and also especial thanks to Ian Richardson and Lan Jian, who are always asking the right questions. Für meine österreichisch-kroatische Familie, mit der ich gerne wieder in Kontakt treten möchte: Manuela, Mateja, Astrid, Isi, Jasa, Karin, Aarón, Veronika, Bin, Bojan, Stephan.

A mis compañeros más cercanos: Thanks to Georgie for pretty much everything you've done for me, from the first meeting to the last ride; gràcies per el meu company i amic Dani, cuando seamos vecinos te ganaré al tenis; thank you to the article-machine, Jingnan, that has been always teaching and taking care of me; Nils, we still have a pending match; Rahul, Dear Lord of Spicules and Remote-Sensing Waves Inferring with h... I hope to see you all soon.

A la gente de Crisa que me introdujo en este mundo y me enseñó a programar "decentemente", como Mario, Justo e Ignacio. A mis compañeros de máster: a Fernando, la persona que he visto quejarse menos de su propia tesis doctoral, a mi pseudo-quasi-congénere Irene que fue la primera persona que me enseñó lo que es una CMEh y me hizo menos pesados los trabajos en la biblioteca, y a la locuaz y bella persona, Álvaro. A mis compañeros de grado, a Alberto, Dávila, Antonios, Mariano, Monty, Diego, Max, María. A todo el mundo de Aarhus, a mi mejor amigo Diego, quien tristemente decidió dejarnos hace siete años y medio en Preikestolen antes de que la edad le hiciera mella. Also to Konrad, Momo, Yuri, Emmanuel...

Los motivos por los que soy quien soy y a los que por desgracia ya no veo tanto: a los innumerables compañeros y profesores del instituto y del conservatorio. Entre ellos, a Vicente Toldos, Posse, Sonia, Olga, Samu, Alex, Sylvia, Rocío, Gus, Ana, Rubén, Luz, Rufus, Isaac, Charo, Manuela, Juande, Inma, Antonio López, Lorenzo y Juan...

A la gente que viste y adecenta mi vida: Lorechan, Ana, Cris, Guille, David, Alicia, Jose, Cuchi. A todo mi entorno de mis años en teatro, a Fátima, Víctor, Juan, Saúl, Cotu, Amparo. Y a los descerebrados que se entramparon conmigo donando y coordinando la donación de pantallas contra la COVID-19 y la gente de REXUS/BEXUS: Ángel, Isma, Raúl, Víctor, Manolo y Agustín.

A mi pareja, apoyo, compañera de piso, mejor amiga y modelo a seguir, Elba. Creo que pocos ejemplos hay de tanta profesionalidad y esfuerzo que estén siempre acompañados de una sonrisa y ambición de éxito, a la que no le basta con sacarse tres carreras y dos másteres, sino que me ayuda a corregir mi tesis, y a su familia, Alberto, Rudy, Rodolfo, Rocío, Consolación, Alicia y Sofía, que desde el primer momento me acogió como a uno más. A mi hermano de montaña Juanma con el que volví a nacer después de horas bajo cero, a su mujer Noe, y las dos perlas doradas Arya y Sofía. Al arquitecto-bombero

medieval Jacobillo, y los dos doctores que ayudaron a mejorar esta tesis: súper Román y mi primo Jesús. También a la ingeniosa Mel, a los siempre agradables Sandra, Felipe y Alba, y también a Bea, a Rocío y Javi.

Y, por supuesto, a las tres personas que siempre han estado ahí creyendo en mí, sin dudar ni un momento: mis padres, Teresa y Paco, y mi hermano Fran. Y también a mi afortunadamente inmensa familia directa y postiza: Manuel, José Fernando, Roberto, María Teresa, María, José Fernando, Claudia, Candela, José Antonio, Maite, María Ángeles, Joan, Marta, Manuela, mi madrina, José Luis, Dolo, Salva, Mari Carmen, José Fernando, Josefitas, Juani, Ramón, María José, Ignacio, Joaquina, Carmen, Miguel, Miguelito, Sergi, Ferrán, Antonia, Ramonet, Anita, Ana, Serafín, Salva García, Paqui, Rafa, Elena, Nela, Helena... y a los que desgraciadamente nos han dejado: Ana, Joseíco, Tere, mi tío Antonio, y mis abuelos.

Finally, I want to acknowledge the financial support by the Spanish MINECO-FPI-2016 predoctoral grant with FSE, and its project ESP2017-88436-R. We would also like to thank the different instrument teams of STEREO mission for their open-access data policy. This PhD work uses data from the Heliospheric Shock Database, generated and maintained at the University of Helsinki.

Esta y mucha más gente que seguro que me dejo, han hecho posible que yo hoy entregue mi tesis.

A todos, gracias.

Fernando Carcaboso Morales

List of Acronyms

ACE	Advanced Composition Explorer.
AR	Active Region.
BDE	Bi-Directional suprathermal Electrons.
CH	Coronal Hole.
CIR	Co-rotating Interaction Region.
CME	Coronal Mass Ejection.
CR	Cosmic Ray.
DF	Distribution Function.
EPD	Energetic Particle Detector.
ESA	European Space Agency.
EUI	EUV full-Sun and high-resolution Imager.
FD	Forbush Decrease.
FIELDS	Electromagnetic Fields Investigation.
FR	Flux Rope.
GCS	Graduated Cylindrical Shell.
GGS	Global Geospace Science.
GONG	Global Oscillation Network Group.
HCS	Heliospheric Current Sheet.
HFD	Heat Flux Dropout.
HSO	Heliophysics System Observatory.
ICME	Interplanetary Coronal Mass Ejection.
IMF	Interplanetary Magnetic Field.

IMPACT	In-situ Measurements of Particles and CME Transients.
IP	interplanetary.
IS⊙IS	Integrated Science Investigation of the Sun.
MAG	Magnetometer.
MC	Magnetic Cloud.
MO	Magnetic Obstacle.
NASA	National Aeronautics and Space Administration.
PA	Pitch Angle.
PAD	Pitch-Angle Distribution.
PFSS	Potential-Field Source-Surface.
PHI	Polarimetric and Helioseismic Imager.
PLASTIC	PLAsma and SupraThermal Ion Composition.
PSP	Parker Solar Probe.
RPW	Radio and Plasma Wave analyser.
RTN	Radial-Tangential-Normal.
s/c	spacecraft.
SDO	Solar Dynamic Observatory.
SECCHI	Sun Earth Connection Coronal and Heliospheric Investigation.
SEP	Solar Energetic Particle.
SEPT	Solar Electron Proton Telescope.
SI	Stream Interface.
SIR	Stream Interaction Region.
SNR	Signal-to-Noise-Ratio.
SOHO	Solar and Heliospheric Observatory.
SolO	Solar Orbiter.
SoloHI	Solar Orbiter - Heliospheric Imager.
SOOP	Solar Orbiter Observing Plan.
SPICE	EUV spectral Imager.
SSN	Sun Spot Number.
STEREO	Solar Terrestrial Relations Observatory.
STIX	Spectrometer Telescope for Imaging X-rays.
SW	Solar Wind.
SWA	Solar Wind Analyser.

SWAVES	STEREO/WAVES.
SWEA	Solar Wind Electron Analyzer.
SWEAP	Solar Wind Electrons Alphas and Protons.
SWEPAM	Solar Wind Electron, Proton, and Alpha Monitor.
TSA	Time-Shifting Analysis.
VDA	Velocity Dispersion Analysis.
VDF	Velocity Distribution Function.
WISPR	Wide-field Imager for Solar Probe.

Contents

List of Acronyms xi

Contents xiii

List of Figures xvii

List of Tables xxiii

1. Introduction - The Sun 1

1.1. Layers of the Sun . . . 2

1.2. Ubiquitous Solar Plasma and Magnetic Field . . . 3

1.2.1. Solar Wind and Interplanetary Magnetic Field . . . 7

1.2.2. Suprathermal Electrons . . . 8

1.3. Solar Activity Phenomena . . . 12

1.3.1. Solar Flares . . . 13

1.3.2. Radio Bursts . . . 14

1.3.3. Coronal Mass Ejections . . . 15

1.3.3.1. Modelling Interplanetary/Coronal Mass Ejections . . . 18

1.3.4. Stream Interaction Regions . . . 19

1.3.5. Solar Energetic Particles . . . 21

1.4. Main Goal of the Thesis . . . 23

1.5. Coding and Development . . . 24

2. Instrumentation and Catalogues 27

2.1. Near-Earth Missions . . . 27

2.2. The STEREO Mission . . . 29

2.3. Parker Solar Probe and Solar Orbiter . . . 31

2.3.1. Parker Solar Probe . . . 32
2.3.2. Solar Orbiter . . . 33
2.4. Catalogues . . . 34

3. Studying Suprathermal Electron Pitch-Angle Distributions 37
3.1. Pitch-Angle Distribution Characterisation . . . 38
3.2. Isotropy and Bi-Directional Suprathermal Electrons . . . 43
3.2.1. Defining the Isotropy . . . 43
3.2.2. Defining the Bi-directionality . . . 46
3.2.3. Long-term Variation of Isotropy and Bi-directionality . . . 49
3.2.4. Catalogues of Bi-directional and Isotropic Periods . . . 51
3.3. Anisotropy . . . 52
3.3.1. Anisotropy Variation . . . 52
3.3.2. Heliomagnetic Latitude Dependency . . . 56

4. Interplanetary Coronal Mass Ejection Research 59
4.1. Variations of Isotropy and Bi-directional Suprathermal Electron . . . 59
4.1.1. Bi-directionality . . . 59
4.1.2. Isotropy . . . 62
4.2. Approaching the Flux Rope Topology . . . 64
4.2.1. Topology . . . 64
4.2.2. Mathematical description . . . 68
4.2.2.1. Parameters . . . 68
4.2.2.2. Model Updates . . . 69
4.2.2.3. Equations . . . 70
4.2.3. Flux Ropes in the Solar Wind . . . 72
4.2.3.1. Identification . . . 72
4.2.3.2. Analysis . . . 72

5. Energetic Electrons 79
5.1. Radio Burst Tracer Model . . . 79
5.1.1. Plasma Density and Radio Emissions . . . 80
5.1.2. Measuring Distances with Time Differences . . . 81
5.1.3. Defining Interface Conditions . . . 81

5.1.4. Model Representation 82
5.1.5. Fitting Process and Considerations 82
5.1.6. Application 83
5.1.6.1. 2 and 3 December 2013 Events 84
5.1.6.2. 26 February 2011 Event 85
5.1.6.3. 2 May 2014 Event 89
5.2. Quasi-relativistic and Suprathermal Electrons Comparison 89

6. Summary and Conclusions **97**
6.1. Summary 97
6.2. Conclusions 100
6.2.1. Suprathermal Pitch-Angle Distribution Research 100
6.2.1.1. Long-Term Variation 100
6.2.1.2. Energy and Latitude Dependency 100
6.2.2. Interplanetary Coronal Mass Ejection Research 101
6.2.2.1. Suprathermal Electron Pitch-Angle Distribution inside Interplanetary Coronal Mass Ejections 101
6.2.2.2. Flux Rope Statistical Analysis 102
6.2.3. Energetic Electron Analysis 102
6.2.3.1. Type III Radio Burst Tracer Model Case Studies 102
6.2.3.2. Statistical Analysis of Impulsive Solar Energetic Particle Events 103
6.3. Future Work 103

Bibliography **105**

Appendix **117**

List of Figures

1.1. Variation of the electron temperature (red) and density (blue) with respect to the relative height to the solar surface accompanied by the corresponding layer's name. Figure corresponding to Figure 1.1 from Howson (2019), which is based on data from Avrett & Loeser (2008). 4

1.2. Upper panel shows the number of sunspots over time showing the different catalogued solar cycles. The number of sunspots is higher in solar maximum and lower in solar minimum. Second panel shows the latitudinal distribution and density of the sunspots over time in the so-called *butterfly diagram*. Source: ISES/NOAA/Space Weather Prediction Center. 5

1.3. Contributions to the oxygen fluence observed by Advanced Composition Explorer (ACE) from October 1997 to June 2000. Some periods are tagged indicating the source. Credit: Mewaldt et al. (2001). 6

1.4. Sketch of the typical velocity distribution of the SW electrons. Colour scale in logarithmic scale indicates the number density n as a function of two components of the velocity (V_x and V_y for top panel, $V_{\parallel}$ and $V_{\perp}$ to $\vec{B}$ for bottom one). The beam of electrons aligned with the magnetic field (B, orange arrow, top) represents the *strahl* population. The behaviour of the populations show the different shown distributions. See text for more details. Credit: Graham et al. (2017) (top); Verscharen et al. (2019) (bottom). 9

1.5. Sketches of suprathermal electrons PAD patterns observed in the IP medium. Horizontal axis represents the cosine of the PA, while the vertical axis shows the VDF in linear scale (arbitrary units). (Image adapted from Carcaboso et al., 2020) 11

1.6. Sketch of solar radio burst dynamic spectra (frequency and intensity versus time). See text for description. Credit: Ganse et al. (2012). 15

1.7. Representation of a possible mechanism for the emergence of a CME with the electromagnetic emission associated to each region. a) sketches a stable FR (blue lines) below a magnetic arcade (orange lines), both of them with their foot-points near active regions with opposite polarity. b) and c) represent the reconnection of arcade with opposite direction and the subsequent emergence produced by the energy release of the phenomenon. d) shows a cross-section view of the process indicating the origin of different emissions. Figure adapted from Klein et al. (2018). 16

1.8. Representation of a SIR. The interaction between fast and slow SW can produce more intense magnetic field near the stream interface (IF) and the region can be bounded by a Fast Forward shock (FS) and a Fast Reverse Shock (RS). Source: NASA's Cosmos, ase.tufts.edu/cosmos. 20

1.9. Sketch of the observed time profiles of plasma properties during the transit the Fast Forward (FF) and Fast Reverse (FR) shocks. V stands for the bulk velocity, while B is the magnetic field strength, N represents the density and T the temperature. Image modified from wind.nasa.gov/mfi/ip_descr.html 21

2.1. Currently operating solar (as in April 2020), heliospheric and magnetospheric observatories and their relative position in the IP space. These observatories form the the Heliophysics System Observatory (HSO). Some missions inside the magnetosphere (purple bubble) own an orbit which may often cross the Earth's magnetosphere boundary. Source: svs.gsfc.nasa.gov/30822. 28

2.2. Sketch of the orbit of the STEREO mission. Left: heliocentric trace of both STEREOs and Earth; right: fixed Sun–Earth line and the relative position of both s/c. Credit: (Kaiser et al., 2008). 30

3.1. Distribution function of the Legendre Polynomials up to fifth order in arbitrary units. Even harmonics are symmetric along $cos(\theta) = 0$, and odd harmonics are antisymmetric. 40

3.2. STEREO-A/SWEA PAD for channel 120–190 eV on March 2012 (bottom). Zoomed boxes shows the snapshots of the corresponding shown timestamps and represents the DF (blue dots) and the Legendre polynomials fit (red line). Grey box is isotropic, green shows BDE -counterstreaming-, and blue and red shows single *strahl* with outward and inward polarity, respectively. 41

3.3. 2D histograms showing the relation between the log_{10} of the anisotropy coefficient γ and the log_{10} of the plasma β for the entire period under study (2007 – 2014) for STEREO-A (top) and STEREO-B (bottom). Horizontal black line shows γ_{th} (see text for details), and colour bar indicates the number of events for each bin in logarithmic scale. 45

3.4. Two-dimensional histogram showing the number of occurrences of the anisotropy coefficient γ versus the result of A_1/A_0, which represents the first order anisotropy value (see e.g. Tan et al., 2007). 46

3.5. STEREO-A observations during a period in September 2013 including two intervals of isotropic flux of suprathermal electrons shaded in yellow. From top to bottom: SW proton speed, proton density, proton temperature, IMF magnitude accompanied by its polarity (red, negative; green, positive; yellow, ambiguous), IMF azimuthal angle in the RTN coordinate system complemented with the two possible nominal Parker Spiral angles (red, negative; green, positive) calculated from the proton speed, IMF latitudinal angle in the RTN coordinate system, RTN magnetic field separated components, plasma β, the anisotropy coefficient for suprathermal electrons γ (*ripple*, see Section 3.1), the bi-directionality coefficient SNR_{24} (see section 3.1), and 119–194 eV suprathermal electron PAD colour-mesh (y-axis is the angle in degrees, z-axis represents the DF in logarithmic scale). 47

3.6. Histograms of the calculated SNR_{24} for the selection of ICMEs with longer periods of BDE (red, listed in appendix), and for quiet SW (blue). 48

3.7. Temporal variation of the time percentage during 3 months of isotropic periods (blue) and bi-directional periods (green). From top to bottom: Percentages of time appearance calculated for a running window of three months of isotropy for STEREO-A, isotropy for STEREO-B, and overplotted the heliocentric distance of both s/c; BDE for STEREO-A, BDE for STEREO-B, accompanied by the time transit of ICMEs listed in *ICME Catalogue* (see Section 2.4); finally, SSN and latitudinal angle of the HCS. (See text for more details) 50

3.8. Temporal variation of the anisotropy coefficient γ calculated for 252 eV energy channel for STEREO-A/SWEA, STEREO-B/SWEA and 272 eV energy channel for ACE/SWEPAM. Dimmed lines represent the 5-day mean value, while stronger ones correspond to high-pass-filtered ones. 53

3.9. Temporal variation of the anisotropy coefficient γ for the different energy channels (legend indicates the center of each channel in eV) of both STEREOs. (Top, A; bottom, B) 53

3.10. Cumulative histograms of the anisotropy coefficient γ for the different available energy channels (in eV) of STEREO-A (top) and STEREO-B (bottom) 54

3.11. Yearly histograms of the anisotropy coefficient γ calculated for the 272 eV energy channel measured by ACE/SWEPAM (left); Monthly sunspot number in black and smoothed values in purple (right). Red crosses indicate the median value of the histograms. 55

3.12. Mean value of the anisotropy coefficient γ with respect to the heliomagnetic latitude described in Section 3.3.2 for each observatory, calculated from June 2009 to June 2011 (Green: ACE; red: STEREO-A; blue: STEREO-B. See text for more details). Error bars correspond to the standard error of the mean. 58

4.1. Histograms showing the mean value of the time-percentage of BDE for each interval during all the ICMEs transits catalogued in *ICME Catalogue* for all the events (top), with shock at the beginning (center), and without (bottom). The colours show the different catalogued regions (see text for more details) and the labels correspond to equi-timed periods of the transit of those regions (S – Sheath, MO – Magnetic Obstacle, P – Post-ICME). The error bars indicate the standard error of the mean. 61

4.2. STEREO-A observations during an ICME observed on October 08–13 2011. The panel contents follow the same format as in Figure 3.5. 63

4.3. Histograms of mean value of the time-percentage of isotropy of each sector during all the ICMEs transits catalogued in *ICME Catalogue* for all the events (top), with shock at the beginning (center) and without (bottom). Colours and labels follow the same format as in Figure 4.1. 65

4.4. STEREO-B observations during an ICME observed on October 03–05 2013. The panel contents follow the same format as in Figure 3.5. 66

4.5. Recreation of an example of the global morphology of a MC according to Hidalgo's Model, with the legs attached to the Sun and the cross-section at the front part (i.e. the *nose*) is wider than at the legs. The blue line represents the axis of the cross section -with only axial component-, while the green one shows the boundary of the FR -with a mixture of axial and helicoidal field-. In between these two, orange mesh reproduces the lines as an addition of both components. 67

4.6. Observations of STEREO-A from July 5, 2008 to July 6, 2008. Figure follows similar format as Figure 3.5. See text for more details. 74

4.7. Observations of STEREO-B from June 6, 2008 to June 8, 2008. Figure follows similar format as Figure 3.5. See text for more details. 75

4.8. Scatter plot representing the orientation of each fitted FR for each year. Colour indicates the average speed during the transit of the FR and the size of the circle represents the cross-section radius as inferred from Hidalgo's model. Note: 2007 and 2014 panels do not cover the full year. 77

5.1. Sketch of a hypothetical propagation of a beam (curved yellow arrow) which originates a radio emission observed by two separated s/c (A, green; B, blue). Left panels show the onset for different frequencies at the two s/c and the time difference due to the light propagation. See text for more details. 83

5.2. Radio burst released at 11:04 2 December 2013 corresponding to the SEP event studied by Gómez-Herrero et al. (2017). Radio spectrograms with the corresponding fits and orbital position (red, STEREO-A; blue, STEREO-B; green, Earth; yellow, Sun) and the modelled beam (Top: axis of MC, Bottom: Nominal Parker spiral, PS). See text for more details. 86

5.3. Radio burst released at 18:55 3 December 2013 associated to the second event studied by Gómez-Herrero et al. (2017) with the corresponding fit. Panels follow the same format as in Figure 5.2 87

5.4. Radio burst released at 06:25 26 February 2011 studied by Klassen et al. (2012) and the best obtained fits. Panels follow the same format as in Figure 5.2. 88

5.5. Radio burst released at 05:01 2 May 2014 studied by Klassen et al. (2015) and the propagation of the beam crossing STEREO-A (top), STEREO-B (middle) and an intermediate point (bottom). The rest of the panels follow the same format as in Figure 5.2. 90

5.6. SEP event observed by STEREO-B on November 3 2009 and tagged as number 31 in the STEREO/SEP catalogue. From top to bottom: SW speed (left) and orbital position (right; red for STEREO-A, blue for STEREO-B and yellow for Sun); azimuthal and latitudinal angles, and strength of the IMF as in Figure 3.5; suprathermal electron anisotropy coefficient γ (ripple); radio spectrograms as seen by STEREO-A and STEREO-B; electron intensity for the four STEREO/SEPT telescopes; angular pointing of the telescopes; combination of the field of view of the telescopes and the observed intensity; intensity for each inverse velocity (derived from the energy channel) relative to the speed of light for the four STEREO/SEPT telescopes. See text for more details. 93

5.7. Scatter plot of the average anisotropy coefficient γ of suprathermal electrons from $\sim$ 180 eV to $\sim$ 366 eV versus the relation between the nominal Parker spiral length based on the SW speed and the theoretical one inferred from travel of the particles calculated from the time delay between the type III radio burst and the time arrival of the SEPs as catalogued in the *STEREO/SEP catalogue*. Error bars in y-axis correspond to the standard error of the mean. **Colours:** (Based on the catalogues listed in Section 2.4) green: MO; blue: post-ICME; purple: SIR before the SI; pink: SIR after the SI; yellow: close to shock; grey: uncatalogued. **Symbols:** (Based on the SW classifier. See text for details.) $\times$: ejecta; $\star$: CH; $\blacktriangledown$: sector reversal; $\bullet$: streamer belt. 95

List of Tables

1.1. Flare classifications based on Hα and soft X-ray emissions in terms of area and size. Credit: Table 4.3 Russell et al. (2016) 13

4.1. Parameters that define some physical plasma properties (IMF and current density) in Hidalgo's Model for MCs. 68

4.2. Parameters that establishes topological characteristics of the MCs (section variation orientation and deformation, impact factor, and orientation based on Hidalgo's Model. 69

1. Table showing the selection of the candidates with long and clear periods of BDE observed by STEREO-A and STEREO-B. 123

2. List of FRs observed by STEREO from 2007 to 2014 accompanied by the Hidalgo's model fitting parameters. 133

Chapter 1

Introduction - The Sun

The Sun is the closest star to the Earth. Its light has made possible the existence of life on the planet and for this reason it has been venerated and studied since the very beginning of humanity. Nowadays many of the physical properties of the Sun are known with fairly good accuracy. We also have determined its modulation in tides and the existence of the solar cycle and its influence in Cosmic Ray (CR) modulation and geomagnetic activity. But still, there are many unexplained properties and phenomena of the Sun that need to be explained.

From an astrophysical point of view, the Sun is classified as a G2V star, i.e. it has a spectral class G2 (Yellow, effective temperature of a black body of 5,780 K) and a luminosity class is V, corresponding to the main sequence in the Hertzsprung–Russell diagram (Russell, 1914). It is composed by a plasma principally consisting of hydrogen (73.46 %) and helium (24.85 %), and its age is 4.6 billion years.

The Sun is quasi-spherical, suffering of flattening on the poles, owns an equatorial radius of 695,000 km, and the average density is 1.4 g/cm^3. Its mass is 1.989 x 10^{30} kg, which corresponds to the 99.87% of the total mass of the Solar System. The star is also streaming plasma to the interplanetary (IP) medium with a rate between 1.3 x 10^9 and 1.9 x 10^9 kg/s (Schrijver & Zwaan, 2000). This continuous mass loss constitutes the plasma denominated Solar Wind (SW) analogously to Earth's meteorology. The amount of mass contained in the star is sufficient to make the star collapse due to the gravity force, nevertheless the gas pressure produced by the nuclear reactions and the heat tends to expand the plasma, which keeps it stable in a hydrostatic balance.

The Sun is orbiting the nucleus of the galaxy where it is contained (the Milky Way) with an orbital radius of about 27,000 light-years, and it is located in the Orion Arm. Also, the Sun is spinning with angular velocities that depend on the heliographic latitude. This phenomenon is called *differential rotation*. At the equator, the Sun takes 25.05 sidereal days to rotate on its axis, while a total rotation in the poles takes approximately 34 days.

1.1. Layers of the Sun

Going from the center of the sphere to outer locations, the star can be divided into different layers based on their physical properties and the dominant energy transfer processes:

- **Core** goes up to 0.25 solar radii and it is where almost all the hydrogen-nuclei fusion reactions occur to produce helium in a proton-proton chain reaction (Salpeter, 1952). It is also the hottest region ($\sim$ 15 million K) of the Sun and the most dense too ($\sim$ 150 g/cm^3). The density of the star decreases from this layer to the external ones.
- **Radiation Zone** corresponds to the region where the dominant energy transport process is electromagnetic radiation and the thermal conduction. The temperature at its outer boundary, which can be found at 0.8 solar radii, is 1.5 million K. The drop in temperatures is produced because a photon mean free path in this region is approximately 1 cm -taking thousand of years to be released from this region-, which produces a shift of the photons' frequencies to lower ones, reducing their energy.
- **Tachocline** is the very thin region ($<$ 5% percent of the solar radius Dikpati, 2006, and references therein) where the Radiation and the Convection zones interact. This region suffers a huge shear stress in a small space due to the sudden change of the properties of the plasma, as the interior layer rotates rigidly and the exterior one flows with differential rotation (Spiegel & Zahn, 1992). That exterior layer is called the Convection Zone.
- **Convection Zone** is the layer that is found when the density is reduced enough to allow efficient energy transport from the interior to external layers by convective heat transport (approximately at 0.86 solar radii). The differential rotation above mentioned (being slowly at the poles and quicker at the equator, Beck, 2000) and the convection movements are thought to be the ultimate causes of the existence of the intense magnetic field of the star, caused by the complex process denominated *solar dynamo* as explained in the Babcock-Leighton model (Babcock, 1961; Leighton, 1964, 1969), although there are still features of the model under debate (Charbonneau, 2007).
- **Outer Layers** (or solar atmosphere) correspond to those layers that can be directly observed by their electromagnetic emission and absorption.

  Photosphere (or solar surface) corresponds to the solar disk in visible light. It has a width of approximately 500 km where its temperature goes from 4,500 to 6,000 K and becomes lower with increasing height. The intense magnetic field originated by the solar dynamo is manifested on the photosphere by darker regions with respect to the surroundings, due to their lower temperature. These areas are denominated *sunspots* and they are variable in time as described below (see Section

1.2). The magnetic field of the photosphere can be measured by magnetographs, and the sunspots can have positive polarity, negative polarity, or both of them.

Chromosphere. The density of this layer decreases dramatically ($\sim 10^4$ times) and continues dropping with higher altitudes. In contrast to the photosphere, the temperature decreases from 6,000 K to 4,000 K and then increases until 8,000 K in $\sim 2,000$ km. The chromosphere presents emitting hair-like filaments denominated spicules, generated by the rising of plasma travelling at 20 km/s. The physical mechanism or mechanisms that produce them are still under debate.

Transition Region is a very thin layer ($<\sim$ 100 km), where the temperature increases from 8,000 K up to 500,000 K. The ultimate cause of this sudden change is still unknown. A similar phenomenon occurs on the corona, and it is denominated *coronal heating*.

Corona and Heliosphere. The matter that forms the heliosphere is called SW, which presents a still-unknown mechanism that increases its temperature (about 10^6 K, see Klimchuk (2006) and references therein), which might be produce by the absorption of alfvenic waves (Rosner et al., 1978). The inherent magnetic field of the SW is denominated Interplanetary Magnetic Field (IMF). It is very intense and complex and present typical topologies as described in the following sections. Although there is not physical boundary between the solar corona and heliosphere, the last one is considered to be the outer and largest layer of the Sun, which contains all the planets of the Solar System and extents up to the heliopause (approximately 120 au, (Krimigis et al., 2013; Richardson et al., 2019)), while the first one is the region observed by coronographs (up to $\sim$ 30 solar radii). Beyond the heliopause, the interstellar space is found.

So far, the heliosphere is the only layer whose properties can be measured with in-situ instruments onboard space observatories (except Parker Solar Probe (PSP) in the lower corona, approaching to within 9.86 radii, see Chapter 2). The heliosphere is continuously being influenced by the variability of the solar conditions. Apart from the gravity, the electric and magnetic fields dominate in the IP medium. All these conditions create typical topologies and phenomena which are described in the following sections.

1.2. Ubiquitous Solar Plasma and Magnetic Field

As mentioned above, one of the main manifestations of the magnetic activity can be located on the solar surface at the sunspots. Dimensions, clustering, and magnetic polarity of these regions are variable and the number and behaviour are also different in time. Independently of the surroundings, they can have positive and negative polarity, often found close to each other. This can be measured by the use of magnetographs,

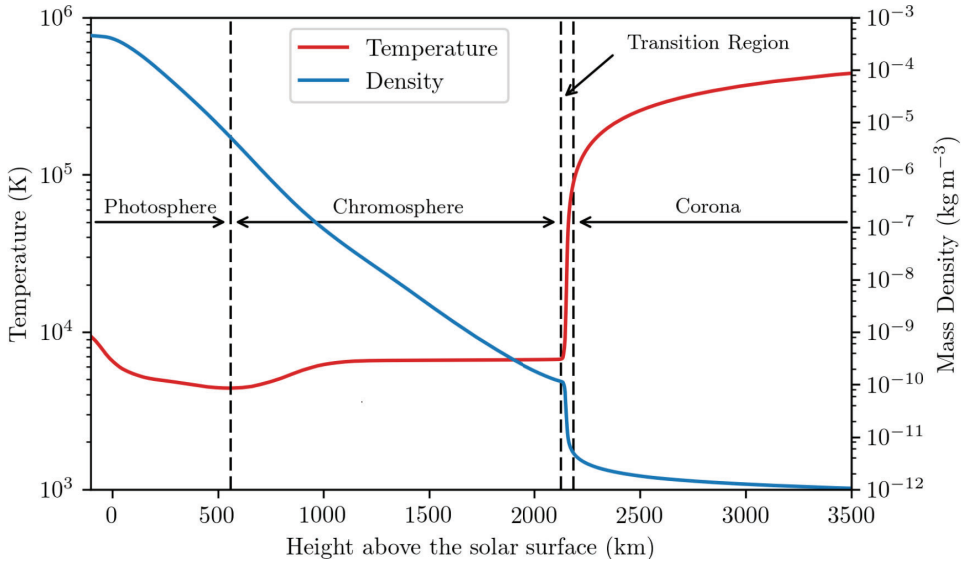

Figure 1.1: Variation of the electron temperature (red) and density (blue) with respect to the relative height to the solar surface accompanied by the corresponding layer's name. Figure corresponding to Figure 1.1 from Howson (2019), which is based on data from Avrett & Loeser (2008).

which measures the remote magnetic field on the solar surface. The photosphere owns an average magnetic field strength that goes from $\sim$ 1 G to tens of G, while the sunspots have typically values around 3,000 G.

Although the quiet-Sun's magnetic topology predominantly shows a nearly magnetic dipole topology -at least during solar quiet periods-, every approximately 11 years the dipole reverts and, during the process, the bi-modal behaviour is smeared. After $\sim$ 22 years, the poles are back to their original configuration. This periodic behaviour is denominated the *solar cycle*. While the switch is taking place, the activity of the Sun goes from being more dynamic with more frequent eruptive events to quieter. For this reason, it is said that the solar cycle owns a *solar maximum*, where the activity is higher (i.e. more intense and with frequent eruptive events), and a *solar minimum*. The process begins (considering the solar minimum) with the sunspots, regions magnetically intense, emerging at latitudes around $\pm$30 degrees. During the 11-year period, the sunspots overall evolve in number and size. They also tend to approach the heliographic equator when the activity is higher. The number of sunspots is commonly utilised as an indicator of the solar activity. They have been observed since the first telescopic observations during the 17th century until now, and registered and numbered since the 18th century as Figure 1.2 shows, although the actual solar sunspot number may be slightly different as Acero et al. (2017) show.

Sunspots are typically indicators of Active Regions (ARs) in higher layers. ARs show a disturbed magnetic field which may twist and reconnect (i.e. magnetic field is rearranged, splicing to one another, modifying the initial conditions) at some point sometimes producing high-energy phenomena as solar flares, Coronal Mass Ejections (CMEs) or Solar Energetic Particle (SEP) events (see Section 1.3).

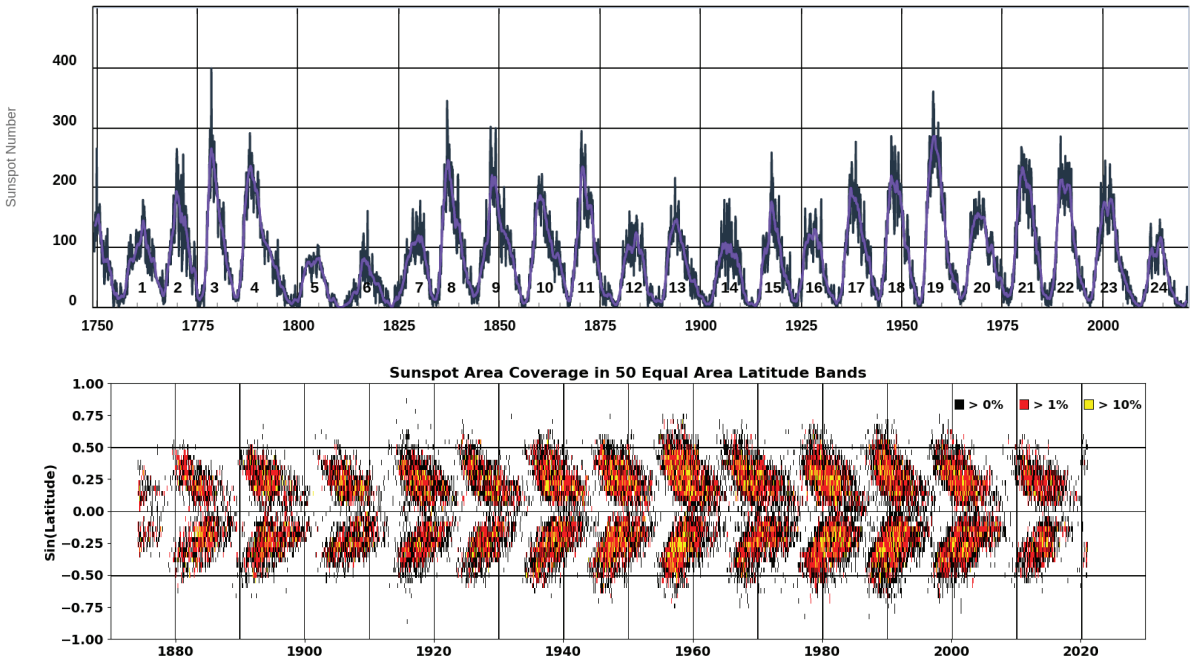

Figure 1.2: Upper panel shows the number of sunspots over time showing the different catalogued solar cycles. The number of sunspots is higher in solar maximum and lower in solar minimum. Second panel shows the latitudinal distribution and density of the sunspots over time in the so-called *butterfly diagram.* Source: ISES/NOAA/Space Weather Prediction Center.

The magnetic field in these places can indirectly be observed by the confined plasma which is commonly forming coronal loops, solar prominences, or helmet streamers. The poles of the Sun mainly present almost stationary open field lines generating fast SW in the so-called *polar coronal holes*, while close to the solar equator shows closed magnetic field lines forming the helmet streamers, which are meant to be source of slow SW.

All the variability of the magnetic field during several cycles is known as the solar climate. It affects the IMF topology and diverse properties, the amount of released plasma and the electromagnetic radiation, as well as it could indirectly influence the planetary climates (e.g. Owens et al., 2016, and references therein) although there are some controversy on this point (see e.g. Dunne et al., 2016).

The presence of high activity of the Sun acts as a shield for galactic CRs across the heliosphere, making harder their penetration to the inner heliosphere. For this reason, the arrival of low energy CRs is modulated and anticorrelated with the number of sunspots. The modulation of CRs mainly affects the energy below $\sim 10^{10}$ eV. At 1 au, the thermal energy can be found at energies below $\sim$ 10 keV/n for ions (Allegrini et al., 2016), $\sim$ 60 eV for electrons (Feldman et al., 1975). Figure 1.3 shows the spectrum for the oxygen (similar behaviour is observed for other ionic species) for the energy range from thermal energies up to the energy where the solar modulation has less influence (around 60 MeV/n). Other particle populations are marked, such as the suprathermal and the SEPs.

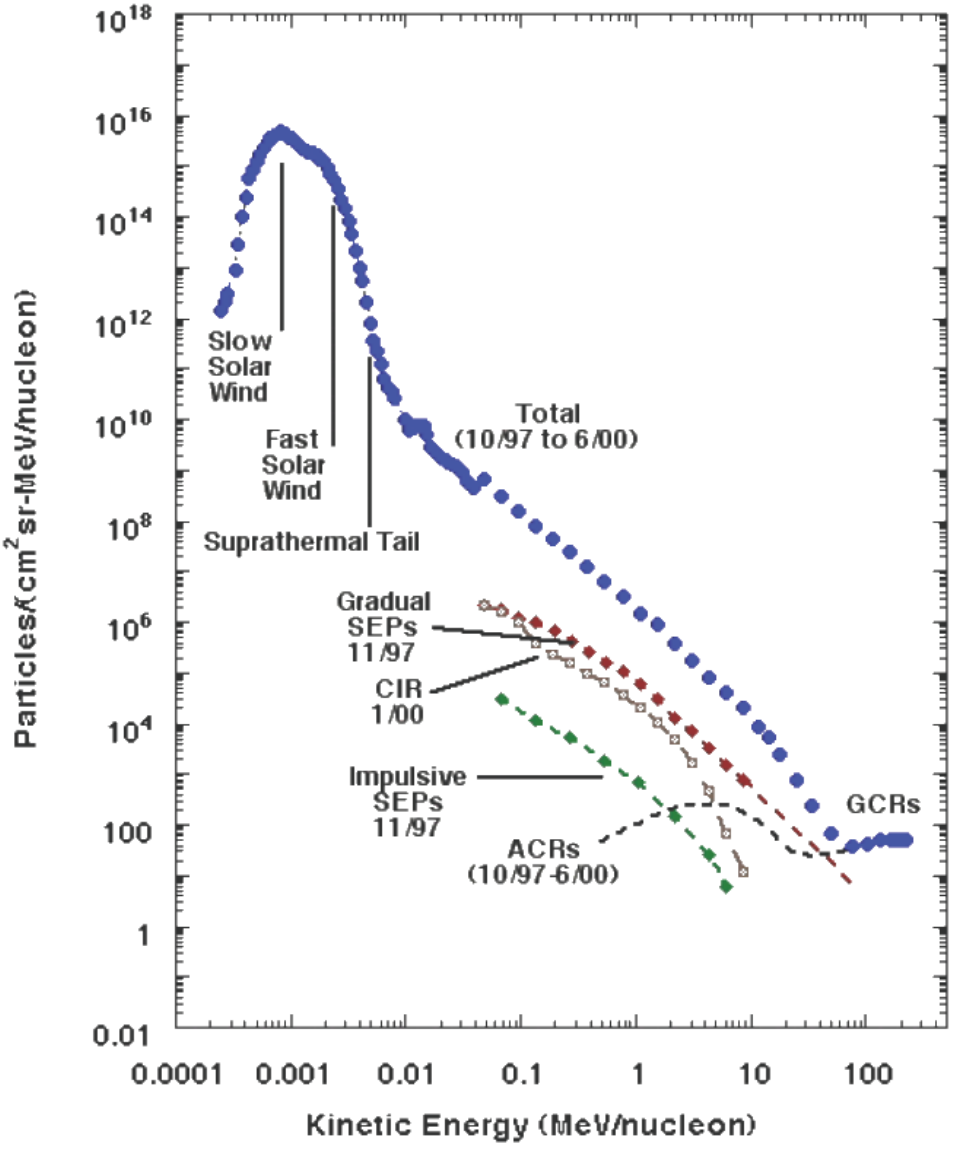

Figure 1.3: Contributions to the oxygen fluence observed by Advanced Composition Explorer (ACE) from October 1997 to June 2000. Some periods are tagged indicating the source. Credit: Mewaldt et al. (2001).

1.2.1. Solar Wind and Interplanetary Magnetic Field

As mentioned above, the SW is a continuous stream of plasma, mainly composed by electrons, protons, and alpha particles, which continuously flows almost radially from the solar corona to the IP medium. The velocity of the SW increases following a natural logarithmic function of the radial distance (r), so the speed practically remains constant from r $>\sim$ 60 million km until the heliopause (Parker, 1963). The SW is practically collision-less and owns a high conductivity. The SW owns an IMF whose magnitude decreases as long as one goes further from the star with a relation of approximately r^{-2}, being r the radial distance to the Sun.

The nominal behaviour of the the IMF frozen in the carried plasma in quiet conditions is originated by the radial release of the SW emerging from open field lines plus the differential rotation of the Sun, which produce curved IMF lines describing an Archimedean spiral, denominated as Parker spiral named after the author's postulation in Parker (1958). On account of the constant variation of the magnetic field of the star, some solar phenomena may occur varying and modifying the nominal behaviour of the SW as explained in Section 1.3.

The presence of a dipole at the Sun and the SW emerging from it and propagating in the heliosphere extends this topology up to the heliopause. Due to the coexistence of juxtaposed polarities of the IMF, the layer found in between (with a width of ∼10,000 km at 1 au) shows a very weak magnetic field strength and a relatively high electrical current ($\sim 10^9$ A, Israelevich et al., 2001) with a predominant radial component (Wilcox & Ness, 1965). For this reason, this layer is denominated the Heliospheric Current Sheet (HCS). The neutral line of the solar dipole is very rarely aligned to the equator of the star. This originates a waving that propagates in the IP following the Parker spiral, producing the so-called ballerina's skirt shape (Rosenberg & Coleman, 1969).

Depending on the source region of the Sun, the SW can present differences in its characteristics such as the composition, IMF strength and polarity, the temperature or the speed. The SW is traditionally classified into two different types: slow (with typical velocities under 400 km/s) and fast ($\sim$ 700 km/s), but it is not necessarily always associated so clearly with the speed. Other properties such as the proton density ($\sim$ 8.3 cm^{-3} for slow SW, $\sim$ 2.7 cm^{-3} for fast SW), temperature (around 34 $\cdot 10^3$ K for slow, and around 230 $\cdot 10^3$ K for fast SW), etc. might differ too SW, mainly due to their different solar origin (Schwenn & Marsch, 1990; Balogh et al., 1999). Slow SW is produced close to the equatorial zone during solar minimum and can also be produced close to the poles during solar maximum, mainly in regions with 'clearly' both magnetic foot-points linked to the star (closed loops and helmet streamers), while fast SW is streamed from Coronal Holes (CHs). The CHs are regions where the magnetic field lines apparently does not connect to another point of the Sun, i.e. their other foot-point is uncertain. They appear to be *open* lines and are more likely found at the solar poles during solar minimum. These regions

are identifiable as darker areas in the solar atmosphere when it is observed at extreme ultraviolet and soft X-ray wavelengths.

1.2.2. Suprathermal Electrons

Suprathermal electrons (from $\sim$ 60 eV to $\sim$ 2 keV at 1 au) are almost continuously streaming from the solar corona following the IMF lines (Viñas et al., 2000; Štverák et al., 2008; Che & Goldstein, 2014; Graham et al., 2017). Due to this directionality and anisotropy, they are a good tracer of the IMF topology, in opposition to thermal electrons which are isotropic following a Maxwellian distribution. Also, by looking at the distribution of the angle between the IMF direction and the one of the the suprathermal electrons velocity –Pitch Angle (PA)–, some trends can be appreciated. Furthermore, when emerging from the Sun, the higher energy electrons carry out lower energy ones. Based on these behaviours, SW electrons are commonly separated in three different populations: thermal core, suprathermal halo and *strahl* (Anderson et al., 2012, and references therein). The first two are present at all PA (i.e. they are mostly isotropic), while the third population tend to be primarily aligned with the IMF. Figure 1.4 shows a sketch of the commonly observed Velocity Distribution Functions (VDFs) and when presenting these functions against the IMF, so called Pitch-Angle Distribution (PAD), a further analysis of the conditions of the field can be performed. The less energetic (i.e. slower, closer to thermal speed) electrons in the middle behave as an isotropic population denominated the core, which typically follows a Maxwellian distribution. The nearly isotropic population with higher energies corresponds to the halo, usually distributed as a Kappa function.

The energy where thermal and suprathermal electrons are distinguished is denominated the suprathermal breakpoint and varies with the radial distance to the Sun. This energy is approximately 60 eV at 1 au (Feldman et al., 1975), and it goes lower as soon as the observer gets closer to the star. Due to their low energy, their gyroradius is $<$ 22 km (for 1 keV and 5 nT). In their travel they undergo some processes as scattering or adiabatic focusing depending on the IMF conditions (Owens et al., 2008). Due to this, the *strahl* can be scattered becoming part of the halo population (producing a broader distribution in PA), and the halo can be focused to form part of the *strahl*. The importance of these processes depends on the energy range, the IMF conditions, as well as the heliocentric distance. Nevertheless, the interdependency of all these factors is a complex issue, and there are contradictory examples of *strahl* width becoming narrower or broader depending on the situation (e.g. Anderson et al., 2012; Pagel et al., 2007; Berčič et al., 2019a; Fitzenreiter et al., 1998; Horaites et al., 2018; Hammond et al., 1996; Graham et al., 2017). In order to identify the IMF topology among other physical conditions, it is crucial to accurately characterise the different types of suprathermal SW electron PAD. This is one of the main objectives of this thesis work.

The behaviour of the suprathermal electrons adds substantial information about the

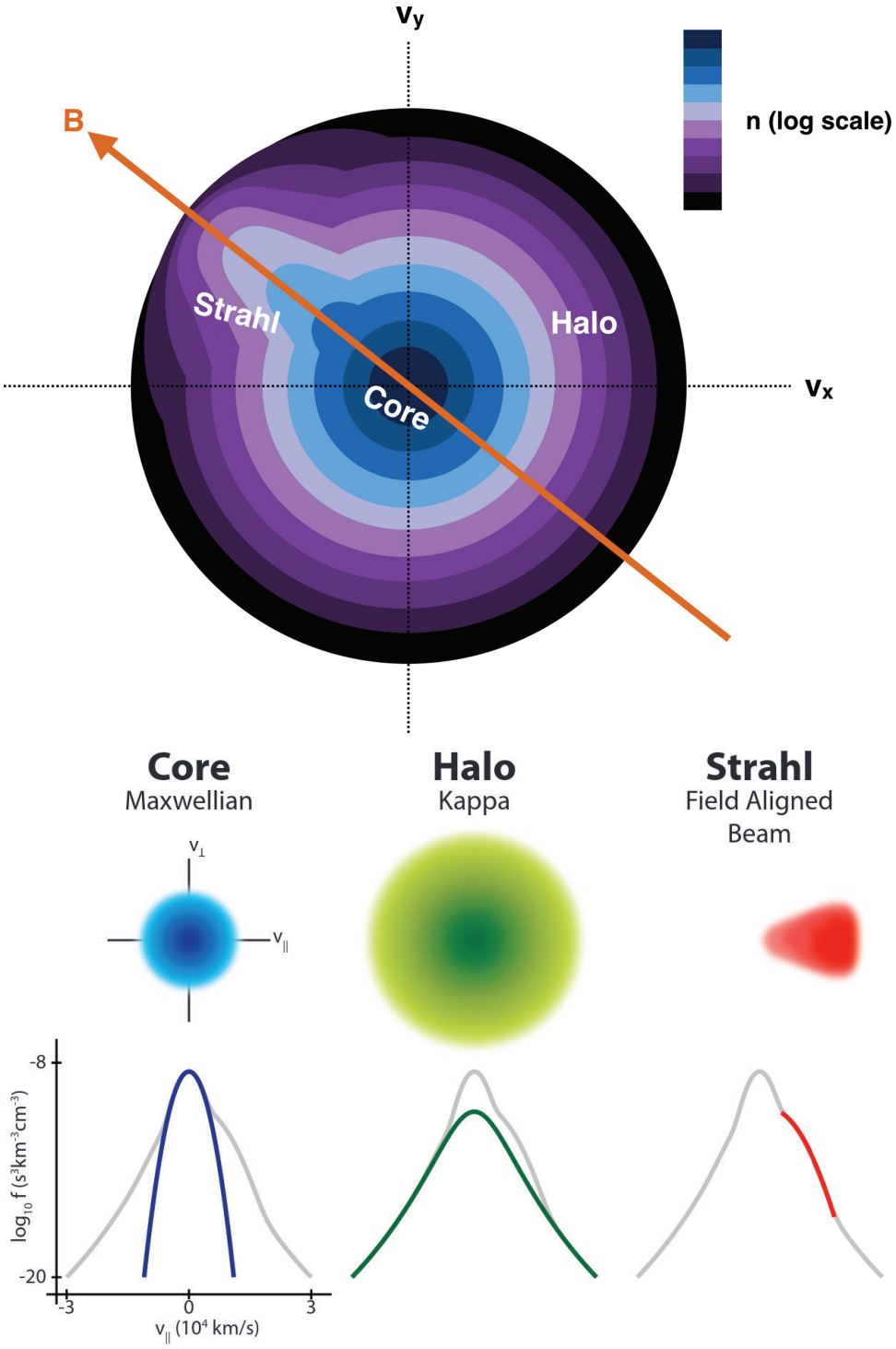

Figure 1.4: Sketch of the typical velocity distribution of the SW electrons. Colour scale in logarithmic scale indicates the number density n as a function of two components of the velocity (V_x and V_y for top panel, $V_\parallel$ and $V_\perp$ to $\vec{B}$ for bottom one). The beam of electrons aligned with the magnetic field (B, orange arrow, top) represents the *strahl* population. The behaviour of the populations show the different shown distributions. See text for more details. Credit: Graham et al. (2017) (top); Verscharen et al. (2019) (bottom).

topology of the IMF lines and the magnetic connectivity between the Sun and the observer. Their velocity is higher compared to the bulk's, which allows to extract information of the upstream conditions (Owens & Forsyth, 2013). As the suprathermal electrons are streaming from the Sun (which adds a reference about the directionality), the shape of the PAD provides information of the in-situ topology and acts as a complement for understanding the basics of the suprathermal electrons' propagation. One of the direct applications of the information taken from the study of suprathermal electron PADs could be the computation of the heliospheric open solar flux (Owens & Crooker, 2006; Owens et al., 2013), or unravelling the IMF topology among others (Kasper et al., 2019; Li et al., 2016). Some commonly observed types of PADs of particular interest (sketched in Figure 1.5) are:

- **An unique *strahl***, which can be identified as a PAD clearly peaking either at 0 or 180 degrees. Assuming that there are no kinks in the IMF lines (causing an apparent sunward propagating *strahl* case, Owens et al., 2013, 2017; Squire et al., 2020), a VDF peaking at 0 degrees would correspond to positive (outward) IMF polarity, while if it peaks at 180 degrees, the IMF line would have negative (inward) polarity. Moreover, the width of the *strahl* contains information about the IP scattering process (Berčič et al., 2019a; Maksimovic et al., 2005). In-situ observations beyond 1 au suggest that the scattering from the *strahl* to the halo decreases with heliocentric distance and the *strahl* still exists up to at least 10 au (Hammond et al., 1996; Owens et al., 2008; Walsh et al., 2013; Graham et al., 2018).

- **Counterstreaming** (Gosling et al., 1987) appears when the PAD shows two clear maxima at 0 and 180 degrees. This can be as a result of a mixture of two different beams coming along and against the IMF lines (i.e. a double *strahl*). As it results from a double stream, it is also commonly associated with a closed IMF line (coming out from and back to the Sun).

- **Loss-cone** (Phillips et al., 1996). This phenomenon is produced when a simple *strahl* is being reflected from beyond the location of the observer due to a constriction of the IMF lines (acting as a magnetic mirror, see Appendix). The extremely field-aligned electrons can pass through the constriction region, while the ones with larger pitch-angles (i.e. larger giroradii) are reflected back by the mirroring process. The observer then sees the addition of the simple (peaking at PA 0 or 180) and the reflected electrons (with a PAD with a maximum closer to 90 degrees).

- **Butterfly** distribution is characterised by a local minimum around 90 degrees, surrounded by two maxima at both sides, decreasing again near 0 and 180 degrees. It has been mostly studied for relativistic electrons inside planetary radiation belts (Artemyev et al., 2015), and it could be explained as a double mirroring effect in both directions.

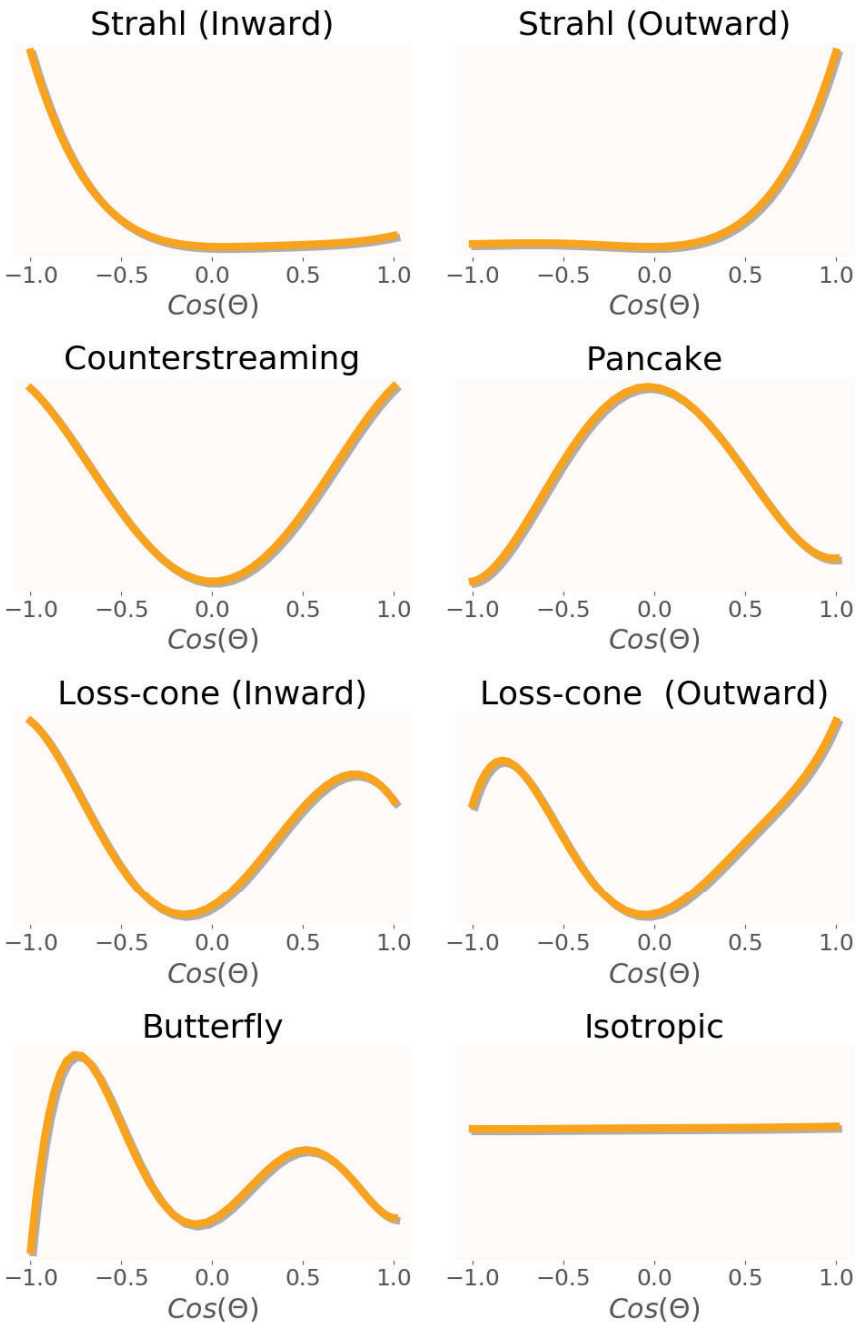

Figure 1.5: Sketches of suprathermal electrons PAD patterns observed in the IP medium. Horizontal axis represents the cosine of the PA, while the vertical axis shows the VDF in linear scale (arbitrary units). (Image adapted from Carcaboso et al., 2020)

- **Pancake** (Kajdič et al., 2014). This distribution is symmetric with the absolute maximum at 90 degrees (inverted parabola) associated for instance by a betatron acceleration, produced by the reconnection of the magnetic field (see e.g. Liu et al., 2017; Wu et al., 2013, and references therein).

- **Isotropic flux**. Associated either to intense scattering (Gurgiolo & Goldstein, 2017), which smears the PAD, or to IMF lines detached from the Sun. (Wang et al., 2018). One of the events characterised by almost-isotropic suprathermal electron PADs are the Heat Flux Dropouts (HFDs) (McComas et al., 1989; Crooker et al., 2003; Pagel et al., 2005a,b; Chollet et al., 2010), often found close to HCS crossings. As suprathermal electrons are continuously streaming from the Sun, the lack of *strahl* and the isotropic PAD has been interpreted either as an indication of magnetic structures disconnected from the Sun (via reconnection) or as a consequence of strong IP scattering (see Pagel et al., 2005a, and references therein).

The PAD types listed above are examples of distributions commonly observed in the SW, but they do not cover all the possible PADs that can be measured. Moreover, in some situations, there could be more than one different explanations for their existence in the SW.

Another commonly used term is Bi-Directional suprathermal Electrons (BDE), which normally refers to the presence of beams propagating in both the field and anti-field aligned direction. Possible mechanisms for this behaviour are the double *strahl*; one *strahl* being reflected back; or adiabatic focusing and mirroring too. This would include not only counterstreaming but also loss-cone, butterfly PADs or even 90-degree depletions (Gosling et al., 2001).

1.3. Solar Activity Phenomena

Thanks to the above-mentioned fusion reactions in the solar core, the convection movements and the presence of differential rotation around its axis, a very intense and complex magnetic field is produced and it extents up to the end of the heliosphere. This magnetic field is continuously varying and twisting, and predominates and influences the SW environment. There are notorious manifestations of the intense magnetic field and its variability as described below in the following sections.

The discipline that studies the direct or indirect influence of solar phenomena on a specific point of the Solar System and the heliosphere is denominated Space Weather,which also puts a special stress on the Earth's environment, as the phenomena might cause damage to humans or human technologies and activities such as for instance the satellites and communications, or different pipelines on the planet's surface.

Hα class	Area (deg^2)	Soft X-ray class	Log flux at 0.1–0.8 nm
S	2.0	A(1 – 9)	-8 to -7
1	2.0 – 5.1	B(1 – 9)	-7 to -6
2	5.2 – 12.4	C(1 – 9)	-6 to -5
3	12.5 – 24.7	M(1 – 9)	-5 to -4
4	24.7	X(1 – N)	> -4

Table 1.1: Flare classifications based on Hα and soft X-ray emissions in terms of area and size. Credit: Table 4.3 Russell et al. (2016)

1.3.1. Solar Flares

A solar flare is a violent intensification of the brightness at different parts of the electromagnetic spectrum that develop in a few seconds, can last for hours and it is not necessarily related to a plasma release. They were first observed as an intensification of brightness of the star by Carrington and Hodgson in 1859 (Carrington, 1859). Flares are originated due to magnetic reconnection typically in ARs, when two opposite magnetic fields encounter and reconfigure, which can release up to 10^{25} J in a few minutes. The reconnection usually affects all solar atmospheric layers (photosphere, chromosphere and corona). They are usually characterised and classified by looking at two wavelength ranges: soft X-rays and Hα , and are mainly tagged by the intensities of the burst. The Hα emission is used to classify the area of the flare and the soft X-ray establishes the logarithm of flux at 0.1 – 0.8 nm (see Table 1.1).

This sudden release, can cause other reconnections and flares in the vicinity, and even solar quakes (i.e. seismic waves in the interior of the star, as well as a possible shock wave in the external layers) which can extent several tens of degrees (Kosovichev & Zharkova, 1998). Those solar flares which last longer commonly shows three different phases: pre-flare stage, impulsive phase and gradual phase. By looking at different wavelengths, it is possible to distinguish in the first phase a faint increase in the intensity of the H_α and soft X-rays, which are associated to the heating process of the region. After this, the reconnection is produced, which quickly releases the highest amount of energy which may cause a considerable acceleration of a large number of energetic particles in a brief period of time (SEPs, see Section 1.3.5). During the reconnection process, which lasts for few minutes or seconds, it can reach emissions of hard X-rays and even γ rays. In the gradual phase, hard X-rays and γ emissions start to decay for few minutes, while soft X-ray intensity is still increasing until an eventual peak is reached. Then, it starts to decrease with a longer decay than the shorter-wavelength emissions. This process can last for hours. If the solar flare releases SEPs, it could also emit in microwaves and radio, producing non-shock-associated radio bursts, which are described in the following sections.

1.3.2. Radio Bursts

Sporadically, other electromagnetic radiation enhancements are produced at lower frequencies (below 2 GHz), which correspond to radio wavelengths. This type of emission is denominated radio burst and the frequencies, as well as their variations in time, allow to identify the source of radiation. This is possible considering that the frequency of these types of emissions depends on the local plasma frequency (see Section 5.1), which derives from the density of the region where it is produced. Depending on the time profile and nature of the measured spectra (Wild, 1951, and references therein), the radio bursts can be classified as follows:

- **Type I** – They have a duration of few seconds, but they could be produced several times in a cascade that could last for hours or even days. The frequency range goes from 80 MHz to 200 MHz and it is produced in ARs, commonly associated with flares.
- **Type II** – They have a slow drift, meaning that the frequency of the fundamental harmonic goes from 20 to 150 MHz with a time duration from few minutes up to one hour, because they are commonly produced at IP shocks that are accelerating SEPs. They are normally accompanied by a second -and even third- harmonic.
- **Type III** – These radio bursts are associated to an impulsive release of SEPs, which provokes a quick drift. The beam of electrons between $\sim$ 10 keV and $\sim$ 100 keV (Reames, 2017) excite the local plasma, which is progressively less dense, producing the radio emissions covering from 10 kHz to 1 GHz and that could last for hours.
- **Type IV** – Type IV radio bursts can be sub-classified into:

  Moving – Their duration is shorter (from 30 minutes to 2 hours) but the energy range can reach up to 400 MHz. These radio bursts are mainly produced in association with the CMEs, and often preceded by a type II burst. The emission is though to result from energetic electrons trapped within the magnetic field lines of the closed structure.

  Stationary – They can last for days covering from 20 MHz to 2 GHz and are associated with flares or type I radio bursts.

  Flare Continua – They have the same origin as the Stationary ones, and can last from a few minutes to one hour, covering the range 25–200 MHz.
- **Type V** – Type V radio bursts (10–200 MHz) occur just before type III radio emissions, and last from 1 to 3 minutes. It is probably caused by harmonics associated with the beam of electrons that causes the associated type III ones.

Figure 1.6 shows a schematic representation of the different radio bursts described. As mentioned above, the study of each type of radio burst can be used to trace the

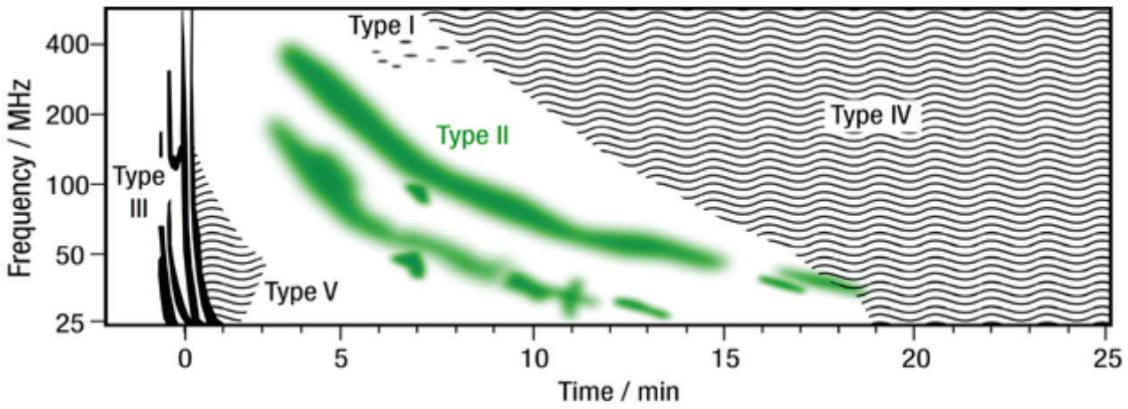

Figure 1.6: Sketch of solar radio burst dynamic spectra (frequency and intensity versus time). See text for description. Credit: Ganse et al. (2012).

radio source, but more detailed studies can be performed by using interferometry (e.g. Röttgering, 2003) or if the emission is measured from different points of observation. The multipoint analysis of the electromagnetic radiation can provide information about the conditions of the IMF remotely as explained in Section 5.1.

1.3.3. Coronal Mass Ejections

Coronal Mass Ejections (CMEs) are a release of a large amount of magnetised plasma ($\sim 10^{30} kg$) with its own magnetic field. Their release is usually accompanied by a solar flare, but not necessarily. One of the main-thought mechanisms that could produce the eruption of the CMEs (Kallenrode, 2004) is the one sketched in Figure 1.7, corresponding to the Raadu and Kuperus (R-K) configuration (Raadu & Kuperus, 1973; Kuperus & Raadu, 1974). Generally, the sunspots with opposite polarity closer enough are connected to each other through a flux tube. This structure is magnetically stable, and the gravitational force prevents it to expand to the IP medium but, when any perturbation occurs, the reconnection of magnetic field lines surrounding the tube with opposite polarity may happen. The energy released is able to push the structure with an acceleration and consequent velocity great enough to escape from the solar gravitational influence. The CMEs can reach supersonic velocities (up to $\sim 3,000$ km/s), which is indeed much faster than the ambient SW. If the velocity of the structure is faster than the sound in those conditions, the plasma found by the Coronal Mass Ejections (CMEs) trajectory compresses, and the hydrodynamic and magnetic pressure produced commonly forms a shock that can later be observed in-situ in the IP medium (see e.g. Temmer, 2016, for a comprehensive summary of their kinematics).

The IP counterpart of the CMEs are denominated Interplanetary Coronal Mass Ejections (ICMEs) and their properties can be measured with in-situ instruments onboard heliospheric observatories. Based on in-situ observation of plasma and magnetic field properties, an evolved ICME can usually be divided into the following parts (e.g. Jian

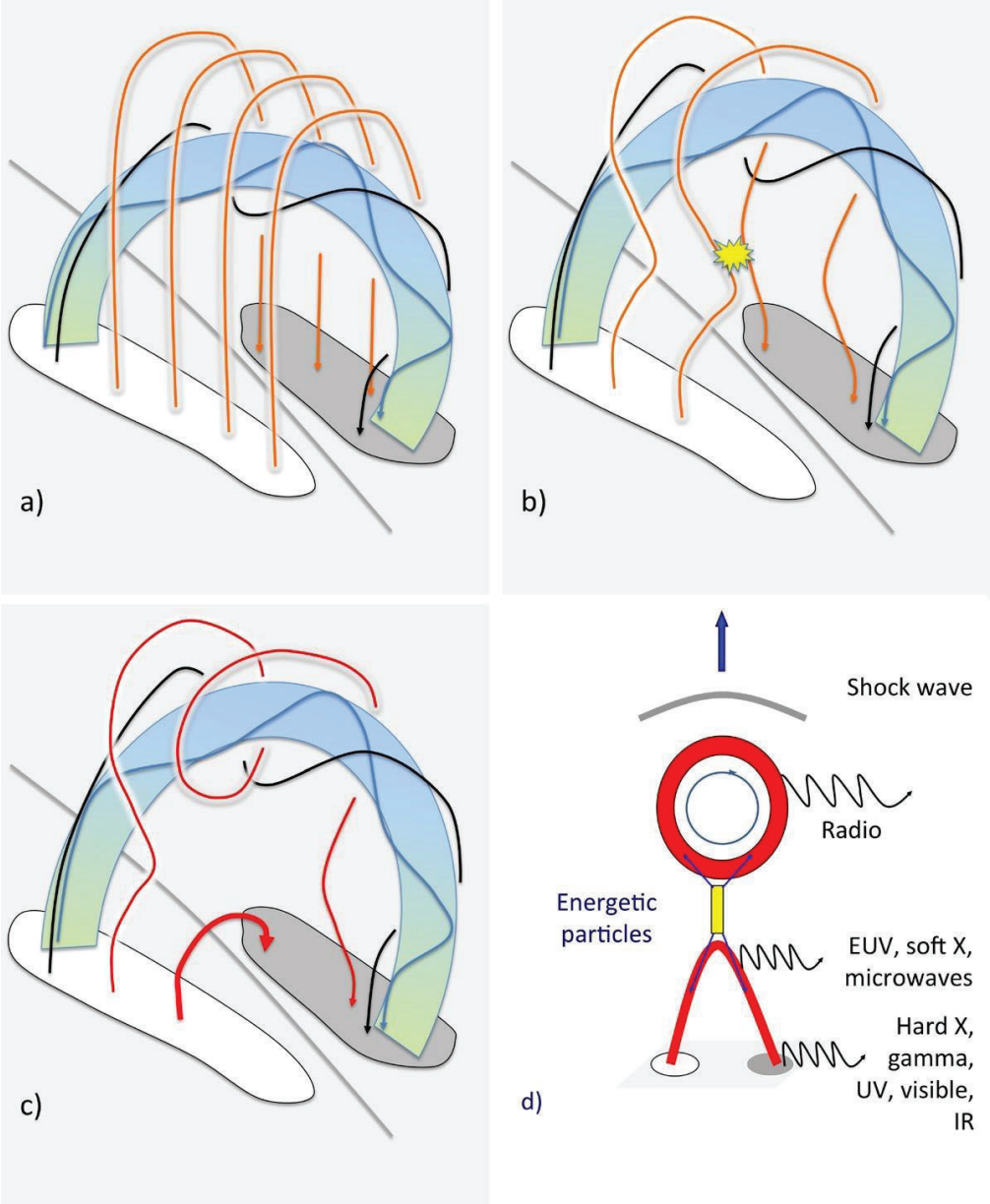

Figure 1.7: Representation of a possible mechanism for the emergence of a CME with the electromagnetic emission associated to each region. a) sketches a stable FR (blue lines) below a magnetic arcade (orange lines), both of them with their foot-points near active regions with opposite polarity. b) and c) represent the reconnection of arcade with opposite direction and the subsequent emergence produced by the energy release of the phenomenon. d) shows a cross-section view of the process indicating the origin of different emissions. Figure adapted from Klein et al. (2018).

et al., 2018, and references therein):

- **Shock.** It can be produced due to the supersonic behaviour of some ICMEs and corresponds to a discontinuity of the SW. The shocks are mainly characterised by a sudden increase in bulk speed, magnetic field strength and proton density. The transit of a shock produced by ICMEs through a static observer is commonly less than 1 hour. Not all the ICMEs are preceded by a shock, as it depends on the ambient SW conditions and mainly on the speed of the structure.

- **Sheath.** The travel through the IP medium of the ICMEs compresses the ambient SW in the front part. The evolution of the compression produces a region where the magnetic field is very irregular in short time (i.e. turbulent). This region presents higher densities as well higher temperatures than the surroundings because of its compression which also facilitates the reconnection/erosion of the magnetic field lines, what increases the thermal energy. The transit through sheaths tend to last for approximately 10 hours depending on the speed of the ICME.

- **Magnetic Obstacle (MO).** After the sheath, a region with quieter and more intense magnetic field might be found. The cross through this region tends to last about 24 hours. Depending on some physical parameters, the MOs can be subdivided into different categories:

  Flux Ropes (FRs). When smooth and continuous IMF rotations are found, then it is said that the MO presents a FR topology. If a FR also shows other properties such as low plasma β (due to an enhanced IMF and their low proton temperature and density), decreasing SW speed, Bi-Directional suprathermal Electrons (BDE) among others is traditionally called Magnetic Cloud (MC) (Zurbuchen & Richardson, 2006). If there is no interaction with other solar phenomena, the MCs tend to expand, showing a gradual decrease of the bulk speed during the transit through the observer's location. Roughly a third of the ICMEs shows MC characteristics (Richardson & Cane, 2010).

  Multiple FRs. Inside the same MO, it is not rare to find two or more independent FRs. They commonly show similar properties because are originated in the same AR. Two of these properties are the orientation and the speed. Having similar orientation is crucial to keep the IMF uneroded, while having similar velocities allows to not compress each other.

  Complex ejecta. Sometimes, when two FRs are released consecutively it could happen they interact, influencing each other or being eroded and smeared. The signatures that characterise a MC are then unclear. A similar scenario could be reproduced by an originally CME with non-flux-rope-like topology, or when the observation is performed through a flank of the structure.

- **Post-ICME.** There is a non-well-defined region after the end of the Magnetic Obstacles (MOs) where the characteristics of the SW are not as the ones found in the nominal SW nor in the observed MO, derived from the conditions after the magnetic reconnection in the lower corona (e.g. Vršnak et al., 2009) and their propagation in through the IP medium. In this region signatures like BDE can be found, but no smooth IMF nor decreasing speed, for example (Gosling et al., 2007; Kilpua et al., 2013), and the time-crossing duration takes much longer than for the actual ICME ($\sim$ 35 h, Carcaboso et al., 2020).

The post-ICME may be produced by the erosion of the magnetic field lines of the structure while propagating through the IP medium. In addition, the boundaries between the rear part and the MO are not always clear, and this is because the erosion is a process which depends on the ICMEs itself, but it is also strongly influenced by the changing medium where the structure is propagating. The multipoint observation of these structures helps to understand the mechanisms involved in the erosion/reconnection processes. One of these examples is Heinemann et al. (2019), which tries to track the propagation of an ICME and its interaction with a SIR, and to observe its evolution by comparing the observations with different models. The interaction between these structures is very complex and mixes properties of each media, which hinders the possible analysis (Burlaga et al., 1987).

The propagation of the ICME perturbs the nominal conditions of the IP medium, often accelerating particles if accompanied by a shock, compressing regions, eroding magnetic field lines and reducing the arrival of higher energetic particles. Forbush Decreases (FDs) consist on a notable decrease of the arrival of CRs for a certain period of time, mainly produced by the presence of an IP shock, a denser region of the plasma (e.g. the stream interface of SIRs) or an uneroded MO, which all could act as a shield of these particles. Some works, as for example Dumbović et al. (2020), show the radial evolution of a single ICME and its effect in the presence of CRs and the agreement with a developed FD model.

1.3.3.1. Modelling Interplanetary/Coronal Mass Ejections

The remote-sensing observations of CMEs can be used to investigate further their global topology, and to infer some physical properties such as their velocity during the eruption and their orientation. There are multiple models which infer the topology or geometry of the CMEs from the observations, such as the Graduated Cylindrical Shell (GCS) described in Thernisien (2011). This model requires multipoint observations to reproduce their geometry, as it allows a geometrical 3D reconstruction of the erupted CMEs based on multipoint coronograph observations. This is possible now thanks to missions as the Solar Terrestrial Relations Observatory (STEREO) and the recently launched Solar Orbiter (SolO), as explained in Chapter 2.

Reproducing the global topology of the ICMEs is a complex task, as normally there is a single point observation of structures whose cross-section can reach up to 0.25 au at 1 au (Burlaga et al., 1981). For this reason, there are several analytical, empirical and numerical models that try to reproduce the ICME topology or each different part of them. Inside the numerical models, there are two main groups: force-free and non-force-free models, considering the last ones as $\vec{J} \times \vec{B} \neq 0$, where $\vec{J}$ corresponds to the current density and $\vec{B}$ is the magnetic field of the plasma. Force-free models are generally simpler, as they assume the magnetic field unperturbed and typically as frozen structures. This is typically translated into less accurate topology of the MCs but, on the other hand, non-force-free models need to add the current as free parameters as there are not direct and independent measurements of this physical parameter. Apart from that, non-force-free models can infer better the actual topology and physical properties of the MCs, but at the cost of having more free parameters, such as the existence of electrical currents contributes to them, and bigger assumptions -for instance, the topology- which may differ to the actual plasma properties. One of the non-force-free models that can reproduce the global topology of the MCs is the Hidalgo's model (Hidalgo, 2013), which is the one used in this work (see Section 4.2). Apart from this, there are multiple analytical models that are widely known and typically used for scientific purposes, such as: Burlaga et al. (1981); Burlaga (1988); Farrugia et al. (1992, 1993); Romashets & Vandas (2003); Cid et al. (2002); Nieves-Chinchilla et al. (2019); Hidalgo (2016), among others.

1.3.4. Stream Interaction Regions

The CHs are a source of fast SW streams. Those streams overtake and compress the preceding slow SW, which is always present in the heliosphere (Hundhausen, 1973, e.g.). The interaction between the different SWs can produce a large-scale region called Stream Interaction Regions (SIRs) in the IP medium. The slow SW has more curved Parker spiral magnetic field lines, while the lines of the fast SW are more radial. The encounter also produces an enhancement in the density and temperature of the local plasma, as the material of both streams piles up while interacting. The frontier between the two regimes with usually the highest pressure is denominated the stream interface (Burlaga, 1974). Figure 1.8 shows a sketch of the interaction between slow (A) and fast (B) SW. The same Figure also sketches how magnetic field intensifies in the region where the two different winds meet. The SIR can be bounded by two shock waves: forward shock and reverse shock. These shocks are defined as a discontinuity in some plasma properties (Figure 1.9 shows the time profiles of the two shocks, which can be observed for other structures) and they can accelerate energetic particles (see Section 1.3.5).

When fast streams coming out from the same CH are stable and reappear for one or more rotations of the Sun, the SIRs are denominated Co-rotating Interaction Regions (CIRs), although in the past this term has been applied for one-single rotation SIRs too.

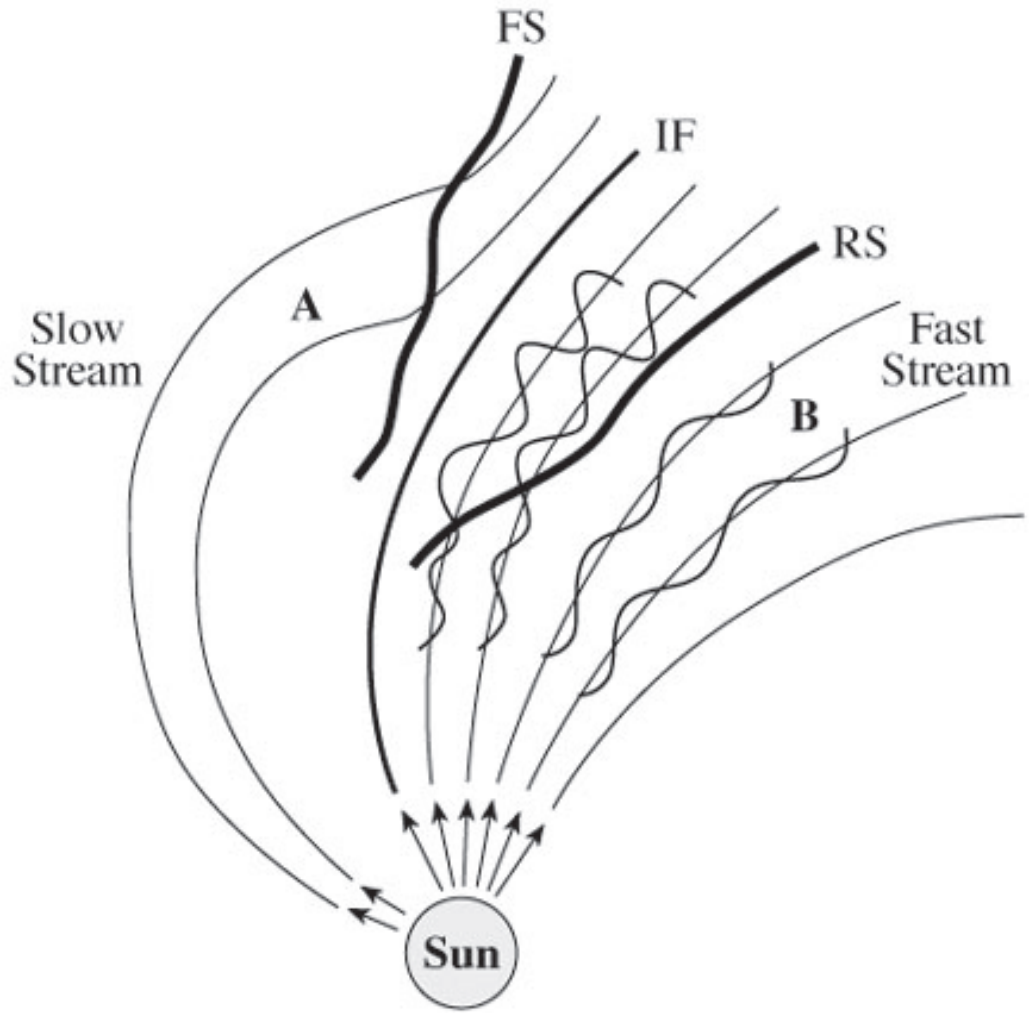

Figure 1.8: Representation of a SIR. The interaction between fast and slow SW can produce more intense magnetic field near the stream interface (IF) and the region can be bounded by a Fast Forward shock (FS) and a Fast Reverse Shock (RS). Source: NASA's Cosmos, ase.tufts.edu/cosmos.

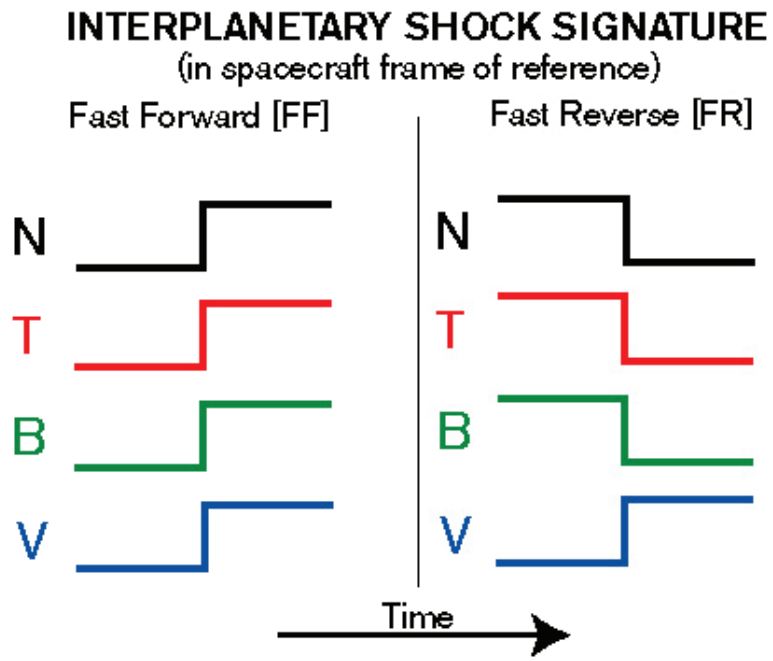

Figure 1.9: Sketch of the observed time profiles of plasma properties during the transit the Fast Forward (FF) and Fast Reverse (FR) shocks. V stands for the bulk velocity, while B is the magnetic field strength, N represents the density and T the temperature. Image modified from wind.nasa.gov/mfi/ip_descr.html

1.3.5. Solar Energetic Particles

SEPs events are a release of high-energy particles due to the acceleration during magnetic reconnection or different physical processes of particle acceleration at shock waves in the corona and the IP medium (see e.g. Vainio & Afanasiev, 2018, for a compilation of theoretical mechanisms). Their propagation in the IP medium following the magnetic field lines is normally accompanied by a solar radio burst, as the accelerated electrons from 10 to 100 keV excite Langmuir waves at the local plasma frequency. Depending on the acceleration process, the trace of the radio burst has also different properties as mentioned in Section 1.3.2.

The acceleration mechanism draws an, in principle, identifiable imprint when measuring the arrival of SEPs in-situ. The SEPs are traditionally classified into two different types: gradual and impulsive. Although the two terms may suggest a relation with the duration of the event, they are not necessarily associated to their time duration but also to other characteristics. These types have the following properties:

- **Impulsive SEP Events** are commonly associated to reconnection in a very specific point of magnetic field lines with opposite directions in the lower atmosphere. The reconnection produces a release of energy, which might be manifested as a solar flare, high enough to suddenly accelerate the surrounding particles, reaching high energies in a short period of time. This quick travel of the SEPs often produces an imprint in the radio generating a type III radio burst as previously seen. The SEPs rapidly

propagate along the nearest magnetic field lines. In addition, the source is small and very localised in the region where the reconnection occurs. For these reasons, it is very unlikely to observe very broad particle spreads in longitude or latitude. This behaviour produces a relative narrow beam, contrary to the gradual events (see below), whose mechanisms implies the propagation of the particles following multiple magnetic field lines (Reames, 1999). Impulsive SEP events are electron rich (proton poor) and are usually characterised by significant enrichment in heavy elements and ^3He with respect to the coronal abundances. One of the well-known properties used for their identification is the ^{3}He/^{4}He ratio observed in-situ, which is much higher than typical SW abundances and can be higher than one in in-situ observations, when the ambient SW shows a ratio of $\sim 10^{-4}$ (Reames, 2017). These events typically last for few hours, as there is only a quick acceleration mechanism, thought to be resonant wave-particle interaction (e.g. Miller, 1998; Temerin & Roth, 1992) which accelerates the surrounding particles of the reconnection region.

- **Gradual SEP Events.** Because of the propagation of an IP shock through the heliosphere (e.g. due to a supersonic CME), the particles can be accelerated by two main mechanisms: diffusive shock acceleration (Jones & Ellison, 1991; Lee, 2005; Zank et al., 2015) and shock-drift acceleration (Ball & Melrose, 2001). As the shock propagates through the IP medium, the element abundances that can be found are different than for the impulsive events. In this case, the composition is closer to the one that can be found at the solar corona (Webber, 1975; Meyer, 1985). This continuous acceleration produces a gradual increase of the intensity when they arrive to the observer, which can last several days at energies of a few MeV per nucleon. As previously mentioned, gradual events can be observed simultaneously by several s/c widely separated in longitude, which can reach the 360 degrees (e.g. Gómez-Herrero et al., 2015). Gradual SEPs are less common than the impulsive ones and can be extremely intense, increasing the radiation dose. Because of the long duration damage and the wide spatial coverage, it is very relevant for the Space Weather field.

Nevertheless, several authors pointed out that it is also possible to find events which present characteristics of both types. The solar origin is not always clear and the observations may correspond to the coexistence of both categorised SEPs too. In addition, it is possible to find impulsive events which might be shock-accelerated afterwards (e.g. Kocharov & Torsti, 2002). Those cases are categorised as *hybrid* events.

The SEPs are strongly influenced by the path they follow to arrive to the observer, and their properties measured in-situ provide information about the source and the IP propagation conditions, although that could also affect their identification and classification. When representing the different intensities at diverse energy (i.e. velocity) ranges of the particles, it is possible to extract valuable information from the Velocity Dispersion Analysis (VDA), such as the effective path length (see e.g. Rodríguez-García et al., 2021).

Also, it is possible to estimate the time travel for each individual energy range by using Time-Shifting Analysis (TSA) (e.g., for both methods, Vainio et al., 2013).

The study of the anisotropy (i.e. from where and how the particles are predominantly coming) plays an important role on the understanding of the particle propagation and the properties of the medium they have travelled along, and even more when compared to the IMF direction (i.e. the analysis of the PAD of the particles). Scattering and adiabatic focusing (Earl, 1976) are two antagonist physical processes processes that energetic charged particles may suffer during their propagation and can be interpreted from the analysis of the anisotropy. The main trigger of scattering processes is the turbulence of the IMF, while for having magnetic adiabatic focusing is the existence of diverging lines, as corresponds to the Parker spiral topology.

There are models that try to reproduce the behaviour of particles while propagating in the IP space until they reach the observer. Some of these models are gathered and classified in Klein & Dalla (2017).

1.4. Main Goal of the Thesis

Magnetic connectivity between a specific point in the heliosphere and the Sun is a pivotal question for many aspects of Heliophysics. The topology of the IMF is complex and variable and it cannot be characterised always only by observing the magnetic field components from a single point in space. This work shows new approaches by the use of multispacecraft observations and using suprathermal electrons, radio emissions, solar flares and SEPs as a proxy for tracing the IMF topology over different spatial scales in the most frequently observed conditions: quiet SW, inside ICMEs and inside SIRs. This thesis work aims to go further in the investigation of the IP magnetic field topology by the combined use of some multi-messengers as the suprathermal electron or the almost-relativistic electrons, as well as other properties of the SW plasma. The main objectives of this work are:

- To analyse the variability of the suprathermal electron PADs for different conditions of the SW.
- To understand the topology and the evolution of the ICMEs by looking at the suprathermal electrons imprints as well as other properties of the plasma during the transit through the observer's location.
- To understand how the different physical conditions of the of the IMF affect the propagation of impulsive SEP events, and find if there is a connection to the variation of the suprathermal PADs.

For that purpose, the data provided by different solar and heliospheric observatories have been analysed. In Chapter 2, those missions are presented, and the data collected

from their instruments, as well as some catalogues that have been utilised for the study and developed during the PhD thesis. The specific methodologies that has been applied and developed and the different data analyses are explained in each sub-study, which are divided in the following chapters: Chapter 3, where the study of the PAD of the suprathermal electrons is analysed to reveal the dependency with the solar cycle in the heliosphere and also with the energy range of observation; Chapter 4, where the ICMEs are analysed from different perspectives, such as the variation of the suprathermal electron PADs and the statistical differences about characteristics of the FRs as based on Hidalgo's model (Hidalgo, 2016) and in-situ plasma measurements; Chapter 5, where a comparative between the properties of impulsive SEPs and the suprathermal electrons is presented, as well as the description of a type III radio burst tracer model and three case studies. Finally, a brief summary, discussion, and future work are shown in Chapter 6.

The complexity of the SW implies the use of a wide variety of different approaches in order to analyse its properties, as the coordinated multipoint observation, the development of analytical models of different topologies of the IMF or new mathematical approximation to the plasma properties. In this work some methods have been upgraded and applied to the obtained data from different s/c (see Chapter 2). The three methods are a mathematical characterisation for the PADs (Section 3.1), an updated model for FRs (Section 4.2) and the development of a simple model to trace the type III radio bursts (Section 5.1). Also, it must be mentioned the use in this work of different programming tools which made the analysis feasible and are explained in Section 1.5.

Part of the content of this thesis study has been previously gathered in some international publications indexed on the first and second quartiles of the Journal Citations Report in collaboration with researchers of multiple institutions.

1.5. Coding and Development

All the data analysis has been mainly performed using Python 3.7 (Van Rossum & Drake, 2009), and sporadically BASH, C, Matlab and IDL. Python is a dynamically typed programming object-oriented language. It has a comprehensive standard library which easily allows to implement pieces of code with different specific purposes with the so-called packages. In this work, some of the most supported packages for data analysis has been used: Pandas (Wes McKinney, 2010), Numpy (Harris et al., 2020), Lmfit (Newville et al., 2014, 2019), Matplotlib, Seaborn, Scipy, PyQt5, PyCDF, Sunpy and Astropy, among many others.

Also, as a multitude of instruments from different missions have been analysed, a series of tools and widgets were developed under the Amun Solar Application (Amun-SA) to make the reading and processing data easier. Amun-SA allows to represent the data of several heliospheric observatories and to use the different methodologies explained in

previous Sections such as 4.2 and 5.1. The application can be found in a portable version at http://espada.uah.es/gitlab/Fernando/amun-sa.git.

Chapter 2

Instrumentation and Catalogues

The IMF topology could not be unravelled without spaceborne observatories that measure the properties of the plasma inside the heliosphere, because the Earth's atmosphere and magnetosphere act as a shield for the SW and particles with higher energy, as the CRs or SEPs, as well as the atmosphere absorbs and reflects some electromagnetic wavelengths too. The data used in this work are mainly provided by solar and heliospheric observatories that form part of the National Aeronautics and Space Administration (NASA) and European Space Agency (ESA) fleets.

Having multiple points of in-situ measurements and remote sensing observations together is necessary for understanding the large-scale structures in the heliosphere. Besides, as it is impossible to have a full grid of observations of the SW, it is necessary the development of new methodologies that help to reproduce the IMF topology.

2.1. Near-Earth Missions

Part of the data used in this thesis work is taken from the missions in Earth's vicinity. In particular, these missions are located at at the first Sun-Earth Lagrange point (L1, $\sim$ 1.5 million km from Earth) as in this place the gravitational forces of both bodies compensate each other, which makes easier to position s/c there and to have less attitude manoeuvres as there are fewer gravitational disturbances. This point is out of the Earth's atmosphere and magnetosphere, what allows to have a full coverage of both electromagnetic and particle measurements. However, the relatively close presence of the bow-shock of the magnetosphere (65,000 km from Earth) might interfere sometimes, for example with the presence of upstream particle events (e.g. Klassen et al., 2008). Being located at L1 has also advantages for the Space Weather field, as it might be also possible to forecast and anticipate events that may affect the planet. The main missions whose data were used during the development of this thesis work are:

- Wind (Ogilvie & Desch, 1997) was launched in November 1, 1994 on a Delta II

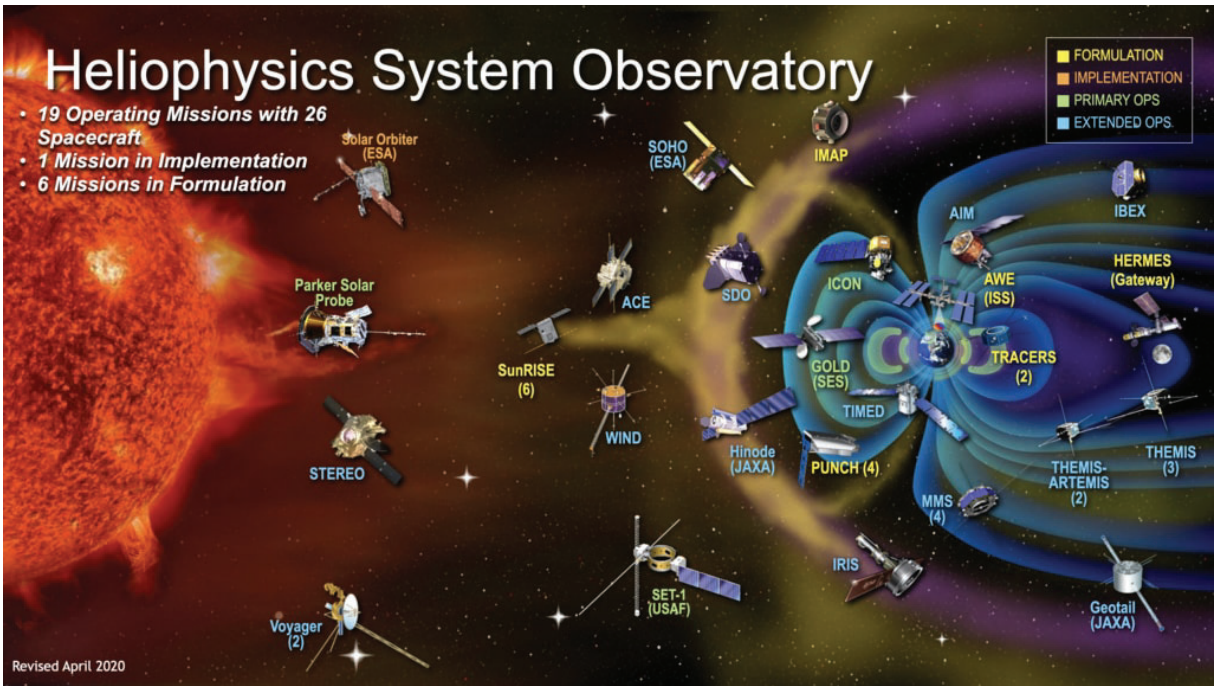

Figure 2.1: Currently operating solar (as in April 2020), heliospheric and magnetospheric observatories and their relative position in the IP space. These observatories form the the Heliophysics System Observatory (HSO). Some missions inside the magnetosphere (purple bubble) own an orbit which may often cross the Earth's magnetosphere boundary. Source: svs.gsfc.nasa.gov/30822.

rocket. It is now located at L1 although it has had multiple orbits along the mission time, as a halo orbit around L1 with two Moon gravity assist manoeuvres per year, or petal orbits going out of the ecliptic plane. It carries multiple instruments to measure the in-situ conditions of the plasma, such as the composition, the magnetic field, etc. Wind is part of the space programme Global Geospace Science (GGS). These missions' main objective is to study the regions where the SW interacts with the Earth's magnetosphere at different locations.

- Solar and Heliospheric Observatory (SOHO) (Domingo et al., 1995) is a mission resulting from the international collaboration between ESA and NASA. It was launched on December 2, 1995 on a Atlas Centaur II rocket. The mission has in-situ and remote-sensing instruments onboard, although currently only some of them are still active and providing data. In addition, SOHO not only provides heliospheric data, but it is the mission that more comets has ever discovered (over 3,000).

- Advanced Composition Explorer (ACE) (Stone et al., 1998) is a NASA s/c that was launched on August 25, 1997 from Cape Canaveral on a Delta II rocket equipped with in-situ instrumentation. It began its nominal science operations on January 21, 1998 with a halo orbit about L1. The main objective of this mission is to analyse the composition of the SW and the galactic CRs. This work uses data from the Solar Wind Electron, Proton, and Alpha Monitor (SWEPAM) instrument (McComas et al., 1998) and from the twin triaxial magnetometer onboard (Smith et al., 1998)

originally designed as the spare model of the Wind mission. Besides, SWEPAM is a modification of the spare model of the solar wind electron and ion sensors onboard Ulysses (Wenzel et al., 1992), and it is designed to measure an energy range from ∼1 eV to ∼900 eV for electrons. The s/c is spinning every 64 s, so the instruments aim to have a full view of the sky. ACE is considered to be in good conditions, and it is going to be extended at least until 2024, once the propellant which keeps its attitude control is totally consumed.

- Solar Dynamic Observatory (SDO) (Pesnell et al., 2011) was launched on February 11 2010 complementing the measurements of SOHO as it is equipped with remote sensing instruments that allows to study in a wide range of wavelengths with new-generation equipment allowing higher spatial resolution and acquisition cadence. Besides that, combined with the described below STEREO mission, it allows an 3D reconstruction of the Sun from the ecliptic plane perspective, which is crucial for the understanding of the evolution of the solar features such as ARs or CHs, and provides relevant information for the Space Weather forecasting.

There is an implicit limitation of these missions: their orbits are very closely located in the heliosphere. This issue hampers the possibility of observing simultaneously other parts of the Sun, being implausible to see what is close to the limb or behind the solar limb from the point of view of the Earth, which does not allow for instance to keep track of the evolution of solar features for longer than half solar rotation nor to observe the source where SEPs release as they may occur on the non-observable regions, and studying the global structure of the SW and the IMF. For these reasons, it is extremely helpful to complete the observations and measurements with other s/c located at other points of the heliosphere. Thus, the data from other heliospheric observatories is crucial for probing the IMF, and this thesis work makes use of the twin s/c mission at 1 au Solar Terrestrial Relations Observatory (STEREO) (Kaiser et al., 2008), and set the basis for future data analysis from the two recently launched Parker Solar Probe (PSP) (Fox et al., 2016) and Solar Orbiter (SolO) (Müller et al., 2020; Forveille & Shore, 2020), which are located at different radial distances during their orbit.

2.2. The STEREO Mission

This PhD work is primarily based on the analysis of different data sets provided by instruments onboard the STEREO mission. It is a mission composed by two almost identical s/c, STEREO Ahead (STEREO-A) and STEREO Behind (STEREO-B), that were launched at the same time on October 25 2006. Their particular heliocentric orbit (STEREO-A ∼ 0.96 au and STEREO-B ∼ 1.04 au on average) allows to have stereoscopic imaging of solar features in the ecliptic plane, as it gives two new points of observations close to the Earth's orbit moving away from the planet in opposite directions with a

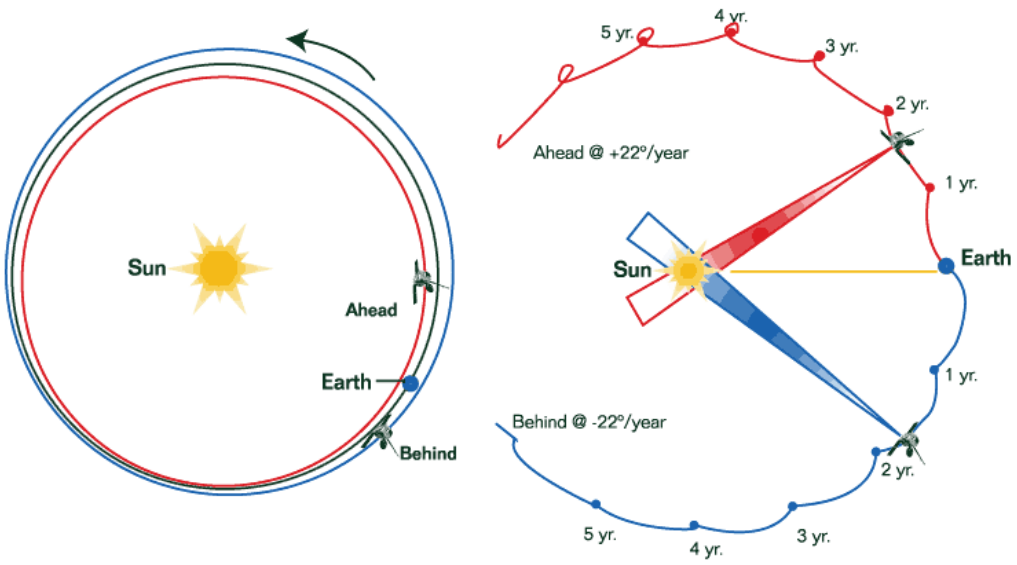

Figure 2.2: Sketch of the orbit of the STEREO mission. Left: heliocentric trace of both STEREOs and Earth; right: fixed Sun–Earth line and the relative position of both s/c. Credit: (Kaiser et al., 2008).

constant relative translation of ~ 22 degrees per year as Figure 2.2 shows. The superior conjunction happened during summer 2014. In this period some technical problems were reported in part because of the reduced communications due to the solar obstruction, which derived into the loss of attitude control of STEREO-B, hampering the possibility of acquire data from this s/c. On the contrary, STEREO-A is operating normally.

They are 3-axis stabilised s/c, i.e. they are facing the Sun continuously almost without rotations to allow a continuous remote-sensing observation. Together with the missions surrounding Earth and the earth-based telescopes, STEREO has allowed to reproduce the geometrical topology of CMEs, observe SEP events with wide angular separation, keep track of the evolution of the CHs or ARs, or among other things, measure the in-situ properties of the plasma which allows to analyse the spatial and temporal variations.

Each s/c has onboard remote-sensing as well as in-situ instrumentation. The remote-sensing instruments are part of the Sun Earth Connection Coronal and Heliospheric Investigation (SECCHI), which consists of two heliospheric imagers, two coronographs and an extreme ultraviolet telescope. Also, STEREO is equipped with the following in-situ instrument suites:

- In-situ Measurements of Particles and CME Transients (IMPACT)[1] (Luhmann et al., 2008) is composed by seven different instruments used to measure the characteristics of the IMF, the distribution of plasma electrons, and the properties of the SEPs. Those used in this work are:

  IMPACT-MAG (Acuña et al., 2008) is a triaxial magnetometer located at the boom of the s/c. It provides data with a cadence of 0.03 seconds in burst mode.

[1] https://stereo-ssc.nascom.nasa.gov/data/ins_data/impact/level2

Solar Wind Electron Analyzer (SWEA) (Sauvaud et al., 2008) is able to measure the DF of SW core and halo electrons from $\sim$ 1 eV to 3 keV. [2] It consists of a hemispherical electrostatic analyser located at the s/c boom, which has a sectorised field of view of 360 $\times$ 120 degrees with a geometrical factor at 0 degrees of 8.4 $\times$ $10^{-3}(sr \cdot cm^2)$. The team provides the PAD with 12 bins for 16 different energy channels with an acquisition of $\sim$ 2 counts per minute as a Level 2 data product. During the period from 14 February 2008 to 16 April 2009 for STEREO-A, and from 16 February 2008 to 16 April 2009 for STEREO-B, the PAD data product covers a slightly different energy ranges that affect some long-term analyses described below.

Solar Electron Proton Telescope (SEPT) (Müller-Mellin et al., 2008) can measure electrons from 20 to 400 keV and protons from 35 keV up to 6.5 MeV thanks to the double-ended magnet/foil detector with a field of view of 52.8 degrees for electrons and 52.0 for protons. The instrument is composed by four of these telescopes located at different faces of the observatory. They are nominally pointing to the ecliptic north and south, as well along the ideal Parker spiral in both directions. Data provided has a time resolution up to 1 minute.

- PLAsma and SupraThermal Ion Composition (PLASTIC) (Galvin et al., 2008) measures the properties of protons, alpha particles, and heavy ions, such as the kinetic proton temperature, the proton density, or the components of the bulk plasma velocity.
- STEREO/WAVES (SWAVES) (Bougeret et al., 2008) captures radio-emissions by the use of three orthogonal monopole antennas of 6 meters and covers from 10 kHz to 16 MHz. The data provided by the team are sampled with a cadence of 1 minute.

2.3. Parker Solar Probe and Solar Orbiter

The STEREO mission faces a limitation on the observation it can perform, as well as the Earth's vicinity missions: they are almost at the same radial distance and in the same plane of observation: the ecliptic. The first issue does not allow to measure the radial evolution of the SW in the heliosphere, while the second one struggles the possibility of having enough observational coverage to observe the polar regions of the Sun.

There are missions that have gone farther from the Sun as the two Voyagers (Stone, 1977) and already observed the physical properties of the heliopasue (the outer boundary of the heliosphere. See Section 1.2.1). Another landmark case is the one done by the recently launched NASA's PSP, which is the mission that has approached the closest to the star, and will have a maximum approach of 9.86 solar radii during the nominal mission phase. With this probe it is possible to have a better understanding of the SW inside the

[2] Although the SWEA was designed to measure from 1 eV to 3 keV, due to unexpected ionisation problems the energy channels below 60 eV are not reliable (Fedorov et al., 2011).

Mercury's orbit and it complements other missions with farther orbits. Also, previous missions as Ulysses (Wenzel et al., 1992), launched in 1990, already went out of the Ecliptic plane, but without remote-sensing instruments onboard. Solar Orbiter (SolO) is the recently launched ESA's (February 2020, currently in cruise phase) heliospheric observatory that will leave the ecliptic plane equipped with remote-sensing -as well as in situ- instruments and with an orbit whose perihelion is located closer to the Sun than Mercury's orbit.

2.3.1. Parker Solar Probe

It was launched in August 12 2018 on a Delta IV Heavy. The mission will have a lifetime of 7 years. Its orbit is approximately between Earth's and 9.86 solar radii, being the closest artificial object to reach that close to the star. The mission carries four different suites of instruments to measure different properties of the Heliosphere. Those suites are:

- Electromagnetic Fields Investigation (FIELDS) (Bale et al., 2016) can acquire data of different physical properties of the plasma such as the IMF, the absolute density, the temperature or radio waves, among others.
- Integrated Science Investigation of the Sun (IS⊙IS) (McComas et al., 2016) measures the properties of energetic particles such as electrons, protons, and heavy ions and it is divided into two different instruments (EPI-Hi and EPI-Lo) for studying different ranges of energy.
- Solar Wind Electrons Alphas and Protons (SWEAP) (Kasper et al., 2016) measures SW properties such as the velocity density and temperature of thermal and suprathermal electrons, protons, and helium ions.
- Wide-field Imager for Solar Probe (WISPR) (Vourlidas et al., 2016) counts with optical telescopes similar to the heliospheric imagers onboard STEREO and SolO that allows to observe the solar corona and the inner Heliosphere.

These instruments have as main scientific objectives:

1. Trace the flow of energy that heats the corona and accelerates the SW.
2. Determine the structure and dynamics of the magnetic fields at the sources of SW.
3. Determine what mechanisms accelerate and transport energetic particles.

This thesis work tries to help in answering part of all of them, by providing a method to characterise the PAD of the suprathermal electrons (1, Section 3.1), studying large-scale structures as the ICMEs and the nominal Parker spiral (2, Sections 4.2 and 5.1) and by looking at the characteristics of the propagation of SEPs (3, Sections 5.1 and 5.2).

2.3.2. Solar Orbiter

SolO, launched on February 10 2020, is a nominally seven-year ESA mission -which could be extended to 2030- and will approach the Sun to approximately 60 solar radii, inside Mercury's perihelion. At the extended phase of the mission, it will also leave the ecliptic plane with an inclined orbit of > 25 degrees. The s/c is equipped with a high-sophisticated shield that protects both in-situ and remote-sensing instrumentation. SolO has six different remote-sensing instruments onboard, that can measure a wide range of the electromagnetic spectrum, from white light to X-rays, with the following instruments: EUV full-Sun and high-resolution Imager (EUI, Rochus et al., 2020), Solar Orbiter - Heliospheric Imager (SoloHI, Howard et al., 2020), EUV spectral Imager (SPICE, Anderson et al., 2020), and Spectrometer Telescope for Imaging X-rays (STIX, Krucker et al., 2020), and a coronograph (Metis, Antonucci et al., 2020) as well as a magnetograph (Polarimetric and Helioseismic Imager, PHI, Solanki et al., 2020), which allows to measure the magnetic conditions of the solar surface. In addition, the following in-situ instruments onboard complete the payload:

- Energetic Particle Detector (EPD, Rodríguez-Pacheco et al., 2020). This suite counts with several instruments that allow to measure different populations of the plasma particles. It is able to measure composition, counting and DFs of suprathermal and energetic particles from few keV/n to hundreds of MeV/n with directionality as it owns multiple fields of view.
- Magnetometer (MAG Horbury et al., 2020). The magnetometer of SolO can provide 16 vectors (128 in burst mode) of the IMF with a cadence of ≤ 0.01 s in burst mode (≤ 0.1 s in nominal behaviour) and a sensitivity of 4 pT. Its sensors are located at different points of the lowest magnetically perturbed place of the s/c: the boom.
- Radio and Plasma Wave analyser (RPW, Maksimovic et al., 2020) can measure magnetic and electric fields, which are caused by plasma waves near the s/c, as well as those due to radio bursts.
- Solar Wind Analyser (SWA, Owen et al., 2020) is a suite of sensors -Proton and Alpha particle Sensor, Heavy Ion Sensor, and Electron Analyser System- that can measure SW ion and electron bulk characteristics, as the density, speed, and temperature, as well as the ion composition (from C to Fe). The Electron Analyser System is located at the boom and has a full coverage of the sky (except the sector blocked by the s/c, Figure 3 of cited paper).

SolO has as a main objective to answer the following four main scientific goals (Owens & Forsyth, 2013; Müller et al., 2020):

1. How and where do the SW plasma and magnetic field originate in the corona?

2. How do solar transients drive heliospheric variability?
3. How do solar eruptions produce energetic particle radiation that fills the heliosphere?
4. How does the solar dynamo work and drive connections between the Sun and the heliosphere?

Communications for data downlink, as well as commanding, are limited as the s/c is several times eclipsed by the star and there are complex gravitational assist manoeuvres and, in addition, all the instrumentation, specially the remote-sensing ones, generate a huge amount of data. For this reason, the coordination between the different instruments and the definition of some established operational mode scenarios are crucial to ensure an efficient use of the telemetry budget and the achievement of the scientific goals of the mission. With that purpose, SolO mission has a variety of Solar Orbiter Observing Plans (SOOPs) that are described in Zouganelis, I. et al. (2020). The data provided by the instrument teams can be located at SolO archive `soar.esac.esa.int/soar`.

2.4. Catalogues

When studying the collected data from different observatories (either remote-sensing observations of the Sun or in-situ measurements of the space plasma), one of the key points is the identification of diverse patterns related to possible structures/substructures as well as the definition of the nominal behaviour. The existence of previous catalogues makes the classification and analysis of any type of solar phenomena easier, as well as could be used for improving models or for feeding machine learning algorithms. The identification of the different structures is, among others, important for the Space Weather discipline.

As this thesis work is based on the study of different populations of the electrons to probe the IMF, it is important to characterise, to the extent possible, the magnetic topology and conditions of the local plasma and its solar origin. It is also necessary to identify the presence of SEPs, which carry information about their origin and their travel to the observer (see Section 1.3.5), and to extract the information provided by the suprathermal electron distributions, extremely dependant on the IMF conditions (see Section 1.2.2). To achieve this, some catalogues have been used as well as some other features have been collected and classified during the development of the work as described in following Chapters. The following catalogues publicly available and based on data from different missions have been used in this thesis:

- **Shock catalogue**[3]**.** Denominated the *Heliospheric Shock Waves Database* and maintained by the University of Helsinki, contains a wide extended list of IP shocks observed by multiple missions, providing their orientation as well as other parameters.

[3] `http://ipshocks.fi`

- **Solar Electron Event List**[4]**.** This catalogue indicates the onset of multiple events observed by the STEREO/SEPT instrument, indicating the onset of the electrons at the range of 55–85 keV, as well as the time of the peak intensity. Also, some other comments such as the type of event (see Section 1.3.5). It is maintained by part of the IMPACT/SEPT team (University of Kiel, Germany).
- **ICME Catalogue**[5]**.** It is maintained by the STEREO/MAG team. It has a selection of different ICMEs observed by both STEREO s/c. The comments show some properties of each MO, such as the presence of BDE or the relative value of plasma β, among others. The selection of the ICMEs have been performed based on the criteria enshrined by Jian et al. (2018, 2013, 2006a)
- **SIR Catalogue**[6]**.** It provides a catalogued of SIRs crossed by the two STEREOs. There it is indicated the beginning, the end and peak in hydrostatic pressure inside the structure. The list is also maintained by L. Jian and the SIR selection criteria can be found in Jian et al. (2006b, 2019).

[4] www2.physik.uni-kiel.de/STEREO/downloads/sept_electron_events.pdf
[5] https://stereo-ssc.nascom.nasa.gov/pub/ins_data/impact/level3/ICMEs.pdf
[6] https://stereo-ssc.nascom.nasa.gov/pub/ins_data/impact/level3/SIRs.pdf

Chapter 3

Studying Suprathermal Electron Pitch-Angle Distributions

Chapter 2 introduced the dataset from different observatories and the catalogues utilised in this work that aims to unravel the IMF topology for different SW conditions. Charged particles such as the electrons, protons and ions travel along the IMF, so the study of the PADs of these species can be very useful to discern the topology and conditions of the field. The distribution of the particles depends on their origin, such as the acceleration process, and the different conditions of the plasma they have encountered until the arrival to the observatory, for instance the IMF topology, the turbulence, etc.

A great part of this thesis work is focused on the study of the suprathermal electrons in the IP medium. They provide directional information as they are continuously emerging from the Sun, and their gyroradius is smaller than the one of higher energy particles ($<$ 22 km for 1 keV and 5 nT). These characteristics allow to probe IMF local lines and the conditions that the population encountered from their emergence until their observation. In addition, their directional distributions are well characterised because the detectors have typically a wide field of view with smaller sectors and no loosing flux statistics (see chapters 1 and 2), which allows a better directional distribution over 4π.

The following sections are divided into three different topics: the description of a characterisation method of the suprathermal electron PAD (Section 3.1); the analysis of two of the most common PADs after the simple *strahl* typical of the unperturbed ambient SW, the isotropy and the BDE, which can provide substantial information about the local features of the IMF (Section 3.2); and the analysis of the variability over time of the absolute anisotropy for a given energy, its dependency with the solar-cycle and also with the heliomagnetic latitude (Section 3.3). The studies of this Chapter are mainly based on data from STEREO/SWEA and ACE/SWEPAM instruments.

3.1. Pitch-Angle Distribution Characterisation

The PAD function (i.e. DF vs PA) analysis may require of a mathematical process in order to extract the information that provides its actual shape. There are previous methods that aim to obtain different pieces of information from the PADs, such as the degree of isotropy by using similar parameters to the variance of the DF (e.g. Crooker et al., 2003) or the width of the *strahl* population by the use of Gaussian fitting (e.g. Anderson et al., 2012; Graham et al., 2018). Nevertheless, there are other approaches that try to reproduce the shape of the distribution and, from the derived mathematical approximation, to extract the desired information. For example, Chen et al. (2014) utilises Legendre polynomials applied to the directionality of energetic electrons trapped in the Earth's outer radiation belt to infer the PAD given a topology by using unidirectional or omnidirectional flux from a point in the defined topology. Other examples are the ones in Balogh (1971); Sanderson et al. (1983, 1985); Agueda & Lario (2016), that use the same approximation for quasi-relativistic electrons in order to quantify the anisotropy, among others. This work uses Legendre polynomials similarly to them, but the method defined below has been applied in order to study the general shape of suprathermal electron PAD data provided by STEREO/SWEA and ACE/SWEPAM (however, this method can be applied to other species and populations) and characterised using signal processing analysis. The definition and some of the analyses shown in this work were already published in Carcaboso et al. (2020).

Under the assumption of a gyrotropic trajectory (i.e. the PAD equally behaves inside the cylinder surrounding the angle of observation due to the helical movement of the population), the suprathermal electron PADs can be characterised using an expansion of the orthogonal Legendre polynomials on the cosine of the PA.

$$f(\theta) = \sum_{i=0}^{\infty} A_i P_i(\cos\theta) = \sum_{i=0}^{\infty} F_i(\theta) \tag{3.1}$$

where θ represents the PA, A_i are numeric coefficients and $P_i(x)$ are the Legendre polynomials, given by Rodrigues formula (e.g. Howlett et al., 2007):

$$P_i(x) = \frac{1}{2^i} \sum_{k=0}^{i} \binom{i}{k}^2 (x+1)^{i-k}(x-1)^k \tag{3.2}$$

Legendre polynomials formally include infinite harmonics ($i \to \infty$). However, the experimental data constitutes a discretisation which limits the maximum meaningful order. The process followed in this work has been to fit the summation of a certain number of Legendre Polynomials to all the mentioned PADs data with total the total number of sectors are covered by the IMF direction, and corrected for ion bulk flow by using a least squares fitting algorithm Levenberg-Marquardt under the Python 3.6 *lmfit* package

(Newville et al., 2014, 2019, see Section 1.5). Apart from that filtering, those fits not converging by the algorithm are excluded.

Due to the discretisation, artificial oscillations at the boundaries of the studied interval may occur. This problem is known as the Runge's phenomenon and occurs when a polynomial is fitted to a set of equispaced data points. For this reason, it is necessary to have a well-conditioned approximation (Dahlquist et al., 2014), and the order of the harmonics must accomplish $i < 2\sqrt{n}$ (where n is the number of data points) if a least-squares fitting is performed. As seen in the previous Chapter 2 Sections 2.2 and 2.3, the analysed PADs cover 12 equiangular data points for every sample in the case of STEREO/SWEA, and 20 points in the case of ACE/SWEPAM. Despite this last instrument provides more points, in order to have directly comparable results, all of them are fitted up to the fifth harmonic, which results from truncating equation 3.1. The obtained equations are:

$$F_0(\theta) = A_0 \tag{3.3}$$

$$F_1(\theta) = A_1 cos\theta \tag{3.4}$$

$$F_2(\theta) = A_2 \frac{1}{2}(3cos^2\theta - 1) \tag{3.5}$$

$$F_3(\theta) = A_3 \frac{1}{2}(5cos^3\theta - 3cos\theta) \tag{3.6}$$

$$F_4(\theta) = A_4 \frac{1}{8}(35cos^4\theta - 30cos^2\theta + 3) \tag{3.7}$$

$$F_5(\theta) = A_5 \frac{1}{8}(63cos^5\theta - 70cos^3\theta + 15cos\theta) \tag{3.8}$$

The shape of these six terms are shown in Figure 3.1 and the different coefficients A_i are obtained by fitting the summation of the six terms (equations from 3.3 to 3.8) to the experimental PAD data points at a given time. Some examples of the performed fits to experimental data can be found in Figure 3.2, where a period measured by STEREO-A is observed.

Even Legendre Polynomial terms (i.e. F_2, F_4) are symmetric with respect to 90 degrees ($\cos\theta = 0$), while the odd ones (i.e. F_1, F_3, F_5) have antisymmetric shape. Also, F_0 corresponds to the mean value of the PAD. The actual shape of the experimental PAD is determined by the relative contribution of each harmonic, and thanks to this, different pieces of information can be extracted contemplating the following assumptions:

- As a first approximation, BDE can be considered as a symmetric distribution, peaking at both the cosine of PA +1 and -1. An ideal counterstreaming would appear when the second and fourth coefficients are positive and have much higher absolute value than the others, while loss-cone PADs or 90 degrees depletions would also present symmetry, but their identification requires further interpretation of the coefficients. Finally, the butterfly distribution would appear when the second coefficient

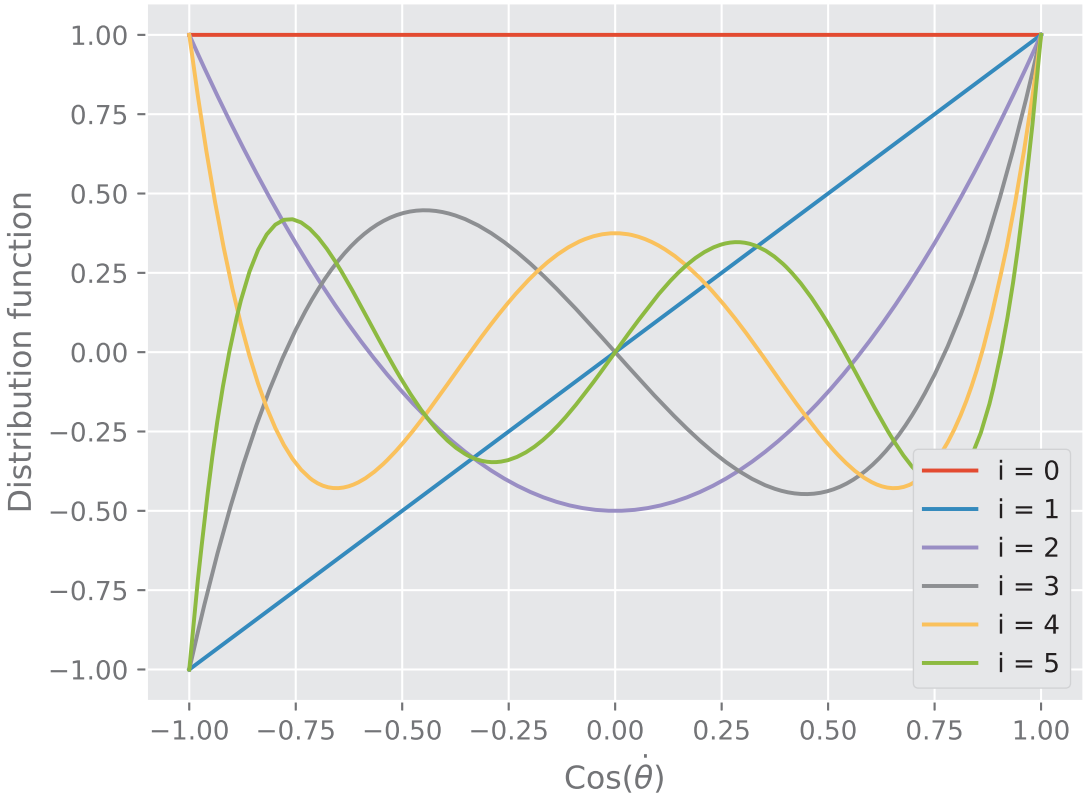

Figure 3.1: Distribution function of the Legendre Polynomials up to fifth order in arbitrary units. Even harmonics are symmetric along $cos(\theta) = 0$, and odd harmonics are antisymmetric.

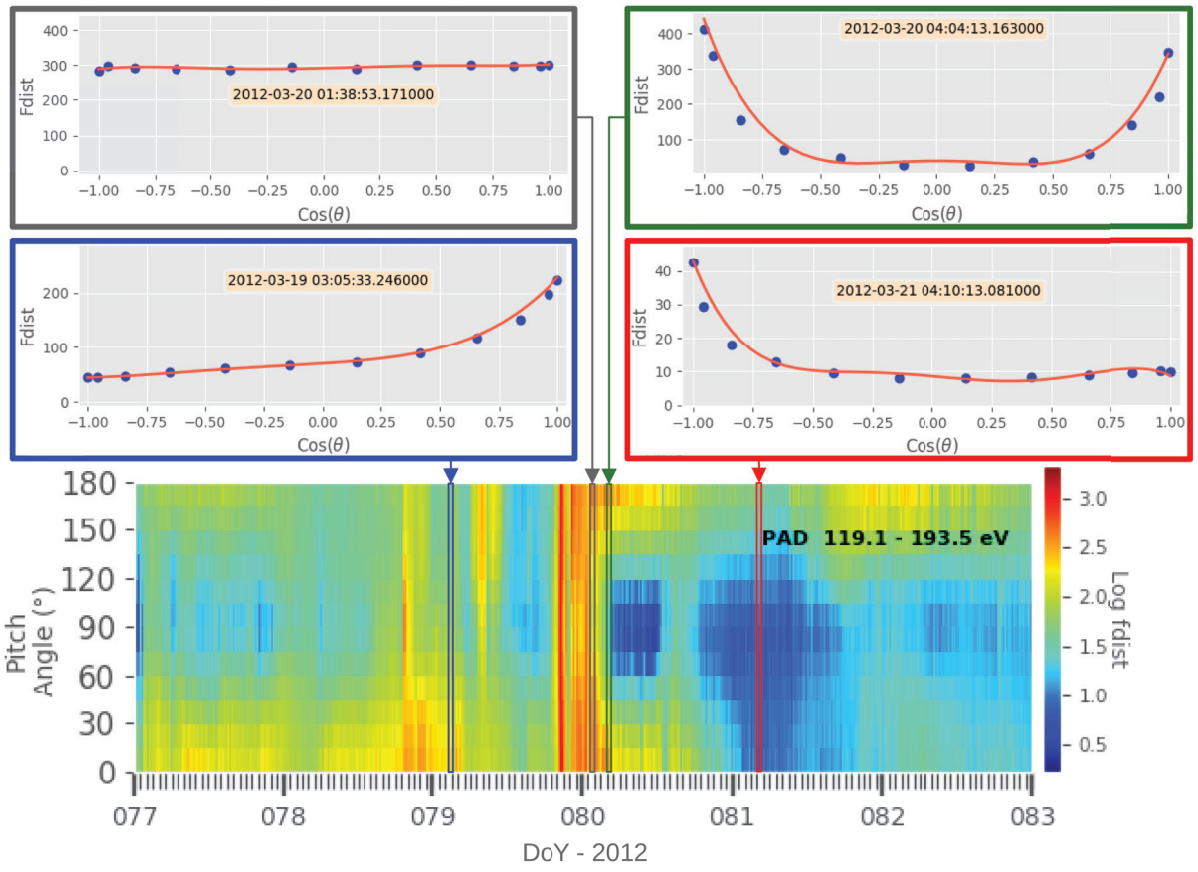

Figure 3.2: STEREO-A/SWEA PAD for channel 120–190 eV on March 2012 (bottom). Zoomed boxes shows the snapshots of the corresponding shown timestamps and represents the DF (blue dots) and the Legendre polynomials fit (red line). Grey box is isotropic, green shows BDE -counterstreaming-, and blue and red shows single *strahl* with outward and inward polarity, respectively.

is positive, the fourth is negative and it contributes significantly to the final shape.

- A pancake distribution is a symmetric PAD too, but in contrast to the counter-streaming case, the second coefficient must be negative and the second harmonic must dominate over the others.

- The simple *strahl* distribution has a clear non-symmetric behaviour, peaking at cosine +1 or -1 depending on the IMF polarity. For this reason, the odd harmonics are the ones that contribute the most to the final shape.

- When the mean value (i.e. *harmonic* 0, determined by the A_0 coefficient) prevails over all the other terms, then the PAD would be isotropic.

The importance of the contribution of each term to the final PAD can be characterised using a logarithmic relative power scale as it is commonly performed in signal processing methods, with the calculation of a Signal-to-Noise-Ratio (SNR) coefficient. In this case, the 'signal' would correspond to the harmonic/s desired for the study and the rest of the harmonics must be considered the 'noise' of the total PAD (see equation 3.9).

$$SNR_{dB} = 10 \cdot log_{10} \left(\frac{\mathcal{P}_{signal}}{\mathcal{P}_{noise}} \right) \tag{3.9}$$

where $\mathcal{P}_{signal}$ and $\mathcal{P}_{noise}$ are the power calculated for one or for the summation of various harmonics. The power of any harmonic/s is defined as:

$$\mathcal{P}_i = \frac{1}{2\pi} \int_{-\pi}^{\pi} |F_i(\theta)|^2 d\theta \tag{3.10}$$

As mentioned above, the second and the fourth harmonics are the ones that define the symmetry of the PAD. For this reason, a more symmetric PAD will drop a higher SNR of the sum of both harmonics (SNR_{24}). In order to distinguish between the different types of BDE and also the pancake, it is necessary to take into account the possible combinations of the sign of each coefficient too. By looking at the weight of the coefficients and the relation between all of them, a finer classification could be performed.

When the PAD is nearly isotropic, the possible contributions of the harmonics are negligible compared to the value of A_0 (mean value). For this reason, it is necessary to quantify the predominance of the harmonics with respect to the F_0. Analogously to signal processing methods, the *ripple* of the signal (γ) can be used in this case to identify how significant are the angle-dependent deviations. The ripple is an dimensionless coefficient defined as:

$$\gamma = 100 \cdot \frac{f_{rms}}{A_0} \ [\%] \tag{3.11}$$

where

$$f_{rms} = \sqrt{\frac{1}{2\pi}\int_{-\pi}^{\pi} \mid f(\theta) \mid^2 d\theta} - A_0 \tag{3.12}$$

A perfect isotropy would be defined by the unique contribution of F_0 to the final PAD ($\gamma = 0$). Furthermore, larger values of γ can be interpreted as higher grade of anisotropy in the PADs. The definition of a threshold in γ (γ_{th}) makes the identification of isotropic and anisotropic periods easier, while the combined use of SNR_{24} and γ_{th} allows to classify the BDE periods in the SW. This permits a massive analysis of the data provided by the previously mentioned missions.

3.2. Isotropy and Bi-Directional Suprathermal Electrons

In Section 3.1, two different coefficients were defined in order to quantify the anisotropy (γ, Equation 3.11) and the bi-directionality (SNR_{24}, based on Equation 3.9) of any PAD. In this Chapter, these coefficients are calculated for a long-term analysis of the PAD of the suprathermal electrons acquired by STEREO/SWEA for the period March 2007 (after both s/c went outside the Earth's magnetosphere) until the end of July 2014 (before the superior solar conjunction); for ACE from January 1, 1998 to September 25, 2005 (before the instrument gain change) for part of the analysis and from September 25, 2005 to June 1, 2012 (before the mission control attitude change, where the s/c's spinning axis varied on October 23, 2012)[1].

3.2.1. Defining the Isotropy

It is well established that there is a correspondence between plasma β and the anisotropy of suprathermal electrons in the SW, where the value of plasma β is anticorrelated with the anisotropy (Crooker et al., 2003). High-β plasmas are prone to scatter suprathermal electrons, and this reduces heat flux coming from the Sun. In this case, plasma β is defined as the ratio of the gas pressure (calculated as $P_g = N_pKT_p + N_eKT_e + N_{He}KT_{He}$, where N is the density, K the Boltzmann constant, and T temperature, and p corresponds to proton, e to electrons and He to helium) to the magnetic pressure. The latter is calculated as $P_{mag} = B^2 \,/\, 2\mu_0$ (with B the magnetic field and μ_0 the magnetic permeability of vacuum), while the gas pressure is estimated considering the contribution of protons, alphas and electrons as explained in Mullan & Smith (2006), assuming T_e and an alpha/proton ratio constant with a value of 140,000 K and 0.04 respectively (Newbury, 1996; Bürgi, 1992).

In order to validate the characterisation of the degree of anisotropy based on γ, Figure 3.3 shows a 2D histogram of this parameter versus $log_{10}(\beta)$ for the entire period under

[1] http://www.srl.caltech.edu/ACE/ASC/level2/swepam_l2desc.html.

study for the two STEREOs. In both cases, there is a clear decreasing trend of γ (see also Figure 4 in Crooker et al. (2003), where the authors characterise the anisotropy using the variance of the experimental PAD data). This confirms that γ can be used as a reliable anisotropy index. It can also be noticed that values of γ are bounded between $\sim 1\%$ ($log_{10}(\gamma) = 0$) and $\sim 320\%$ ($log_{10}(\gamma) = 2.5$), and that the contribution of the harmonics to the final DF is rarely higher than 3.2 times the value of A_0.

There are observations where the actual contribution of the harmonics is negligible with respect to the mean value of the DF. In other words, there is no clear predominance of any direction (i.e. the distribution is isotropic), which drops the nonexistence of *strahl* population. This aspect is very relevant for identifying the topology of the IMF and adds relevant information about the factors that may affect those lines as previously shown in Section 1.2.2. The typical situations that could explain the isotropy could be the total smearing of the *strahl* population due to turbulent conditions or the existence of IMF lines not connected to the Sun, so there is no distinguishable *strahl* population. For this reason, in order to have a clear separation between the isotropy and the anisotropy, a threshold value must be defined. Thus, the fit results obtained by STEREO-A were analysed. Figure 3.4 represents a 2D histogram of the anisotropy coefficient γ versus the first order anisotropy. The two notorious branches correspond to simple *strahl* with different polarities and it can be seen the existence of a region below $\sim 15\%$ where there is no clear predominance from any direction. This value means that at least a 15% of the PAD corresponds to the contribution of the harmonics, and has been defined as threshold ($\gamma_{th} = 15\%$) to discern between isotropy and anisotropy for the following analyses. Black line in Figure 3.3 corresponds to γ_{th}.

As an example, Figure 3.5 shows a period observed by STEREO-A in September 2013 including two closely-spaced time intervals where the PAD becomes isotropic. Both intervals are shaded in yellow for all panels. The panels represent the bulk plasma velocity (a); proton density (b); panel c shows the observed kinetic temperature in blue and the yellow line represents an empirically predicted kinetic temperature based on the proton speed as explained in Elliott et al. (2012); proton thermal pressure (d); IMF strength (e) and the corresponding polarity derived from the azimuthal angle within ± 60 degrees (green, positive; red, negative; yellow, undefined); panel f shows the azimuthal angle of the IMF with the estimated angles of the Parker spiral based on the bulk velocity (positive, green; negative, red), while g indicates the latitudinal IMF angle; panel h shows the three different components of the IMF in RTN coordinate system; plasma β (i); panel j shows the anisotropy coefficient γ, which is coloured in red when the flux is isotropic ($\gamma \leq \gamma_{th}$); panel k shows the SNR_{24}; and panel l shows the actual PAD for SW suprathermal electrons with an energy of 119–194 eV (y-axis is the angle in degrees, z-axis represents the DF in logarithmic scale).

The two highlighted periods are identifiable with very sharp boundaries, clearly pre-

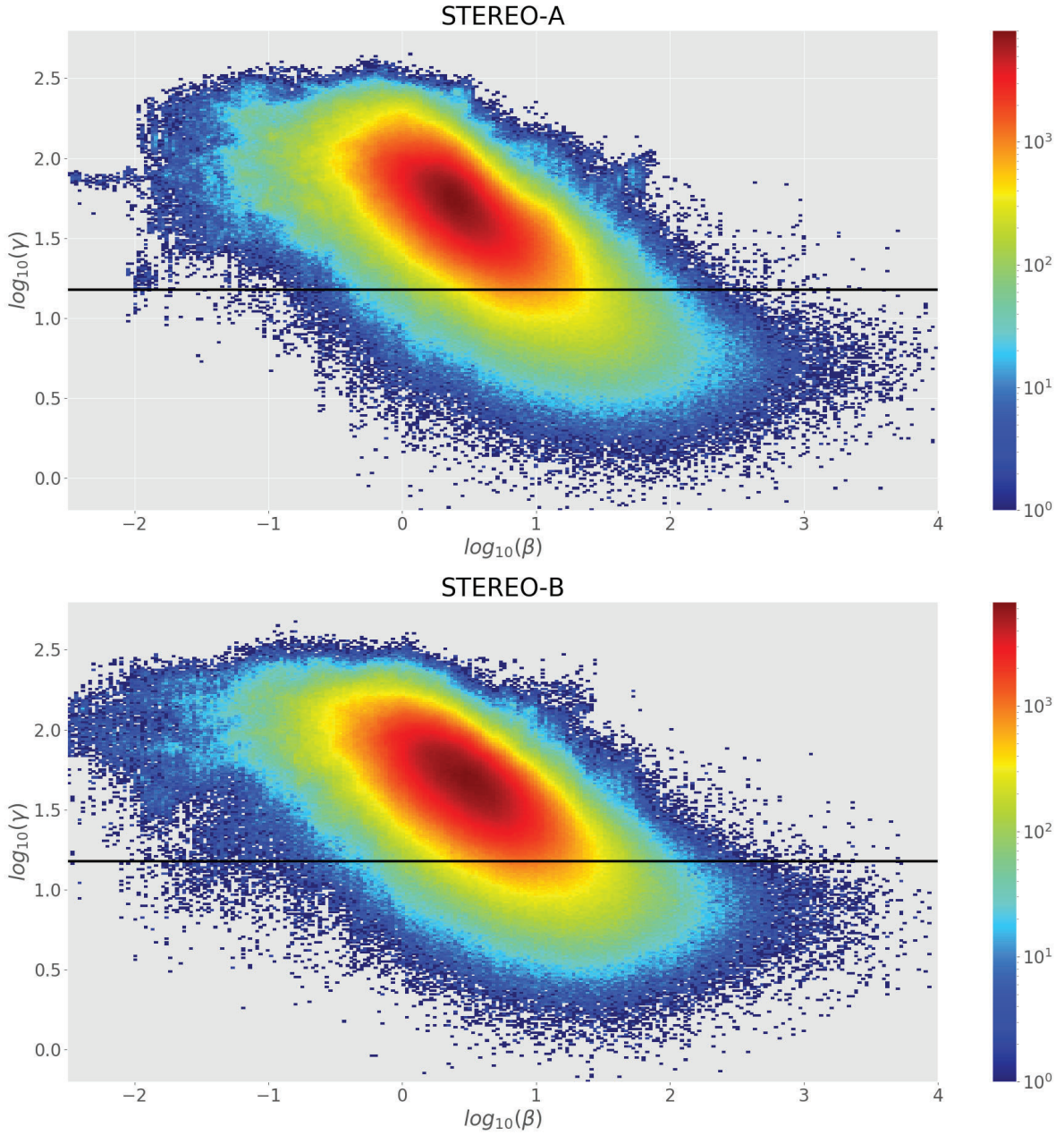

Figure 3.3: 2D histograms showing the relation between the log_{10} of the anisotropy coefficient γ and the log_{10} of the plasma β for the entire period under study (2007 – 2014) for STEREO-A (top) and STEREO-B (bottom). Horizontal black line shows γ_{th} (see text for details), and colour bar indicates the number of events for each bin in logarithmic scale.

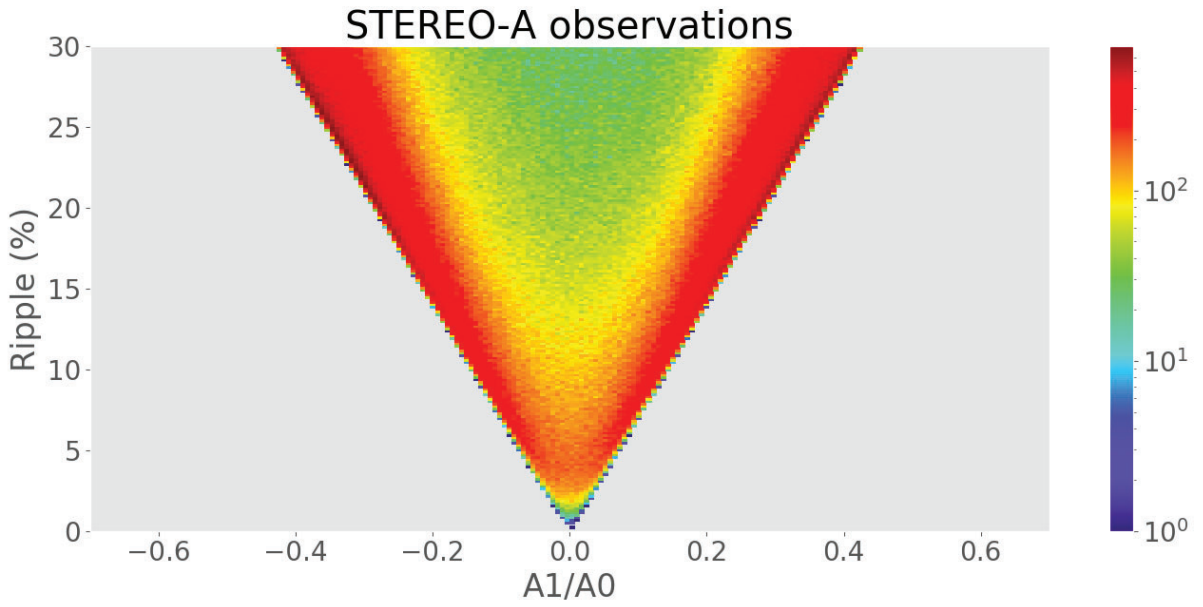

Figure 3.4: Two-dimensional histogram showing the number of occurrences of the anisotropy coefficient γ versus the result of A_1/A_0, which represents the first order anisotropy value (see e.g. Tan et al., 2007).

senting the following SW signatures different with respect to the surroundings: discontinuities in the bulk plasma velocity; IMF strength decrease, proton density and kinetic temperature enhancements with the corresponding increase on the hydrodynamic pressure and consequently, the plasma β too; a sudden change in the polarity, going from predominantly positive polarity to negative for the first interval, positive between the first and the second, ambiguous for the second interval and positive afterwards, which suggests sustained tangential crosses through the HCS; low values of the anisotropy coefficient γ, below the threshold which defines the isotropy, while the rest of the shown interval is characterised by a *strahl* during a period with outward magnetic polarity and higher values of γ; the SNR_{24} remains below 0 dB during almost all the presented observation due to the lack of symmetric PADs.

Using the defined threshold of γ_{th}, a complete survey of isotropic PADs has been performed for both STEREOs, and it is gathered in the Catalogue of Isotropic Periods presented in Section 3.2.4.

3.2.2. Defining the Bi-directionality

In order to establish a reliable criterion for the identification of BDE periods, observations of suprathermal electron PADs from $\sim$ 119 eV to $\sim$ 193 eV inside ICMEs (as they are structures whose topology allows the observation of BDE. See Section 1.2.2) and in the quiet SW are compared. The quiet SW is defined as the whole period under study for both STEREOs, removing the transit of the catalogued ICMEs +12 hours, SIRs $\pm$12 hours and shocks $\pm$2 hours. A subset of those ICMEs observed by both STEREOs with particularly long and clear periods of BDE was filtered by eye (see Appendix). After this

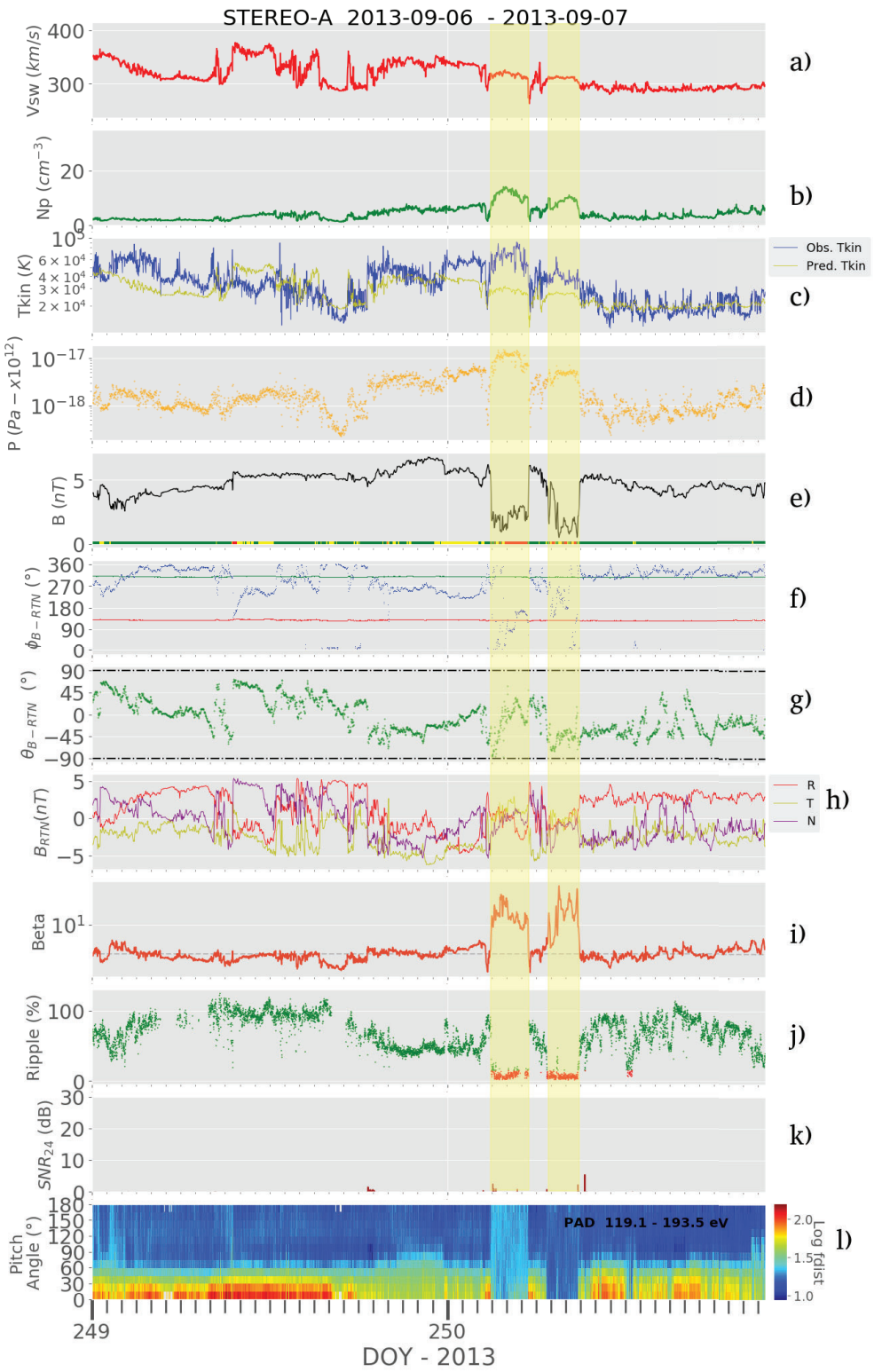

Figure 3.5: STEREO-A observations during a period in September 2013 including two intervals of isotropic flux of suprathermal electrons shaded in yellow. From top to bottom: SW proton speed, proton density, proton temperature, IMF magnitude accompanied by its polarity (red, negative; green, positive; yellow, ambiguous), IMF azimuthal angle in the RTN coordinate system complemented with the two possible nominal Parker Spiral angles (red, negative; green, positive) calculated from the proton speed, IMF latitudinal angle in the RTN coordinate system, RTN magnetic field separated components, plasma β, the anisotropy coefficient for suprathermal electrons γ (*ripple*, see Section 3.1), the bi-directionality coefficient SNR_{24} (see section 3.1), and 119–194 eV suprathermal electron PAD colour-mesh (y-axis is the angle in degrees, z-axis represents the DF in logarithmic scale).

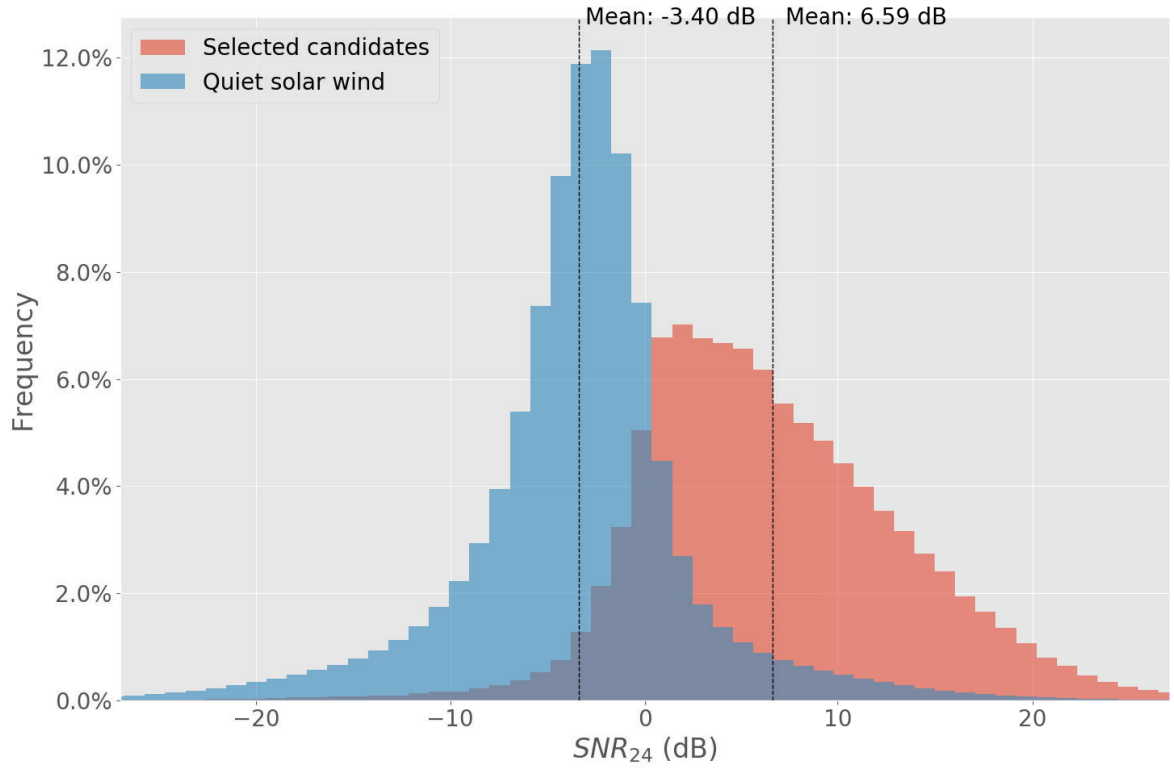

Figure 3.6: Histograms of the calculated SNR_{24} for the selection of ICMEs with longer periods of BDE (red, listed in appendix), and for quiet SW (blue).

selection, the data were filtered further using the above defined criteria of $\gamma > \gamma_{th}$ (i.e. non-isotropic) and $A_2 > 0$ (i.e. not peaking near pitch-angle 90 degrees). Once they were filtered, the SNR_{24} was calculated. In addition, the same procedure was performed for the selection of quiet SW periods.

Histograms of the calculated SNR_{24} for each sample are presented in Figure 3.6. For the quiet SW (blue), the distribution is almost symmetric, centred at a mean value of SNR_{24} of -3.40 dB. As expected, the distribution for the selected ICMEs (red) is significantly shifted to higher values of SNR_{24}, showing an asymmetric distribution with a mean value of 6.59 dB, and a median value of 5.79 dB of a total of 370,875 fits. Both distributions intersect near 0 dB and show some overlapping due to the occasional presence of BDE in the quiet SW (e.g. due to non-catalogued ICMEs, small scale transients or post-ICME periods showing significant bi-directionality as it will be discussed in Chapter 4) and the absence of BDE during certain periods of the selected ICMEs too.

The median of the SNR_{24} histogram for the selected ICMEs has been defined as a threshold to set a reliable identification criterion of periods with clear BDE ($SNR_{th} = 5.79$ dB). This restrictive threshold does not imply that values below do not correspond to bi-directional PADs, but it assures that those above 5.79 dB are almost certainly bi-directional. The stated threshold (SNR_{th}) is used in following studies in sections 3.2.3, 4.1 and the previously mentioned catalogues (Section 3.2.4). It should be noted that this

selection threshold is used for relative comparisons of different periods, and not as an absolute indicator of BDE because this the criterion is very restrictive an BDE can be present below the threshold. As well as the case of the isotropy, the defined threshold of SNR_{th} has been used to list BDE periods observed by both STEREOs as described in Section 3.2.4.

3.2.3. Long-term Variation of Isotropy and Bi-directionality

In order to explore the solar-cycle dependency of suprathermal electron bi-directionality and isotropy, the first four panels shown in Figure 3.7 represent the time variation of the percentage of isotropy (blue) and BDE (green) for both STEREOs, with moving windows of 3 months. The grey dashed lines show the mean percentage of the whole period under study. On the first two charts, the red line corresponds to the radial distance to the Sun of each s/c, while on the following two, the orange line indicates the time in hours per month of transit of ICMEs listed in *ICME Catalogue* (see Section 2.4). The bottom panel represents the daily average Sun Spot Number (SSN) and the average tilt angle of the HCS (Hoeksema, 1995). As previously explained in Section 2.2, the energy range used for the data product has a slight difference due to changes in the energy ranges of the instrument, covering from $\sim$ 127 eV to $\sim$ 180 eV instead of the nominal range from $\sim$ 119 to $\sim$ 193 eV. The two vertical black lines of the first fourth panels mark the period where this difference is present.

In spite of the small angular separation between STEREO-A and STEREO-B (less than 11 degrees) during March–May 2007, significant discrepancies were observed in both isotropy and BDE. Some contribution of electrons escaping from the Earth's magnetosphere at STEREO-B (Opitz et al., 2014) or a shielding effect of the magnetospheric obstacle cannot be discarded as a possible source of this discrepancy at the earliest part of the plots.

The isotropy (panels 1 and 2 in Figure 3.7) show periodic variations, roughly coincident with the orbital period for both s/c. However, while STEREO-B tends to always observe more isotropy when it is located farther from the Sun, the origin of the periodicity for STEREO-A is unclear and not obviously correlated with the heliocentric distance, heliographic latitude nor planetary connections along the IMF (not shown in the Figure). Since the amplitude of the heliocentric distance variation along its orbit is higher for STEREO-B than for STEREO-A, the recurrence observed at STEREO-B could be the result of increasing cumulative effects of scattering and/or disconnection events, however, given the narrow interval of variation of heliocentric distances covered by both s/c (below 0.087 au for STEREO-B and below 0.012 au for STEREO-A), the ultimate origin of the quasi-periodic behaviour at both s/c requires further investigation.

Apart from this periodicity, a prominent increase of the isotropy during late 2009 and early 2010 was observed by both s/c, in coincidence with the quick rise of the HCS

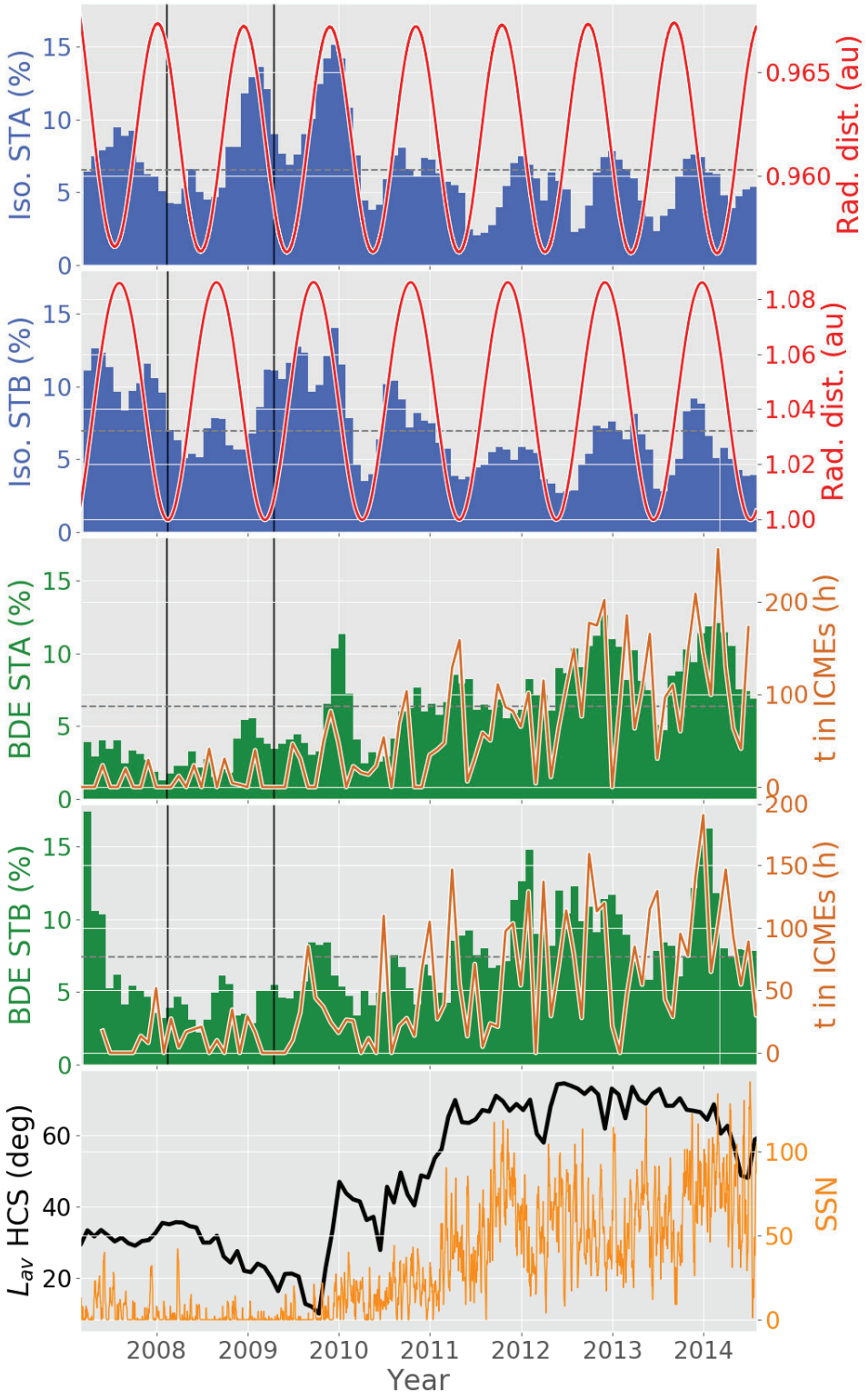

Figure 3.7: Temporal variation of the time percentage during 3 months of isotropic periods (blue) and bi-directional periods (green). From top to bottom: Percentages of time appearance calculated for a running window of three months of isotropy for STEREO-A, isotropy for STEREO-B, and over-plotted the heliocentric distance of both s/c; BDE for STEREO-A, BDE for STEREO-B, accompanied by the time transit of ICMEs listed in *ICME Catalogue* (see Section 2.4); finally, SSN and latitudinal angle of the HCS. (See text for more details)

tilt angle, which marks the end of the solar minimum and the start of the rising phase of solar cycle 24. It should be noted that suprathermal electron isotropy is frequently observed near IP HCS crossings (Crooker et al., 2003), therefore subject to the influence of the global HCS tilt angle and the s/c latitude. For both s/c, the isotropy is overall more frequent near solar minimum (2008–2010) than during the increasing phase of the solar cycle (2011–2014), although this tendency is weak compared with the recurrent fluctuations.

The bi-directionality (panels 3 and 4 in Figure 3.7) roughly follows an increasing trend with the increasing solar activity level (SSN and HCS tilt angle). This means that bi-directional periods are longer and more frequent during solar maximum than near solar minimum. At the same time, the fraction of time corresponding to ICME transits (solid line in panels 3 and 4) follows the same trend. This result matches what was expected, as one of the properties of the ICMEs is to present BDE (Zurbuchen & Richardson, 2006), and the ICME occurrence rate increases during solar maxima (Owens et al., 2007; Richardson & Cane, 2010; Li et al., 2018). It is also notable that STEREO-A observed a local maximum in the rate of BDE during late 2009 and early 2010, just after the quick increase of the HCS tilt angle.

3.2.4. Catalogues of Bi-directional and Isotropic Periods

Using the method described above, the PADs can be easily identified as isotropic or bi-directional. This opens the possibility of having better identification of other types of PADs. Both distributions (isotropy and BDE) have a special interest as they add relevant information of the topology of the IMF as explained in Chapter 1. Two different catalogues of isotropic and bi-directional periods have been created for STEREO-A and STEREO-B. For collecting the candidates, a moving window ($\sim$ 20 minutes) was used to calculate the time percentage where the imposed thresholds are fulfilled (see Sections 3.2.1 and 3.2.2). If the condition is fulfilled for at least 10 minutes of that moving window (i.e. a 50 percent), the period is a candidate for the list. When two or more candidates have a separation of less than 2 hours, they are considered as the same event. The list shows the start and the end of each event, its duration and the column *Catalogued* shows if the corresponding period coincides with some of the structures listed in Section 2.4. The catalogues of isotropy and BDE are already published and can be found in `cdsarc.u-strasbg.fr/viz-bin/cat/J/A+A/635/A79`.

3.3. Anisotropy

3.3.1. Anisotropy Variation

The anisotropy coefficient γ has been analysed for long periods of time in order to analyse solar cycle, orbital position and energy dependencies of the suprathermal electrons in the SW. Figures 3.8 and 3.9 show the 3-day and 5-day-averaged, respectively, values of γ for both STEREOs and ACE for the available data of each mission (see Section 3.2.2). In order to avoid misinterpretations, the period corresponding to the change in energy ranges for STEREO/SWEA PAD has been avoid. This period goes from 14 February 2008 to 16 April 2009 for STEREO-A, and from 2008-02-16 to 2009-04-16 for STEREO-B (see Section 2.2).

Figure 3.8 shows the anisotropy coefficient γ for both STEREOs and ACE for similar energy channels (STEREO/SWEA 252 eV, ACE/SWEPAM 272 eV). The data is filtered using a Savitzky Golay smoothing (Savitzky & Golay, 1964). All the s/c present remarkably similar behaviour, even when there is a substantial longitudinal separation between the s/c, although a consistent offset is almost all the time present. This offset could be produced due to the radial distance difference between both STEREOs, and instrumental differences for ACE's case are not discarded. All of the missions have a clearer peak which seems to repeat almost every $\sim$ 13 months, and coincide with the lower values of isotropy shown in Figure 3.7. The ultimate reason of this apparent periodicity, as well as the one found in the isotropy, requires further study.

Figure 3.9 shows the anisotropy coefficient in the different energy channels of STEREO/SWEA for both s/c. On the one hand, almost systematically the anisotropy coefficient is higher for higher energy channels. Due to the predominance of an unique *strahl* in the SW (corresponding to open IMF lines), this behaviour is in agreement with the studies Fitzenreiter et al. (1998); Horaites et al. (2018), which found that the *strahl* width narrows with energy. On the other hand, there are also periods where the lower energy channels seem to be the ones more anisotropic, which is in agreement with the postulations from Pagel et al. (2007); Berčič et al. (2019b) too, which found the opposite behaviour, i.e. that the *strahl* population width broadens with the energy. It seems that, on average, the tendency is to present higher anisotropy for higher energies, but in certain sustained moments this tendency is not such, as Anderson et al. (2012) also pointed out.

In order to corroborate this assumption, the study of the data gathered by all the energy channels of both STEREOs is presented in Figure 3.10. In every energy channel, γ follows a distribution similar to a Maxwell-Boltzmann, with a peak higher than for the previous channel, confirming the idea that higher energies present higher anisotropy most of the time. The periods where this seems not to be the rule must be studied in detail.

Furthermore, as Figures 3.8 and 3.9 show, the same apparent periodicity previously observed with regards to the isotropy (see Section 3.2.3) seems to exist also for the grade

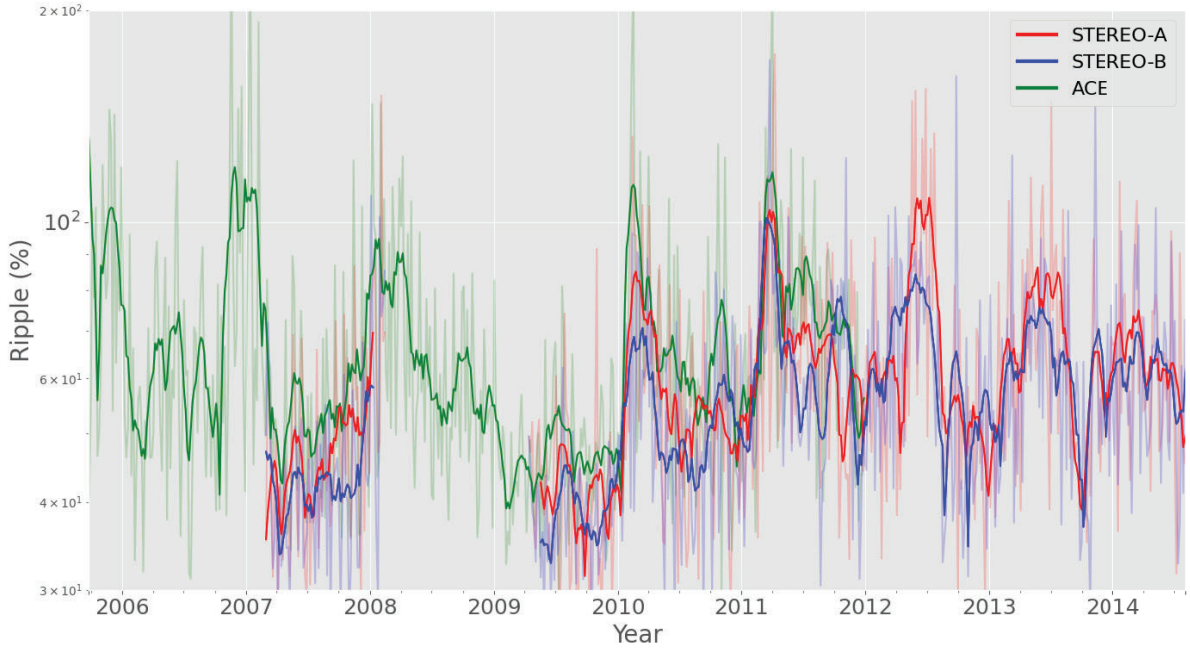

Figure 3.8: Temporal variation of the anisotropy coefficient γ calculated for 252 eV energy channel for STEREO-A/SWEA, STEREO-B/SWEA and 272 eV energy channel for ACE/SWEPAM. Dimmed lines represent the 5-day mean value, while stronger ones correspond to high-pass-filtered ones.

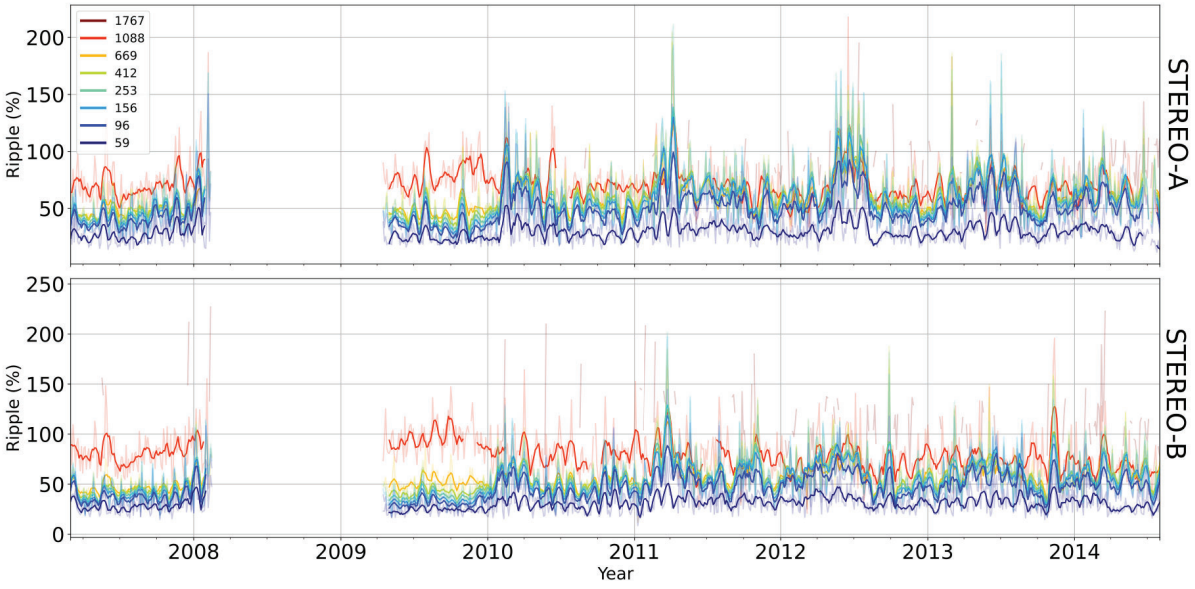

Figure 3.9: Temporal variation of the anisotropy coefficient γ for the different energy channels (legend indicates the center of each channel in eV) of both STEREOs. (Top, A; bottom, B)

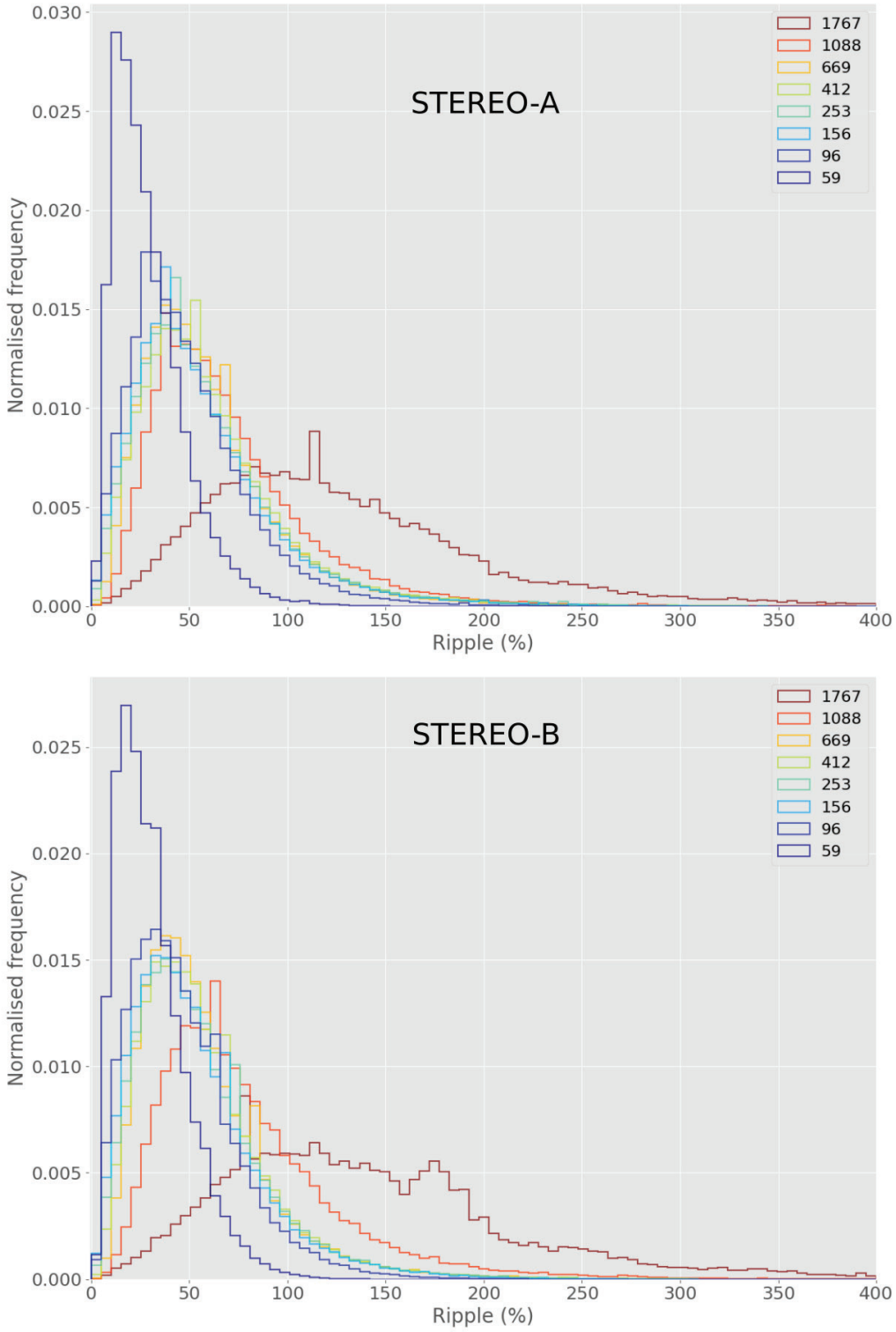

Figure 3.10: Cumulative histograms of the anisotropy coefficient γ for the different available energy channels (in eV) of STEREO-A (top) and STEREO-B (bottom)

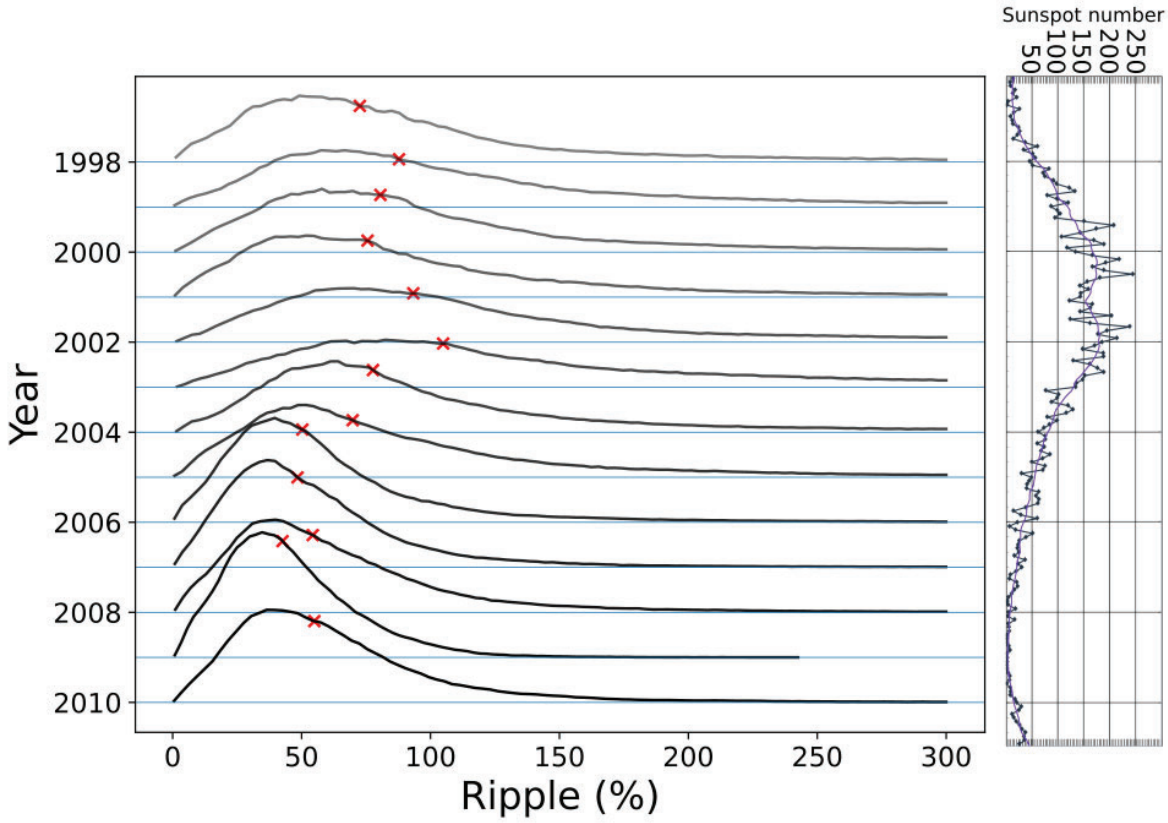

Figure 3.11: Yearly histograms of the anisotropy coefficient γ calculated for the 272 eV energy channel measured by ACE/SWEPAM (left); Monthly sunspot number in black and smoothed values in purple (right). Red crosses indicate the median value of the histograms.

of anisotropy in all the channels and missions. None of the main peaks in the anisotropy coefficient observed by each s/c seem to correspond to any planetary connection nor specific region in the heliosphere. Moreover, it can be seen a similar solar-cycle-dependency behaviour, having higher anisotropy in solar maximum and lower in solar minimum, in opposition to the isotropy. Figure 3.11 shows the temporal variation of the yearly normalised histograms of the anisotropy coefficient γ for the 272 eV ACE/SWEPAM energy channel, which is the one with more available data for the period under study. The distribution is more spread and with a higher mean in the solar maximum, and narrower with lower mean in the solar minimum, supporting the idea of the dependency with the solar cycle and being more probable to have isotropy during solar minimum. This is also coherent with the idea presented in the study performed in Section 3.3.2.

Besides all this, the quantification of anisotropy of the suprathermal electrons and its analysis in the time domain allows also to study higher frequency periodicities, and even finer with better instrument cadence, which could be useful for the analysis of turbulence of the plasma.

3.3.2. Heliomagnetic Latitude Dependency

No obvious correlation of the isotropy or the ripple with the heliographic latitude was found during the study in performed in Section 3.2.3. On the other hand, the excursions above and below the heliographic equator for in-ecliptic s/c are very modest (±7 deg) and therefore, not well-suited for the study of latitudinal variations. The last panel of Figure 3.7 suggest that the s/c location relative to the HCS may play a role and therefore the distance of the s/c to the HCS, or better, the angular separation between the s/c magnetic foot-point and the neutral line at the SW source surface could be a relevant parameter to organise the observations.

In this thesis work, the heliomagnetic latitude of a s/c has been calculated trying to estimate the angular separation from the ballistic point up to 2.5 solar radii to the remote HCS. For doing this, the calculations are based on the Potential-Field Source-Surface (PFSS) model (Schatten et al., 1969; Altschuler & Newkirk, 1969; Hoeksema, 1984; Wang & Sheeley, 1992) from Wilcox Solar Observatory, from where the HCS tilt angle is also extracted (from now on, Wilcox Model, Hoeksema, 1995). Also, the nominal Parker spiral topology based on the SW speed is assumed.

As explained in Section 1.2.1, there are two regimes of the SW that have different properties, produced essentially by their origin in the star. Previous studies such as Balogh et al. (1999) already show a dependency of the SW velocity and an estimation of the heliomagnetic latitude. In order to see the dependency of the anisotropy of the suprathermal electrons with their solar origin a similar process has been performed with the data provided by the STEREO and ACE missions.

As an input, the Wilcox model needs to know the magnetic configuration of the Sun. The magnetograms from the Earth-based Global Oscillation Network Group (GONG) can give insight about the polarity and the strength of the magnetic field in the solar surface from the point of view from the plane. There are no magnetograms that cover the entire star, but there are methods to reconstruct what is in the non-observable regions of the Sun. In this case, the synoptic maps provided by the Wilcox Solar Observatory have been utilised in order to perform the heliomagnetic latitude calculation.

The estimation of the heliomagnetic latitude has been performed under the assumption of a non-perturbed nominal behaviour of the Parker spiral, where the ballistic foot-point of the IMF up to 2.5 solar radii based on the in-situ SW speed is calculated. The heliomagnetic latitude is then calculated as the minimum angular separation of the foot-point to the neutral line.

This method is more reliable when the Sun is in solar minimum conditions, as the star's magnetic field behaves as a simple dipole with a more defined and single neutral line, while in solar maximum other considerations must be taken into account, such as the eruptive events that would modify the magnetic field lines, but are not contemplated

by the Wilcox model.

Figure 3.12 shows the mean value of the anisotropy coefficient γ for the three mentioned s/c during the quietest period of the solar minimum (June 2009–June 2011) sectorised with 6 equi-angular windows of the heliomagnetic latitude. The three of them seem to have the same behaviour, presenting lower γ closer to the HCS, increasing monotonously with the absolute value of the heliomagnetic latitude. The asymmetry of the windows is due to the nonexistence of periods with latitudes higher than positive 60 degrees in the heliospheric latitude. This is probably due to the existence of an offset between neutral line and the ecliptic plane.

As previously pointed out in Crooker et al. (2003) and Section 3.2.1, the isotropy of the suprathermal electron tends to be present during periods with high values of plasma β. These periods usually occur within regions where two opposite polarities are interacting, as it is the case of the HCS. In Section 3.2.3, an apparent relation between a sudden increase in the tilt angle of the IP HCS and the time observation of isotropy was shown. On the other hand, Figure 3.12 also supports the idea that the proximity to the neutral line on the solar surface (which might not be the same to the HCS in the IP medium) reduces the grade of anisotropy, as well as that as the farther the connection to this line, the more anisotropic the flux is, reaching up to a factor of two for $\sim |60|$ degrees. The results also suggest that periodicity found in both isotropy and anisotropy might be produced by the crossings of the HCS, whose tilt angle is varying over time, added to the solar rotation. Nevertheless, further analysis with different latitudes and longer periods are necessary.

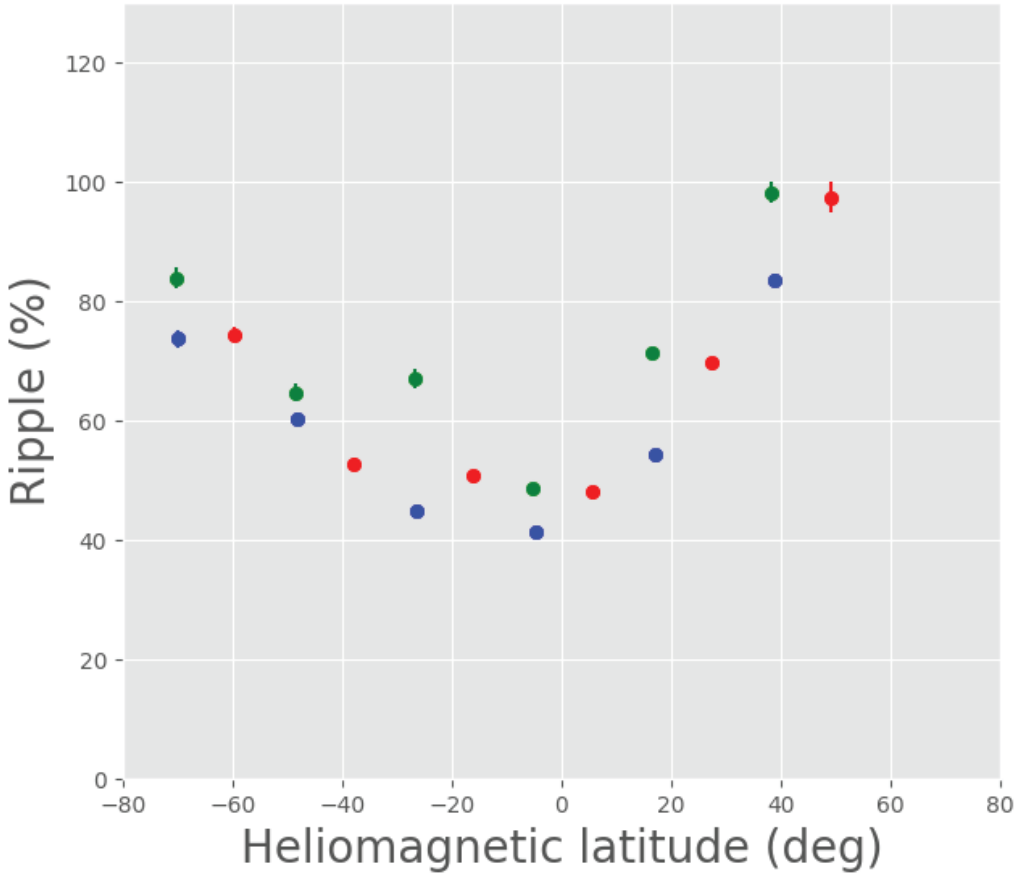

Figure 3.12: Mean value of the anisotropy coefficient γ with respect to the heliomagnetic latitude described in Section 3.3.2 for each observatory, calculated from June 2009 to June 2011 (Green: ACE; red: STEREO-A; blue: STEREO-B. See text for more details). Error bars correspond to the standard error of the mean.

Chapter 4

Interplanetary Coronal Mass Ejection Research

The CMEs and their IP counterpart, the ICMEs are one of the most important manifestations of the solar activity. They have a complex IMF topology which is distinguishable from the surroundings, and it is important to understand how they behave and how they evolve in the IP medium, interacting with their surroundings. For the Space Weather discipline, they are one of the most relevant structures of the SW, as the might directly affect the Earth surrounding conditions, and the satellite functioning, and it is important to interpret their orientation from the in-situ measurements to infer possible perturbations to the magnetosphere, among other things. Knowing the topology of these structures, and how they evolve and interact with the ambient SW and other possible structures is crucial too for having a better understanding of how they could affect the planet.

Considering the definition of isotropy and bi-directionality previously characterised in Sections 3.2.1 and 3.2.2 respectively, a superposed epoch analysis of the ICMEs gathered in the *ICME Catalogue* (see Section 2.4) has been performed in order to study the evolution of these two types of PADs as seen in Section 4.1. Apart from that, Hidalgo's model has been updated, with some additional constrains and reduction of the free parameters (Section 4.2). Then, a selection of periods with clear rotations in the IMF components observed by both STEREOs has been performed and an individual Hidalgo's model fitting procedure has been done for every period (Section 4.2.3).

4.1. Variations of Isotropy and Bi-directional Suprathermal Electron

4.1.1. Bi-directionality

During the transit of an ICME, the s/c sometimes observe noncontinuous BDE, or even periods with total absence of them (Larson et al., 1997; Winslow et al., 2016).

This is mainly due to the erosion processes or the reconnection at the footpoints that suffer the magnetically closed structures, characterised by presenting counterstreaming of suprathermal electrons, as previously shown in Section 1.3.3.

In order to study how BDEs are distributed during the transit of ICMEs, and in the immediately trailing region, a superposed epoch analysis has been performed, considering all the ICMEs listed on the *ICME Catalogue* (see Section 2.4) observed by both STEREOs during the period under study (317 events in total, excluding those affected by data gaps). The study has been performed by dividing the ICME time-transit into different sections, and the time-percentage mean value of BDE (where SNR_{24} is higher than the previously defined threshold SNR_{th}) has been calculated for each of them. Later on, the average of all the mean values in each section has been obtained. The MO has been divided into four parts, while the sheath (if present) has been divided into thirds because of the lack of statistics due to its shorter duration. Also, the interval following the ICMEs (from now onward, post-ICME) has been studied, excluding those cases where any other catalogued structure (ICME, SIR or IP shock) is present. The duration of this final region for each event has been set as 1.2 times the total duration of each ICME, and has been divided into four chunks. The criterion of 1.2 times the total duration of the ICME is selected because it corresponds to the minimum time required to recover the quiet mean value of BDE. Figure 4.1 shows a series of cumulative histograms of the time-percentage mean value of BDE in every portion of the sheath (red), MO (blue) and post-ICME (green) has been calculated. The error bars are the standard error of the mean. The ICMEs have been classified into two different types: with and without shock (middle and bottom histograms in Figure 4.1, respectively) based on the catalogues used throughout the study. The horizontal dashed line corresponds to the time-percentage mean value observed in the quiet SW, and the top panel shows the mean percentage of each sector for all the ICMEs, where it can be observed that mean value is within the error bars of the last sector of the post-ICME.

The average duration of the sheath region is 9.9 $\pm$ 0.5 hours (15 events for ICMEs without shock, and 67 for ICMEs with shock), while the MO has a mean duration of 24.3 $\pm$ 0.8 hours (139 events for ICMEs without shock, and 178 for ICMEs with shock). Finally, the post-ICME region lasts for 34.6 $\pm$ 2.0 hours (45 events for ICMEs without shock, and 42 for ICMEs with shock). Note that post-ICMEs are not considered if another catalogued event overlaps.

Based on the results shown in Figure 4.1, there is a clear tendency for both types of ICMEs (with and without shock) to have a gradual increase of the time presenting bi-directionality until the end of the first half of the MO, where it starts to decrease. As shown e.g. in Feldman et al. (1999), there is a tendency of having longer periods of BDE present inside of the ICMEs to be higher inside the MOs. The amount of BDE time-percentage becomes maximum in the central part of the MO, more shielded from the

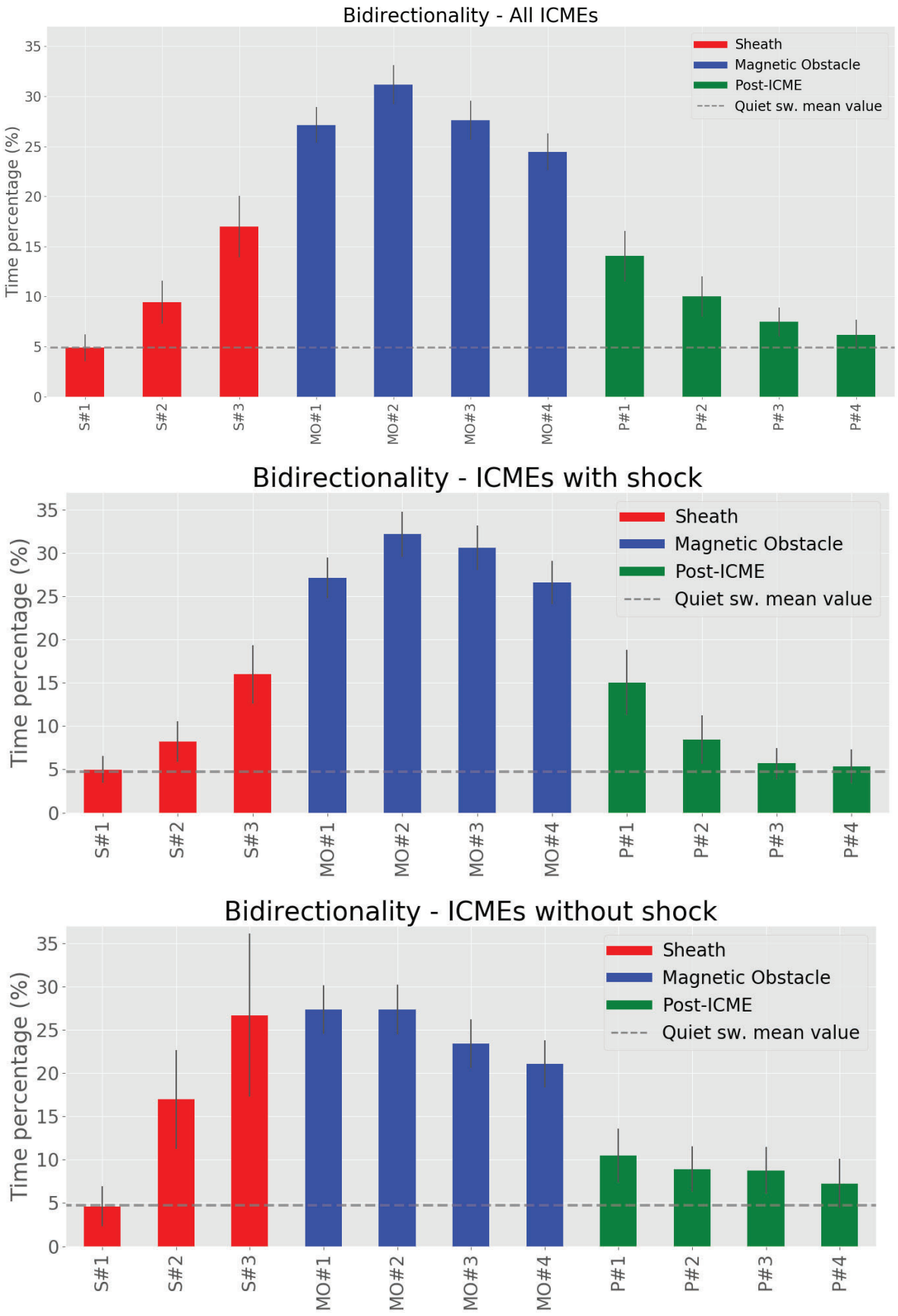

Figure 4.1: Histograms showing the mean value of the time-percentage of BDE for each interval during all the ICMEs transits catalogued in *ICME Catalogue* for all the events (top), with shock at the beginning (center), and without (bottom). The colours show the different catalogued regions (see text for more details) and the labels correspond to equi-timed periods of the transit of those regions (S – Sheath, MO – Magnetic Obstacle, P – Post-ICME). The error bars indicate the standard error of the mean.

surrounding fields and therefore less susceptible to erosion by reconnection. The presence of BDE inside the sheath is a likely indication of the existence of some closed loops in that region.

In the case of ICMEs with shock, the MO presents longer periods of BDE and the difference between the amount of BDE inside the MOs and the sheath and post-ICME is clearer than in the case of ICMEs without shock. A possible explanation is that those events driving an IP shock constitute a subset of the fastest ICMEs, which consequently have less time for undergoing erosion during the IP propagation to 1 au. Another possibility could be the addition effect of the streamed electrons and those accelerated or reflected in the shock, observing in-situ the summation of both distributions, as well as a possible diffusion mechanism produced by the MO as explained in Rodríguez-Pacheco et al. (2003) for the case of suprathermal ions.

On the other hand, ICMEs without shock do not show a symmetric profile of the percentage of BDE inside the MO, as one could expect considering that they are composed by flux-ropes and the IMF lines crossed by the s/c are the same at the front and the rear part. In contrast, the first half of the MO shows more BDE than the second one. This could be an indication of stronger erosion in the trailing edge of the expanding MO.

In both cases, it is notable that the post-ICME contains periods with longer bi-directionality than the quiet SW, especially for the ICMEs without shock, and that it is decreasing gradually. The existence of BDE at the post-ICME indicates the presence either of structures, or special IMF conditions after MOs. Some of the multiple explanations to this may rely in the existence of isolated closed lines in post-ICME, or the presence of uncatalogued flux ropes (in *ICME Catalogue*) after the ones studied. Another explanation could be the reflection of *strahl* occurring in converging IMF lines around the ICME (or at the shock, if it exists) or generated loops after the eruption of the CME.

As an illustrative example, Figure 4.2 shows an ICME with behaviour resembling the average profile of BDE time-percentage previously shown in Figure 4.1, for the MO and the post-ICME period. The ICME is preceded by a simple *strahl* with inward IMF and followed by a $\sim$ 1.5 days of BDE, and accompanied by a noticeable shock. The BDE during the MO and the post-ICME period are easily identified by the enhanced values of the SNR_{24} *-k)* panel-. As previously seen in Section 3.2.1, panel *j)* shows the *ripple* γ. Periods corresponding to $\gamma \leq \gamma_{th}$ are red-tagged (flagged as isotropic periods). In the plot, this corresponds to the midday of the day of year 276 and during the sheath region of the ICME. Isotropy during and after ICMEs will be discussed in the following Section 4.1.2.

4.1.2. Isotropy

Similarly to previous section 4.1.1, a study of the time-percentage of isotropy inside ICMEs and during the post-ICME region has been performed.

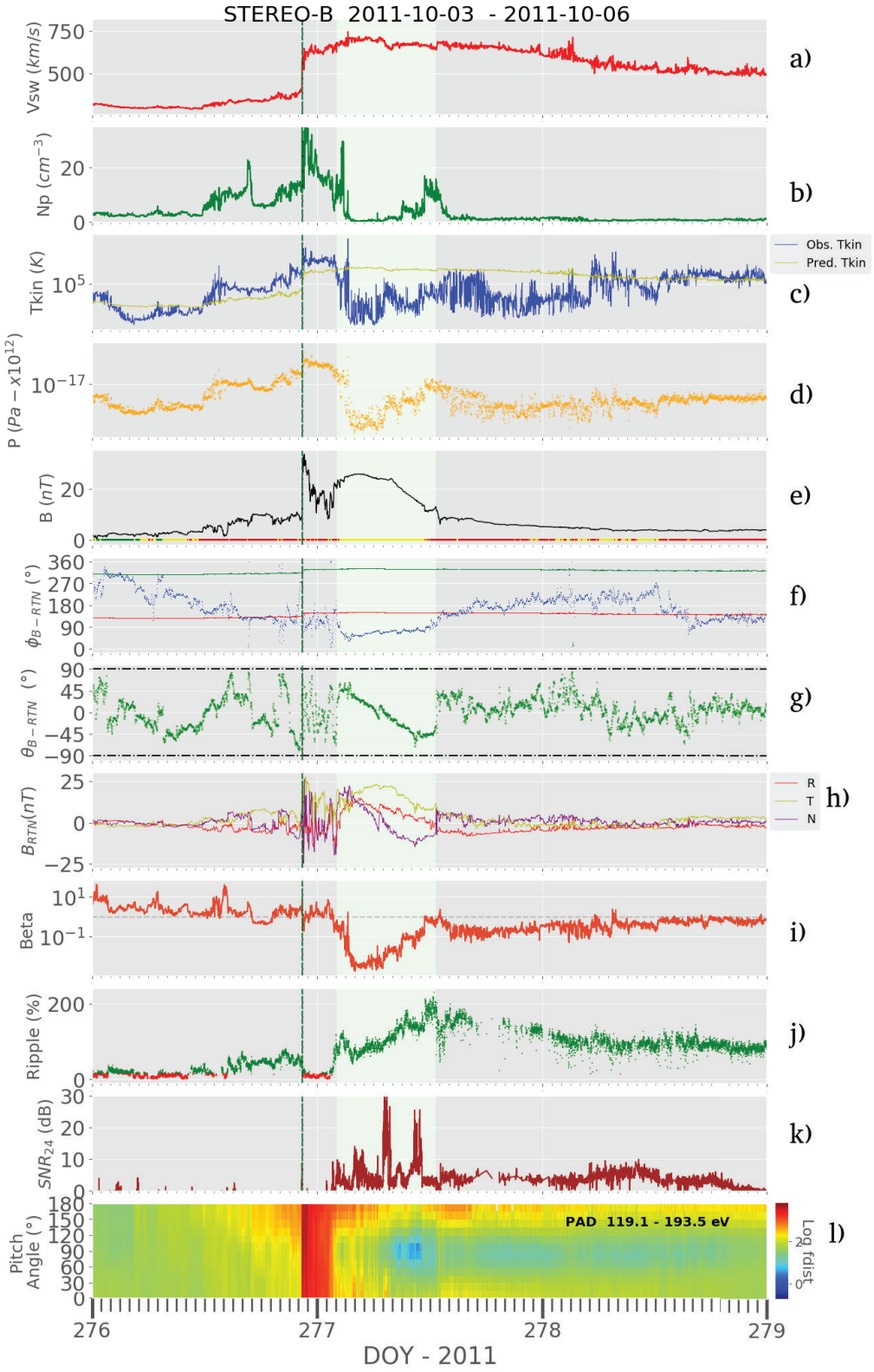

Figure 4.2: STEREO-A observations during an ICME observed on October 08–13 2011. The panel contents follow the same format as in Figure 3.5.

Figure 4.3 shows the same superposed-epoch sample of ICMEs presented in Figure 4.1 but, in this case, representing the fraction of time showing isotropy, defined as $\gamma \leq \gamma_{th}$. The grey-dashed line marks the average percentage of isotropy observed in the quiet SW (as defined in Section 3.2.2). The MO (blue) presents the lowest probability of presenting isotropy, always below the average isotropy in the quiet SW, while the sheath (red) and the post-ICME (green) have higher values. Also, ICMEs with shock show higher rate of isotropy in the sheath. Since the sheath is a compressed turbulent region (see e.g. Kilpua et al., 2017), this isotropy could be partly due to enhanced scattering conditions. The enhanced isotropy in the post-ICME region could be an indication of the presence of formerly closed field lines that became fully disconnected from the Sun at both ends.

The ICME event previously shown in Figure 4.2 is a good example of the existence of isotropy in the sheath region. Figure 4.4 shows one of the studied ICMEs observed by STEREO-B during solar maximum (October 2013), which clearly shows isotropy in the post-ICME region. That ICME is preceded by a shock (vertical green-dashed line) listed in *Shock Catalogue* (see Section 2.4) and presents clear signatures such as decreasing SW speed, enhanced IMF, low plasma β, low proton temperature, and BDE. The MO is shaded in green. The sheath is in between the shock and the MO, and the post-ICME lasts until the end of 12th October (day of year 285).

4.2. Approaching the Flux Rope Topology

As previously seen, the topology of the ICMEs are complex and difficult to understand due to their size and the casuistry derived from the surrounding conditions. One of the best known type of MO is the MCs. They have been analysed from different perspectives and another possibility to unravel their topology is by the use of analytical models. In this thesis work, a model described in the series of articles Hidalgo & Nieves-Chinchilla (2012); Hidalgo (2013) has been used for a statistical analysis of MCs observed by both STEREOs. In those articles, the authors proposed an analytical model that can be fitted to the three experimental IMF components of a MC and provide the orientation of the FR axis in the IP medium, among other characteristics. Also, the model has been tweaked in order to reduce the number of free parameters and obtain a global topology closer to reality, as explained below.

4.2.1. Topology

The model assumes that the MCs have a closed magnetic topology formed by a single magnetic FR, where the plasma is contained, and have non-force-free character, which in this case, implies that the total pressure is not uniform (i.e. $\nabla P \neq 0$) inside the structure as it evolves during the expansion and may have further irregularities too.

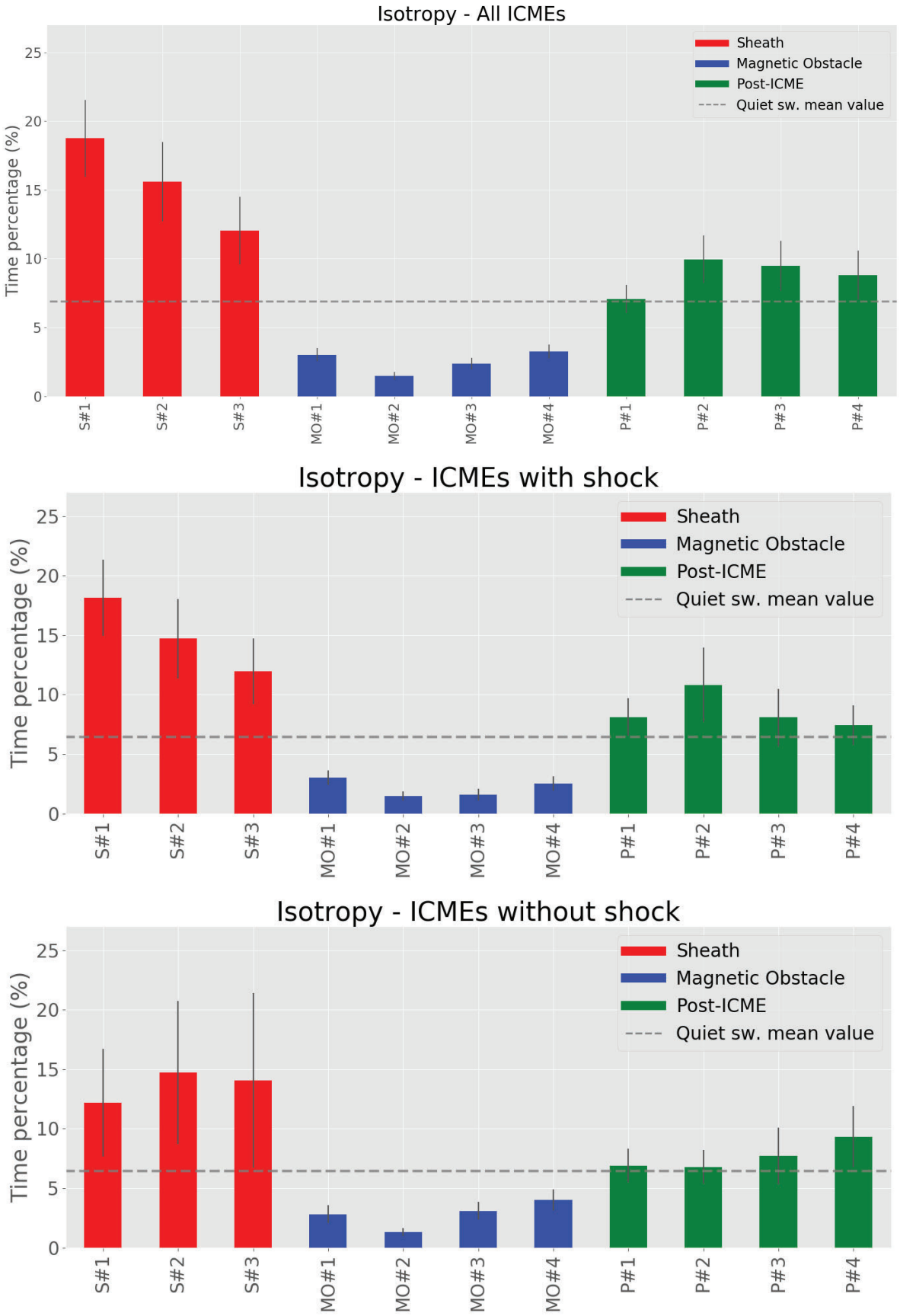

Figure 4.3: Histograms of mean value of the time-percentage of isotropy of each sector during all the ICMEs transits catalogued in *ICME Catalogue* for all the events (top), with shock at the beginning (center) and without (bottom). Colours and labels follow the same format as in Figure 4.1.

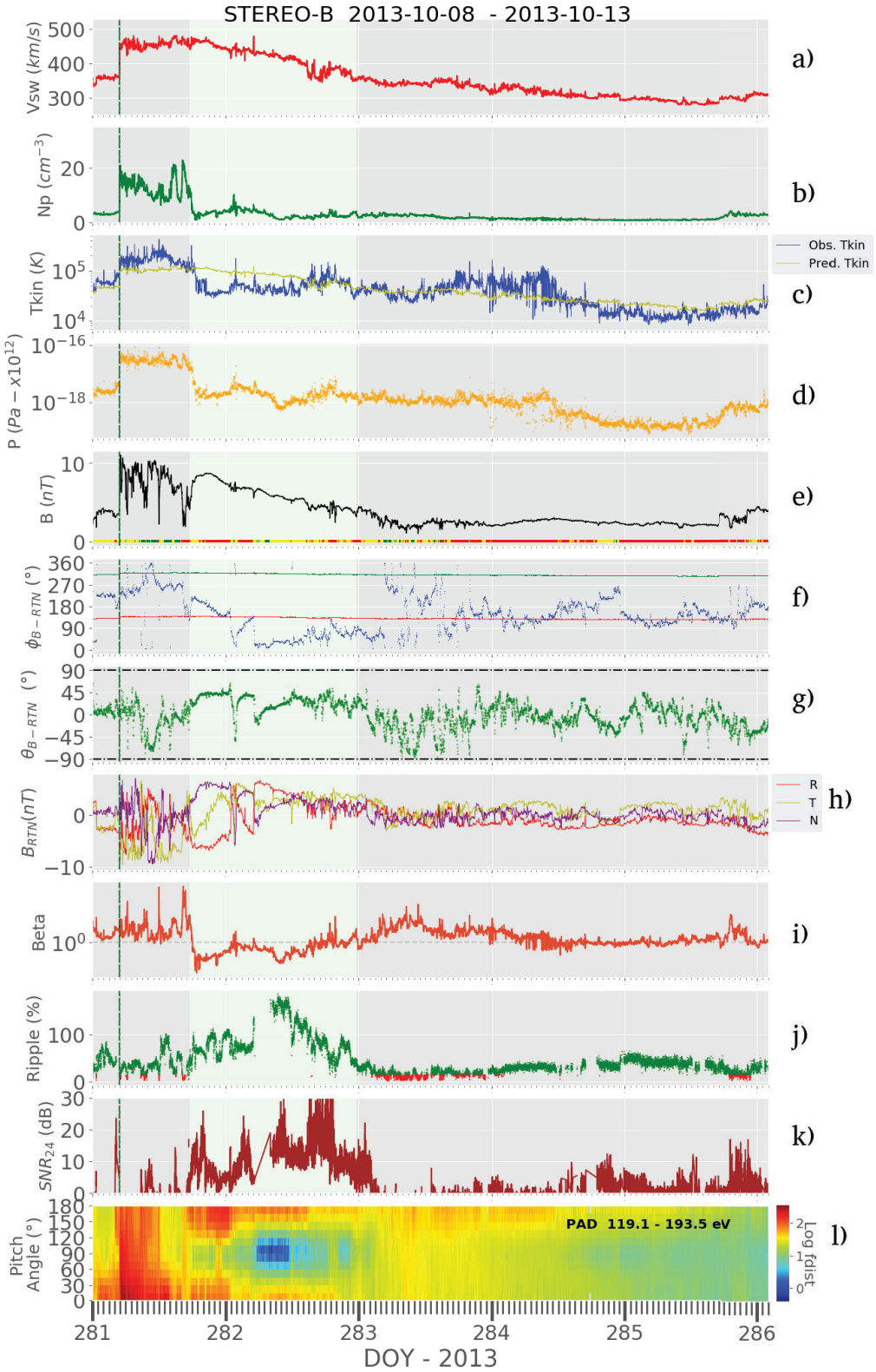

Figure 4.4: STEREO-B observations during an ICME observed on October 03–05 2013. The panel contents follow the same format as in Figure 3.5.

The global magnetic shape of the MC, according to the model, is described by a torus whose legs (the closest part to the star) become narrower towards the Sun -where it remains attached after the emergence-, with non-uniform cross section, as a consequence of the expansion that occurs during the evolution in the IP medium. In addition, the model defines the IMF of the structure as helicoidal lines which become narrower as closer it goes to the axis of the FR's cross-section. Figure 4.5 represents a three-dimensional sketch of the model.

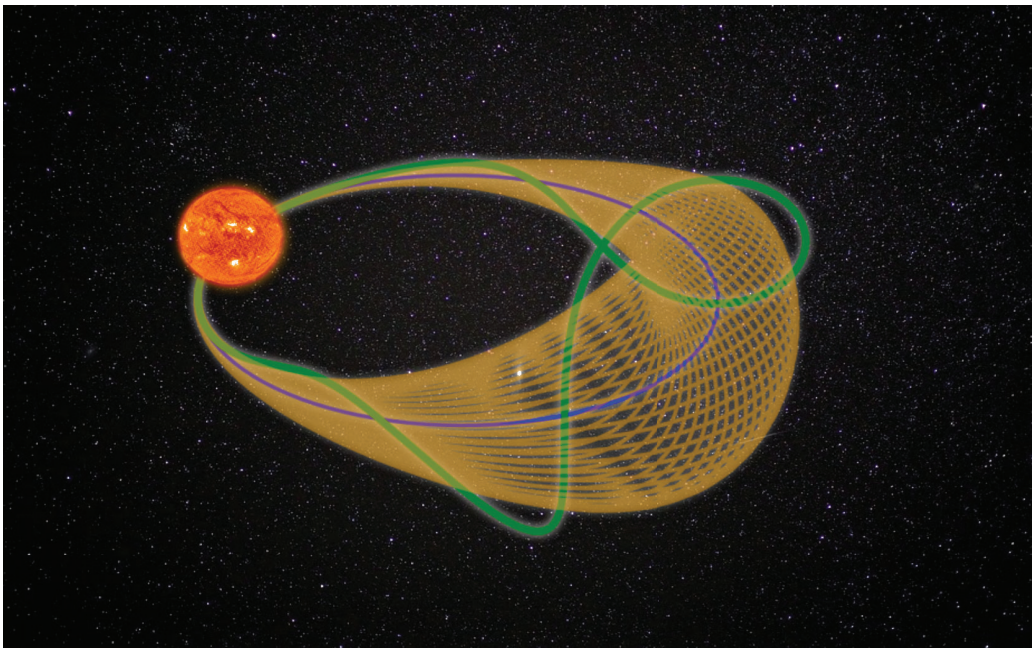

Figure 4.5: Recreation of an example of the global morphology of a MC according to Hidalgo's Model, with the legs attached to the Sun and the cross-section at the front part (i.e. the *nose*) is wider than at the legs. The blue line represents the axis of the cross section -with only axial component-, while the green one shows the boundary of the FR -with a mixture of axial and helicoidal field-. In between these two, orange mesh reproduces the lines as an addition of both components.

The topology represents one of the biggest constrains in order to define the interface conditions of the model. As explained in previous Section 1.3.3, the complexity of a model implies having a larger number of free parameters. Nevertheless, simpler FR models (i.e. with less parameters) can be found. For example, there are cylindrical models (e.g. Nieves-Chinchilla et al., 2016) that only reproduce the orientation and section radius of a hypothetical local FR with a cylindrical topology based on the surrounding IMF, but do not provide information about the global structure. Simpler models can find a final result more easily than the more complex ones as the parametric space is smaller, but at the cost of being less accurate in the description of the topology of the structure (see Section 1.3.3 for more information).

4.2.2. Mathematical description

4.2.2.1. Parameters

As mentioned above, the model can be fitted to three components of the IMF for a selected period by making use of some mathematical procedures which allow to reconstruct the global topology of the established FR.

After selecting the desired period, the first step lies in defining a reference system for the own structure. Once everything is referenced to the same coordinate system, it is necessary to solve the Maxwell's equations analytically, where physical parameters are calculated. The model assumes a very large global mean radius compared to the actual cross-section radius. Then, it imposes a circular cross-section with the mentioned variation of the radius from the *nose* to the legs of the torus, and this circular cross-section is later modified by a factor, converting the circular section into an ellipsoid.

All these modifications are defined by a series of parameters that are the output of the model, with an independent variable, which is the time that the s/c expends inside the MC while it is propagating. The parameters weight the different components that are on the equations defined in Section 4.2.2.3. A detailed description of Hidalgo's model is out of the scope of this work and is available in Hidalgo & Nieves-Chinchilla (2012) and Hidalgo (2013). However, a brief description of the model parameters is provided hereunder. The free parameters can be divided into two different groups depending on their nature:

- Those related to physical plasma properties (Table 4.1).
- Those associated to the geometry and topology, as the orientation of the global structure and also the cross trajectory of the s/c (Table 4.2).

Parameter	Description
B_0^{ζ}	Representative of the poloidal magnetic field component
B_0^{Θ}	Representative of the axial magnetic field component
α	Related to poloidal component of the plasma current density
λ	Related to axial component of the plasma current density

Table 4.1: Parameters that define some physical plasma properties (IMF and current density) in Hidalgo's Model for MCs.

After obtaining the parameters from the fitting process, the global topology of the FR is defined. There are also interesting properties that can be derived from the results of the fitting, such as the following formulae:

- The maximum approach of the s/c to the axis of the FR, $y_0 = z_0 \frac{cos(\theta) \cdot cos(\phi)}{\sqrt{1 - cos^2(\theta) \cdot sin^2(\phi)}}$

Parameter	Description
C	Establishes how wide the section is on the *nose* with respect to the legs
η	Shows the distortion of the circular cross section
Z_0	Distance between the point where the s/c impacts the FR and the equatorial plane of the torus
ϕ	Azimuth angle of the local axis for the given coordinate system
θ	Altitude angle of the local axis for the given coordinate system

Table 4.2: Parameters that establishes topological characteristics of the MCs (section variation orientation and deformation, impact factor, and orientation based on Hidalgo's Model.

- Handiness defined as $H = sign\left(\frac{B_\psi(t=0)}{B_\phi(t=0)} cos(\theta)\right)$ when $cos(\theta) \neq 0$, $H = sign\left(\frac{B_\psi(t=0)}{B_\phi(t=0)}\right)$ when $cos(\theta) = 0$. If positive, right handed; if negative, left handed.
- The helicity of the FR defined as $tan(\delta) = \frac{B_\psi(t=0)}{B_\phi(t=0)}$.
- The expansion velocity of the torus, $V_{exp} = \frac{r(t=x)-r(t=0)}{t_0}$.

4.2.2.2. Model Updates

During the development of this thesis work, two previously free parameters of the model where set by the use of in-situ plasma measurements, reducing the degrees of freedom of the model. These parameters were the time of transit of the s/c through the structure and the expansion factor (t_0).

The time transit is established by the difference between the last and first timestamps of the measured magnetic field components, while t_0 requires to add the SW velocity as an input. There are multiple approaches to infer the expansion of a MC in the IP medium but, in this case, it was necessary the definition of a factor which depends only on the time transit and not on the actual velocity, as there are many factors that could affect the relative observed components of the expansion velocity, but not to the local transit. For this reason, t_0 corresponds to the time span between the beginning of the MC and the cross with the x-axis of the SW velocity curve once fitted to a first order function. Negative values would correspond to a structure being compressed, while positive ones are being expanded.

Furthermore, in previous versions of the model, the radius of the torus was fixed by the position of the s/c. With almost-perpendicular crosses through the observer this assumption does not suppose a big issue, but the error increases as far as the cross is closer to one of the legs of the MC. Also, this assumption implied that the torus was not attached to the Sun in some cases. Taking into account the angles of the global FR, the correction of the radius has been performed as follows, assuming that the global topology has to cross both the s/c and the Sun:

$$\rho_0 = \frac{R}{2|cos(\phi)cos^2(\theta) + sin^2(\theta)|} \tag{4.1}$$

where R represents half of the radial distance from the solar surface to the s/c at the moment of the crossing through the MC.

4.2.2.3. Equations

The mathematical description below explains the model once the previous shown modifications are applied. As mentioned above, the first step consists on defining a coordinate system inside the own structure (indicated by the sub-indexes *MC*), and it is necessary to establish the position of the observer in that coordinate system for a specific instant t. The relative position is defined as follows:

$$x_{MC} = V_{sw}(t + T_{MC})cos(\phi) \tag{4.2}$$

$$y_{MC} = -V_{sw}(t + T_{MC})sin(\phi)cos(\theta) - z_0 sin(\theta) \tag{4.3}$$

$$z_{MC} = V_{sw}(t + T_{MC})sin(\theta)sin(\phi) - z_0 cos(\theta) \tag{4.4}$$

where V_{sw} corresponds to the mean measured SW bulk speed, T_{MC} corresponds to the total time duration inside the structure and the others unknowns are the free parameters defined in previous Section 4.2.2. These Cartesian coordinates are transformed into poloidal and toroidal ones by:

$$\zeta = arctan\frac{z_{MC}}{\sqrt{x_{MC}^2 + y_{MC}^2} - \rho_0} \tag{4.5}$$

$$\Theta = arctan\frac{y_{MC}}{x_{MC}} \tag{4.6}$$

$$\chi = \frac{z_{MC}}{sin(\zeta)} \tag{4.7}$$

where ζ corresponds to the poloidal angle, Θ to the toroidal one, χ to the distance with respect to the local X-Y plane. The different components of the physical parameters shown below are referenced to this coordinated system.

Additionally, the current density is composed by the summation of both toroidal and poloidal components. Also, stationary conditions (at the time period when the s/c is crossing the MC) are assumed, so this mean that the variation of the conditions of the plasma, such as for its density, is zero. Furthermore, the model asumes a neutral plasma, which implies that $\bigtriangledown j_p = -\bigtriangledown j_e$. This condition together with the Maxwell equations

allow to obtain the plasma current density components:

$$j^{\zeta}_{MC} = \lambda(t_0 - t)sin\left(\frac{\Theta}{2}\right) \tag{4.8}$$

$$j^{\Theta}_{MC} = \frac{\alpha(t_0 - t)\chi\left|cos\frac{\Theta}{2}\right|}{A} \tag{4.9}$$

being

$$A = cosh\left(-\rho_0\eta + Csin(\frac{\Theta}{2})\right) \tag{4.10}$$

The magnetic field is also composed by poloidal and toroidal magnetic field, as well as a radial one. These are defined as follows:

$$B^{\zeta} = \frac{B^{\zeta}_0 \cdot (t_0 - t) \cdot r_{MC} \cdot cos(\zeta)sin\left(\frac{\Theta}{2}\right)}{A - \mu_0 \cdot jt_{MC} \cdot r_{MC}} \tag{4.11}$$

$$B^{\Theta} = B^{\Theta}_0(t_0 - t)\left|cos\left(\frac{\Theta}{2}\right)\right| + \mu_0 \cdot jp_{MC} \cdot r_{MC} \tag{4.12}$$

$$B^{\chi} = -2cos(\zeta) \cdot sign(sin\Theta)\frac{B^{\Theta}_0(t_0 - t)sin\left(\frac{\zeta}{2}\right) + \mu_0\alpha(t_0 - t)r^2_{MC}}{A \cdot C} \tag{4.13}$$

The final magnetic field components referenced back to the internal MC Cartesian coordinate system are then:

$$Bx_{MC} = -sin(\zeta)cos(\Theta)B^{\zeta} - sin(\Theta)B^{\Theta} - cos(\zeta)cos(\Theta)B^{\chi} \tag{4.14}$$

$$By_{MC} = -sin(\zeta)sin(\Theta)B^{\zeta} + cos(\Theta)B^{\Theta} - cos(\zeta)sin(\Theta)B^{\chi} \tag{4.15}$$

$$Bz_{MC} = cos(\zeta)B^{\zeta} + \frac{Csin(\zeta)\chi Acos(\Theta/2)}{2\rho_0}B^{\Theta} - sin(\zeta)B^{\chi} \tag{4.16}$$

Once the parameters are calculated, it is necessary to reference all to the coordinated system of the magnetic field components again. To do this, the following transformation is performed:

$$B_x = Bx_{MC}cos(\phi) - By_{MC}sin(\phi)cos(\theta) + Bz_{MC}sin(\phi)sin(\theta) \tag{4.17}$$

$$B_y = Bx_{MC}sin(\phi) + By_{MC}cos(\phi)cos(\theta) - Bz_{MC}cos(\phi)sin(\theta) \tag{4.18}$$

$$B_z = By_{MC}sin(\theta) + Bz_{MC}cos(\theta) \tag{4.19}$$

The fitting process can be performed by different algorithms. The one used in this thesis work is Levenberg-Marquardt (e.g. Lourakis, 2005), which applies small variations to the parameters until the absolute value of the difference between the real data and the synthetic one finds a clear minimum. The different components of the magnetic field defined in equations 4.17, 4.18, 4.19 are subtracted independently to the measured ones in order to find the possible minima. The obtained geometrical parameters would be referenced to the one used in the measured IMF components. Note that in this thesis work the magnetic components are defined in RTN coordinates.

4.2.3. Flux Ropes in the Solar Wind

4.2.3.1. Identification

The classification of the different structures observed in the heliosphere allows a better understanding of the SW, like for instance how it evolves in different regimes, and also provides insights about their solar origins. It also opens the possibility to develop automated classifiers and can be used as inputs for Space Weather applications, or onboard algorithms for operation changes like the shock detection developed for the SolO/RPW instrument, which triggers a synchronised burst-mode acquisition of all the in-situ instruments onboard (Walsh, A. P. et al., 2020).

A variety of catalogues have been used for this work, such as for ICMEs, SIRs or shocks. One of the main parts of the ICMEs are the MOs, and those presenting a FR topology and certain characteristics such as the low plasma β, low temperature, enhanced magnetic field strength, etc. are denominated MCs (Zurbuchen & Richardson, 2006). Although the presented *ICME Catalogue* compiles a wide number of them, it does not focus on the classification of the different MOs that can be found, as well as it is also centred on the more noticeable ICMEs and does not pay attention to the smaller structures.

Aiming to supply these scarcities, the in-situ plasma data provided by both STEREOs during the period 2007-2014 were analysed by eye at different time scales, performing a selection of the potential transits of FRs through each s/c. A FR in this case is defined by a clear rotation of the IMF components while crossing the structure. All the gathered periods with a FR topology can be found listed at the Appendix (Table 2). Timestamps of the boundaries are indicative and they are selected based on discontinuities of any of the observed SW parameters.

4.2.3.2. Analysis

The updated version of Hidalgo's model (see Section 4.2) was fitted one by one to these periods and both physical in-situ plasma properties and the fitting results were analysed.

Figures 4.6 and 4.7 show two examples of the selected periods with the results of the performed fits. Both figures show similar format as previous Figure 3.5, avoiding the defined coefficients related to the suprathermal electron PADs.

Figure 4.6 shows observations from STEREO-A from July 5, 2008 to July 6, 2008 presenting decreasing bulk plasma speed, with relative low proton density and colder temperature than the expected as defined in Elliott et al. (2012), and also low thermal pressure, enhanced magnetic field strength and the subsequent low plasma β. The obtained fit is marked as dashed curves for the different components and angles of the IMF. The selected period has the clearest rotation and is accompanied by a clear suprathermal BDE in the range from 257.3 to 366 eV. The beginning of the period was selected based on the temperature drop and change in the IMF components tendency. Same last criterion was used for defining the end. The fit results draw an orientation of the MC of $\phi = 80$ degrees and $\theta = 170$ degrees (crossing the nose and contained in the ecliptic plane). The rest of the parameters can be observed in Table 2.

Figure 4.7 shows measurements performed by STEREO-B from June 6, 2008 to June 8, 2008. The selected FR shows decreasing bulk plasma speed and low proton density. The temperature in this case is similar to the one expected, and the thermal pressure is lower with respect to the surroundings. This fact and the enhanced magnetic field strength also drops a low plasma β. The dashed curves correspond to the result of the fitting process and shows the period with the FR topology. The changes in density and temperature, as well as the changes of the tendency in the components of the IMF delimit the period. This period is also characterised by the non-existence of BDE, but contains an intense and smeared flux of suprathermal electrons as compared to the surroundings. The fit results draw an orientation of the MC of $\phi = 165$ degrees and $\theta = 100$ degrees (observer very far from the *nose* and structure inclined with respect to the ecliptic plane). The rest of the parameters can be observed in Table 2.

With regards to the Space Weather discipline, one of the key points to be able to forecast potential damages on Earth is to know the orientation of the ICMEs, because when the magnetic field of the structures is the opposite than the one of the Earth's magnetosphere the odds of reconnection highly increase; or if they are oriented in the same direction, the magnetosphere suffers compression and could induce geomagnetic storms (Gonzalez et al., 1994), among other possibilities. In order to see any dependency of the properties of the FR within the solar conditions, Figure 4.2.3.2 shows the different orientations obtained from the performed fits for each year of the solar minimum of the solar cycle 23 and rising phase of the solar cycle 24. Most of the structures are observed with an angle ϕ close to 90 degrees (i.e. close to the *nose* of the MC). The tilt angle θ shows a predominance of more inclined structures. This behaviour seems to be stronger during the years of the rising phase of the solar cycle. The tendency is similar to the one obtained by Nieves-Chinchilla et al. (2019), although the tilt angles are considerably higher in this

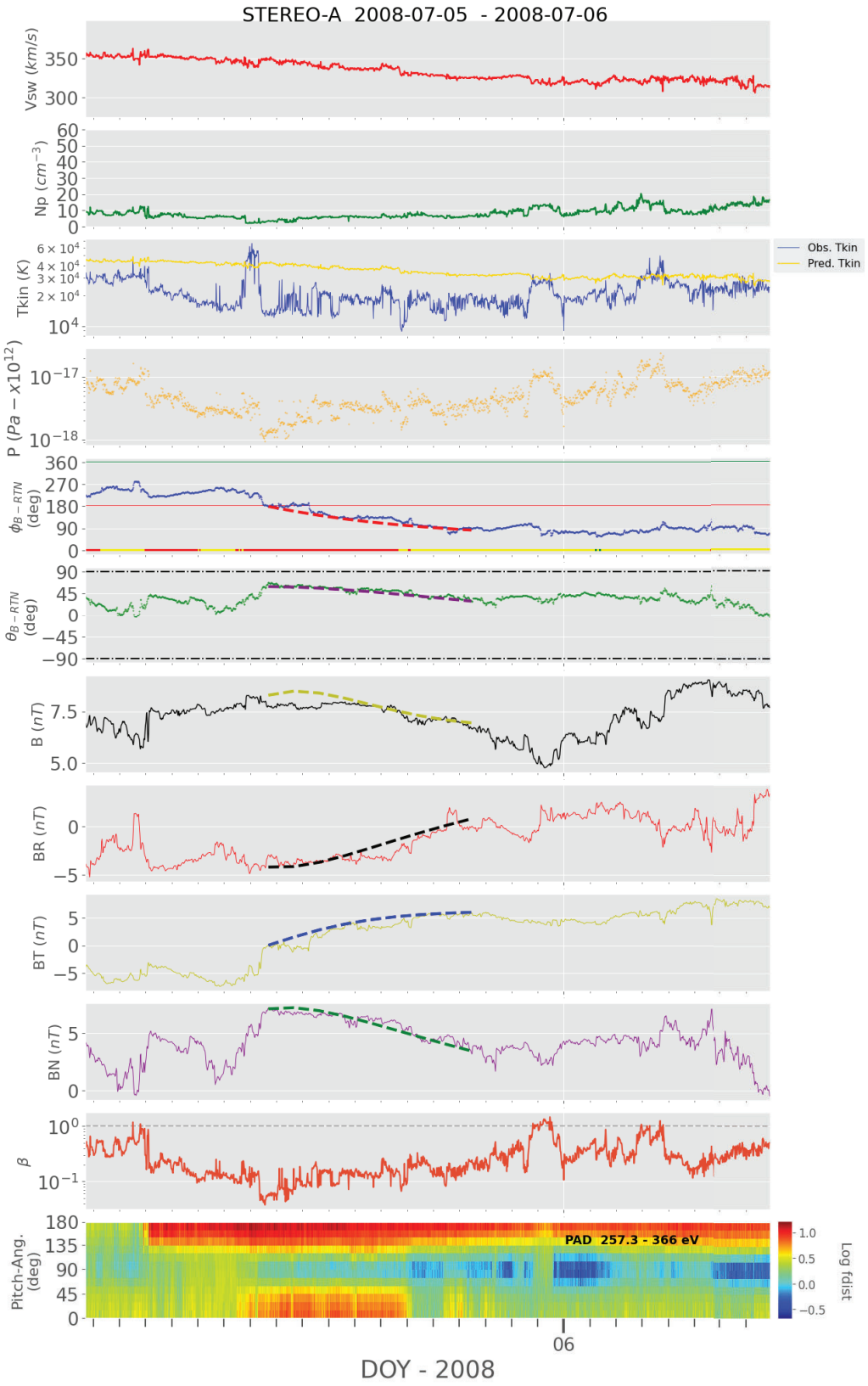

Figure 4.6: Observations of STEREO-A from July 5, 2008 to July 6, 2008. Figure follows similar format as Figure 3.5. See text for more details.

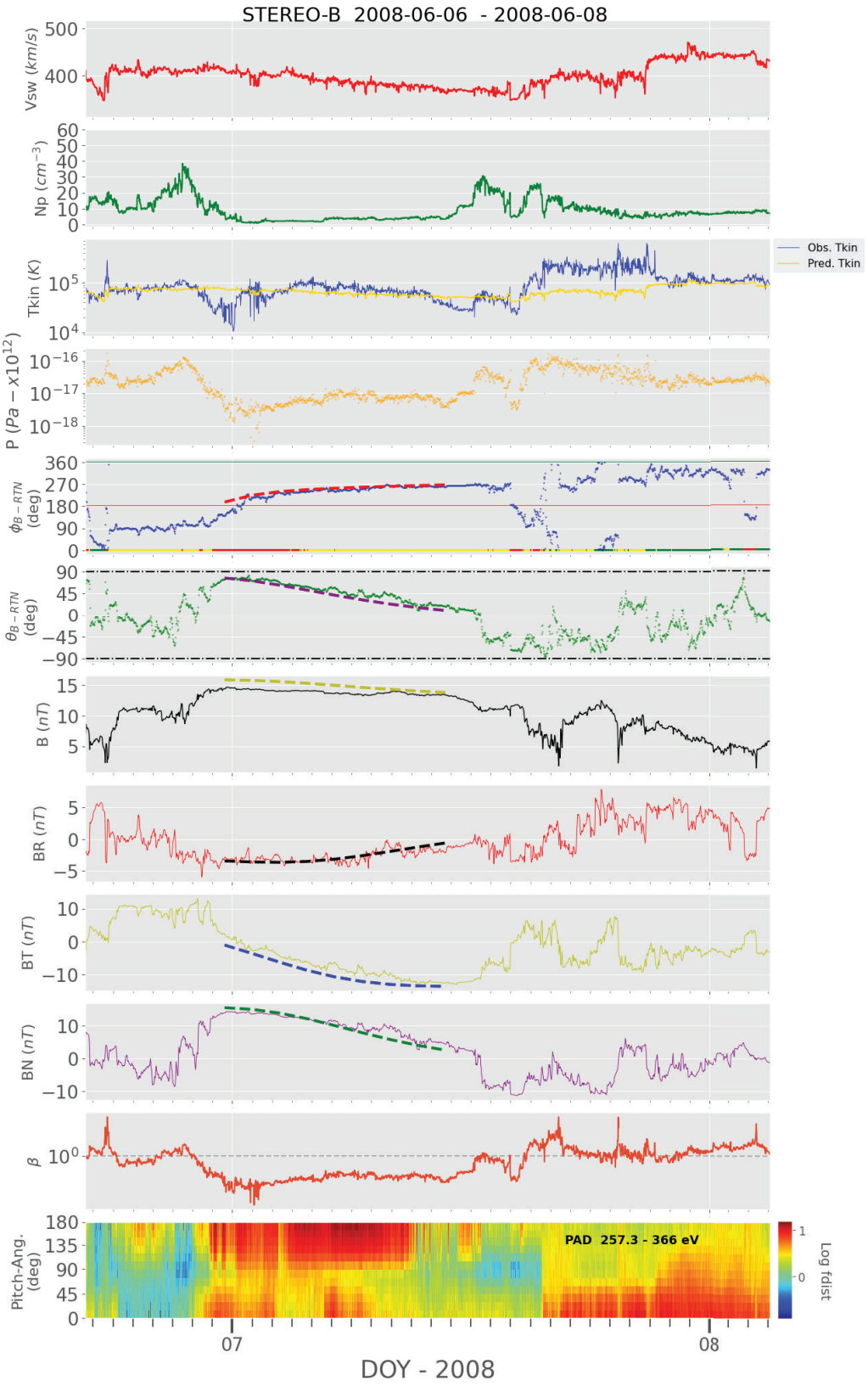

Figure 4.7: Observations of STEREO-B from June 6, 2008 to June 8, 2008. Figure follows similar format as Figure 3.5. See text for more details.

thesis work. Nevertheless, these results require further analysis and a comparison with the orientation of the original seed CME, in order to validate the results from the updated model, as well as analyse other solar cycles.

Other interesting property of the FR is the actual cross-section of the structure (which is not necessarily corresponding to the transit time of the s/c), as it is directly proportional to the FD depletion and time duration as shown in Dumbović et al. (2018). For this reason, same Figure represents the section (proportional to the diameter of each circle). The different sections of a single FR go from approximately $20 \cdot 10^5$ km (~ 0.01 au) to $\sim 140 \cdot 10^5$ km (~ 0.1 au). This result differs from the one shown in Burlaga et al. (1981), where they found that the cross-section could reach up to approximately 0.25 au. This might be due to the stricter criteria of selection of the period of the FRs followed in this work.

To have a better understanding of the circumstances of each event, the representation is accompanied by their colour-coded mean velocity. In the Figure, it can be seen that the amount of catalogued FRs is higher in the rising phase of the solar maximum as it was expected, because the number of ICMEs is higher in the solar maximum (e.g. Owens et al., 2007; Richardson & Cane, 2010; Li et al., 2018). Furthermore, there is no apparent relation between the section or orientation of the FRs and the velocity or the phase of the solar cycle.

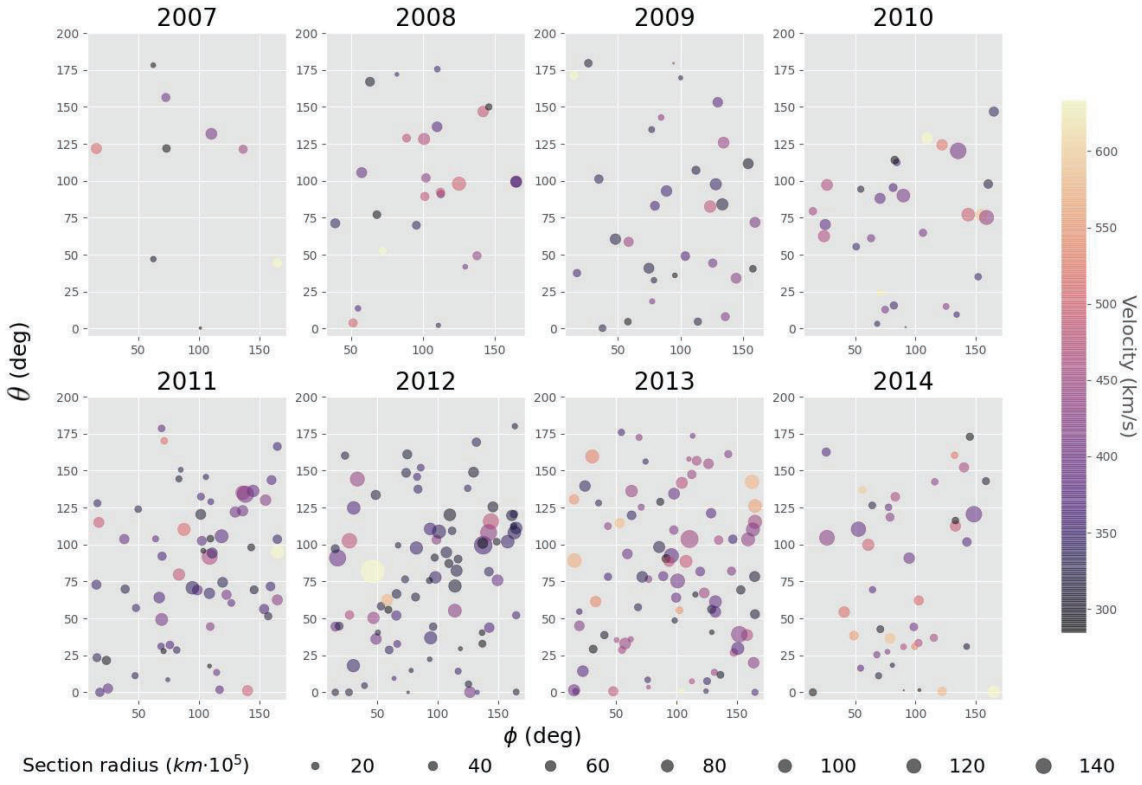

Figure 4.8: Scatter plot representing the orientation of each fitted FR for each year. Colour indicates the average speed during the transit of the FR and the size of the circle represents the cross-section radius as inferred from Hidalgo's model. Note: 2007 and 2014 panels do not cover the full year.

Chapter 5

Energetic Electrons

Energetic electron measurements can be used to trace the IMF topology, as well as to extract information from the environment. In particular, impulsive and anisotropic SEPs can add knowledge from the solar source and the path they follow until they reach the s/c. This is because these electrons travel very quickly (tens of minutes since the release to 1 au), they are directly affected by the conditions of the followed path (mainly the topology of the structure and the turbulence of the IMF), and the source can usually be identified, allowing the study of their origin and acceleration. These measurements add substantial information which contributes to the knowledge of the local topology, main focus of this thesis work.

In this Chapter, two different approaches are used for studying the topology of the IMF from impulsive SEP electrons. Section 5.1 shows a simple model that aims to reproduce the path of the electrons as they excite the local plasma emitting type III radio bursts for two different conditions: ambient SW and inside FRs based on the time difference of the onset of the burst. Section 5.2 shows the connection between the previously validated suprathermal electron anisotropy coefficient γ and the arrival of the impulsive SEPs in a statistical analysis, which helps to understand if the conditions that affect the suprathermal electrons might also directly or indirectly affect the more energetic ones.

5.1. Radio Burst Tracer Model

Impulsive SEP events often are associated to type III radio bursts. As described in Section 1.3.2, the radio bursts are produced by the beam of energetic electrons which excite the local plasma. This Section describes the development of a simple model which aims to trace the beam of electrons travelling in the IP medium. The characterisation of the radio burst allows the indirect estimation of the IMF lines, as they strongly constrain the path that the electrons follow. With two or more observatories and the assumptions described below, the model is able to remotely estimate the trace the IMF topology.

5.1.1. Plasma Density and Radio Emissions

When SEPs, specifically electrons from $\sim$ 10 keV to $\sim$ 100 keV, propagate through the corona and the IP medium often excite the local plasma during their travel (Reames, 2017). This excitation (i.e. oscillation) produces plasma oscillations denominated Langmuir waves that can generally produce radio waves, and it is directly proportional to the square root of the plasma density (e.g. Graham et al., 2012) at the location of the excited plasma. Additionally, the density profile tends to be inversely proportional to the radial distance to the star (Khnlein, 1996), so the emission of the type III radio bursts shows higher frequency when it is produced closer to the star and reduces its frequency when the exciter beam is moving away. There are several models that try to reproduce the radial variation of the plasma density in the corona and in the heliosphere. In this work, the model explained in Mann et al. (1999) is used to estimate the plasma density in the IP medium as a dependency of the radial distance and subsequently, the plasma frequency within an error of approximately 8 %. The expression (Equation 14 in Mann et al. (1999)) is:

$$N(r) = N_{1au}\left(\frac{r}{R_{1au}}\right)^{-\alpha} \tag{5.1}$$

where N is the density, r is the radial distance, $N_{1au} = 6.53\ cm^{-3}$, $R_{1au} = 150 \cdot 10^6$ km, and $\alpha = 2.16$.

Besides, assuming the whole plasma has no net charge and ignoring the thermal behaviour of the particles, the Coulomb force will act over any kind of displacement of a single or a group of charged particles (generally electrons as their movement is much easier than the ions') that will oscillate with the plasma frequency $\nu_{\mathrm{pe}} = \sqrt{\frac{n_e e^2}{m^* \varepsilon_0}}/2\pi$ [Hz], where n_e corresponds to the electron density, e is their electric charge, m^* is their effective mass, and ε_0 represents the permittivity of free space. This frequency corresponds to radio wavelengths for normal conditions of the SW plasma.

As mentioned in Section 1.3.2, the variety of radio bursts are related to different scenarios of the propagation of SEPs in the IP medium. This model focuses on the case of the impulsive events which usually generate type III radio bursts, as they generally have a narrower beam which is easier to track and can travel in the inner part of structures such as the MCs (see e.g. Gómez-Herrero et al., 2017). Type III radio bursts typically are linked to impulsive quasi-relativistic electron events, which are observed in-situ in the IP medium, although there is some controversy on the possibility that the population that generates the radio emission is the same as the one detected in-situ by energetic electron detectors (see Section 1.3.2).

5.1.2. Measuring Distances with Time Differences

Due to the large distances between the source at the Sun and any of the available s/c, the emission of the radio bursts is measured minutes after the release ($\sim$ 8 minutes at 1 au, as the speed of light is $299.8 \cdot 10^6$ m/s). If the released beam that produces the radio burst moves away from the observer, the emission would take progressively longer to arrive to the observer, while if the beam moves towards the observer, the time travel would decrease.

5.1.3. Defining Interface Conditions

The model uses as inputs the radio spectrograms of at least two observatories and their orbital positions. By looking at the onset time of the type III radio burst for each frequency channel (which depends on the density), it is possible to infer a hypothetical sphere where the source could be (Section 5.1.1), while by focusing on the time difference between those onsets, it is feasible to deduce whether the source is closer or farther to one of the observatories (Section 5.1.2). Taking this into account, it is possible to roughly trace the propagation of the beam. In order to do this, it is important to know the release time, which must be seen by the observers. The error of the estimation would be reduced if the number of observers increases, as well as the relative distance between them or their instrumental cadence.

Additionally, by considering ideal topologies of the IMF, it is possible to estimate the most similar magnetic topology where the beam is propagating along, and obtain not only the discrimination between different topologies, but also some of their properties such as, for instance, the velocity of the SW as described below. In this work, two simplified common topologies are considered: the nominal Parker spiral and the MCs. The reasons for selecting these two schemes are because the Parker spiral is expected to be the most common one, and because the frequent release of CMEs makes plausible the propagation of SEPs inside these structures and their study can add substantial information about the global topology.

Assuming there are no curves, the Parker spiral can only vary its length (by reducing the curvature) depending on the velocity of the SW, while the MCs can have different orientations, radius and section diameter. In this case, the beam of electrons is considered to travel along the axis of the MC and, as a first approximation, the global axis of the MC could be considered as a circumference (see Section 4.2). Summing up, the parameters are: the SW velocity and the longitude for the Parker spiral, and the radius and orientation for the MCs. The parameters can be reduced to three if there are evidences of the beam passing through one of the observers (SW velocity for Parker spiral, two angles of orientation for MCs).

In order to perform this analysis, some additional assumptions must be considered:

- The radio-emission is generated by a narrow electron beam with a single speed.
- There is no significant turbulence, so the electrons propagate along the defined topologies.
- There is no absorption nor refraction of the radio emission in the IP medium.
- The first onset is considered to be the fundamental harmonic (which is usually more intense and shows lower frequencies).
- Density and other parameters inside the MCs can be considered similar to the one found in the ambient SW (Crooker et al., 2000). The radial density variation follows the model shown in Mann et al. (1999), and Equation 5.1.

5.1.4. Model Representation

The model presented in this work would fit the onset profiles of the radio intensity at different frequencies of two or more observers. Figure 5.1 shows a sketch of a hypothetical beam (curved yellow arrow) propagating along a nominal Parker spiral and two observers (s/c A, green; s/c B, blue). Left panels show the onset times of the type III radio burst for four different frequency channels of the two s/c, shifted in time to coincide with the first observation. The bottom panel shows both observations together and the red line represents the time difference due to the time travel to each s/c. This difference can be related with the lengths of the different straight lines from the theoretical position of the radio source (pink dots) to each observer. The beam is approaching first to s/c A and going farther from s/c B. For this reason, the radio emission arrives earlier to s/c A than to s/c B. The circumferences correspond to different radial distances and indicate the theoretical density and the corresponding frequency as explained in Section 5.1.1.

5.1.5. Fitting Process and Considerations

Changing the assumed IMF topologies and their parameters (SW speed for the case of the Parker spiral; orientation and global radius for the MCs) would drop different onset profiles. When comparing these onsets to the ones observed by at least two s/c, a fitting could be performed. Due to the technical difficulties of establishing a reliable onset for all the channels, in this thesis work a visual fitting is performed based on the different scenarios drawn by the variation of the parameters. The two proposed topologies are analysed. The assumption of the event occurring in the nominal Parker spiral would be consider first, and the velocity of the SW would be varied to change the path length until obtaining the best fit. Later, the beam is considered to be inside of a fraction of circumference (corresponding to part of the axis of a MC), which rotates from 0 to 360 degrees in latitude and longitude, and varies its radius, and whose radio-emission trace is compared with the observed one for obtaining the best fit. Once both scenarios are

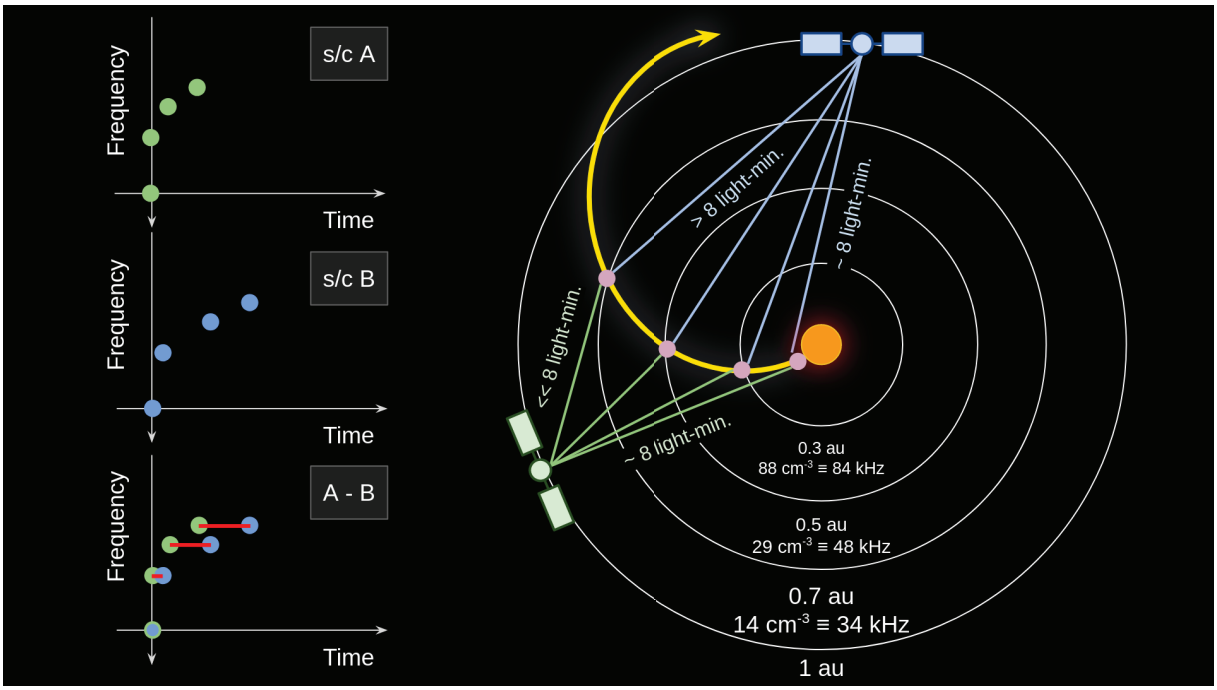

Figure 5.1: Sketch of a hypothetical propagation of a beam (curved yellow arrow) which originates a radio emission observed by two separated s/c (A, green; B, blue). Left panels show the onset for different frequencies at the two s/c and the time difference due to the light propagation. See text for more details.

obtained, the most similar result would be considered as the most probable one and would drop the ideal parameters.

It is also feasible to add some constrains that could help the model to have a more accurate result. For example, it is possible to check the coordinates of the source or the existence of CMEs with remote-sensing observations or, furthermore, the position of the beam at a certain moment if there are direct measurements of the particles through one of the observers. This last case is analysed in the following Section 5.1.6 for four different events measured by both STEREOs. Apart from the work here shown, there are other pieces of information that could be extracted from the differences in the radio burst time profiles (and not only from the onset time difference) observed by the s/c, as the intensity, the width of the radio burst, the lack of emission at specific frequencies or the antenna pointing, among others. Also, other topologies may be implemented, as well as the absorption of specific frequencies by the SW or the obstruction of the Sun.

5.1.6. Application

In order to show the reliability of the type III radio burst tracer model described above, some already studied SEP events associated with type III radio bursts have been selected for a comparative analysis. These events are accompanied by in-situ SEP observations, with a localised solar source but with different conditions of the IMF and correspond to:

1. The events studied in Gómez-Herrero et al. (2017). According to the authors, two

impulsive and very anisotropic SEP events were detected and the particles were traveling along the *longest* leg of a MC, with sunward direction, in both 2 and 3 December 2013.

2. One of the events studied in Klassen et al. (2012). A train of type III radio bursts were observed during 26 February 2011 in quiet slow SW conditions and a correspondence with some electron spikes with energies below 300 keV was found. These events were very anisotropic and with short duration.

3. In 2 May 2014, when the STEREO mission was close to the solar conjunction, with a separation of 38 degrees, an impulsive event was simultaneously observed by both s/c with similar electron intensity profiles. This event was analysed in Klassen et al. (2015) and some scenarios were proposed to explain that wide observation of an impulsive event. In this thesis work, a comparison with their results is performed.

All the events are analysed assuming that the beam generating the radio emission corresponds to 10 keV without energy loses, as the obtained results are considerably much closer to the real observations than for higher energies (not shown). This may suggest that the energy of the beam of electrons that provokes the radio emission is closer to 10 keV supporting previous works as e.g. Haggerty & Roelof (2006) or that the electrons are being strongly decelerated during the first phase of their travel in the lower corona as Reid & Kontar (2013) proposes, but further analyses are required. Apart from that, as the selected studies measure the SEP flux enhancement in-situ, the model forces the exciter beam to have a cross through the s/c that observes the particles. This allows to reduce the parameters of the fitting process.

5.1.6.1. 2 and 3 December 2013 Events

Figure 5.2 and Figure 5.3 show the STEREO/SWAVES observations of two radio bursts in 2 and 3 December 2013. They are accompanied by the the best model fit obtained by eye for the axis of a MC (upper panels). In addition, the results obtained for the nominal Parker spiral (bottom panels) are also presented in order to compare the best results of both topologies. The obtained parameters of the fitting process are in the title of the panels (Θ corresponds to the angle with respect to the ecliptic plane; ϕ is the angle within the ecliptic plane; PS states for Parker spiral).

The first two left panels show the radio spectrograms observed by STEREO-A and STEREO-B respectively. The spectrograms are time shifted to remove the delay between the observations at the beginning of the type III radio burstand synchronise the first release onset. In order to see the time differences of the rest of onsets in frequency, the third panel shows a discretised addition of the two spectrograms. The discretisation has been performed with a threshold value of 8 dB. Blue colour corresponds to only one s/c

measuring the intensity over the threshold, while pink corresponds to the two of them observing an intensity over 8 dB.

The three panels also show the model prediction of the emission produced by the beam. Warmer colours correspond to the beginning of the emission, and corresponds to the same colours as shown in the orbit plot (right one). This last panel shows the orbital position of the different objects (red, STEREO-A; blue, STEREO-B; green, Earth; yellow, Sun) as well as the obtained path of the beam. Dashed line represents 1 au orbit. The two spheres are centred in both s/c and have 1 au radius ($\sim$ 8 light-minute). If the beam goes out, the travel time would increase for the corresponding s/c, and would decrease when approaching to its centre.

The best fit (upper panels) suggest that both events are more likely to happen inside a closed structure, and both of them may occur in MCs with different orientations. The beam of electrons seems to propagate at first further from STEREO-B and then approaching again, as shown in the mentioned paper. The article also states that the inclination of the MCs with respect to the ecliptic plane, based on the version of the Hidalgo's model described in Hidalgo (2013), are 45 degrees in the first case and -53 degrees for the second case. The type III radio burst tracer model suggests that the inclination with respect to the ecliptic are 20 degrees (first case) and 300 degrees (-60^{o}, second case). The obtained results support the previously suggested orientation of both MCs, which can be found almost perpendicular to each other.

The best result for the Parker spiral topology (bottom panels) draws an unrealistic scenario of the SW presenting a velocity of 200 km/s.

5.1.6.2. 26 February 2011 Event

Figure 5.4 shows the second event under study, occurred in 26 February 2011 at 6:25 with the best results for both topologies as it was presented in the previous one. The beam of electrons was only observed in-situ by STEREO-A. Both STEREOs had a separation of approximately 180 degrees with a distance between them of almost 2 au ($\sim$ 16.5 light-minute). The separation can be noticed on the third panel, as the time delay between the onsets of the radio burst seen by both s/c at lower frequencies is increasing with time, as the beam is approaching STEREO-A. It can also be noticed that the radio burst observations stop at some point for STEREO-B, probably because the exciting electron beam is being hidden by the Sun (i.e. the beam is aligned with the Sun and STEREO-B). The best results of the model cannot fully reproduce the behaviour of the visible part of the radio burst by STEREO-B. Nevertheless, it draws that the event occurred in similar conditions of a nominal Parker spiral with a velocity of approximately 300 km/s. These conditions are very similar to the ones of the shortest leg of a MC in the ecliptic plane, and further analyses would be required in other studies to discern which would be the actual topology.

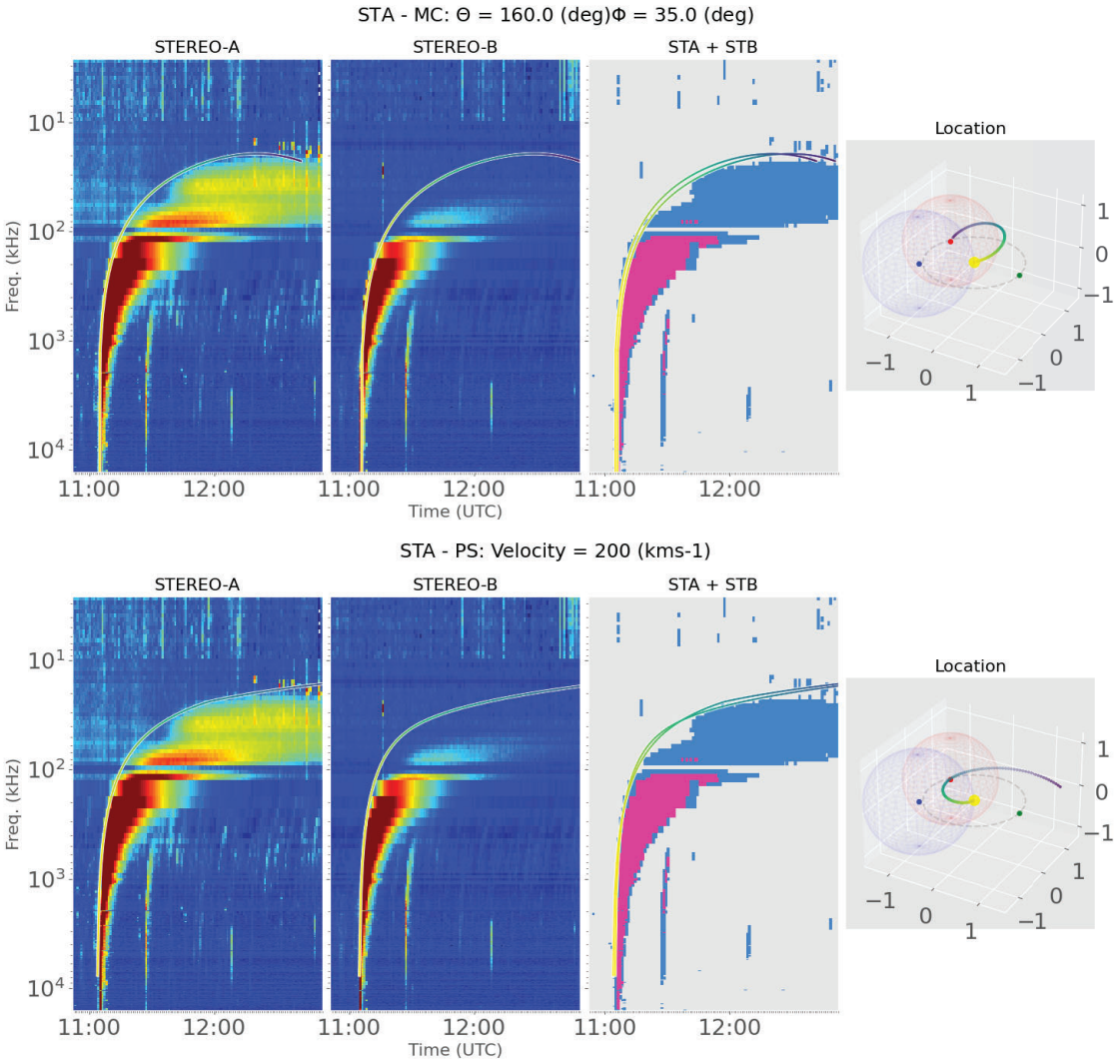

Figure 5.2: Radio burst released at 11:04 2 December 2013 corresponding to the SEP event studied by Gómez-Herrero et al. (2017). Radio spectrograms with the corresponding fits and orbital position (red, STEREO-A; blue, STEREO-B; green, Earth; yellow, Sun) and the modelled beam (Top: axis of MC, Bottom: Nominal Parker spiral, PS). See text for more details.

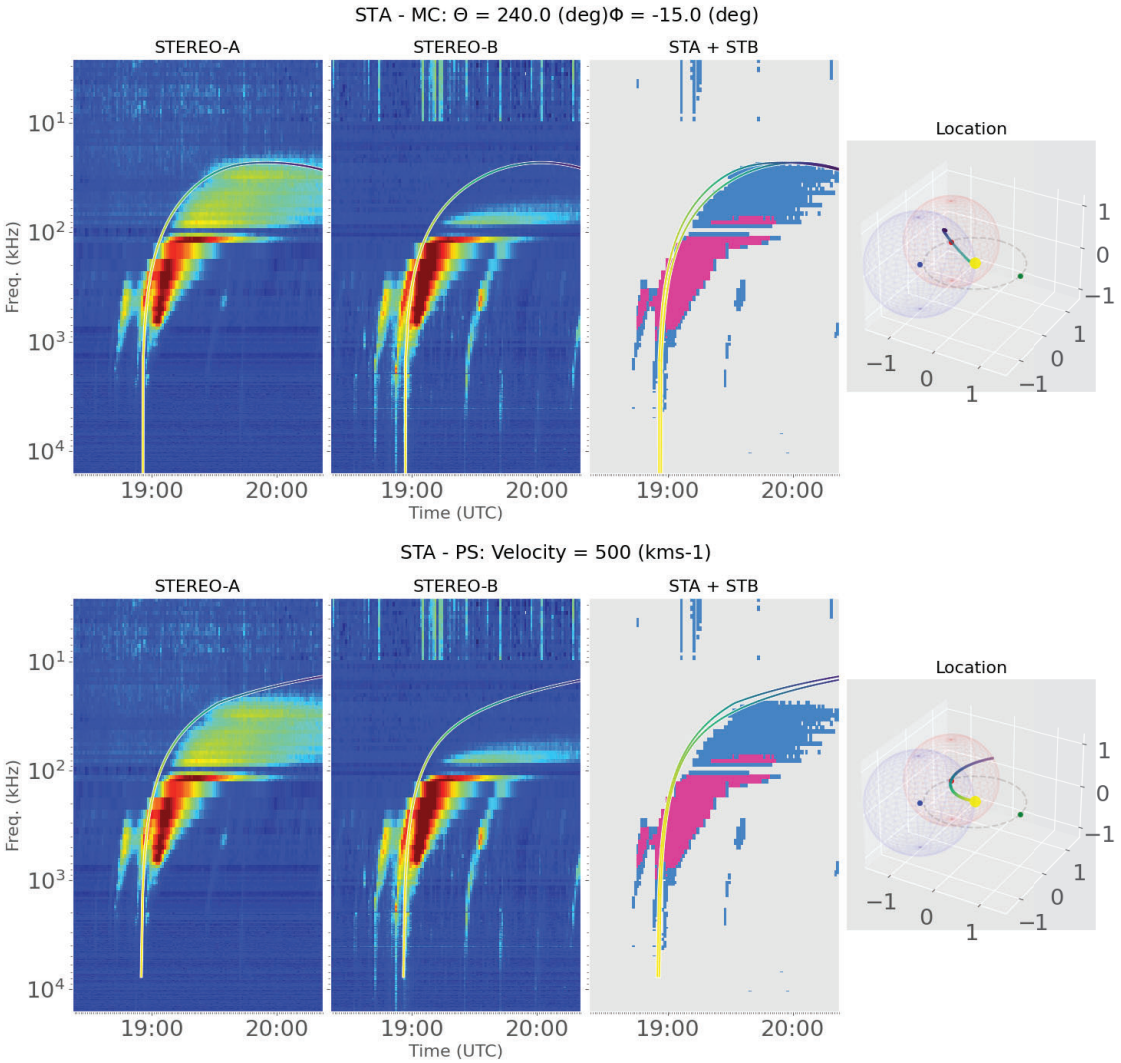

Figure 5.3: Radio burst released at 18:55 3 December 2013 associated to the second event studied by Gómez-Herrero et al. (2017) with the corresponding fit. Panels follow the same format as in Figure 5.2

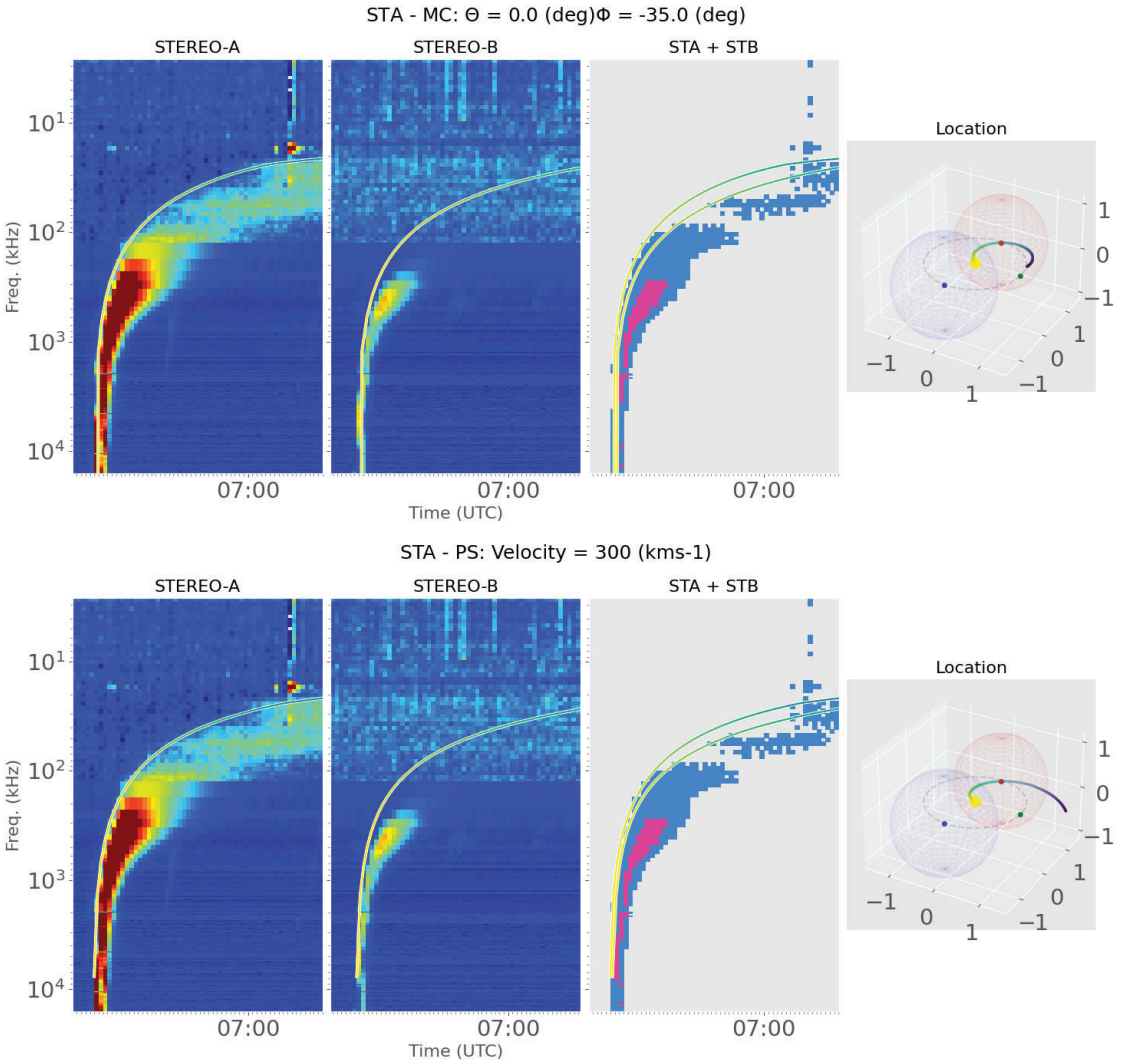

Figure 5.4: Radio burst released at 06:25 26 February 2011 studied by Klassen et al. (2012) and the best obtained fits. Panels follow the same format as in Figure 5.2.

5.1.6.3. 2 May 2014 Event

Finally, Figure 5.5 shows the best fit obtained for the 2 May 2014 event observed by both STEREOs for three different assumptions of the beam geometry: reaching STEREO-A, reaching STEREO-B and in an intermediate point in a nominal Parker spiral (FR cases were discarded because of the null similarity). As it can be seen, none of them can fully reproduce the behaviour of the measured type III radio burst. This event is a clear example of the limitations of the model: the distance between the observatories is relatively close (38 degrees of separation and 0.65 au of straight-line, $\sim$ 5 light-minute) and the time difference between the observations is practically zero for the analysed cadence, which highly constrains the potential of the model. In addition, the two proposed topologies cannot describe the onset profile of the type III radio burst. This could be due to the strong assumptions of the model for the beam propagation or because the actual topology is significantly different to the ones proposed. Nevertheless, due to the proximity of the observations and the similarity of their intensities, it is clear that the beam of electrons is propagating between the two s/c or in the same cone of ejection as proposed in Klassen et al. (2015). The increase of the number of observers with different positions in the IP space could help to better understand the propagation of the beam.

5.2. Quasi-relativistic and Suprathermal Electrons Comparison

As previously shown, suprathermal beams of SW electrons continuously flow outwards along the IMF lines with an energy between $\sim$ 60 eV and $\sim$ 3 keV, and solar activity phenomena such as flares and CMEs often release a considerable number of SEPs (energies higher than 2 keV). The impulsive-type SEPs are accelerated at the solar corona as a consequence of magnetic reconnection and travel following the IMF and the physical processes associated with the IMF may affect the behaviour of both the ubiquitous SW suprathermal electrons and the transient SEPs.

A comparative statistical study between the suprathermal electron anisotropy as given by the coefficient γ and SEP travel time measured by the STEREO mission is performed below in order to discern any correspondence between processes that may affect these two different populations and improve the understanding of their heliospheric transit. Thus, it is necessary to analyse the SW conditions too, as both populations are extremely dependant on the properties of the accompanying plasma.

Previous work by Graham et al. (2018) found indications of a correspondence between the IMF path length calculated using SEP arrival times and the *strahl* width (i.e. scattering of the *strahl* population), which may be indicative of the turbulence of the IMF, the effect of path travelled along the IMF (including possible distortions away from large-scale Parker spiral) and the semi-constant scattering processes that occur within the SW. To

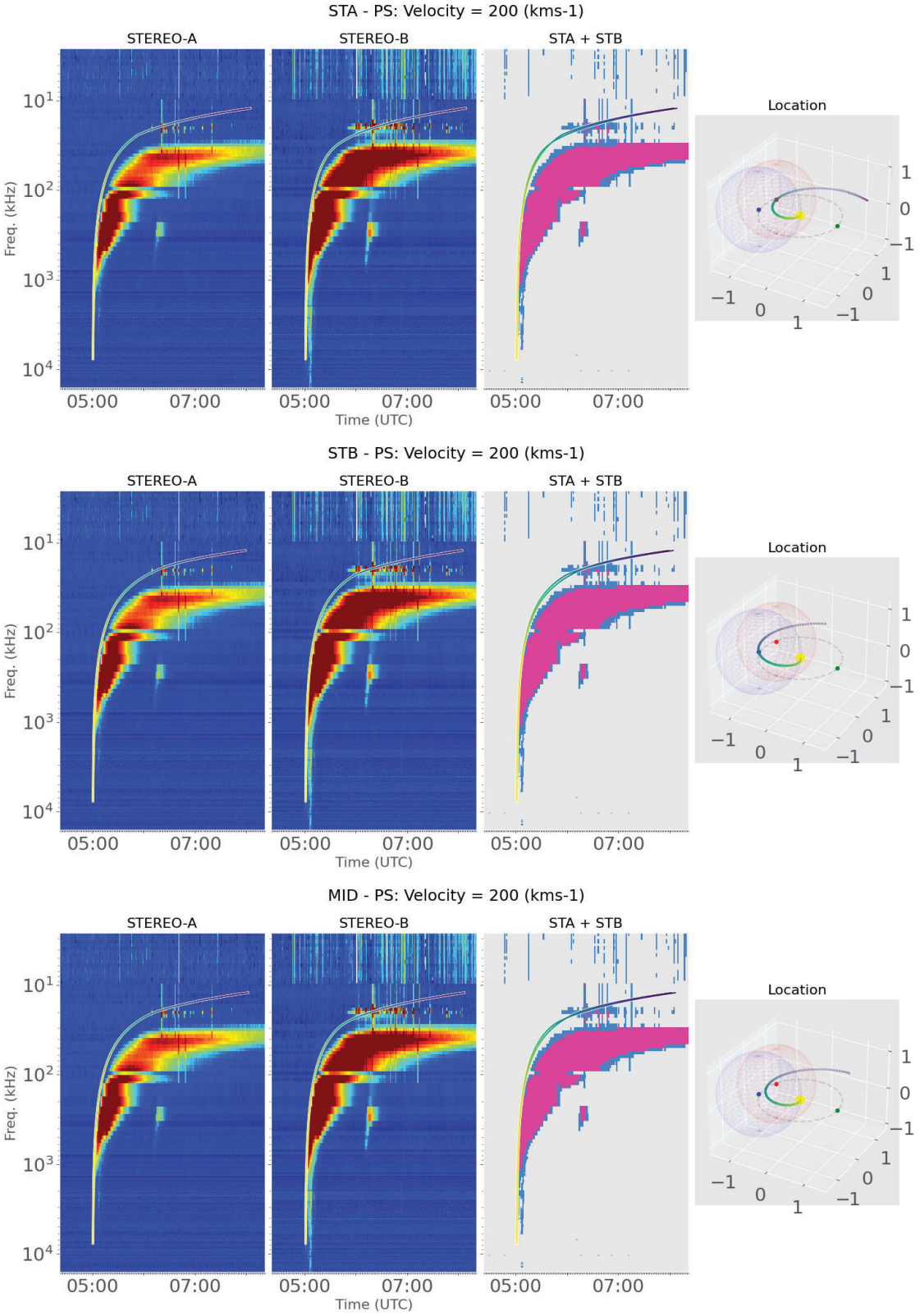

Figure 5.5: Radio burst released at 05:01 2 May 2014 studied by Klassen et al. (2015) and the propagation of the beam crossing STEREO-A (top), STEREO-B (middle) and an intermediate point (bottom). The rest of the panels follow the same format as in Figure 5.2.

understand better the SEP propagation due to the IMF conditions, different SW scenarios have been compared.

The different IP structures define the IMF path length. The effective path length of the particles then would be shorter or larger depending on the structure they travel along. For this reason, it is necessary to have an idea of the SW conditions at the moment of the SEP propagation and thus, the different catalogues presented in Section 2.4 are used. Also, in order to supply the lack of uncatalogued events, the SW classifier described in Xu & Borovsky (2015) is utilised. This last work describes an empirical method that categorises the SW into four different cases using the magnetic field strength (B), the SW velocity (v_{sw}), the proton density (N_p) and the proton temperature (T) as inputs. Based on the following conditions, the SW is categorised into one of each defined types:

$$0.841 \cdot B \cdot N^{-0.315} \cdot T^{-0.222} \cdot V^{-0.171} > 1 \quad (Q_1)$$
$$8.77 \cdot 10^{-11} \cdot T \cdot B^{1.42} \cdot V^{3.44} \cdot N^{-2.12} > 1 \quad (Q_2)$$
$$0.0561 \cdot T \cdot B^{0.752} \cdot V^{0.445} \cdot N^{-1.14} < 1 \quad (Q_3)$$

On the one hand, if Q_1 is true, then according to this study the local SW would correspond to an ICME. On the other hand, if Q_2 is satisfied, the SW would correspond to a CH-originated plasma (i.e. so-called fast SW). Finally, if the Q_3 is true, the in-situ plasma would correspond to a sector-reversal-region and if all of them are false, then it would be a streamer-belt-origin (i.e. slow SW) plasma.

The *STEREO/SEP catalogue* (see Section 2.4) is taken as a basis for the statistical analysis. Each of the events is identified by an onset timestamp based on quasi-relativistic electrons measured from 55 to 85 keV, and the onset is estimated at the moment that the 1-minute mean flux is higher than the 50-minute mean value of the defined window plus 4 standard deviations for two consecutive data acquisitions. When there is poor statistic, lower time resolutions are used. The resolution used for each event is gathered on the *dt* column of the catalogue (for this study, only those with a *dt* equalling 1 minute are used). The peak time and peak intensity are also collected, although it is not used for this study.

Impulsive and anisotropic events carry information more representative of the IMF lines, as they are mainly well connected to the source region and their angular spread is in general much narrower than for gradual events. The catalogue does not indicate whether the listed events are impulsive, gradual or mixed. Thus, it is important to exclude from the analysis those that are susceptible of being considered gradual, as their source regions are extensive, and the acceleration is prolonged over time. A selection of the clearest events with a sudden increase in the intensity time profile, preferably with anisotropic behaviour, with apparent no coexistence with type II radio bursts has been performed.

After the filtering, 42 events were selected[1], and the type III radio burst onsets were determined by eye for both STEREOs. The temporal delay between the onset and the radio burst was calculated after performing the time shifting of the radio measurements to be according to the actual release of the emission. The radio waves time travelling is estimated as $t = \frac{r_{sc} - R_{Sun}}{c}$, where r_{sc} corresponds to the radial distance of the s/c, R_{Sun} is the solar radius and c is the speed of light.

Figure 5.6 shows an example of one of the analysed events observed by STEREO-B on December 22 2009. The panels provide relevant information of the plasma properties, as well as of the particle profiles for different energy ranges, radio data and the orbital position of the two s/c. Top panel shows the speed of the SW, accompanied by the orbital position of both STEREOs (red, STEREO-A; blue, STEREO-B; yellow, Sun. Black dashed line corresponds to 1-au-radius circumference and the green one corresponds to the Sun-Earth line). Following three panels show the angles of the IMF as in Figure 3.5, and the magnetic field strength. After that, the anisotropy coefficient γ for the suprathermal electrons in the energy range from $\sim$ 180 eV to $\sim$ 366 eV. Below, the radio-spectrograms of both STEREOs (shifted to remove the light propagation time). The STEREO-B spectrogram also contains the local plasma frequency (black curve) and the particle onset (red vertical line) as in the catalogue. The following two panels represent the intensity measured by the energy channel 65–75 keV of STEREO/SEPT for the four different telescopes and their pointing with respect to the IMF direction (i.e. PA). Below them, their colour-coded PAD is shown. The rest of the panels represent the velocity dispersion for the four telescopes. The diagonal line represents the expected onset time profile based on a nominal Parker spiral with a longitude of approximately 1.2 au (derived from the bulk speed) with a beam released at the time of the onset of the type III radio burst.

The event occurs in a quiet period with velocities around 350 km/s. The IMF follows the direction of the nominal Parker spiral most of the time with no fluctuations and the strength is around 4 nT. Suprathermal electrons present a relative high grade of anisotropy as a consequence of the low turbulence. The quasi-relativistic electrons show a noticeable anisotropy, as the beginning of the event is almost seen only by the sunward-pointing telescope. The time delay between the type III radio burst and the onset of the electrons is approximately 34 minutes. Nevertheless, the expected time for electrons with those energies, and the calculated Parker spiral length, should be approximately 23.5 minutes for electrons of 65 keV. This time difference is a systematic behaviour for impulsive events and it is an unsolved issue as described e.g. in Haggerty & Roelof (2002).

It is expected that the SEPs arrival occurs earlier if the SW is faster, as the Parker spiral length would be shorter (i.e. less curved, Parker, 1958). The purpose of this work

[1]Events from STEREO/SEP catalogue:
STEREO-A: 31, 67, 80, 82, 84, 132, 133, 134, 136, 137, 146, 168, 181, 223, 224, 352, 366, 391, 417, 632, 650, 654, 662, 717, 719
STEREO-B: 37, 45, 76, 91, 99, 114, 323, 334, 335, 338, 340, 362, 473, 474, 477, 709, 726

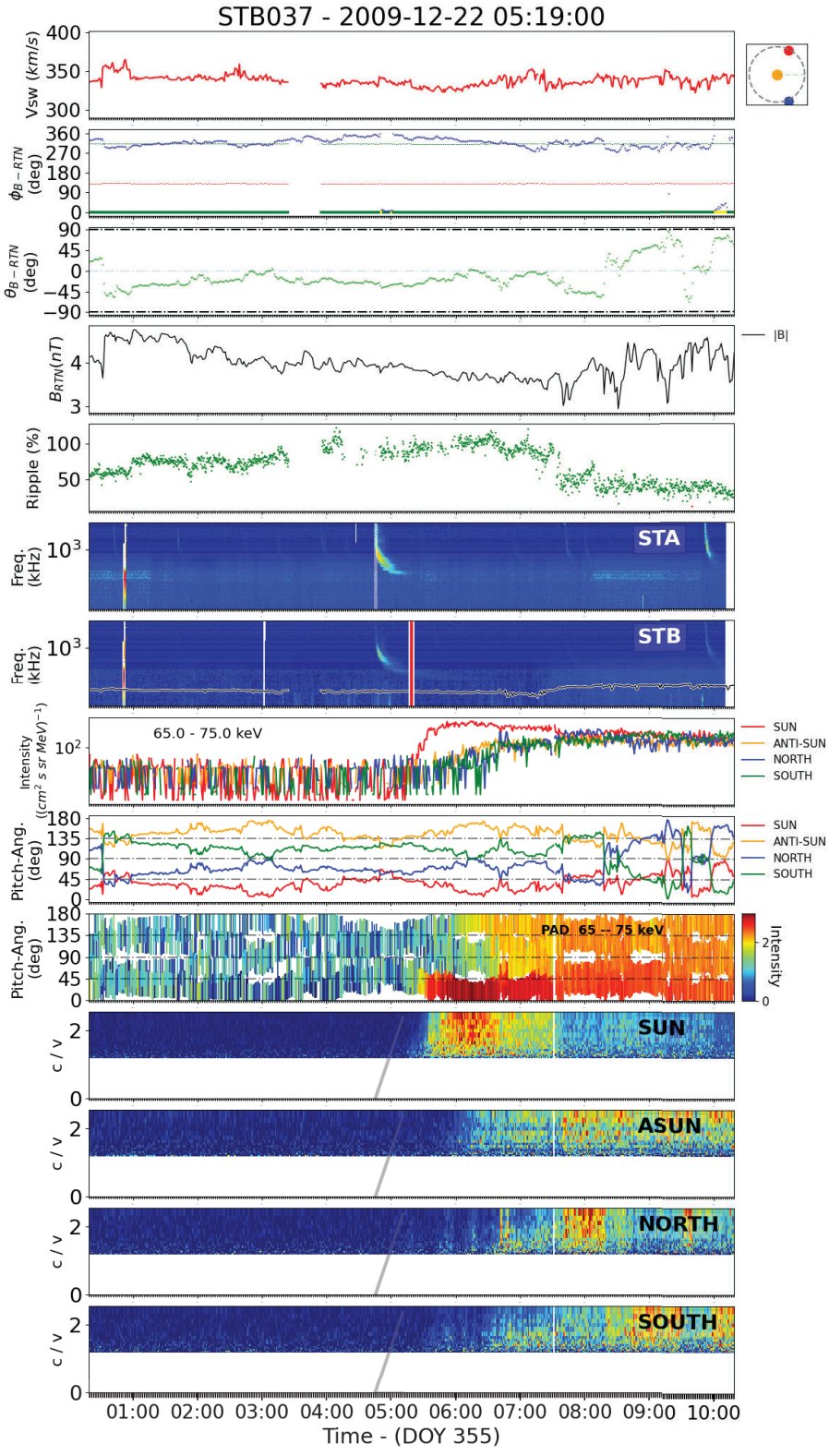

Figure 5.6: SEP event observed by STEREO-B on November 3 2009 and tagged as number 31 in the STEREO/SEP catalogue. From top to bottom: SW speed (left) and orbital position (right; red for STEREO-A, blue for STEREO-B and yellow for Sun); azimuthal and latitudinal angles, and strength of the IMF as in Figure 3.5; suprathermal electron anisotropy coefficient γ (ripple); radio spectrograms as seen by STEREO-A and STEREO-B; electron intensity for the four STEREO/SEPT telescopes; angular pointing of the telescopes; combination of the field of view of the telescopes and the observed intensity; intensity for each inverse velocity (derived from the energy channel) relative to the speed of light for the four STEREO/SEPT telescopes. See text for more details.

is to check if the conditions that affect the PAD of the suprathermal electron population also affect the quasi-relativistic electron propagation, independently of the actual path-length. For this reason, instead of considering the time difference between the radio burst and the arrival of the particles itself, the results are compared to a hypothetical nominal Parker spiral path as a function of the mean bulk speed during the propagation of the SEPs. The path L is estimated as:

$$\begin{aligned} r_{diff} &= r_{sc} - R_{Sun} \\ A &= \frac{1}{2}\frac{\Omega_0}{V_{sw}} \cdot r_{diff} \cdot \sqrt{(r_{diff})^2 + \left(\frac{V_{sw}}{\Omega_0}\right)^2} \\ B &= \frac{1}{2}\frac{V_{sw}}{\Omega_0} \cdot arcsinh\left(r_{diff} \cdot \frac{\Omega_0}{V_{sw}}\right) \\ L &= A + B \end{aligned} \tag{5.2}$$

where r_{sc} corresponds to the orbital radial distance of the s/c, R_{Sun} is the solar radius, V_{sw} is the SW speed, and Ω_0 corresponds to the sidereal solar rotation rate at the equator ($2.87 \cdot 10^{-6}$ $[s^{-1}]$), as it is representative of the longest possible case scenario.

Figure 5.7 compares, for the selected events, the anisotropy coefficient γ for suprathermal electrons (ripple) and the ratio between the length travelled by the particles (derived from the time difference between radio burst and particle onsets) and the theoretical Parker spiral length. The value of γ is the mean value calculated in the period between the particle onset and twenty minutes earlier, and the error bar corresponds to the standard error of the mean. The reason of averaging twenty-minute intervals is because it is approximately the time corresponding to the shortest selected SEP event. Every event is tagged based on the catalogues and the Xu and Borovsky classifier described before.

The relation between the logarithmic anisotropy and the normalised estimated arrival Parker length presents a Pearson correlation of -0.58 overall, which suggests that the circumstances that delay the arrival of the SEPs are related to those which isotropise the suprathermal electrons. One of the key conditions that smears the *strahl* population is the turbulence in the IMF during its propagation. This idea supports previous works as the already mentioned Graham et al. (2018), where the turbulent conditions of the IMF tends to isotropise the *strahl* population, as well as hinders the propagation of the SEPs. It can also be observed that there is no apparent relation between the different structures and the relative length, which is unexpected because there are evidences of the significant differences in both length and turbulent conditions between each topology. Nevertheless, previous works such as Kahler et al. (2011) suggest that although the IMF lines are longer inside the FRs (increasing the propagation time), the delay is decreased due to the non-turbulent conditions. Further analyses with different approaches may be performed in order to clear up this issue.

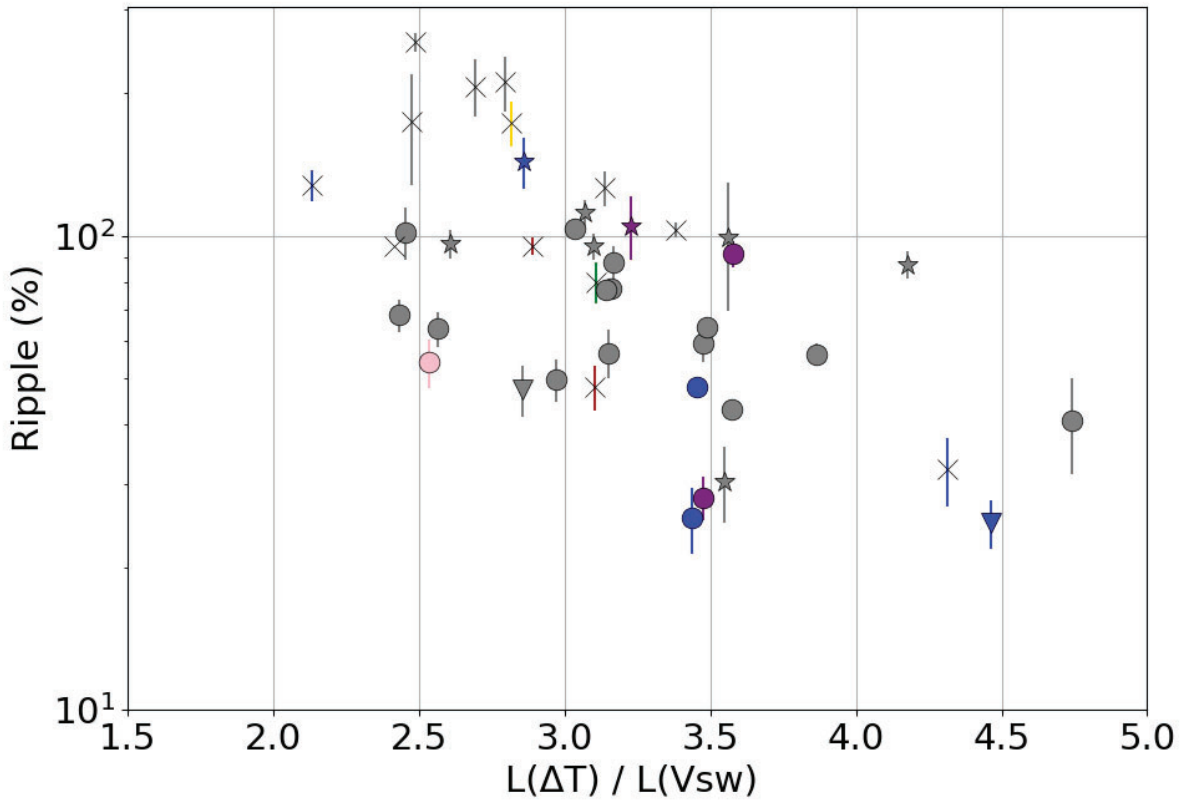

Figure 5.7: Scatter plot of the average anisotropy coefficient γ of suprathermal electrons from $\sim$ 180 eV to $\sim$ 366 eV versus the relation between the nominal Parker spiral length based on the SW speed and the theoretical one inferred from travel of the particles calculated from the time delay between the type III radio burst and the time arrival of the SEPs as catalogued in the *STEREO/SEP catalogue*. Error bars in y-axis correspond to the standard error of the mean.

Colours: (Based on the catalogues listed in Section 2.4) green: MO; blue: post-ICME; purple: SIR before the SI; pink: SIR after the SI; yellow: close to shock; grey: uncatalogued.

Symbols: (Based on the SW classifier. See text for details.) $\times$: ejecta; $\star$: CH; $\blacktriangledown$: sector reversal; $\bullet$: streamer belt.

Chapter 6

Summary and Conclusions

6.1. Summary

The IMF is variable and complex in both, large and small, temporal and spatial scales. Besides, the Earth's magnetosphere and atmosphere do not allow a direct study of the SW nor to observe certain wavelengths with ground-based instruments. Consequently, having space-based observatories is crucial in order to achieve complete observational coverage. Since the beginning of the space age, the heliospheric observatories were equipped with in-situ and remote sensing instruments to measure plasma properties and observe the solar atmosphere, respectively. Many of them are located orbiting Earth or in quasi-stable orbits around the region between Earth and Sun L1 (such as ACE, SOHO or SDO) so there is permanent communication (and therefore near-continuous observations), to measure the Earth's surroundings and forecast potential solar phenomena that may affect the humans. However, using only these missions to study large-scale structures within the SW is almost impossible, since they are all located in the same very small region of space. Deep space observatories at different radial distances, angular locations in the ecliptic plane, and heliographic latitudes thus provide much-needed diversity of measurements.

The twin mission STEREO travelling near the Earth's orbit provide observations of the Sun with wider angular separation. This allows a wider analysis of the large-scale structures and allows to measure the IMF conditions from different from different viewpoints, complementing the L1 missions. This property together to the huge amount of data provided by the two s/c for seven years, covering the solar cycle 24, are the reasons why this mission and ACE have been utilised the most in this thesis work.

Other missions as PSP allow measuring over a range of radial distances close to the Sun, and SolO will provide in-situ measurements out of the ecliptic while also getting closer to the Sun and providing remote-sensing observations, making it the most complete solar mission so far. Unfortunately, the recent launch of these missions did not allow to include them in this study, although the here developed methods will be used as part of future work and are extensible to these missions too.

The analysis of the data provided by these missions makes possible to have a closer approach to the complexity of the SW properties, such as the IMF. Moreover, it is necessary to examine not only the general large-scale plasma and magnetic field properties but also different particle populations from different solar sources and their behaviour. These particles act as an astronomic multi-messenger for the Sun. In particular, electrons in all energy ranges (thermal, suprathermal and quasi-relativistic) can provide valuable information about characteristics of the magnetic field topology and the solar source region.

The main focus of this thesis work is to analyse properties of the more common IMF topologies from different perspectives, mainly using suprathermal and energetic electron distributions as probes to extract the information. The work has been divided into three main topics which focuses on the characterisation of the suprathermal PADs and the analysis of their long-term variation (Chapter 3), the study of the ICMEs as global structure and how the suprathermal electrons are affected by their properties (Chapter 4), and the analysis of the more energetic electrons to infer characteristics of the IMF and how the two different populations (suprathermal and energetic) are affected by similar conditions. The results of these analyses are presented in the following Section 6.2.

In this thesis work, it has been addressed the characterisation of the IMF for understanding different topologies (with special interest in the nominal Parker spiral and the ICMEs) using different complementary approaches, like the use of different electron populations, such as suprathermal, SEPs and generators of type III radio emission, and the use of the previously developed Hidalgo's model (Hidalgo, 2013). Apart from the results, it is important to highlight three varied methods that have been applied to different scenarios (described in Chapters 3, 4, 5) for studying the SW plasma properties:

- **A characterisation method of suprathermal electron PAD.** The shape of suprathermal electron PADs in the SW carries relevant information about the physical conditions at the solar source and during the IP propagation, as well as about the large-scale topology of the IMF. In particular, the presence of BDE is often a signature of closed magnetic field structures, while the presence of isotropic periods could be an indicator of disconnection from the Sun by reconnection, or of enhanced IP scattering.

  The characterisation presented in this thesis work has been proved and allows not only to identify BDE and isotropy in the SW, but also to obtain the intensity, the mean flux, the anisotropy, and the classification of different types of PADs by comparing the Legendre Polynomials fitting coefficients. Previous methods such as Anderson et al. (2012); Chen et al. (2014) or Graham et al. (2017) were only designed to study a specific characteristic of the PADs.

  Applying signal processing analysis to the Legendre Polynomials, two different thresholds (γ_{th} and SNR_{th}) can be used for a simple identification of isotropic and BDE periods. Isotropy is efficiently identified selecting those PAD with $\gamma \leq 15\%$.

The clearest BDE intervals can be selected using the combined condition $SNR_{24} > 0$, $\gamma > 15\%$ and $A_2 > 0$. These cuts have been validated using extensive samples of STEREO/SWEA data during 2007–2014 (see sections 3.2.1 and 3.2.2). Although the selected threshold criterion is very restrictive for BDE (i.e. there are periods that could be not identified as such), establishing a common criteria allows long-term studies using the same dataset. The method is well suited for automatisation, and can be used directly for Space Weather applications.

- **Update of the Hidalgo's model Hidalgo (2013).** As part of the most commons structures of the SW, the FRs are also analysed by using a FR model previously developed Hidalgo (2013). The model has been improved reducing the number of free parameters by introducing other plasma measurements, such as the bulk speed, and the interface conditions have been tweaked to have a closer approach to a more realistic scenario. Also, these modifications have been applied to a statistical analysis of FRs observed by the STEREO mission.

- **Development of a simple model to trace quasi-relativistic electrons.** A model based on the time difference between multiple observatories at different locations of the observed onset time of type III radio bursts has been developed for tracking the radio-source related to impulsive SEPs in the heliosphere, and it has been applied to distinguish if the propagation takes place along the nominal Parker spiral (and infer the corresponding SW speed) or inside a MC (and infer the orientation of the structure).

Furthermore, thanks to the performed analysis and to the methodology, it has resulted in the following catalogues (Chapters 3 and 4):

- Catalogue of periods of BDE observed by both STEREOs from 2007 to 2014 (Section 3.2.4). This catalogue constitutes a very useful data product for the analysis of different magnetically closed structures and interactions between different SW regimes.

- Catalogue of periods of isotropic suprathermal electron fluxes observed by STEREO mission from 2007 to 2014 (Section 3.2.4), which provides relevant information about magnetic interaction (erosion, reconnection) among other characteristics.

- FR catalogue observed by STEREO from 2007 to 2014 (Section 4.2.3), for helping the identification and understanding of partially or totally uneroded structures in the SW.

6.2. Conclusions

6.2.1. Suprathermal Pitch-Angle Distribution Research

6.2.1.1. Long-Term Variation

The long-term behaviour of the fraction of time when the suprathermal electrons show isotropy or bi-directionality has been studied separately for STEREO-A and STEREO-B. This analysis draws the following conclusions:

- The BDE increases with the SSN, at the same time as the number of ICMEs does. The sudden change of the tilt angle of the HCS between late 2009 and early 2010 is accompanied by a large increase in the isotropy rate observed by both s/c (reaching maximum values), as well as in the BDE rate observed by STEREO-A.
- As reported by previous studies, anisotropy anticorrelates with the plasma β and BDEs are frequently found inside ICMEs.
- There are recurrent fluctuations of the isotropy with an apparent periodicity of almost 13 months. The ultimate origin of these periodicities is uncertain and requires further investigation.
- The isotropy is more frequent in solar minimum than during the increasing phase, although this tendency is weak compared with the fluctuations described above.

6.2.1.2. Energy and Latitude Dependency

The PAD of the suprathermal electron population shows a clear dependency with the energy. Higher energy channels tend to show stronger grade of anisotropy, and vice-versa, although in some transient periods this behaviour could be the opposite as shown in Section 3.3.1. The analysis of the time variation of the anisotropy coefficient γ for the available energy channels draws the following conclusions:

- The anisotropy is commonly higher for higher energies, as shown in the studies Fitzenreiter et al. (1998); Horaites et al. (2018). There are also long periods (few weeks) where the lower energy channels are more anisotropic, which is in agreement with the postulations from Pagel et al. (2007); Berčič et al. (2019b). Both tendencies were already gathered in Anderson et al. (2012), where it is suggested that focusing and scattering are competing during the propagation and depends on the variability of the IP conditions, and that the dependency with energy is probably due to different coexisting scattering mechanisms.
- There is a dependency between the grade of anisotropy and the solar cycle, tending to cover wider ranges in solar maximum and lower in solar minimum, probably as a consequence of the higher variability of the SW conditions.

- The anisotropy coefficient γ shows several apparently periodic maxima, similarly to the isotropy. The most intense corresponds to an almost-13-month periodicity. The ultimate cause of this behaviour is still unknown and remains under investigation.
- The anisotropy coefficient γ increases with the heliomagnetic latitude (defined as the minimum distance of the magnetic foot-point to the neutral line) during the quietest period of the solar minimum during Solar Cycle 24. This is indicative of that the *strahl* population is less isotropised when having higher heliomagnetic latitudes.

6.2.2. Interplanetary Coronal Mass Ejection Research

6.2.2.1. Suprathermal Electron Pitch-Angle Distribution inside Interplanetary Coronal Mass Ejections

Using a superposed epoch analysis for a large sample of events, the percentage of BDE and isotropy during the transit of ICMEs and in the post-ICME region (defined as 1.2 times the total duration of an ICME; see Section 4.1) has been analysed. The main conclusions of this analysis are:

- On average, the amount of BDE tends to gradually increase in the sheath (when it exists), reaching maximum values during the transit of the middle part of the MO. It drops at the exit of the MO and gradually decreases in the post-ICME period (defined as 1.2 times the duration of the ICME), which still shows a notable amount of BDE. The observed behaviour can be interpreted in terms of erosion by reconnection with the ambient IMF, i.e. the intervals preceding and following the MO contain some closed field lines mixed with reconnected field lines that were formerly closed. Alternatively, these BDE intervals could result from the reflection in converging lines around the ICME, or at the shock or the sheath, or to a particular diffusion mechanism from the sheath inside the MO.
- Contrary to Shodhan et al. (2000), the results suggest that BDE periods are more concentrated in the middle part of MOs, rather than being randomly distributed, which is consistent the inner parts of the MCs being less eroded by reconnection.
- ICMEs with shock present larger periods of BDE inside the MOs than those without shock. The distinction between MO and sheath and post-ICME in terms of BDE is also clearer for ICMEs with shock. This behaviour suggests that slow ICMEs (those not driving a shock) show a higher degree of erosion by reconnection due to their longer transit times to 1 au.
- Isotropy is much less common inside the MO than in ambient SW, and even less far from its boundaries. This can be interpreted as a direct consequence of the smooth magnetic field (which implies weak scattering conditions due to less turbulence) and

predominantly closed topology (not reconnected) inside the MO. On the other hand, isotropy is more common in the surroundings of the MOs (sheath and post-ICME regions) than on average SW. This is a possible indication of the presence of disconnected field lines and/or stronger scattering conditions.

6.2.2.2. Flux Rope Statistical Analysis

Periods presenting IMF FR topology have been selected from STEREO mission observations. In total, the number of catalogued events is 362 observed by both s/c. On the other hand, the Hidalgo's model has been updated reducing the number of parameters and defining the global radius dependant on the orientation of the structure (see Section 4.2). Using the updated model, a series of fits have been performed for all the FR periods:

- The FRs generally show same characteristics as the signatures that define the MCs (Zurbuchen & Richardson, 2006), and the number of events and the total transit time increase with the solar activity, which is coherent and agrees with previous works.
- The velocity of the structure it is not related to the phase of the solar cycle and there is no apparent relation between the velocity nor the phase of the solar cycle and the cross-section of the FR as derived from Hidalgo's model.
- The cross-section of the studied event ranges from ~ 0.01 au up to ~ 0.1 au , which differs in a factor of two to previous studies as e.g. Burlaga et al. (1981), where they mention that their radial dimensions were approximately 0.5 au. The reason for this could be the strict criteria for the selection of the boundaries of the FRs.
- The FR preferred tilt angle tends to be closer to 90 degrees, i.e. according to the model, the structures are in general found vertical rather than with small inclinations with respect to the ecliptic plane. In addition, there is an apparent relation with the rising phase of the solar cycle, where more inclined structures are found.

6.2.3. Energetic Electron Analysis

6.2.3.1. Type III Radio Burst Tracer Model Case Studies

A simple type III radio burst tracer model defined in Section 5.1 is able, using multipoint observations, to distinguish whether the observations are better suited to an impulsive event propagating along the nominal Parker spiral (e.g. Klassen et al., 2012) or inside a MC (e.g. Gómez-Herrero et al., 2017). Besides that, it allows to estimate of the SW velocity and the orientation of the MCs. However, the simplification of the IMF topologies does not allow to explain the observations performed by two relatively close s/c, as the one previously studied by Klassen et al. (2015). The proximity and the peculiar propagation of the beam hinders the potential of the model, but opens the possibility for future implementations and updates.

6.2.3.2. Statistical Analysis of Impulsive Solar Energetic Particle Events

The comparison between the time arrival of impulsive SEP events and the anisotropy coefficient γ for the suprathermal electrons suggests that there is a tendency to have shorter estimated SEP path-length when γ is higher (i.e. when suprathermal electrons are more anisotropic). This correlation seems to indicate that the conditions that may affect the suprathermal electrons also have an influence on the propagation of the SEPs, supporting previous works as Graham et al. (2018).

The correspondence of the travelling time and the anisotropy could be explained in terms of the turbulent conditions of the IMF. Turbulence causes the *strahl* to scatter, as well as it hinders the propagation of the SEPs, indicating that the conditions that affect one population affects the other too.

Apart from that, there is an unexpected lack of correlation between the propagation, turbulence and the topology where the event is taking place, as there are significant differences between the different IMF topologies. On the other hand, there are studies as Kahler et al. (2011) suggesting that despite the path is longer inside FRs, the time propagation is decreased due to the non-turbulent conditions. Further analyses with more candidates and different approaches should be considered to discern this issue.

6.3. Future Work

The PAD characterisation method presented here can be extended (for instance, using more harmonics if the angular resolution of the instrument is higher, the raw obtained coefficients and their sign, three dimensions and other SNR calculations) to characterise multiple interesting PAD features (such as the pancake or butterfly distributions) or their properties (e.g. width of *strahl*), and use it as input for machine-learning based classifiers (instead of the raw data) or for automatic detection of ICMEs by using the BDE, among other Space Weather applications. Also, an analysis of the data from future missions such as SolO or PSP will contribute to the understanding of the different PAD and especially how the BDE and the isotropy vary with the heliocentric distance and the heliographic latitude. This method opens up new ways for a better understanding of the energy dependence of the *strahl*, its width, and their relation to solar energetic particle events.

The updates of the Hidalgo's model have simplified it by reducing the number of parameters using plasma data and get a closer approach to the actual topology of the MCs by adjusting its global radius to its orientation. Still there are some limitations and room of improvement to get a more accurate results introducing new inputs such as the hydrodynamic pressure or constrains based on multipoint observations.

The type III radio burst tracer model has shown that with a simple density model and two observatories it is possible to extract relevant information of the type III radio burst

observations. Nevertheless, the model has some limitations, which could be reduced by being less restrictive in the assumptions, having better cadence, more observers or adding the direction-finding data product provided by the radio instrumentation, among others.

As mentioned above, some unexplained phenomena require further investigation, such as the presence of periodicity of the isotropic periods (and in the grade of anisotropy), the dependency with the latitude and the radial distance, the ultimate cause of the suprathermal electron BDE presence after the ICMEs, or the apparent lack of correlation between the anisotropy, the IP structure and the arrival time of the SEPs. The massive analysis of all the electron populations observed by three or more s/c is crucial for understanding the evolution of the SW in several conditions by the use of physical plasma magnitudes and the electrons for all energies.

In order to broad our understanding of the IMF topologies and evolution, and how the electrons behave with the different conditions, the following studies are proposed based on the methods and results explained in this thesis work:

- **Long-term SW analysis.** Compile and analyse suprathermal electron PADs for all the available missions in order to find the origin of the periodicities, the radial evolution, etc.
- **Multipoint ICME evolution.** Compile ICMEs observed by several s/c and compare the angular, radial and latitudinal differences for different electron populations. Also, study the source region and the eruption of the CME and compare with the observations in-situ.
- **SEP statistical analysis.** Improve the radio emission model to trace SEP events by using multipoint observation s/c. On the other hand, find and analyse multipoint SEP events, study the dependency and behaviour of the populations with the solar cycle and compare to suprathermal electrons measurements, trying to understand their connection to different IP structures.

Accomplishing these research goals will contribute valuable pieces of information needed to answer two of the key heliophysics science objectives of the SolO mission: *How and where do the SW plasma and magnetic field originate in the corona?* and indirectly, *How does the solar dynamo work and drive connections between the Sun and the heliosphere?* Also, it will open the possibility to analyse in more detail and efficiently data from past and future missions, as well as other scientists as the developed tools for analysing the data, will be shared.

Bibliography

Acero, F. J., Carrasco, V. M. S., Gallego, M. C., García, J. A., & Vaquero, J. M. 2017, The Astrophysical Journal, 839, 98

Acuña, M. H., Curtis, D., Scheifele, J. L., Russell, C. T., Schroeder, P., Szabo, A., & Luhmann, J. G. 2008, Space Science Reviews, 136, 203

Agueda, N. & Lario, D. 2016, The Astrophysical Journal, 829, 131

Allegrini, F., Ho, G. C., Desai, M. I., Ebert, R. W., Nelson, K., & Ogasawara, K. 2016, Journal of Geophysical Research: Space Physics, 121, 11,637

Altschuler, M. D. & Newkirk, G. 1969, Solar Physics, 9, 131

Anderson, B. R., Skoug, R. M., Steinberg, J. T., & McComas, D. J. 2012, Journal of Geophysical Research: Space Physics, 117, n/a

Anderson, M., Appourchaux, T., Auchère, F., Aznar Cuadrado, R., et al. 2020, Astronomy and Astrophysics, 642, A14

Antonucci, E., Romoli, M., Andretta, V., Fineschi, S., et al. 2020, Astronomy and Astrophysics, 642, A10

Artemyev, A. V., Agapitov, O. V., Mozer, F. S., & Spence, H. 2015, Journal of Geophysical Research: Space Physics, 120, 4279

Avrett, E. H. & Loeser, R. 2008, The Astrophysical Journal Supplement Series, 175, 229

Babcock, H. W. 1961, The Astrophysical Journal, 133, 572

Bale, S. D., Goetz, K., Harvey, P. R., Turin, P., et al. 2016, Space Science Reviews, 204, 49

Ball, L. & Melrose, D. 2001, pasa, 18, 361

Balogh, A. 1971, Planetary and Space Science, 19, 533

Balogh, A., Bothmer, V., Crooker, N. U., Forsyth, R. J., et al. 1999, Space Science Reviews, 89, 141

Beck, J. 2000, solphys, 191, 47

Berčič, L., Maksimović, M., Landi, S., & Matteini, L. 2019a, Monthly Notices of the Royal Astronomical Society, 486, 3404

Berčič, L., Maksimović, M., Landi, S., & Matteini, L. 2019b, Monthly Notices of the Royal Astronomical Society, 486, 3404

Bougeret, J. L., Goetz, K., Kaiser, M. L., Bale, S. D., et al. 2008, Space Science Reviews, 136, 487

Bürgi, A. 1992, Solar Wind Seven, 333

Burlaga, L., Sittler, E., Mariani, F., & Schwenn, R. 1981, Journal of Geophysical Research, 86, 6673

Burlaga, L. F. 1974, Journal of Geophysical Research (1896-1977), 79, 3717

Burlaga, L. F. 1988, Journal of Geophysical Research: Space Physics, 93, 7217

Burlaga, L. F., Behannon, K. W., & Klein, L. W. 1987, Journal of Geophysical Research: Space Physics, 92, 5725

Carcaboso, F., Gómez-Herrero, R., Espinosa Lara, F., Hidalgo, M. A., Cernuda, I., & Rodríguez-Pacheco, J. 2020, Astronomy and Astrophysics, 635, A79

Carrington, R. C. 1859, Monthly Notices of the Royal Astronomical Society, 20, 13

Charbonneau, P. 2007, Advances in Space Research, 39, 1661

Che, H. & Goldstein, M. L. 2014, Astrophysical Journal Letters, 795, L38

Chen, Y., Friedel, R. H. W., Henderson, M. G., Claudepierre, S. G., Morley, S. K., & Spence, H. E. 2014, Journal of Geophysical Research: Space Physics, 119, 1693

Chollet, E., Skoug, R., Steinberg, J., Crooker, N., & Giacalone, J. 2010, in AIP Conference Proceedings, Vol. 1216, 600–603

Cid, C., Hidalgo, M., Nieves-Chinchilla, T., Sequeiros, J., & Viñas, A. 2002, Solar Physics, 207, 187

Crooker, N. U., Larson, D. E., Kahler, S. W., Lamassa, S. M., & Spence, H. E. 2003, Geophysical Research Letters, 30

Crooker, N. U., Shodhan, S., Gosling, J. T., Simmerer, J., Lepping, R. P., Steinberg, J. T., & Kahler, S. W. 2000, Geophysical Research Letters, 27, 3769

Dahlquist, G., Björck, A., & Björck, A. 2014, Numerical methods (Dover Publications), 113–174

Dikpati, M. 2006, Advances in Space Research, 38, 839

Domingo, V., Fleck, B., & Poland, A. I. 1995, Solar Physics, 162, 1

Dumbović, M., Heber, B., Vršnak, B., Temmer, M., & Kirin, A. 2018, The Astrophysical Journal, 860, 71

Dumbović, M., Vršnak, B., Guo, J., Heber, B., et al. 2020, Solar Physics, 295, 104

Dunne, E. M., Gordon, H., Kürten, A., Almeida, J., et al. 2016, Science, 354, 1119

Earl, J. A. 1976, The Astrophysical Journal, 205, 900

Elliott, H. A., Henney, C. J., McComas, D. J., Smith, C. W., & Vasquez, B. J. 2012, Journal of Geophysical Research: Space Physics, 117, n/a

Farrugia, C., Burlaga, L., Lepping, R., & Osherovich, V. 1992, in Solar Wind Seven, ed. E. MARSCH & R. B. T. S. W. S. SCHWENN (Amsterdam: Pergamon), 611–614

Farrugia, C. J., Burlaga, L. F., Osherovich, V. A., Richardson, I. G., Freeman, M. P., Lepping, R. P., & Lazarus, A. J. 1993, Journal of Geophysical Research: Space Physics, 98, 7621

Fedorov, A., Opitz, A., Sauvaud, J.-A., Luhmann, J. G., Curtis, D. W., & Larson, D. E. 2011, Space Science Reviews, 161, 49

Feldman, W. C., Asbridge, J. R., Bame, S. J., Montgomery, M. D., & Gary, S. P. 1975, Journal of Geophysical Research, 80, 4181

Feldman, W. C., Skoug, R. M., Gosling, J. T., McComas, D. J., Tokar, R. L., Burlaga, L. F., Ness, N. F., & Smith, C. W. 1999, Geophysical Research Letters, 26, 2613

Fitzenreiter, R. J., Ogilvie, K. W., Chornay, D. J., & Keller, J. 1998, Geophysical Research Letters, 25, 249

Forveille, T. & Shore, S. 2020, Astronomy and Astrophysics, 642, E1

Fox, N. J., Velli, M. C., Bale, S. D., Decker, R., et al. 2016, Space Science Reviews, 204, 7

Galvin, A. B., Kistler, L. M., Popecki, M. A., Farrugia, C. J., et al. 2008, Space Science Reviews, 136, 437

Ganse, U., Kilian, P., Vainio, R., & Spanier, F. 2012, Solar Physics, 280, 551

Gómez-Herrero, R., Dresing, N., Klassen, A., Heber, B., Lario, D., Agueda, N., Malandraki, O. E., Blanco, J. J., Rodríguez-Pacheco, J., & Banjac, S. 2015, Astrophysical Journal, 799, 55

Gómez-Herrero, R., Dresing, N., Klassen, A., Heber, B., et al. 2017, The Astrophysical Journal, 840, 85

Gonzalez, W. D., Joselyn, J. A., Kamide, Y., Kroehl, H. W., Rostoker, G., Tsurutani, B. T., & Vasyliunas, V. M. 1994, Journal of Geophysical Research, 99, 5771

Gosling, J. T., Baker, D. N., Bame, S. J., Feldman, W. C., Zwickl, R. D., & Smith, E. J. 1987, Journal of Geophysical Research: Space Physics, 92, 8519

Gosling, J. T., Eriksson, S., McComas, D. J., Phan, T. D., & Skoug, R. M. 2007, Journal of Geophysical Research: Space Physics, 112

Gosling, J. T., Skoug, R. M., & Feldman, W. C. 2001, Geophysical Research Letters, 28, 4155

Graham, D. B., Cairns, I. H., Malaspina, D. M., & Ergun, R. E. 2012, Astrophysical Journal Letters, 753, L18

Graham, G. A., Rae, I. J., Owen, C. J., & Walsh, A. P. 2018, The Astrophysical Journal, 855, 40

Graham, G. A., Rae, I. J., Owen, C. J., & Walsh, A. P. 2018, , 855, 40

Graham, G. A., Rae, I. J., Owen, C. J., Walsh, A. P., et al. 2017, Journal of Geophysical Research: Space Physics, 122, 3858

Gurgiolo, C. & Goldstein, M. L. 2017, Annales Geophysicae, 35, 71

Haggerty, D. K. & Roelof, E. C. 2002, The Astrophysical Journal, 579, 841

Haggerty, D. K. & Roelof, E. C. 2006, Advances in Space Research, 38, 1001

Hammond, C. M., Feldman, W. C., Mccomas, D. J., Phillips, J. L., & Forsyth, R. J. 1996, Astronomy and Astrophysics, 316, 350

Harris, C. R., Millman, K. J., van der Walt, S. J., Gommers, R., et al. 2020, Nature, 585, 357

Heinemann, S. G., Temmer, M., Farrugia, C. J., Dissauer, K., et al. 2019, Solar Physics, 294, 121

Hidalgo, M. A. 2013, The Astrophysical Journal, 766, 125

Hidalgo, M. A. 2016, The Astrophysical Journal, 823, 3

Hidalgo, M. A. & Nieves-Chinchilla, T. 2012, The Astrophysical Journal, 748, 109

Hoeksema, J. T. 1984, PhD thesis, Stanford Univ., CA.

Hoeksema, J. T. 1995, Space Science Reviews, 72, 137

Horaites, K., Boldyrev, S., Wilson, L. B., Viñas, A. F., & Merka, J. 2018, Monthly Notices of the Royal Astronomical Society, 474, 115

Horbury, T. S., O'Brien, H., Carrasco Blazquez, I., Bendyk, M., et al. 2020, Astronomy and Astrophysics, 642, A9

Howard, R. A., Vourlidas, A., Colaninno, R. C., Korendyke, C. M., et al. 2020, Astronomy and Astrophysics, 642, A13

Howlett, J., Abramowitz, M., & Stegun, I. A. 2007, The Mathematical Gazette, 50, 358

Howson, T. A. 2019, Three Dimensional Mhd Simulations of the Dynamics and Energetics of Coronal Flux Tubes, Tech. rep., University of St Andrews

Hundhausen, A. J. 1973, Journal of Geophysical Research (1896-1977), 78, 7996

Israelevich, P. L., Gombosi, T. I., Ershkovich, A. I., Hansen, K. C., Groth, C. P., DeZeeuw, D. L., & Powell, K. G. 2001, Astronomy and Astrophysics, 376, 288

Jian, L., Russell, C. T., Luhmann, J. G., & Skoug, R. M. 2006a, Solar Physics, 239, 393

Jian, L., Russell, C. T., Luhmann, J. G., & Skoug, R. M. 2006b, Solar Physics, 239, 337

Jian, L. K., Luhmann, J. G., Russell, C. T., & Galvin, A. B. 2019, Solar Physics, 294, 31

Jian, L. K., Russell, C. T., Luhmann, J. G., & Galvin, A. B. 2018, The Astrophysical Journal, 855, 114

Jian, L. K., Russell, C. T., Luhmann, J. G., Galvin, A. B., & Simunac, K. D. 2013in (American Institute of Physics), 191–194

Jones, F. C. & Ellison, D. C. 1991, Space Science Reviews, 58, 259

Kahler, S. W., Krucker, S., & Szabo, A. 2011, Journal of Geophysical Research (Space Physics), 116, A01104

Kaiser, M. L., Kucera, T. A., Davila, J. M., St. Cyr, O. C., Guhathakurta, M., & Christian, E. 2008, Space Science Reviews, 136, 5

Kajdič, P., Kajdič, C. ., Lavraud, B., Zaslavsky, A., Blanco-Cano, X., Sauvaud, J.-A., Opitz, A., Jian, L. K., Maksimovic, M., & Luhmann, J. G. 2014, Journal of Geophysical Research: Space Physics Res. Space Physics, 119, 7038

Kallenrode, M.-B. 2004 (Berlin, Heidelberg: Springer)

Kasper, J. C., Abiad, R., Austin, G., Balat-Pichelin, M., et al. 2016, Space Science Reviews, 204, 131

Kasper, J. C., Bale, S. D., Belcher, J. W., Berthomier, M., et al. 2019, Nature, 576, 228

Khnlein, W. 1996, Solar Physics, 169, 209

Kilpua, E., Koskinen, H. E. J., & Pulkkinen, T. I. 2017, Living Reviews in Solar Physics, 14, 5

Kilpua, E. K. J., Isavnin, A., Vourlidas, A., Koskinen, H. E. J., & Rodriguez, L. 2013, Annales Geophysicae, 31, 1251

Klassen, A., Dresing, N., Gómez-Herrero, R., & Heber, B. 2015, Astronomy and Astrophysics, 580, A115

Klassen, A., Gómez-Herrero, R., Böhm, E., Müller-Mellin, R., Heber, B., & Wimmer-Schweingruber, R. 2008, Annales Geophysicae, 26, 905

Klassen, A., Gómez-Herrero, R., Heber, B., Kartavykh, Y., Dröge, W., & Klein, K. L. 2012, Astronomy and Astrophysics, 542, A28

Klein, K. L. & Dalla, S. 2017, Space Science Reviews, 212, 1107

Klein, K. L., Matamoros, C. S., & Zucca, P. 2018, Comptes Rendus Physique, 19, 36

Klimchuk, J. A. 2006, Solar Physics, 234, 41

Kocharov, L. & Torsti, J. 2002, Solar Physics, 207, 149

Kosovichev, A. G. & Zharkova, V. V. 1998, Nature, 393, 317

Krimigis, S. M., Decker, R. B., Roelof, E. C., Hill, M. E., Armstrong, T. P., Gloeckler, G., Hamilton, D. C., & Lanzerotti, L. J. 2013, Science, 341, 144

Krucker, S., Hurford, G. J., Grimm, O., Kögl, S., et al. 2020, Astronomy and Astrophysics, 642, A15

Kuperus, M. & Raadu, M. 1974, Astronomy and Astrophysics, 31, 189

Larson, D. E., Lin, R. P., McTiernan, J. M., McFadden, J. P., et al. 1997, Geophysical Research Letters, 24, 1911

Lee, M. A. 2005, The Astrophysical Journal Supplement Series, 158, 38

Leighton, R. B. 1964, The Astrophysical Journal, 140, 1547

Leighton, R. B. 1969, The Astrophysical Journal, 156, 1

Li, B., Cairns, I. H., Gosling, J. T., Steward, G., Francis, M., Neudegg, D., Schulten Den Bäumen, H., Player, P. R., & Milne, A. R. 2016, Journal of Geophysical Research A: Space Physics, 121, 925

Li, Y., Luhmann, J. G., & Lynch, B. J. 2018, Solar Physics, 293, 135

Liu, C. M., Fu, H. S., Cao, J. B., Xu, Y., Yu, Y. Q., Kronberg, E. A., & Daly, P. W. 2017, Geophysical Research Letters, 44, 10,116

Lourakis, M. I. 2005, Foundation of Research and Technology, 4, 1

Luhmann, J. G., Curtis, D. W., Schroeder, P., McCauley, J., et al. 2008, Space Science Reviews, 136, 117

Maksimovic, M., Bale, S. D., Chust, T., Khotyaintsev, Y., et al. 2020, Astronomy and Astrophysics, 642, A12

Maksimovic, M., Zouganelis, I., Chaufray, J. Y., Issautier, K., et al. 2005, Journal of Geophysical Research: Space Physics, 110

Mann, G., Jansen, F., MacDowall, R. J., Kaiser, M. L., & Stone, R. G. 1999, , 348, 614

McComas, D., Bame, S., Barker, P., Feldman, W., Phillips, J., Riley, P., & Griffee, J. 1998, Space Science Reviews, 86, 563

McComas, D. J., Alexander, N., Angold, N., Bale, S., et al. 2016, Space Science Reviews, 204, 187

McComas, D. J., Gosling, J. T., Phillips, J. L., Bame, S. J., Luhmann, J. G., & Smith, E. J. 1989, , 94, 6907

Mewaldt, R. A., Mason, G. M., Gloeckler, G., Christian, E. R., et al. 2001, in International Cosmic Ray Conference, Vol. 10, International Cosmic Ray Conference, 3984

Meyer, J. P. 1985, , 57, 151

Meyer-Vernet, N. 2007, Basics of the Solar Wind (Cambridge: Cambridge University Press)

Miller, J. A. 1998, Space Science Reviews, 86, 79

Mullan, D. J. & Smith, C. W. 2006, Solar Physics, 234, 325

Müller, D., St. Cyr, O. C., Zouganelis, I., Gilbert, H. R., et al. 2020, Astronomy and Astrophysics, 642, A1

Müller-Mellin, R., Böttcher, S., Falenski, J., Rode, E., Duvet, L., Sanderson, T., Butler, B., Johlander, B., & Smit, H. 2008, Space Science Reviews, 136, 363

Newbury, J. A. 1996, Eos, Transactions American Geophysical Union, 77, 471

Newville, M., Ingargiola, A., Stensitzki, T., & Allen, D. B. 2014, Zenodo,

Newville, M., Otten, R., Nelson, A., Ingargiola, A., et al. 2019, zenodo

Nieves-Chinchilla, T., Jian, L. K., Balmaceda, L., Vourlidas, A., dos Santos, L. F., & Szabo, A. 2019, Solar Physics, 294, 89

Nieves-Chinchilla, T., Linton, M. G., Hidalgo, M. A., Vourlidas, A., Savani, N. P., Szabo, A., Farrugia, C., & Yu, W. 2016, The Astrophysical Journal, 823, 27

Ogilvie, K. & Desch, M. 1997, Advances in Space Research, 20, 559

Opitz, A., Sauvaud, J.-A., Klassen, A., Gomez-Herrero, R., et al. 2014, Journal of Geophysical Research (Space Physics), 119, 6342

Owen, C. J., Bruno, R., Livi, S., Louarn, P., et al. 2020, Astronomy and Astrophysics, 642, A16

Owens, M. J., Cliver, E., McCracken, K. G., Beer, J., et al. 2016, Journal of Geophysical Research: Space Physics, 121, 6064

Owens, M. J. & Crooker, N. U. 2006, Journal of Geophysical Research: Space Physics, 111, A10104

Owens, M. J., Crooker, N. U., & Lockwood, M. 2013, Journal of Geophysical Research: Space Physics, 118, 1868

Owens, M. J., Crooker, N. U., & Schwadron, N. A. 2008, Journal of Geophysical Research: Space Physics, 113, n/a

Owens, M. J. & Forsyth, R. J. 2013, Living Reviews in Solar Physics, 10, 5

Owens, M. J., Lockwood, M., Riley, P., & Linker, J. 2017, Journal of Geophysical Research: Space Physics, 122, 10,980

Owens, M. J., Schwadron, N. A., Crooker, N. U., Hughes, W. J., & Spence, H. E. 2007, Geophysical Research Letters, 34, L06104

Pagel, C., Crooker, N. U., & Larson, D. E. 2005a, Geophysical Research Letters, 32, 1

Pagel, C., Crooker, N. U., Larson, D. E., Kahler, S. W., & Owens, M. J. 2005b, Journal of Geophysical Research: Space Physics, 110, A01103

Pagel, C., Gary, S. P., De Koning, C. A., Skoug, R. M., & Steinberg, J. T. 2007, Journal of Geophysical Research: Space Physics, 112, n/a

Parker, E. N. 1958, The Astrophysical Journal, 128, 664

Parker, E. N. 1963, Interplanetary dynamical processes.

Pesnell, W. D., Thompson, B. J., & Chamberlin, P. 2011, in The Solar Dynamics Observatory (Springer), 3–15

Phillips, J. L., Feldman, W. C., Gosling, J. T., Hammond, C. M., & Forsyth, R. J. 1996in (AIP), 293–296

Raadu, M. A. & Kuperus, M. 1973, Solar Physics, 28, 77

Reames, D. V. 1999, Space Science Reviews, 90, 413

Reames, D. V. 2017 (Springer International Publishing)

Reid, H. A. & Kontar, E. P. 2013, Solar Physics, 285, 217

Richardson, I. G. & Cane, H. V. 2010, Solar Physics, 264, 189

Richardson, J. D., Belcher, J. W., Garcia-Galindo, P., & Burlaga, L. F. 2019, Nature Astronomy, 3, 1019

Rochus, P., Auchère, F., Berghmans, D., Harra, L., et al. 2020, Astronomy and Astrophysics, 642, A8

Rodríguez-Pacheco, J., Cid, C., Blanco, J. J., & Sequeiros, J. 2003, , 213, 121

Rodríguez-Pacheco, J., Wimmer-Schweingruber, R. F., Mason, G. M., Ho, G. C., et al. 2020, Astronomy and Astrophysics, 642, A7

Rodríguez-García, L., Gómez-Herrero, R., Zouganelis, Y., Balmaceda, L., et al. 2021, Astronomy and Astrophysics

Romashets, E. P. & Vandas, M. 2003, Geophysical Research Letters, 30

Rosenberg, R. L. & Coleman, P. J. 1969, Journal of Geophysical Research, 74, 5611

Rosner, R., Tucker, W. H., & Vaiana, G. S. 1978, , 220, 643

Röttgering, H. 2003, New Astronomy Reviews, 47, 405

Russell, C. T., Luhmann, J. G., & Strangeway, R. J. 2016, Space physics (Cambridge University Press)

Russell, H. N. 1914, Popular Astronomy, 22, 275

Salpeter, E. E. 1952, Physical Review, 88, 547

Sanderson, T. R., Marsden, R. G., Reinhard, R., Wenzel, K. P., & Smith, E. J. 1983, Geophysical Research Letters, 10, 916

Sanderson, T. R., Reinhard, R., van Nes, P., & Wenzel, K.-P. 1985, Journal of Geophysical Research: Space Physics, 90, 19

Sauvaud, J.-A., Larson, D., Aoustin, C., Curtis, D., et al. 2008, Space Science Reviews, 136, 227

Savitzky, A. & Golay, M. J. 1964, Analytical Chemistry, 36, 1627

Schatten, K. H., Wilcox, J. M., & Ness, N. F. 1969, Solar Physics, 6, 442

Schrijver, C. J. & Zwaan, C. 2000, Cambridge astrophysics: Solar and stellar magnetic activity series number 34 (Cambridge, England: Cambridge University Press)

Schwenn, R. & Marsch, E. 1990, Large-Scale Structure of the Interplanetary Medium, ed. R. Schwenn & E. Marsch (Berlin, Heidelberg: Springer Berlin Heidelberg), 99–181

Shodhan, S., Crooker, N. U., Kahler, S. W., Fitzenreiter, R. J., Larson, D. E., Lepping, R. P., Siscoe, G. L., & Gosling, J. T. 2000, Journal of Geophysical Research: Space Physics, 105, 27261

Smith, C. W., L'Heureux, J., Ness, N. F., Acuña, M. H., Burlaga, L. F., & Scheifele, J. 1998, Space Science Reviews, 86, 613

Solanki, S. K., Del Toro Iniesta, J. C., Woch, J., Gandorfer, A., et al. 2020, Astronomy and Astrophysics, 642, A11

Spiegel, E. A. & Zahn, J. P. 1992, , 265, 106

Squire, J., Chandran, B. D. G., & Meyrand, R. 2020, The Astrophysical Journal, 891, L2

Stone, E. 1977, Space Science Reviews, 21, 75

Stone, E. C., Frandsen, A., Mewaldt, R., Christian, E., Margolies, D., Ormes, J., & Snow, F. 1998, Space Science Reviews, 86, 1

Štverák, Š., Trávníček, P., Maksimovic, M., Marsch, E., Fazakerley, A. N., & Scime, E. E. 2008, Journal of Geophysical Research: Space Physics, 113, n/a

Tan, L. C., Reames, D. V., & Ng, C. K. 2007, The Astrophysical Journal, 661, 1297

Temerin, M. & Roth, I. 1992, , 391, L105

Temmer, M. 2016, Astronomische Nachrichten, 337, 1010

Thernisien, A. 2011, Astrophysical Journal, Supplement Series, 194, 33

Vainio, R. & Afanasiev, A. 2018, in Particle Acceleration Mechanisms BT - Solar Particle Radiation Storms Forecasting and Analysis: The HESPERIA HORIZON 2020 Project and Beyond, ed. O. E. Malandraki & N. B. Crosby (Cham: Springer International Publishing), 45–61

Vainio, R., Valtonen, E., Heber, B., Malandraki, O. E., et al. 2013, Journal of Space Weather and Space Climate, 3, A12

Van Rossum, G. & Drake, F. L. 2009, Python 3 Reference Manual (CreateSpace)

Verscharen, D., Wicks, R., Alexandrova, O., Bruno, R., et al. 2019, A Case for Electron-Astrophysics

Viñas, A. F., Wong, H. K., & Klimas, A. J. 2000, The Astrophysical Journal, 528, 509

Vourlidas, A., Howard, R. A., Plunkett, S. P., Korendyke, C. M., et al. 2016, Space Science Reviews, 204, 83

Vršnak, B., Poletto, G., Vujić, E., Vourlidas, A., et al. 2009, , 499, 905

Walsh, A. P., Arridge, C. S., Masters, A., Lewis, G. R., Fazakerley, A. N., Jones, G. H., Owen, C. J., & Coates, A. J. 2013, Geophysical Research Letters, 40, 2495

Walsh, A. P., Horbury, T. S., Maksimovic, M., Owen, C. J., et al. 2020, A&A, 642, A5

Wang, J., Liu, Q., & Zhao, Y. 2018, Solar Physics, 293, 116

Wang, Y.-M. & Sheeley, N. R., J. 1992, The Astrophysical Journal, 392, 310

Webber, W. R. 1975, in International Cosmic Ray Conference, Vol. 5, International Cosmic Ray Conference, 1597

Wenzel, K., Marsden, R., Page, D., & Smith, E. 1992, Astronomy and Astrophysics Supplement Series, 92, 207

Wes McKinney. 2010, in Proceedings of the 9th Python in Science Conference, ed. Stéfan van der Walt & Jarrod Millman, 56 – 61

Wilcox, J. & Ness, N. F. 1965, Journal of Geophysical Research, 70, 5793

Wild, J. P. 1951, Australian Journal of Scientific Research A Physical Sciences, 4, 36

Winslow, R. M., Lugaz, N., Schwadron, N. A., Farrugia, C. J., Yu, W., Raines, J. M., Mays, M. L., Galvin, A. B., & Zurbuchen, T. H. 2016, Journal of Geophysical Research: Space Physics, 121, 6092

Wu, M., Lu, Q., Volwerk, M., Vörös, Z., Zhang, T., Shan, L., & Huang, C. 2013, Journal of Geophysical Research: Space Physics, 118, 4804

Xu, F. & Borovsky, J. E. 2015, Journal of Geophysical Research: Space Physics, 120, 70

Zank, G. P., Hunana, P., Mostafavi, P., le Roux, J. A., Li, G., Webb, G. M., & Khabarova, O. 2015, Journal of Physics: Conference Series, 642, 012031

Zouganelis, I. 2008, Journal of Geophysical Research (Space Physics), 113, A08111

Zouganelis, I., De Groof, A., Walsh, A. P., Williams, D. R., et al. 2020, A&A, 642, A3

Zurbuchen, T. H. & Richardson, I. G. 2006, Space Science Reviews, 123, 31

Appendix

Basics about Charged Particle Motion inside Magnetic Fields

Single Particle Motion

The SW is a plasma mainly composed by charged particles with a total neutral charge, and the electric and magnetic forces are the ones dominating the plasma in the IP medium. The motion of these particles is governed by the Maxwell equations. In the vacuum, these equations are:

$$\vec{\nabla} \cdot \vec{E} = \frac{\rho}{\varepsilon_0} \quad \text{(Gauss's Law)} \tag{1}$$

$$\vec{\nabla} \cdot \vec{B} = 0 \quad \text{(Gauss's Law for magnetic field)} \tag{2}$$

$$\vec{\nabla} \times \vec{E} = -\frac{\partial \vec{B}}{\partial t} \quad \text{(Faraday's Law)} \tag{3}$$

$$\vec{\nabla} \times \vec{B} = \mu_0 \vec{J} + \mu_0 \varepsilon_0 \frac{\partial \vec{E}}{\partial t} \quad \text{(Generalised Ampère's Law)} \tag{4}$$

where $\vec{E}$ corresponds to the electric field, $\vec{B}$ corresponds to the magnetic field, ρ is the charge per unit volume, ε_0 corresponds to the electric permitivitty of vacuum, μ_0 is the magnetic permeability of the vacuum and $\vec{J}$ is the current density.

The following paragraphs summarise those aspects included in the thesis work related to the free motion of particles within the IMF, whose contribution to the bulk plasma can be considered negligible in general terms (Meyer-Vernet, 2007). The SW is a neutral plasma, but the motion of the particles (with positive and negative charges) with different directions constitutes electric currents (and so magnetic fields).

The basic equation of motion for a particle subjected to electric and magnetic fields is:

$$\vec{F} = \frac{\partial \vec{p}}{\partial t} = q(\vec{v} \times \vec{B} + \vec{E}) \tag{5}$$

being $\vec{p}$ the momentum of the particle ($\vec{p} = m\vec{v}$).

The parallel component of the velocity of the particle with respect to the magnetic field (B) remains constant, while the perpendicular force produces a circular motion with a radius known as the Larmor radius o gyroradius (Equation 6) and an angular gyrofrequency or cyclotron angular frequency described in Equation 7 .

$$r_g = \frac{m v_\perp}{qB} \tag{6}$$

where $\alpha = arctan(\frac{v_\perp}{v_\parallel})$ and corresponds to the PA of the particle with respect to the magnetic field direction.

$$\omega_g = \frac{qB}{m} \tag{7}$$

The summation of both components produces an helicoidal movement of the particles. If an external force is applied to the particle (e.g. the one produced by an electrical field to a charged particle), a drift velocity $\vec{V_D}$ is produced as given in Equation 8.

$$\vec{V_D} = \frac{\vec{F}}{q} \times \frac{\vec{B}}{B^2} \tag{8}$$

A variation of the magnetic field would change the gyroradius of the particle as derived from Equation 6, and an additional perpendicular drift is produced, as described in Equation 9. When a particle is travelling along magnetic field lines that are converging (i.e. when the strength, B, increases), the Lorentz force acts reducing the parallel speed of the particle.

$$\vec{V_D} = \left(\frac{mv_\perp^2}{2} + mv_\parallel^2\right) \frac{\vec{B} \times \nabla_\perp B}{qB^3} \tag{9}$$

At a certain point, the particle is reflected back to the weaker magnetic field where it was coming from. This is produced when the perpendicular force (defined as $mv^2 sin^2(\alpha)$) reaches its minimum (at $\alpha = \pi/2$) to compensate the deceleration (because there are no energy losses). This effect is denominated *mirroring*.

Particle Distributions

The IP plasma is complex and the populations (i.e. species and energy intervals) that form the SW are often studied as a whole in order to explain the global behaviour. In addition, it can be instrumentally impossible to measure all particles at the same time, especially for low energies. For these reasons, it is necessary to define a probabilistic mathematical expression as a function of different properties of the bulk of particles. Nevertheless, mainly due to the lack of statistics, it could also be possible to study the properties of a single particle. The mathematical expression is denominated Distribution Function [f($r_x, r_y, r_z, v_x, v_y, v_z$)], which defines the probability of finding a particle with the different velocity components (v_x, v_y, v_z) in a specific point in the space (r_x, r_y, r_z).

For example, suprathermal electrons are almost continuously emerging from the Sun to the IP medium and carry a great amount of the SW heat flux. When a plasma is in equilibrium it can be reproduced with a Maxwellian distribution ($f_M(v)$, see Equation 10). This behaviour is a consequence of the particles being randomly and isotropically

distributed following a Gaussian distribution. This is the case of the SW electron thermal core population. Nevertheless, the presence of a magnetic field can produce some anisotropy in the plasma as the charge particles travel along the field lines as described above. This is the case of the *strahl* population. The non-Maxwellian distribution of the suprathermal tails correspond to halo population, and it can be described as a Kappa distribution ($f_\kappa(v)$, see Equation 11). The Kappa distribution tends to Maxwellian when $\kappa \to \infty$ (Zouganelis, 2008).

$$f_M(v) = n\left(\frac{m}{2\pi k_B}\right)^{3/2} exp\left(-\frac{mv^2}{2Tk_B}\right) \tag{10}$$

$$f_\kappa(v) = \frac{n}{\pi\kappa v_\kappa^2}\frac{\Gamma(\kappa+1)}{\Gamma(\kappa-1/2)}\left(1+\frac{v^2}{\kappa v_\kappa^2}\right) \tag{11}$$

where k_B is the Boltmann constant, $\Gamma(x) = (x-1)!$, T the equivalent temperature, v is the velocity of the particles, v_κ is the effective thermal velocity, m is the mass of specie.

The *strahl* population is then the closer related to the IMF, as well as the existence of an interchange between the halo population and the *strahl* which can provide information of the conditions of the SW. When the halo population becomes part of the *strahl* is produced in *focusing* processes, while when the *strahl* becomes part of the halo is produced by *scattering* . These two processes can be explained as it could be done for a single particle as described above and it could be extrapolated to more energetic charged particles.

Magnetic Obstacle Candidates with Clear Bidirectionality

Table 1 shows a selection of the candidates with long and clear periods of BDE observed by STEREO-A and STEREO-B utilised for defining a threshold in the SNR_{24} coefficient in Chapter 4. The events were presented in the series of papers Jian et al. (2018, 2013, 2006a).

	Candidate no.	Start date (UTC)	End date(UTC)
STEREO-A	1	2008-07-05 06:34	2008-07-06 18:00
	2	2009-07-11 23:10	2009-07-13 05:45
	3	2009-10-16 21:35	2009-10-17 22:16
	4	2009-11-01 08:00	2009-11-03 02:00
	5	2009-12-09 09:00	2009-12-10 23:13
	6	2010-12-15 10:20	2010-12-16 04:00
	7	2011-01-16 05:40	2011-01-17 10:10
	8	2011-02-01 10:25	2011-02-02 18:40
	9	2011-03-12 00:25	2011-03-12 16:47
	10	2011-03-19 23:34	2011-03-21 01:30
	11	2011-03-23 06:55	2011-03-24 23:17
	12	2011-04-06 09:40	2011-04-06 23:41
	13	2011-07-23 09:41	2011-07-24 11:45
	14	2011-11-26 01:30	2011-11-26 13:30
	15	2011-11-27 00:20	2011-11-28 05:00
	16	2012-01-25 22:10	2012-01-26 22:00
	17	2012-03-04 10:34	2012-03-04 22:00
	18	2012-03-17 04:10	2012-03-18 06:00
	19	2012-03-20 05:00	2012-03-20 14:45
	20	2012-07-11 09:10	2012-07-13 04:00
	21	2012-07-16 00:45	2012-07-16 18:00
	22	2012-07-17 03:40	2012-07-18 00:25
	23	2012-10-05 16:10	2012-10-07 12:00
	24	2012-10-11 22:38	2012-10-13 02:30
	25	2012-11-12 15:23	2012-11-13 15:05
	26	2012-11-26 15:00	2012-11-28 01:22
	27	2013-04-23 00:00	2013-04-23 19:30
	28	2013-05-03 05:50	2013-05-04 16:10
	29	2013-06-27 16:17	2013-06-28 00:37
	30	2013-08-10 17:24	2013-08-12 07:00
	31	2013-08-22 23:15	2013-08-24 23:25
	32	2013-09-21 18:20	2013-09-22 23:20
	33	2013-10-23 04:12	2013-10-24 11:37
	34	2013-11-04 20:00	2013-11-06 01:30
	35	2013-11-12 02:00	2013-11-13 03:00
	36	2013-11-14 09:00	2013-11-14 21:00
	37	2013-12-02 06:00	2013-12-04 07:40
	38	2014-02-06 11:34	2014-02-07 20:30
	39	2014-02-16 15:06	2014-02-17 16:15
	40	2014-03-08 02:38	2014-03-08 23:12
	41	2014-04-10 06:05	2014-04-10 15:35
	42	2014-04-12 11:40	2014-04-12 20:33
	43	2014-06-10 04:10	2014-06-10 23:50

	Candidate no.	Start date (UTC)	End date (UTC)
STEREO-B	44	2008-10-19 01:02	2008-10-20 11:32
	45	2008-12-31 02:00	2009-01-01 07:20
	46	2010-09-19 23:22	2010-09-20 06:45
	47	2010-12-02 09:55	2010-12-03 11:11
	48	2011-01-18 00:00	2011-01-18 09:38
	48	2011-03-07 19:10	2011-03-08 17:21
	49	2011-03-11 15:18	2011-03-12 12:00
	50	2011-04-01 04:00	2011-04-01 13:50
	50	2011-06-01 17:35	2011-06-02 18:00
	51	2011-06-17 07:40	2011-06-18 04:00
	52	2011-10-04 02:00	2011-10-04 12:40
	53	2011-12-02 16:03	2011-12-03 11:00
	54	2012-01-11 17:43	2012-01-12 13:42
	55	2012-01-17 07:30	2012-01-18 09:00
	56	2012-01-19 01:46	2012-01-19 16:43
	57	2012-03-09 01:00	2012-03-09 11:30
	58	2012-03-11 01:34	2012-03-12 21:51
	59	2012-03-30 01:37	2012-03-30 08:30
	60	2012-04-17 09:40	2012-04-18 09:05
	61	2012-05-09 13:30	2012-05-10 10:40
	62	2012-05-13 03:00	2012-05-14 04:30
	63	2012-06-18 23:47	2012-06-20 10:00
	64	2012-07-04 11:40	2012-07-05 12:50
	65	2012-07-24 20:00	2012-07-25 12:00
	66	2012-09-04 05:30	2012-09-05 20:58
	67	2012-09-23 23:38	2012-09-24 09:46
	68	2012-10-26 04:00	2012-10-27 10:00
	69	2012-11-04 01:22	2012-11-05 18:00
	70	2012-11-20 02:00	2012-11-20 12:40
	71	2012-11-28 07:37	2012-11-29 07:00
	72	2013-03-08 08:00	2013-03-10 08:45
	73	2013-04-09 23:40	2013-04-10 14:00
	74	2013-05-04 15:00	2013-05-06 09:40
	75	2013-06-02 12:15	2013-06-06 08:52
	76	2013-07-05 07:04	2013-07-07 01:47
	77	2013-08-22 13:00	2013-08-23 07:00
	78	2013-09-16 04:20	2013-09-17 00:25
	79	2013-10-08 17:25	2013-10-09 23:35
	80	2013-11-05 02:43	2013-11-05 23:47
	81	2013-11-06 13:38	2013-11-07 14:00
	82	2013-12-18 02:05	2013-12-20 15:00
	83	2013-12-21 08:25	2013-12-22 00:00
	84	2013-12-29 04:12	2013-12-30 14:00
	85	2014-04-01 04:53	2014-04-01 21:37
	86	2014-05-08 21:00	2014-05-10 08:23
	87	2014-06-10 00:00	2014-06-10 17:10

Table 1: Table showing the selection of the candidates with long and clear periods of BDE observed by STEREO-A and STEREO-B.

Flux Rope Catalogue

Table 2 shows a selection of periods observed by the STEREO mission presenting a clear and sustained smooth rotation was done by eye as explained in 4. Then, a series of fitting of the updated version of Hidalgo's model (see Section 4.2) was performed in order to obtain the different parameters.

STEREO	Beginning (UTC)	End (UTC)	ϕ (deg)	θ (deg)	z_0	B_0^{Θ}	B_0^{ζ}	C	η	α	λ	t_0 (days)
B	2007/05/22 07:17:00	2007/05/22 13:33:00	136,73	121,32	0,65	-6,5097E-16	-7,8274E-15	1,6177	0,017986	0,33537	-0,90568	5,5
A	2007/05/23 03:39:00	2007/05/23 12:05:00	15,46	121,8	-0,88	-1,6885E-16	7,8139E-17	0,52875	1,0404	-0,04128	-0,22505	8,6
A	2007/06/02 03:50:00	2007/06/02 08:14:00	62,51	47,05	1,55	1,4155E-15	6,5885E-16	2,4997	2,1651	-0,57295	-2,6597	5,5
A	2007/06/09 03:32:00	2007/06/09 09:13:00	62,43	178,15	0,04	-2,605E-14	-1,7303E-11	24,042	3,4432E-09	26,404	-119,23	3,1
A	2007/07/06 10:26:00	2007/07/07 00:29:00	110,46	131,77	-3,24	-2,0587E-14	-7,2535E-14	1,2417	6,3241	1,439	-11,764	5,5
A	2007/08/26 00:56:00	2007/08/26 08:41:00	73,36	121,87	5,44	-1,6487E-14	4,0623E-13	2,3527	6,312	41,756	-4,0696	63,5
A	2007/09/08 02:38:00	2007/09/08 08:01:00	165	44,45	-1,23	-3,349E-15	5,4457E-13	0,00913	1,9248	-0,00031	177,33	3,3
B	2007/11/18 19:24:00	2007/11/18 23:23:00	101,32	0,36	28,94	1,8434E-14	8,0646E-16	0,01206	3,3646E-08	-0,0154	-0,05398	7
A	2007/11/20 07:35:00	2007/11/20 20:40:00	72,86	156,36	-4,83	-1,1503E-16	7,2848E-12	1,079	14,694	1,649	9,831	15,7
B	2008/02/05 21:24:00	2008/02/06 08:25:00	57,46	105,53	1,69	8,1443E-16	2,0599E-14	2,6074	0,00033044	-0,52756	6,4003	6,6
B	2008/03/16 01:37:00	2008/03/16 07:52:00	101,4	89,4	7,19	5,1735E-15	4,1306E-13	2,6934	1,9529E-08	286,73	106,36	3,9
B	2008/03/20 10:43:00	2008/03/20 18:02:00	102,2	101,92	3,36	2,6647E-14	6,9886E-13	6,6446	1,1372E-06	-9,6057	58,839	3,6
A	2008/03/21 08:40:00	2008/03/21 18:27:00	51,45	3,84	32,14	4,7358E-15	4,5349E-16	0,69328	1,7468	-0,00463	-3E-05	52,1
A	2008/05/11 12:05:00	2008/05/12 03:28:00	125,19	98,02	-4,64	-7,9277E-13	1,6206E-12	1,3537	1,1838	80,069	1189,7	1,4
B	2008/05/16 05:37:00	2008/05/16 12:55:00	88,71	128,84	5,67	7,7979E-15	3,0424E-16	0,01345	14,558	0,00052	1,4114	6,2
B	2008/06/06 23:37:00	2008/06/07 12:06:00	164,98	99,43	0,37	1,3967E-16	-3,7012E-12	0,05156	8,2829	0,44484	-80,967	4,8
A	2008/07/05 12:42:00	2008/07/05 21:26:00	81,99	171,96	4,47	-1,0564E-14	-5,9574E-11	0,02146	12,166	-0,37051	-168,28	5,1
B	2008/07/11 02:28:00	2008/07/11 07:04:00	72,07	52,64	0,96	4,865E-14	2,1218E-12	0,15467	0,0017116	0,0584	1670,1	-2,3
A	2008/07/14 06:50:00	2008/07/14 14:01:00	137,7	49,28	1,92	5,2507E-15	-4,2292E-12	3,1754	6,6614	-3,2518	-30,381	8,3
A	2008/07/30 02:04:00	2008/07/30 08:19:00	112,55	91,05	-6,77	3,158E-14	-1,9677E-13	1,5405	0,75989	-68,691	-119,62	22,4
B	2008/08/15 15:36:00	2008/08/15 21:27:00	54,86	13,68	-0,04	2,8202E-14	-8,1545E-17	1,3811	9,8954	-15,31	0,86329	6,1
A	2008/09/04 14:19:00	2008/09/05 00:29:00	39,03	71,26	0,53	1,427E-14	1,8049E-13	0,16852	3,051	0,08521	46,695	3,7
A	2008/10/15 01:45:00	2008/10/15 13:24:00	141,99	146,84	2,75	7,0248E-16	-3,3772E-11	0,58366	12,891	-19,905	1,9426	6,5
B	2008/10/17 13:38:00	2008/10/18 00:45:00	110,08	175,5	-16,07	9,4278E-14	-3,6403E-14	1,8165	1,5296	-0,24524	-9,5285	7,5
B	2008/10/19 01:51:00	2008/10/19 14:52:00	165	99,28	0,45	6,7756E-16	5,9587E-09	0,01633	19,293	9,935	502,69	6,9
B	2008/10/23 14:05:00	2008/10/23 20:28:00	145,94	149,94	1,02	-1,8827E-15	4,3588E-16	2,7723	3,2163	-0,13424	-0,05039	5,4
A	2008/10/31 13:08:00	2008/10/31 16:08:00	129,52	41,84	1,76	-3,1166E-16	3,5771E-16	0,01378	2,5763	-0,0001	0,12443	3161,7
A	2008/11/07 02:36:00	2008/11/07 17:06:00	109,94	136,49	-0,94	-2,2031E-14	2,4636E-17	0,81748	1,3756	0,25373	-0,29521	4,8
B	2008/11/17 01:38:00	2008/11/17 08:28:00	110,83	2,21	4,47	-6,5257E-15	-8,1545E-17	1,444	5,261	0,65752	1,7007	13
A	2008/11/28 07:57:00	2008/11/28 16:25:00	68,02	77,07	3,36	5,6896E-16	-2,6125E-10	1,2042	17,445	-150,9	-33,224	28,3
B	2008/12/07 15:47:00	2008/12/08 12:32:00	63,23	166,98	-7,89	-6,7993E-16	3,9281E-10	0,07677	15,555	21,292	75,335	12,8
B	2008/12/16 18:04:00	2008/12/17 02:10:00	95,51	69,92	-3,21	1,1202E-15	-5,081E-12	2,1354	14,128	10,958	-35,129	5,5
B	2008/12/31 04:16:00	2008/12/31 10:30:00	112,3	92,25	-7,04	-6,7286E-15	1,7945E-10	1,0713	15,169	12500	263,15	8,8
B	2008/12/31 06:36:00	2008/12/31 21:00:00	100,88	128,23	0,33	-1,6709E-15	-3,0399E-14	2,9708	3,2241	-0,53474	0,76281	6,5
B	2009/01/13 12:06:00	2009/01/13 21:24:00	135,94	8,09	-12,33	1,6342E-16	6,635E-13	0,31838	5,7878	-0,64082	12,929	7
A	2009/01/21 16:57:00	2009/01/22 02:16:00	58,63	58,69	-5,98	2,3266E-16	-3,3778E-16	0,14073	14,531	440,61	-24,156	4,9
A	2009/01/26 01:57:00	2009/01/26 09:33:00	77,43	18,43	4,94	-1,3484E-15	1,6865E-11	8,9912	6,3116E-12	5,4391	70,741	0,4
A	2009/01/26 13:41:00	2009/01/27 00:15:00	159,67	71,9	0,49	-1,4256E-14	5,7414E-13	6,2351	1,82E-06	-2,2899	13,138	5,1
B	2009/02/02 13:23:00	2009/02/02 19:47:00	157,98	40,46	0,17	-3,3986E-15	2,309E-17	0,10672	1,8671	-0,00414	0,00062	19,3
B	2009/03/15 07:26:00	2009/03/15 16:25:00	125,85	44,31	5,04	-1,1605E-14	1,8746E-13	5,169	0,046555	2,483	13,045	2,2
B	2009/04/24 02:48:00	2009/04/24 11:32:00	100,21	169,63	-8,04	-1,565E-14	-3,392E-10	0,001	17,301	-0,0317	-51,299	3,7
A	2009/06/03 04:06:00	2009/06/03 16:49:00	134,55	125,8	1,75	1,707E-14	1,875E-11	0,001	9,1901	0,01168	181,18	4,4
B	2009/06/14 21:22:00	2009/06/15 03:52:00	17,32	37,57	21,48	5,133E-16	1,3297E-16	0,04884	1,4591E-07	0,01426	-0,3726	5,2
B	2009/06/19 09:33:00	2009/06/20 01:50:00	113,97	4,71	3,42	-1,379E-14	4,2411E-13	0,00143	1,6312	-0,00026	213	3,8

Table 2 continued from previous page

STEREO	Beginning (UTC)	End (UTC)	ϕ (deg)	θ (deg)	z_0	B_0^{Θ}	B_0^{ζ}	C	η	α	λ	t_0 (days)
A	2009/07/11 23:57:00	2009/07/12 16:02:00	133,56	84,05	-0,49	-5,9894E-15	7,4004E-12	0,11269	11,93	3,0249	31,154	6,6
A	2009/07/12 17:32:00	2009/07/13 04:42:00	58,04	4,68	30,86	2,8252E-16	8,7447E-14	0,06213	5,223	-0,00233	1,2604	-49,8
B	2009/07/16 21:24:00	2009/07/17 10:19:00	88,93	93,09	-7,16	-1,1899E-16	-9,2154E-12	21,494	18,24	-162,7	-40,516	5
B	2009/07/31 02:52:00	2009/07/31 08:21:00	84,62	142,79	0,14	-7,2267E-16	1,0016E-10	5,7712	12,187	-122,32	-52,765	4,9
B	2009/08/06 05:18:00	2009/08/06 09:43:00	94,53	179,47	-145,74	3,6894E-16	-6,4841E-11	0,21876	16,93	-0,02947	-1,3926	-3,3
B	2009/08/09 00:50:00	2009/08/09 10:08:00	79,64	83,08	-0,99	3,4622E-16	1,208E-10	0,03965	13,769	0,74426	201,58	5,1
A	2009/08/20 21:15:00	2009/08/21 08:12:00	103,95	49,06	2,03	1,0555E-15	6,5562E-16	3,0785	3,1075E-06	-0,56731	-1,022	5,5
B	2009/08/25 10:33:00	2009/08/26 01:02:00	48,07	60,51	0,62	2,1653E-16	5,8299E-15	0,31537	9,5965	0,43669	-0,08899	40,9
B	2009/08/26 04:19:00	2009/08/26 12:47:00	112,44	107,12	3,77	-6,3666E-16	-2,5517E-12	2,7549	11,982	23,719	-11,011	9,2
B	2009/08/30 20:05:00	2009/08/31 03:29:00	37,72	0,31	0,61	1,0452E-14	1,2697E-12	10,911	0,0012904	0,98461	44,418	7,7
B	2009/09/10 04:30:00	2009/09/10 17:54:00	154,22	111,57	0,53	-6,1246E-16	7,6891E-10	0,18397	20	212,76	21,197	11,6
B	2009/09/28 04:16:00	2009/09/28 11:23:00	78,88	32,73	1,8	4,6604E-15	5,4146E-11	0,02362	12,778	0,4277	122,01	-14,1
B	2009/10/03 05:57:00	2009/10/04 00:05:00	74,82	40,86	1,91	-2,2435E-14	-3,3107E-11	0,1095	9,8633	-0,63	-306,86	4,6
A	2009/10/17 01:43:00	2009/10/17 16:00:00	129,87	153,09	2,44	1,196E-16	6,1502E-16	0,83657	2,3598	0,08175	0,96523	16,2
A	2009/10/30 02:52:00	2009/10/30 14:23:00	144,57	34,09	2,68	-3,0296E-16	-2,5031E-12	0,88962	8,9742	-0,96941	-2,3397	23,6
A	2009/11/01 02:44:00	2009/11/01 07:41:00	15	171,2	37,07	6,0964E-14	2,3172E-13	3,3051	1,2768E-07	-0,11476	18,253	3,5
A	2009/11/01 18:53:00	2009/11/02 07:01:00	123,77	82,56	2,66	5,8082E-15	-2,7056E-11	2,5968	9,593	-24,733	-65,828	7,4
B	2009/11/10 19:09:00	2009/11/11 10:15:00	128,33	97,64	-6,71	-6,9703E-15	1,3614E-11	0,66748	11,015	410,02	94,182	6,8
A	2009/11/15 04:14:00	2009/11/15 12:28:00	26,41	179,5	25,49	1,1387E-13	5,0073E-16	0,8972	2,6299	-1,2271	4,6757	4,1
B	2009/11/27 13:33:00	2009/11/27 19:38:00	77,01	134,62	-3,27	3,753E-15	3,5863E-15	16,165	20	-0,15712	3,0117	-13,2
A	2009/12/09 12:46:00	2009/12/09 21:27:00	34,82	101,17	7,19	5,9083E-16	8,7186E-10	0,06777	20	-1160	27,225	11,1
B	2009/12/30 03:34:00	2009/12/30 08:49:00	95,6	36,03	0,41	1,803E-15	6,7278E-16	4,202	5,5521	0,23248	-2,6008	-38,3
B	2010/01/20 20:31:00	2010/01/21 05:29:00	160,37	97,8	0,22	1,0811E-16	1,6432E-11	0,12239	12,855	7,5988	34,012	2,8
B	2010/01/26 23:09:00	2010/01/27 09:45:00	70,65	88,1	5,38	-2,6862E-16	-4,1626E-11	0,29305	11,683	17,617	-155,01	13,8
A	2010/02/05 14:49:00	2010/02/05 20:34:00	106,28	64,81	0,6	4,6158E-16	2,1279E-17	3,6998	3,6086	-2,2795	-1,4	12,2
A	2010/03/05 19:31:00	2010/03/06 01:15:00	50,89	55,41	0,31	-3,3384E-16	1,8583E-13	5,6274	5,3531	-1,608	-3,1801	4,2
A	2010/04/19 16:29:00	2010/04/19 23:15:00	81,51	95,41	1,23	2,8651E-14	1,9615E-11	2,8137	10,039	-113,61	51,922	2,2
A	2010/04/23 08:11:00	2010/04/23 13:41:00	125,4	15	1	-2,5976E-14	-1,3992E-10	1,2559	11,155	93,494	-32,628	4,9
A	2010/05/31 06:03:00	2010/05/31 11:43:00	63,24	61,12	0,89	-1,1799E-14	-6,2954E-10	0,03482	14,242	-0,92854	-655,46	5,5
A	2010/06/04 09:28:00	2010/06/04 14:48:00	84,52	112,39	1,14	2,0502E-14	-6,9203E-12	3,8483	8,3993	54,154	116,99	-5,3
A	2010/06/17 02:03:00	2010/06/17 12:33:00	26,69	97,18	5,02	1,1458E-14	-8,8391E-11	0,01316	15,222	22,898	-56,019	4,7
B	2010/06/23 21:01:00	2010/06/24 08:25:00	24,19	62,52	-8,19	2,1477E-16	1,431E-11	0,08102	13,137	-415,33	11,578	5,6
A	2010/07/19 17:04:00	2010/07/19 21:51:00	54,67	94,28	0,68	-7,8831E-15	-1,1052E-10	2,1181	12,801	37,058	-68,768	4,8
B	2010/07/22 02:45:00	2010/07/22 10:01:00	91,83	1,03	-50,58	3,107E-13	2,4511E-13	0,82762	0,76911	-0,10455	24,639	3
B	2010/08/03 21:28:00	2010/08/04 06:56:00	109,63	128,88	-0	5,4E-16	-2,8498E-09	1,2715	10,847	68,486	-20273	1,7
A	2010/08/18 14:47:00	2010/08/18 23:23:00	68,3	3,28	38,64	-3,8548E-16	-1,3186E-13	0,31263	8,9895	0,01451	-0,17391	69
A	2010/08/21 02:35:00	2010/08/21 12:04:00	154,71	76,73	0,54	-1,829E-14	3,3767E-13	1,1086	4,3326	-1,1954	34,899	3,1
A	2010/08/31 01:59:00	2010/08/31 07:04:00	15	79,4	-7,7	4,7518E-16	-1,9348E-16	0,10517	13,042	-1949,4	4,5158	-18,9
A	2010/09/07 18:58:00	2010/09/08 08:34:00	143,8	77,1	6,7	-1,0129E-15	-1,2865E-13	0,32302	2,2018	2,9908	-23,014	3,8
A	2010/09/11 17:26:00	2010/09/11 23:28:00	70,95	24,17	1,68	-8,2278E-15	5,9553E-14	3,36	3,9706	0,52039	9,2533	-27,1
A	2010/09/12 10:46:00	2010/09/13 05:13:00	158,94	75,19	9,93	-1,1744E-14	2,9063E-11	0,001	18,541	-5,7075	5,2653	7,6
B	2010/09/16 11:54:00	2010/09/16 16:41:00	134,17	9,49	10,81	-3,1259E-16	-2,1675E-14	4,5043	0,92911	0,00544	-0,03789	-23,5
A	2010/09/18 07:30:00	2010/09/18 21:11:00	74,9	12,86	10,02	-3,0291E-16	2,9203E-10	0,13112	20	34,472	3,469	5,8

Table 2 continued from previous page

STEREO	Beginning (UTC)	End (UTC)	ϕ (deg)	θ (deg)	z_0	B_0^{Θ}	B_0^{ζ}	C	η	α	λ	t_0 (days)
B	2010/10/30 19:01:00	2010/10/31 06:07:00	25,22	70,4	0,62	-3,0014E-16	1,8833E-13	0,0086	3,148	0,00056	53,68	28,4
B	2010/11/08 07:21:00	2010/11/09 09:05:00	135,44	120,24	3,15	1,4239E-14	-7,9134E-13	0,8891	5,106	-0,1905	-37,752	-8,9
B	2010/11/20 10:19:00	2010/11/21 02:11:00	90	90	1	1,6691E-14	6,0729E-16	7,0138	16,026	3584,3	10,805	4
B	2010/11/30 20:35:00	2010/12/01 01:52:00	152	35,1	0,53	4,5233E-15	6,7377E-13	0,02887	11,41	1,9117	-0,04806	-24,5
B	2010/12/02 12:32:00	2010/12/02 22:30:00	165	146,78	0,07	1,3638E-14	-1,6695E-16	0,00484	8,1265	-0,14967	-0,17799	6,2
A	2010/12/15 10:37:00	2010/12/15 20:35:00	122,09	124,3	0	3,2012E-15	4,4583E-12	0,23139	5,6517	-0,01934	376,29	61,3
B	2010/12/17 08:01:00	2010/12/18 04:01:00	82,13	15,67	21,23	-1,74E-16	-2,0923E-10	1,2442	14,042	0,41061	-9,6774	4,1
B	2010/12/26 18:30:00	2010/12/27 03:01:00	82,88	114	0,57	2,1818E-16	2,9804E-16	7,8951	4,446	5,2223	3,748	-10,2
A	2011/01/07 06:45:00	2011/01/07 15:21:00	154,04	56,32	1,01	6,7047E-16	5,6808E-10	0,03535	15,74	-20,141	63,9	3,9
A	2011/01/08 06:48:00	2011/01/08 12:39:00	74,17	8,56	3,18	-2,1895E-16	-2,28E-15	3,6391	7,4563E-09	0,04767	-0,17327	-13
A	2011/02/01 12:51:00	2011/02/01 23:54:00	119,63	74,42	7,67	7,7836E-16	2,6793E-12	6,7854	0,20242	-7,5984	1,1372	14,2
A	2011/02/02 04:45:00	2011/02/02 10:05:00	15,82	127,92	0,07	-7,9894E-15	-2,8583E-16	1,2197	11,027	132,43	0,3165	5,4
A	2011/02/03 10:10:00	2011/02/03 15:24:00	105,8	145,68	1,15	6,2286E-16	2,1331E-13	2,9827	8,3284	-0,61869	2,7727	67,7
A	2011/02/03 21:08:00	2011/02/04 02:47:00	49,64	123,88	-2,75	5,7104E-14	6,8769E-13	1,5273	10,794	-81,622	3,0371	-15,3
A	2011/02/26 07:25:00	2011/02/26 12:19:00	108,75	17,8	1,9	-8,4973E-16	-6,5187E-15	6,7097	4,6441E-07	-0,482	3,8564	9,8
B	2011/02/26 16:22:00	2011/02/27 01:34:00	87,64	110,21	0,34	-1,1994E-14	-3,4769E-11	2,4129	11,899	201,21	-34,397	3,4
B	2011/02/27 04:08:00	2011/02/27 18:34:00	136,26	134,99	-4,91	2,0626E-16	-2,1072E-10	0,12602	13,554	-12,785	-103,4	16,5
B	2011/03/08 05:25:00	2011/03/08 17:03:00	67,08	64,12	-6,97	4,6895E-17	-3,9592E-11	0,12334	14,242	725,71	-25,16	3,8
B	2011/03/11 17:58:00	2011/03/12 03:12:00	98,69	69,21	6,95	1,1435E-13	-1,4989E-12	3,9605	0,00016021	-87,265	-81,16	2,7
B	2011/03/12 07:58:00	2011/03/12 11:22:00	64,05	103,8	1,75	1,8666E-13	7,4801E-11	7,5595	3,8605E-10	520,85	1324,7	0,2
A	2011/03/12 09:14:00	2011/03/12 16:07:00	114,7	13,46	0,39	-1,2738E-14	-1,3157E-11	2,2442	11,66	24,327	60,204	6,9
A	2011/03/20 02:38:00	2011/03/20 10:00:00	38,1	103,66	1,47	-2,0821E-14	-4,7014E-13	0,03898	1,6746	0,0004	-259,78	3,4
B	2011/03/21 11:17:00	2011/03/21 18:38:00	102,41	102,47	-0,03	8,4591E-15	6,8721E-11	0,12261	11,347	0,25572	381,45	11,6
A	2011/03/23 07:45:00	2011/03/23 15:48:00	140,29	1,16	-65,05	1,3526E-16	-2,3166E-15	0,14585	1,444	0,00576	0,18646	-3,2
B	2011/03/24 10:54:00	2011/03/24 19:08:00	83,42	79,67	2,09	-3,0546E-14	-7,8207E-12	3,478	6,8817	-18,743	18,192	3
B	2011/03/28 19:14:00	2011/03/29 10:08:00	108,88	91,65	-6,79	-2,3961E-14	1,5437E-16	15,145	20	79,929	-34,776	3,8
B	2011/04/01 03:36:00	2011/04/01 12:14:00	155,22	130,03	0,02	-6,4338E-14	1,4436E-10	0,001	8,3006	0,02555	966,05	3,2
B	2011/04/01 22:10:00	2011/04/02 07:40:00	130,09	121,97	2,35	3,2009E-15	2,0199E-11	0,12547	6,0623	0,49038	1128,5	3,2
B	2011/04/04 17:18:00	2011/04/05 01:41:00	15	72,84	-8,64	-2,9128E-14	-1,7214E-14	0,33289	0,0019609	1,9581	0,95889	4
B	2011/04/05 04:53:00	2011/04/05 14:16:00	81,58	28,59	6,79	2,1476E-14	-1,4101E-11	0,08015	9,3919	0,00022	-108,59	3,6
A	2011/04/06 09:43:00	2011/04/06 15:50:00	109,38	44,46	7,61	-3,6233E-16	1,7248E-12	1,155	6,5566	-0,00046	16,704	67,9
A	2011/04/12 04:21:00	2011/04/12 10:36:00	17,03	114,95	0,17	3,765E-15	1,8406E-11	0,05742	12,395	2,4389	21,346	4,1
A	2011/04/15 18:54:00	2011/04/16 02:07:00	17,84	0,03	-3,36	1,8226E-14	-1,3755E-17	0,43384	3,5629	-0,93197	-1,6288	9,6
B	2011/04/17 12:34:00	2011/04/17 20:39:00	145,75	69,34	0,11	2,1709E-16	4,069E-12	15,083	6,0796E-12	-5,0437	-2,0593	6,6
A	2011/04/22 02:52:00	2011/04/22 10:55:00	83,38	144,37	-0,07	-1,1224E-14	-1,0629E-16	10,037	0,90614	-0,12957	-8,508	6,1
A	2011/04/22 16:21:00	2011/04/22 23:04:00	157,43	51,49	-0,05	7,9392E-15	7,7893E-13	0,48551	6,6849E-11	-0,04073	605,37	3,9
A	2011/04/23 10:21:00	2011/04/24 00:00	101,5	120,37	1,39	-1,8172E-14	6,8028E-16	4,7639	2,688	0,64403	-19,418	4,7
A	2011/04/28 13:00:00	2011/04/28 19:54:00	68,6	31,1	1,15	1,3549E-14	-2,9625E-13	3,8574	4,2729	-1,6018	-16,658	4,7
B	2011/05/04 21:37:00	2011/05/05 07:58:00	110,97	94,24	-4,68	1,068E-15	-5,1338E-09	0,27454	18,34	1129,1	-1008,9	-7,4
A	2011/05/22 09:36:00	2011/05/22 16:52:00	122,88	66,02	0,83	-5,6281E-16	3,7321E-13	3,6102	3,7549	-14,994	6,2624	3,4
B	2011/06/02 02:53:00	2011/06/02 07:26:00	126,85	60,47	6,22	6,3026E-16	7,2605E-11	0,02677	18,845	68,683	-5,5803	6,3
A	2011/06/06 17:10:00	2011/06/07 00:05:00	165	95	0,61	3,3368E-14	4,9799E-13	0,35684	4,4214	0,47438	64,392	2,1
B	2011/06/08 10:26:00	2011/06/09 00:35:00	69,1	49,28	10,27	5,5833E-15	-2,838E-16	0,02621	0,1419	0,01832	-0,13978	10,4

Table 2 continued from previous page

STEREO	Beginning (UTC)	End (UTC)	ϕ (deg)	θ (deg)	z_0	B_0^{Θ}	B_0^{ζ}	C	η	α	λ	t_0 (days)
A	2011/06/16 21:15:00	2011/06/17 06:43:00	75,94	32,06	1,39	-1,5017E-16	7,3999E-12	0,001	6,0208	0,00213	531,85	5,7
B	2011/06/17 09:02:00	2011/06/17 16:41:00	165	62,54	-4,46	-3,0407E-16	4,9291E-16	12,999	20	0,79318	-14,935	-3,8
B	2011/06/25 13:11:00	2011/06/25 21:28:00	24,59	2,6	0,7	7,3783E-16	1,9601E-11	6,6512	7,955	38,761	198,84	1,4
B	2011/06/30 15:20:00	2011/06/30 22:37:00	15,46	23,48	2,5	5,4086E-15	-7,203E-14	4,2093	1,6894	-0,14553	-3,7882	24,7
A	2011/07/07 00:24:00	2011/07/07 08:01:00	165	103,54	-4,23	-2,8141E-16	-1,6972E-14	2,5701	6,2665	0,10417	-5,5701	-74,2
B	2011/07/08 03:19:00	2011/07/08 14:58:00	117,07	1,77	-60,51	2,8413E-16	2,8587E-15	6,0413	3,7328	-3E-05	-0,05232	5,5
A	2011/07/13 05:47:00	2011/07/13 12:11:00	101,63	132,36	2,54	7,6078E-15	-9,8487E-15	0,88123	2,1254E-05	0,08072	-5,4544	4,5
A	2011/07/14 09:29:00	2011/07/14 15:35:00	47,06	11,26	2,62	2,7007E-17	-1,2528E-14	0,40778	3,672	0,21657	-1,4743	2,5
B	2011/07/23 08:11:00	2011/07/23 11:41:00	103,61	95,73	0,03	4,0223E-16	-1,5617E-14	15,36	5,6026E-08	-0,09405	3,7043	10,2
B	2011/07/26 01:52:00	2011/07/26 08:27:00	69,42	92,1	6,86	2,774E-14	5,0173E-11	8,0212	0,00013809	-4301,5	348,88	2,4
A	2011/08/13 23:19:00	2011/08/14 11:39:00	145,02	136,22	-6,2	-2,8019E-15	1,061E-12	0,07441	2,7966	0,03907	219,27	8,6
B	2011/08/21 00:15:00	2011/08/21 12:19:00	108,68	66,96	2,32	1,3716E-15	1,9327E-16	2,3442	4,3481	18,213	-6,8422	3
A	2011/09/10 20:06:00	2011/09/11 01:56:00	47,83	57,07	-4,69	1,0963E-14	4,8019E-12	0,00884	9,9966	-3,0315	30,317	-6,6
B	2011/10/03 11:42:00	2011/10/04 03:06:00	118,78	105,56	-5,35	-5,3593E-17	-3,1848E-10	1,043	12,628	218,36	-1515,1	6,4
B	2011/10/04 03:25:00	2011/10/04 10:39:00	71,22	170,12	-17,42	-1,4581E-15	-5,1897E-11	0,06884	10,838	-8,5632	-79,821	4,6
A	2011/10/14 22:34:00	2011/10/15 04:11:00	84,89	150,54	0,32	5,666E-15	2,5592E-14	4,2344	2,0464	-0,16999	0,22261	6,7
B	2011/10/18 20:30:00	2011/10/19 03:03:00	164,98	166,3	-11,51	-3,8181E-14	2,6882E-13	12,518	5,2284	-0,0297	185,99	3,7
B	2011/10/30 01:00:00	2011/10/30 18:51:00	94,57	70,75	0,95	-8,1181E-15	6,1404E-16	3,8345	4,2097	-8,504	-0,79868	3,3
B	2011/11/07 03:25:00	2011/11/08 02:37:00	138,56	134	-2,76	-3,5359E-14	2,5648E-13	0,74996	0,91294	0,28398	192,69	3,4
A	2011/11/22 08:31:00	2011/11/22 16:05:00	159,35	71,64	-0,54	2,1185E-16	-8,2895E-14	0,91461	1,3231	0,09844	-65,611	4,4
A	2011/11/27 16:29:00	2011/11/28 03:41:00	69,05	178,49	-64,11	-1,1317E-16	7,701E-16	0,15388	1,8586E-09	0,00146	0,29296	4,5
A	2011/12/18 06:06:00	2011/12/18 13:44:00	160,19	143,59	-1,85	-7,6908E-15	2,2587E-12	0,95571	0,81089	0,05906	1783,1	6,6
B	2011/12/19 12:37:00	2011/12/19 19:27:00	109,49	103,91	0,09	1,8309E-17	-5,094E-13	1,5857	10,65	-2,9527	-0,35601	12,1
B	2011/12/21 09:36:00	2011/12/21 15:56:00	143,34	98,06	-7,35	1,0668E-15	5,1456E-09	0,04404	19,113	49794	187,47	4,2
B	2011/12/23 13:54:00	2011/12/23 20:36:00	70,69	27,87	0,55	-1,2695E-15	-7,6445E-12	0,10014	13,515	0,54289	-9,4319	14,8
B	2011/12/25 11:34:00	2011/12/25 21:48:00	23,29	21,61	-10,27	-8,4648E-17	-1,2443E-15	0,26985	5,9189	5,0542	-3,3149	15,3
B	2011/12/27 12:43:00	2011/12/27 20:38:00	38,83	69,83	-5,45	-1,8703E-14	-1,75E-16	13,01	20	0,00037	9,7872	8,5
A	2012/01/05 21:29:00	2012/01/06 10:04:00	98,03	77,78	0,94	-3,4247E-16	6,5815E-16	2,5267	7,0666	-0,53142	0,03725	-214,1
B	2012/01/06 01:24:00	2012/01/06 09:22:00	59,04	55,86	-0	9,1428E-13	6,185E-12	8,0586	7,0123	-58,223	967,7	0,5
B	2012/01/07 19:51:00	2012/01/07 23:21:00	67,11	99,44	0,26	4,2978E-15	8,5524E-11	0,05575	15,613	3,7388	51,727	-17,4
B	2012/01/11 06:04:00	2012/01/11 10:49:00	165	52,12	-8,62	3,8766E-17	4,3114E-17	1,0941	5,7106	7,712	-6,4114	-2,7
B	2012/01/17 13:53:00	2012/01/18 07:57:00	114,27	71,94	2,87	3,3223E-17	1,2225E-15	1,7557	5,249	6,2627	-1,0982	10,1
B	2012/01/19 02:51:00	2012/01/19 09:13:00	66,4	32,75	-3,99	2,6824E-16	6,5709E-16	9,8745	3,138	0,00013	-3,4066	-12,8
B	2012/01/21 03:38:00	2012/01/21 16:23:00	165	111,16	-0,15	-1,0609E-15	1,0164E-10	0,04968	14,628	0,59681	51,409	11,3
B	2012/01/21 18:19:00	2012/01/22 10:29:00	30,02	18,07	9,18	5,0959E-15	2,1053E-15	3,4412	0,36266	-3E-05	-1,4708	4,1
A	2012/02/20 11:11:00	2012/02/20 19:05:00	136,99	32,89	0,03	-3,994E-15	1,2074E-13	6,6139	1,1223	-1,5651	3,4944	3,8
A	2012/02/21 05:38:00	2012/02/21 08:57:00	75,37	0	3,7	2,1308E-13	-3,3268E-12	3,4454	9,3081E-12	-2,838	-2262,1	1,9
A	2012/03/03 12:47:00	2012/03/03 18:01:00	72,91	76,44	0,66	1,1705E-15	-2,2091E-12	0,3272	7,0119	-0,40223	-71,29	2,3
A	2012/03/04 11:51:00	2012/03/04 21:04:00	83,58	137,42	0,32	-1,8758E-16	7,5552E-16	3,6895	0,61692	-0,01124	-0,16368	-97,1
B	2012/03/09 07:06:00	2012/03/09 11:16:00	26,84	52,3	-5,01	3,3409E-14	4,5453E-13	6,1934	0,15401	-21,879	-2,6999	7,6
B	2012/03/11 06:43:00	2012/03/11 19:56:00	33,33	144,24	-10,38	-3,3172E-16	3,9181E-10	0,02003	13,646	-70,309	17,482	3,4
B	2012/03/12 07:34:00	2012/03/12 21:12:00	30,29	124,74	-2,54	8,9376E-16	4,1735E-10	0,03122	14,952	21,782	90,846	4
B	2012/03/16 09:48:00	2012/03/16 17:43:00	82,84	145,76	0,17	6,4827E-15	-2,5161E-18	2,4131	17,225	-218,42	164,31	6,5

Table 2 continued from previous page

STEREO	Beginning (UTC)	End (UTC)	ϕ (deg)	θ (deg)	z_0	B_0^{Θ}	B_0^{ζ}	C	η	α	λ	t_0 (days)
A	2012/03/17 02:28:00	2012/03/18 05:14:00	137,68	99,51	6,42	-1,4275E-15	1,6599E-13	1,7598	3,2391	0,61243	5,0705	10,1
A	2012/03/19 06:48:00	2012/03/19 15:32:00	65,65	51,95	2,73	-2,539E-14	-8,7366E-11	0,75059	12,612	217,39	-74,082	12,7
A	2012/03/19 12:18:00	2012/03/19 15:29:00	63,76	9,43	1,36	1,6007E-16	-2,3332E-13	0,74528	18,059	-19,959	-5,1934	10
A	2012/03/20 05:13:00	2012/03/20 14:13:00	46,69	50,35	2,34	2,0089E-14	-4,1281E-09	0,00519	16,27	-0,06355	-689,2	3
B	2012/03/29 01:53:00	2012/03/29 07:09:00	98,94	103,25	0,32	2,9905E-16	9,0339E-14	3,7188	6,2331	-1,2848	-0,54345	47,5
B	2012/03/29 11:49:00	2012/03/29 17:54:00	15,18	44,48	-0,83	4,9772E-14	-1,5708E-14	24,811	20	-0,88476	-10,535	1,5
A	2012/04/17 10:40:00	2012/04/18 02:06:00	129,65	148,89	3,19	-5,6282E-15	-7,5913E-15	0,0331	8,3426	-0,14467	1,2782	9,2
B	2012/04/17 22:37:00	2012/04/18 08:20:00	48,83	36,08	1,51	-2,2822E-18	-6,6091E-17	7,1133	0,44337	0,07053	0,98576	7,4
A	2012/04/19 13:41:00	2012/04/19 20:22:00	52,93	58,24	-1,65	-1,2477E-15	-2,971E-13	1,611	11,593	-6,7531	-0,21834	-30
B	2012/04/21 08:55:00	2012/04/21 14:18:00	163,16	120,58	-2,08	-1,9339E-14	-5,9163E-09	0,01131	15,662	15,105	-645,02	4,5
B	2012/05/08 19:14:00	2012/05/09 02:07:00	116,88	14,31	1,53	-2,7293E-14	-6,3255E-13	2,664	4,0147	-7,114	-5,8082	3,3
B	2012/05/09 22:41:00	2012/05/10 09:04:00	132,03	169,21	-1,2	-6,2189E-15	9,7069E-12	0,01453	0,077551	0,00145	7664,4	3,3
A	2012/05/19 01:35:00	2012/05/19 14:16:00	144,04	115,65	-10,5	7,1282E-14	1,5723E-15	0,83472	1,967	-3,3808	2,0122	3
A	2012/05/28 09:16:00	2012/05/28 14:46:00	58,15	62,46	4,56	-5,5086E-13	5,4626E-12	3,7257	1,4264	83,465	643,32	1,6
A	2012/05/28 19:18:00	2012/05/29 06:25:00	26,74	102,52	4,95	-3,2116E-14	2,3399E-15	0,87897	0,00016756	-2,2188	-12,152	2,6
B	2012/06/05 14:57:00	2012/06/05 20:06:00	136,75	40,35	-1,41	1,0892E-14	1,7464E-14	0,00534	2,2192	-0,21764	13,046	11,4
B	2012/06/19 13:45:00	2012/06/20 07:09:00	100,99	108,71	-1,23	-1,2137E-14	-2,0766E-11	0,01014	1,0533	0,00122	-14485	9,6
A	2012/06/20 10:28:00	2012/06/21 00:59:00	73,76	148,48	-4,09	-9,1873E-15	3,128E-14	0,81505	2,9953	0,24463	13,315	-13,2
B	2012/06/28 09:32:00	2012/06/29 04:20:00	16,95	90,88	1,42	-7,134E-15	-1,3473E-14	0,52915	2,1391E-06	-0,07783	-11,115	4,6
B	2012/07/04 16:44:00	2012/07/05 08:48:00	142,14	108,03	1,64	-5,1839E-14	8,4558E-14	3,2334	5,5174E-09	0,02901	3,8416	3,4
A	2012/07/11 18:32:00	2012/07/12 07:25:00	126,7	0,11	8,24	1,1695E-14	2,7746E-14	2,9809	0,00011763	0,00112	1,1733	2,8
A	2012/07/16 10:50:00	2012/07/16 15:46:00	15,05	0	8,74	7,3644E-16	3,4035E-13	4,4554	1,1102E-15	0,16161	37,987	3,3
A	2012/07/16 21:10:00	2012/07/17 02:59:00	26,39	0,01	21,44	-3,3105E-13	-7,3291E-14	1,9828	1,7335	0,51564	-24,498	-6,8
A	2012/07/21 14:00:00	2012/07/22 02:12:00	114,13	55,24	1,12	7,008E-15	5,2117E-16	1,2809	6,1332	-2,6343	-2,1271	5,2
A	2012/07/24 04:35:00	2012/07/24 22:58:00	45,98	81,83	-0,02	1,4197E-13	4,83E-16	2,7097	2,1071	-6,5735	122,69	2,2
B	2012/07/24 20:52:00	2012/07/25 04:54:00	109,24	87,16	-0,36	3,8483E-14	1,3895E-13	12,896	3,0561	-20,077	-75,596	0,4
B	2012/07/28 17:30:00	2012/07/29 00:44:00	142,4	81,64	2,23	-2,001E-14	2,3924E-10	7,6718	8,7018E-09	-885,36	2238,4	0,4
A	2012/08/06 04:28:00	2012/08/06 13:07:00	85,84	151,95	-4,01	9,0416E-15	2,6521E-09	0,001	18,518	1,864	331,92	3,2
B	2012/08/22 18:18:00	2012/08/23 08:02:00	137,23	100,83	-7,74	3,5821E-16	-1,3546E-12	0,11213	11,196	107,81	0,63173	10,6
B	2012/08/24 22:44:00	2012/08/25 02:16:00	163,92	180	-0	4,4967E-14	2,7763E-12	3,563	11,401	-75,354	10,711	1
B	2012/08/31 11:15:00	2012/08/31 17:25:00	97,47	91,12	-7,46	-4,7911E-15	-7,4514E-12	8,7686	20	305,91	-77,762	9,2
B	2012/09/03 13:59:00	2012/09/03 17:09:00	118,75	29,52	-0,78	2,0108E-14	1,3874E-13	0,69919	0,31679	0,05099	99,912	2,7
A	2012/09/09 00:40:00	2012/09/09 09:19:00	125,48	5,55	-65,36	-3,6185E-16	-1,9896E-12	2,826	9,6267	0,00184	-2,7564	18,8
B	2012/09/10 02:08:00	2012/09/10 06:56:00	39,26	4,54	5,98	2,5565E-14	-3,3444E-14	0,86545	1,5739	0,01557	-8,4184	1,6
A	2012/09/12 15:06:00	2012/09/12 22:12:00	15	97,15	-0,51	4,4314E-16	2,0299E-17	2,0861	6,0286	-0,50545	3,1983	-5,2
B	2012/09/15 06:56:00	2012/09/15 18:58:00	161,38	119,64	0,99	-7,0285E-14	-3,9708E-10	0,04598	11,006	-11,267	-828,18	0,7
A	2012/09/20 16:30:00	2012/09/21 08:24:00	163,46	108,09	-6,23	-6,2504E-16	2,3034E-14	1,8861	0,88298	0,96172	9,132	19,1
B	2012/09/23 12:05:00	2012/09/23 19:55:00	81,59	64,44	0,51	-1,1071E-13	-1,5833E-13	6,9263	1,9845E-06	5,4189	115,42	0,7
A	2012/09/23 22:42:00	2012/09/24 07:10:00	149,55	75,8	0,17	1,2988E-15	2,1528E-11	0,022	9,123	0,083	303,62	5,3
B	2012/09/24 00:38:00	2012/09/24 09:41:00	65,81	66,58	2,52	-2,1753E-13	2,6223E-10	2,2112	8,9819	1037,4	1108,9	0,5
B	2012/09/24 18:54:00	2012/09/24 21:15:00	132,74	0,02	0,99	-7,036E-14	3,8892E-10	0,09994	5,6847	-0,76417	12381	1,8
B	2012/09/26 14:30:00	2012/09/27 03:21:00	93,67	110,51	-3,61	-1,5112E-13	-1,0655E-09	0,03165	13,878	69,458	-1634,2	1,4
A	2012/10/05 16:14:00	2012/10/06 01:01:00	59,7	28,68	6,32	-8,492E-14	5,2117E-16	1,0389	5,95	17,103	17,34	3,5

Table 2 continued from previous page

STEREO	Beginning (UTC)	End (UTC)	ϕ (deg)	θ (deg)	z_0	B_0^{Θ}	B_0^{ζ}	C	η	α	λ	t_0 (days)
A	2012/10/06 03:51:00	2012/10/06 16:09:00	145,73	125,45	-1,91	-5,4485E-14	-6,4149E-14	1,103	2,757E-06	0,74205	-40,147	6,3
B	2012/10/08 18:26:00	2012/10/09 00:00	148,88	101,84	0,1	5,5289E-15	1,8417E-13	5,1303	7,5237	-0,84675	7,0549	5,8
A	2012/10/12 03:07:00	2012/10/13 01:35:00	74,71	160,94	-3,85	8,0057E-16	-5,8331E-12	0,001	10,788	-0,00705	-30,176	17,7
B	2012/10/13 07:55:00	2012/10/13 12:04:00	165	0,22	-0,09	2,4995E-13	-2,6453E-11	0,00023	4,6367	963,46	956,37	16,7
B	2012/10/17 18:08:00	2012/10/17 23:07:00	93,07	75,64	-0,91	-8,183E-15	5,3335E-17	18,479	20	0,04491	3,8294	-7,7
A	2012/10/23 21:30:00	2012/10/24 01:19:00	50,35	40,42	0,33	1,3252E-15	4,0148E-16	0,75636	10,553	2,4278	1,0119	8,1
B	2012/10/26 10:50:00	2012/10/27 00:00	115,57	82,32	1,39	7,801E-15	-7,9093E-12	3,1618	8,2521	-0,56225	-30,279	-10,3
A	2012/10/26 13:11:00	2012/10/26 20:03:00	18,24	44,81	0	1,8455E-13	1,7539E-12	1,6877	1,5137	-1,1396	1351,4	-5,1
A	2012/10/26 22:48:00	2012/10/27 09:40:00	48,57	133,51	0,52	8,8024E-17	4,7035E-12	0,01003	1,0337E-07	0,0007	3739,6	6,5
A	2012/10/27 00:34:00	2012/10/27 07:15:00	111,89	109,23	2,65	-3,2665E-14	4,6886E-10	0,11522	11,609	-10,789	1945,6	3,7
A	2012/11/01 17:22:00	2012/11/01 23:39:00	23,13	160,11	1,06	6,1586E-15	-5,6004E-11	0,4879	7,4146	-13,998	-16,596	5,7
B	2012/11/04 04:07:00	2012/11/04 22:38:00	109,97	120,06	2,06	1,3858E-15	4,9053E-16	3,7562	7,6944	-1,1121	10,147	7,5
B	2012/11/05 04:55:00	2012/11/05 16:47:00	107,11	94,68	0,96	9,7157E-16	-1,3665E-11	5,0117	7,2985	53,971	-18,309	0,7
B	2012/11/12 01:37:00	2012/11/12 15:37:00	82,27	97,66	-1,45	1,5584E-15	3,5466E-15	10,4	11,045	-0,26129	3,1248	7,7
A	2012/11/12 15:36:00	2012/11/13 14:03:00	94,1	36,85	2,62	-7,4134E-17	-6,9055E-14	7,0571	1,7392E-09	-0,99398	2,5413	4,7
A	2012/11/14 11:18:00	2012/11/15 02:07:00	157,93	101,95	1,33	-4,7179E-14	2,7978E-13	0,38178	1,1053	-0,16197	162,33	3,5
B	2012/11/19 18:02:00	2012/11/19 23:15:00	124,84	137,97	-0,72	1,4822E-14	1,419E-14	15,758	13,128	-0,95409	13,312	-3,7
B	2012/11/20 03:24:00	2012/11/20 11:49:00	96,17	44,41	-8,34	3,7457E-14	-2,5004E-10	0,07622	11,27	-16,605	-399,88	2
A	2012/11/26 15:32:00	2012/11/26 23:54:00	142,67	43,77	-3,56	-8,1919E-16	-6,5155E-10	0,00569	16,019	-15,456	-35,818	3
B	2012/12/04 04:38:00	2012/12/04 11:03:00	93,26	22,4	1,33	-7,7507E-15	-2,4745E-13	0,35764	3,5262	0,06421	-50,82	3,8
B	2012/12/17 00:13:00	2012/12/17 06:39:00	77,93	14,83	10,77	1,8864E-14	2,4987E-11	0,006	10,044	0,01175	99,661	5
B	2012/12/20 00:54:00	2012/12/20 08:01:00	116,83	90,14	7,43	5,2151E-16	-1,638E-11	0,001	7,8905	-9,2948	72,706	4,5
B	2012/12/25 16:28:00	2012/12/25 21:10:00	162,95	112,48	0,35	7,5604E-15	-8,6371E-17	5,0155	0,00029762	-0,30639	2,2456	-5,9
B	2013/01/02 10:14:00	2013/01/03 00:00	24,03	139,56	-2,84	1,6055E-15	6,7675E-15	2,8102	2,4365	0,03051	5,5172	5,7
B	2013/01/06 08:33:00	2013/01/06 13:37:00	98,43	48,63	1,31	8,9645E-15	-9,4488E-14	5,792	1,2147E-05	-0,57725	-9,9488	6,8
A	2013/01/09 13:25:00	2013/01/10 15:26:00	110,74	103,71	4,58	1,184E-15	-2,1757E-12	1,9783	8,611	-3,0811	-0,92806	10,7
B	2013/01/15 22:32:00	2013/01/16 06:40:00	146,61	103,55	-2,68	-2,7909E-15	-1,0189E-11	0,00101	11,423	-0,00761	-45,835	-13,6
B	2013/01/23 08:15:00	2013/01/23 11:43:00	129,17	40,63	-1,96	-1,4374E-15	2,4505E-12	8,3367	1,657E-07	2,8676	15,486	8,6
A	2013/02/09 00:46:00	2013/02/09 09:00:00	40,12	38,75	1,57	-1,8547E-16	7,0142E-16	2,535	1,4393E-08	-0,09578	-1,4976	7,6
B	2013/02/19 01:41:00	2013/02/19 05:16:00	62,04	35,92	31,84	6,1265E-16	4,4503E-16	0,20984	20	-18,207	0,76112	-4,1
A	2013/02/19 10:47:00	2013/02/19 21:14:00	128,59	121,16	-4,53	3,8893E-16	2,2674E-09	0,52348	11,57	-230,45	9653,1	2,6
A	2013/02/19 22:37:00	2013/02/20 05:59:00	97,72	109,75	0,83	1,0345E-15	3,1767E-12	4,8062	7,482	-10,975	5,1855	25
A	2013/03/02 05:16:00	2013/03/02 11:38:00	134,87	102,97	-0,18	2,2796E-14	-7,0277E-14	2,6448	2,9178	-0,3725	-67,583	2,2
A	2013/03/03 22:35:00	2013/03/04 08:07:00	99,61	64,04	0,57	-8,7997E-15	4,1471E-12	3,278	9,9057	3,5053	33,837	6
B	2013/03/07 19:08:00	2013/03/08 06:48:00	107,81	88,61	6,23	-2,9147E-15	-2,3229E-09	1,0463	16,343	6628,4	-547,28	3,4
B	2013/03/08 23:01:00	2013/03/09 03:30:00	43,06	112,41	0,31	1,728E-17	1,1296E-12	0,15586	1,1102E-15	-0,0211	895,28	-4,9
B	2013/03/21 11:43:00	2013/03/21 16:02:00	76,73	76,56	4,19	2,3577E-16	-3,9173E-09	0,18055	20	-125,89	-237,78	82
B	2013/03/24 08:18:00	2013/03/24 12:55:00	124,38	0,83	12,38	5,9875E-17	6,8068E-15	0,70324	2,7692	-0,0152	1,0736	-41,3
A	2013/03/26 14:32:00	2013/03/26 19:45:00	131,32	13,57	2,84	4,7744E-16	1,0456E-11	0,14826	10,827	-0,51569	11,859	90,7
B	2013/04/10 00:47:00	2013/04/10 13:44:00	164,73	78,31	2,43	-4,98E-16	-6,5582E-12	0,78736	10,165	7,3684	-31,764	21,6
B	2013/04/10 02:44:00	2013/04/10 13:05:00	164,98	52,87	4,46	2,4004E-15	9,0292E-11	0,03859	11,782	8,525	38,081	6,1
A	2013/04/16 15:56:00	2013/04/17 06:51:00	57,34	33,01	1,87	-2,6563E-14	-1,7935E-13	1,7574	4,7769	4,1414	-2,7459	4,4
A	2013/04/16 17:19:00	2013/04/16 23:00:00	112,67	7,44	9,31	7,663E-14	1,5219E-11	0,31018	7,1253	-2,5671	228,33	2,1

Table 2 continued from previous page

STEREO	Beginning (UTC)	End (UTC)	ϕ (deg)	θ (deg)	z_0	B_0^{Θ}	B_0^{ζ}	C	η	α	λ	t_0 (days)
A	2013/04/18 06:13:00	2013/04/18 10:48:00	16,44	0,61	-0,08	6,6593E-16	2,137E-11	1,4564	4,5833	-4,7643	24,645	8,7
A	2013/04/23 08:29:00	2013/04/23 17:05:00	32,88	61,42	-0,07	1,2931E-16	5,0885E-12	0,34827	11,949	5,0821	12,68	11,1
B	2013/04/24 16:40:00	2013/04/24 21:20:00	35,32	128,08	-0,88	-5,1418E-14	-6,451E-15	2,8376	2,9006	1,1219	-1,8564	2,2
A	2013/05/04 01:52:00	2013/05/04 14:07:00	126,42	154,6	-11	-1,9349E-13	5,2117E-16	0,15262	11,796	923,2	75,843	0,8
B	2013/05/04 17:21:00	2013/05/05 06:57:00	76,01	8,5	2,49	1,5872E-14	-1,4815E-14	3,7486	0,17342	0,65363	6,0684	2,1
B	2013/05/07 04:58:00	2013/05/07 11:19:00	54,79	28,72	1,49	6,7409E-16	3,6945E-14	1,7728	4,9895E-08	0,81974	6,7895	1,4
B	2013/05/07 12:38:00	2013/05/07 18:36:00	43,14	78,16	0,4	-9,6287E-15	-1,4684E-17	2,9991	6,9616E-07	-0,24211	2,6439	6,4
A	2013/05/13 02:54:00	2013/05/13 14:48:00	165	126,05	-1,32	3,9547E-16	1,2054E-11	2,3566	9,8157	-19,511	122,91	2,7
A	2013/05/14 04:04:00	2013/05/14 14:34:00	47,46	0,72	0,47	-1,3093E-14	-3,5887E-14	11,313	8,6777	0,37446	-8,5101	6
B	2013/05/16 02:01:00	2013/05/16 09:08:00	104,32	0,74	-65,32	-2,1539E-16	-3,0038E-16	0,08522	5,0769	0,00284	-0,07837	25
B	2013/05/17 17:08:00	2013/05/17 23:41:00	15	130,48	0,02	-8,2466E-15	3,3811E-16	1,1242	1,8089	-0,09423	-0,08426	8
B	2013/05/21 14:18:00	2013/05/21 22:22:00	119,58	81,73	0,41	1,1158E-15	-1,8249E-13	1,937	4,5121	3,3267	-1,0374	2,6
B	2013/05/22 18:52:00	2013/05/23 05:50:00	163,85	20,04	1,84	1,361E-14	1,9903E-18	2,4136	3,9812	0,0003	-27,657	-2,6
A	2013/05/29 21:05:00	2013/05/30 06:30:00	59,21	93,62	5,86	-1,9003E-14	-2,1547E-11	1,8435	6,7588	-147,4	-343,95	3,7
A	2013/05/30 14:46:00	2013/05/31 10:18:00	100,86	75,34	-5,34	4,0996E-15	1,4486E-15	5,7169	8,5163	-7E-05	-1,6056	11,8
B	2013/06/03 02:10:00	2013/06/03 12:56:00	158,44	38,75	-1,65	-4,9112E-16	-9,5605E-10	0,41336	13,16	65,532	-46,104	4,5
B	2013/06/15 22:14:00	2013/06/16 07:32:00	68,86	172,45	-13,01	1,2342E-15	1,1099E-14	1,0899	2,6397	0,02372	3,3453	8,2
B	2013/06/19 22:10:00	2013/06/20 02:37:00	102,29	55,49	-0,58	2,3572E-16	-2,354E-16	0,20042	20	-11,543	2,4008	6
A	2013/06/20 12:00:00	2013/06/21 09:06:00	95,66	92,37	6,52	-1,4003E-14	-5,9385E-11	9,2749	7,4311E-10	2126,1	-323,5	4,7
B	2013/07/05 07:16:00	2013/07/05 16:46:00	125,26	7,59	14,65	-5,7201E-14	-3,8193E-11	0,57564	8,3142	18,878	-107,18	5,9
B	2013/07/06 16:17:00	2013/07/07 01:56:00	129,07	56,19	-1,1	1,0883E-15	-8,3749E-10	0,02926	16,881	3,648	-157,01	-12,2
B	2013/07/21 22:31:00	2013/07/22 08:23:00	62,68	119,73	6,63	-9,4467E-16	-2,1009E-13	0,90962	2,8662E-10	-0,15031	-70,137	14,6
A	2013/07/25 20:19:00	2013/07/26 12:12:00	104,35	141,7	-1,18	2,4943E-14	2,0494E-13	6,3877	4,9892E-11	-4,5277	35,679	3,7
A	2013/07/26 23:41:00	2013/07/27 12:30:00	15	1,41	-17,96	-1,0402E-13	-2,8925E-16	1,4223	0,52928	0,07515	-0,05837	7,7
A	2013/07/28 08:45:00	2013/07/28 23:20:00	30,03	159,53	1,5	-1,6947E-14	-5,1737E-17	0,00118	12,995	-1,7416	-2,9496	5,3
A	2013/08/10 21:57:00	2013/08/11 14:44:00	97,89	134,37	-3,75	1,0097E-15	3,67E-12	0,31507	12,382	74,18	26,451	4,4
B	2013/08/22 13:45:00	2013/08/22 20:06:00	52,9	114,51	-0,01	-1,0882E-14	-3,5765E-12	0,02289	1,7169	0,00055	-1987,8	6
A	2013/08/23 04:49:00	2013/08/23 20:16:00	132,19	61,31	2,89	-2,4613E-14	-5,2808E-13	0,00587	0,74787	-0,00837	-377,39	2,9
A	2013/09/01 10:03:00	2013/09/01 17:56:00	54,24	175,82	8,13	-1,2697E-14	-5,096E-12	0,13296	6,5864	-0,00022	-92,611	4,3
B	2013/09/04 18:30:00	2013/09/04 21:24:00	50,29	35,4	-0	-5,0545E-14	-9,9378E-14	44,832	20	0,90765	-41,009	2,6
B	2013/09/10 07:17:00	2013/09/10 11:02:00	110,22	157,8	-0	-1,3873E-13	9,286E-11	5,4664	9,895	58,209	1981	3,2
B	2013/09/16 05:03:00	2013/09/16 20:45:00	62,68	136,16	-3,45	-3,0941E-16	-7,4612E-13	1,4493	8,8293	-5,3494	-35,442	3,2
A	2013/09/16 21:25:00	2013/09/17 12:52:00	165	115,31	1,92	2,2931E-14	-6,6609E-14	4,491	2,2204E-15	1,4453	4,8371	1,4
A	2013/09/17 05:55:00	2013/09/17 11:50:00	142,82	161,12	3,27	1,226E-14	1,0643E-14	4,5326	0,56008	-0,04158	6,8637	5,4
A	2013/09/21 21:01:00	2013/09/22 21:22:00	151,95	39,33	5,63	3,2108E-14	7,5234E-13	3,5266	2,1838	-6,34	4,3822	5,3
A	2013/09/22 08:04:00	2013/09/22 21:16:00	132,13	54,42	-4,25	1,9251E-14	1,1752E-15	6,8093	8,121	-0,68927	-0,64318	4,9
A	2013/10/05 02:26:00	2013/10/05 17:25:00	85,55	98,28	-7,02	-5,0203E-14	-2,5692E-11	1,2277	12,954	4472,5	-47,663	7
A	2013/10/06 11:56:00	2013/10/06 20:27:00	86,44	128,87	7,14	-4,2618E-16	1,925E-13	4,8901	6,8421E-08	0,57546	6,1454	10,3
A	2013/10/07 12:14:00	2013/10/07 19:16:00	74,27	156,11	16,49	-2,4027E-17	1,516E-11	7,6119	2,8539E-08	0,00027	8,3026	6,9
B	2013/10/08 18:30:00	2013/10/09 00:18:00	147,51	26,97	-13,53	7,9691E-13	-1,5806E-12	1,4892	3,9523	-13,827	-133,49	3,5
B	2013/10/09 05:30:00	2013/10/09 14:29:00	19,39	44,97	0,07	9,1473E-15	8,8367E-14	2,6115	1,5975	-8E-05	69,045	5,1
A	2013/10/17 17:41:00	2013/10/18 07:33:00	71,51	78,11	-5,68	-2,1597E-16	2,3917E-17	11,153	15,999	2,9168	-3,7031	5,1
B	2013/10/22 11:38:00	2013/10/22 21:07:00	30,83	29,24	-1,32	-1,3583E-14	4,1423E-12	0,44324	0,4128	0,02413	3279	-11

Table 2 continued from previous page

STEREO	Beginning (UTC)	End (UTC)	ϕ (deg)	θ (deg)	z_0	B_0^{Θ}	B_0^{ζ}	C	η	α	λ	t_0 (days)
A	2013/10/23 11:58:00	2013/10/23 19:00:00	68,02	57,57	1,08	-6,2126E-16	-1,1612E-13	5,0061	3,7576	-0,98117	0,71424	29,3
A	2013/11/02 08:35:00	2013/11/03	159,27	103,45	2,9	-4,7471E-16	1,8058E-12	0,97384	1,8691	-0,44131	526,37	5,6
A	2013/11/05 00:05:00	2013/11/05 13:00:00	162,49	142,39	-1,92	-5,4927E-14	-2,1093E-12	0,12783	1,0765	0,05387	-1188,1	3,3
B	2013/11/06 17:44:00	2013/11/07 02:45:00	91,28	90,44	-7,05	-4,6696E-16	-2,3734E-10	0,06736	10,619	93,718	-1944,8	10,8
A	2013/11/12 06:24:00	2013/11/12 10:50:00	165	0	0,4	1,0894E-15	1,0702E-16	1,8418	3,7035	0,70496	-1,1045	52,8
A	2013/11/14 09:19:00	2013/11/14 13:40:00	70,69	125,24	1,55	-2,0475E-16	-1,3514E-16	3,2286	4,7258	3,0207	4,0958	12,4
A	2013/11/19 03:27:00	2013/11/19 12:37:00	153,19	69,29	-0,13	-1,7602E-14	-2,5698E-11	0,05535	10,155	0,13807	-182,2	3,9
A	2013/11/19 17:17:00	2013/11/19 21:19:00	115,56	66,15	0,7	3,2196E-16	5,8224E-16	2,0646	9,603	15,414	-2,4669	-14,2
B	2013/11/21 17:18:00	2013/11/22 02:24:00	122,89	67,25	0,31	-9,0135E-16	-4,7626E-16	2,6671	4,7086	0,17624	0,32523	30,9
B	2013/11/24 05:33:00	2013/11/24 11:21:00	113,33	173,46	26,99	-5,6715E-14	1,0629E-15	0,3246	7,3206	1,7494	-0,0478	6,2
A	2013/12/02 09:35:00	2013/12/02 22:19:00	15,35	89,15	0,35	-5,9825E-14	9,7181E-13	0,11994	2,528	-0,05876	372,83	4,5
A	2013/12/03 21:20:00	2013/12/04 07:29:00	112,6	147,39	-1,53	4,4109E-15	5,9567E-10	0,00727	12,285	0,03352	1415,7	11,6
A	2013/12/05 04:13:00	2013/12/05 17:07:00	22,28	14,32	-2,23	-1,7152E-16	5,5062E-10	0,15963	8,43	-18,53	42,582	19,2
B	2013/12/09 11:55:00	2013/12/10 00:00	116,61	156,64	-7,41	2,5882E-13	-3,4737E-13	1,2997	2,8488E-07	-3,802	-122,38	1,4
B	2013/12/10 09:43:00	2013/12/10 18:29:00	88,92	78,59	-5,04	-5,9592E-14	-7,7647E-13	1,9873	2,5769	8,0831	-571,57	3,6
A	2013/12/14 15:20:00	2013/12/14 19:05:00	19,34	54,62	1,21	4,1133E-17	2,0417E-17	8,8686	2,3121	-0,00125	-0,44545	-15,9
A	2013/12/28 09:30:00	2013/12/29 02:50:00	150,73	29,67	-0	-2,9339E-15	-3,5964E-10	0,04112	9,9184	0,44183	-174,74	6
B	2013/12/29 09:31:00	2013/12/29 18:05:00	93,71	88,57	6,8	1,6536E-14	-1,7547E-11	7,1964	3,7597E-06	14570	-862,98	1,5
B	2013/12/31 16:48:00	2014/01/01 08:57:00	163,25	110,11	0,75	-2,5531E-15	-4,2103E-15	4,3915	0,0012834	-0,05771	-0,04306	11,6
B	2013/12/31 22:56:00	2014/01/01 05:14:00	145,49	82,03	0,2	-9,5174E-15	-4,0352E-13	0,05122	2,1214	-0,00168	-190,47	7,7
B	2014/01/11 09:03:00	2014/01/11 15:46:00	158,45	142,86	-1,43	-2,1583E-15	-1,4265E-09	0,00173	14,273	0,71525	-15,462	-58,4
B	2014/01/11 09:04:00	2014/01/11 16:00:00	80,86	18,34	4,27	3,7759E-16	-3,0444E-13	0,04223	1,5076	0,0043	-152,63	-11,6
B	2014/01/29 22:13:00	2014/01/30 08:33:00	78,97	36,48	8,14	-1,7499E-14	1,414E-13	0,22483	7,2523E-07	0,00011	41,763	2,6
A	2014/02/03 04:15:00	2014/02/03 12:04:00	142,66	101,7	0,63	2,1585E-18	-4,2724E-14	3,3807	4,4322	0,44982	-0,14593	47,8
A	2014/02/05 19:12:00	2014/02/06 03:22:00	98,65	44,25	1,64	-6,5875E-16	-5,2711E-10	0,1098	17,016	-61,304	-142,94	3,9
A	2014/02/05 20:02:00	2014/02/06 03:16:00	68,01	25,42	2,67	3,6001E-14	2,8597E-11	0,72774	11,029	-95,517	39,45	3,6
B	2014/02/06 13:01:00	2014/02/06 23:58:00	94,81	90,77	7,45	-7,9048E-16	5,7257E-08	1,5424	19,326	-2070,5	-1825,6	0,6
A	2014/02/08 07:23:00	2014/02/08 14:14:00	78,92	118,46	1,24	6,1409E-18	2,6002E-16	6,0828	2,3397E-07	2,0439	-5,2109	4,4
A	2014/02/08 09:28:00	2014/02/08 13:56:00	76,79	27,45	3,32	3,0781E-16	9,7127E-11	0,04364	8,6548	-1,1653	1632,3	2,3
A	2014/02/17 05:13:00	2014/02/17 15:29:00	60,88	99,77	-1,45	-1,4228E-14	1,3641E-14	1,5502	5,7557E-07	0,17587	6,4264	6,1
A	2014/02/26 01:27:00	2014/02/26 07:49:00	54,55	16,36	9,53	-1,0092E-14	1,3475E-13	0,17131	5,794	-0,0013	3,5013	-7,4
B	2014/03/04 08:53:00	2014/03/04 16:53:00	26,05	162,53	-7,72	-9,9784E-15	-4,2994E-16	0,49715	2,0254	0,03258	-0,13859	14,2
B	2014/03/04 22:04:00	2014/03/05 10:19:00	69,45	11,21	4,44	1,6488E-16	-9,2542E-13	2,6391	7,8502	-0,42363	-1,614	8
B	2014/03/08 20:43:00	2014/03/09 04:08:00	102,78	62,15	1,84	-2,2039E-14	-2,0925E-14	4,5626	3,7459	-28,489	67,196	2,4
A	2014/03/12 04:35:00	2014/03/12 12:08:00	102,53	33,46	-2,87	1,1031E-16	1,51E-08	0,06399	19,72	-316,47	1051,6	2,8
A	2014/03/12 17:05:00	2014/03/13 13:13:00	26,69	104,53	0,18	3,5613E-16	-4,9231E-13	12,281	0,4496	-0,44363	1,7084	5
B	2014/03/15 05:51:00	2014/03/15 10:31:00	132,48	160,34	-0,76	-4,4383E-14	-2,7537E-10	0,51631	11,582	34,218	-360,68	7,7
B	2014/03/15 11:13:00	2014/03/15 18:04:00	64,18	126,42	-0,17	-9,6566E-14	8,3922E-12	1,6485	1,1541	1,1492	6742,9	0,4
B	2014/03/18 01:52:00	2014/03/18 10:31:00	83,28	132,29	-9,97	-2,7375E-16	-3,2519E-15	0,00441	1,1569E-12	0,0017	-0,04442	360,9
B	2014/03/18 12:35:00	2014/03/18 21:35:00	133,15	112,47	0,05	1,1431E-14	1,1991E-10	0,07166	13,201	1,3585	193,77	4,8
B	2014/03/18 23:23:00	2014/03/19 08:30:00	140,28	152,14	0,02	5,4009E-16	1,2278E-15	3,4597	1,9155	-0,05221	0,68635	-13,5
B	2014/03/26 18:53:00	2014/03/27 01:21:00	133,17	116,21	-0,01	-1,6023E-15	-3,4287E-13	0,13884	4,5232	0,01237	-54,043	7
B	2014/03/27 03:56:00	2014/03/27 11:26:00	15	0	-38,21	-2,179E-16	-1,3602E-14	0,60055	1,886	0,00437	-0,53186	49,5

Table 2 continued from previous page

STEREO	Beginning (UTC)	End (UTC)	ϕ (deg)	θ (deg)	z_0	B_0^{Θ}	B_0^{ζ}	C	η	α	λ	t_0 (days)
B	2014/03/27 04:41:00	2014/03/27 11:19:00	115,32	36,89	1,95	5,4009E-16	5,4628E-16	2,3457	4,2064	-0,44898	0,25615	-13,5
B	2014/03/29 05:38:00	2014/03/29 10:45:00	142,44	30,97	0,29	2,1508E-15	-2,3798E-15	2,5725	5,1161	-2,8593	-0,09873	7,7
A	2014/03/31 02:51:00	2014/03/31 12:05:00	165	0,25	-78,4	4,9242E-14	3,3113E-16	0,17268	0,60087	0,00063	0,99884	2,2
A	2014/03/31 08:35:00	2014/03/31 12:33:00	56,34	136,93	2,25	-6,4887E-14	2,5225E-12	0,00292	5,4459	-0,02153	194,86	2,7
B	2014/03/31 19:24:00	2014/04/01 04:17:00	70,9	42,72	0,74	5,2186E-15	-8,6247E-13	4,2301	6,4481	-3,1784	-17,996	7,2
A	2014/04/01 15:39:00	2014/04/01 21:09:00	90,12	30,78	0	-5,345E-16	-1E-07	11,167	17,835	-1011,8	-17491	4,8
B	2014/04/06 01:13:00	2014/04/06 05:45:00	64,42	69,43	3,24	9,2616E-14	-2,3458E-17	4,2675	3,009	-45,246	-116,89	2,3
A	2014/04/10 07:29:00	2014/04/10 12:51:00	77,69	125,17	3,42	1,2464E-16	-1,1297E-11	0,39144	20	-45,863	-0,63149	10,9
A	2014/04/12 12:24:00	2014/04/12 18:03:00	116,05	142,41	4,57	2,1622E-14	8,587E-14	0,01459	4,7635	0,01422	13,124	3,2
B	2014/04/12 21:02:00	2014/04/13 22:04:00	148,46	120,47	-6,98	3,0745E-14	-3,3829E-10	0,49389	9,2321	-150,83	-2306,5	4,1
B	2014/05/09 00:07:00	2014/05/09 21:35:00	52,76	110,35	2,59	6,0608E-16	3,8073E-11	0,27845	13,328	-55,711	47,774	3,7
A	2014/05/11 20:26:00	2014/05/12 03:08:00	48,93	38,41	-0,47	-1,1854E-14	-9,2208E-09	0,00521	15,297	-1,1706	-1796,5	8,2
A	2014/05/12 09:20:00	2014/05/12 15:01:00	99,38	30,95	4,21	-1,8997E-13	-7,0382E-11	0,92361	9,4984	300,08	-301,89	3,1
A	2014/05/12 20:36:00	2014/05/13 05:44:00	122,21	0,68	26,64	-9,45E-16	-1,205E-13	0,2701	6,2802	0,01058	-0,95056	28,7
A	2014/05/14 18:56:00	2014/05/15 04:19:00	40,95	54,3	2,34	-5,0264E-15	6,3432E-13	0,44258	1,0816E-07	-0,09147	468,9	2,5
A	2014/05/20 23:31:00	2014/05/21 08:18:00	145,12	172,87	7,66	-2,1689E-15	1,4347E-12	0,04368	5,3212	0,00206	18,69	23,2
B	2014/05/28 05:23:00	2014/05/28 12:59:00	90,32	1,33	14,31	3,5254E-16	-3,957E-12	0,05454	13,117	-0,17506	-3,849	-40,1
B	2014/05/29 07:44:00	2014/05/29 13:10:00	103,31	1,57	28,3	-3,7357E-16	-9,6555E-10	0,22038	18,018	2,0844	-29,286	4

Table 2: List of FRs observed by STEREO from 2007 to 2014 accompanied by the Hidalgo's model fitting parameters.